Identifying genetic determinants of impaired PfEMP1 export in *Plasmodium falciparum*-infected erythrocytes

Aaron T. Neal
Green Templeton College
University of Oxford

A thesis submitted for the degree of
Doctor of Philosophy

Michaelmas 2014

Abstract

Identifying genetic determinants of impaired PfEMP1 export in *Plasmodium falciparum*-infected erythrocytes

Aaron T. Neal
Green Templeton College
A thesis submitted for the degree of *Doctor of Philosophy*
Michaelmas 2014

The virulence of *Plasmodium falciparum* is largely attributed to the ability of asexual blood-stage parasites to cytoadhere to the microvascular endothelium of the human host. This pathogenic behavior is mediated by the primary parasite virulence factor *P. falciparum* erythrocyte membrane protein 1 (PfEMP1), an understanding of which is crucial to develop interventions to ameliorate the morbidity and mortality of *P. falciparum* malaria. The work presented in this thesis describes the application of a phenotype-to-genotype experimental approach to identify novel parasite proteins involved in the trafficking and display of PfEMP1. Guided by the overall hypothesis that the *in vitro* culture-adapted parasite line 3D7 harbors 1 or more genetic determinants of impaired PfEMP1 trafficking, surface PfEMP1 levels were first measured in 3D7, the presumably trafficking-competent parasite line HB3, and 16 unique progeny from an HB3 x 3D7 genetic cross (**chapter 2**). These phenotypes were then combined with genome-wide SNP data in QTL analysis to identify genetic polymorphisms potentially responsible for the impaired trafficking in 3D7 (**chapter 3**). A near-significant QTL containing a single protein-coding gene, the putative kinesin *Pf3D7_1245600*, was identified, characterized, and investigated in CRISPR-Cas9-driven allele-exchange parasite transfection experiments to establish a causal link between the gene and PfEMP1 trafficking (**chapter 4**). The parasite transfections were unsuccessful, but the potential role of *Pf3D7_1245600* in PfEMP1 trafficking was indirectly assessed through the disruption of microtubules with colchicine (**chapter 4**), which significantly impacted the surface PfEMP1 levels of HB3 but not 3D7. The findings of this thesis suggest that kinesins and microtubules may play previously unconsidered roles in the regulation, production, or trafficking of PfEMP1.

Statement of work performed

Under the guidance of Christopher Newbold, Ph.D., at the University of Oxford and Rick Fairhurst, M.D., Ph.D., at the National Institutes of Health, the experiments detailed in this thesis were conceived, conducted, and analyzed by me, with a few notable exceptions. In chapter 2, the scanning electron microscopy work was performed in the Electron Microscopy Unit of the NIAID Rocky Mountain Laboratories by Bryan Hansen, B.S., using samples I had prepared. In chapter 3, the genetic maps for the HB3 x 3D7 genetic cross progeny were prepared by Lisa Ranford-Cartwright, Ph.D., at the University of Glasgow using genotype data she previously obtained. Dr. Ranford-Cartwright also performed the QTL analysis and provided me with the relevant results. In chapter 4, the DNA sequencing was performed by Macrogen Corporation in Rockville, Maryland, USA, using samples I had obtained. Also in chapter 4, the pCas9 and pCGT vector backbones used to develop complete plasmids for parasite transfection experiments were originally constructed by Richard Eastman, Ph.D., at the National Institutes of Health. This thesis, in its entirety, was written solely by me with minor editing by Professor Newbold and Dr. Fairhurst.

Acknowledgements

The work presented in this thesis could not have been accomplished without the significant support and guidance of many individuals. First and foremost, I would like to thank Chris Newbold and Rick Fairhurst for generously providing me with the opportunity to work under them. I have benefited immensely from their knowledge, expertise, guidance, mentorship, and unwavering support. I would also like to thank the numerous members of the Newbold and Fairhurst laboratories, whose encouragement, advice, and comradery played an unquestionable role in my success as a student and scientist. I would like to acknowledge the National Institutes of Health Oxford-Cambridge Scholars Program for its continued financial and administrative support, as well as the NIAID Laboratory of Malaria and Vector Research and the Weatherall Institute of Molecular Medicine for hosting me and offering scientific support as I pursued my doctoral research. Last, but certainly not least, I would like to thank my family, friends, and Catherine for their constant support and encouragement in all that I do and hope to accomplish in life.

Table of Contents

List of Figures

List of Tables

Abbreviations

Ab	antibody
APC	allophycocyanin
APS	ammonium persulphate
ATS	acidic terminal segment
BLAST	basic local alignment search tool
Cas9	CRISPR-associated protein 9
CD36	cluster of differentiation 36
CIDR	cysteine-rich interdomain region
CRISPR	clustered, regularly interspaced, short palindromic repeats
CSA	chondroitin sulphate A
DBL	Duffy binding-like
ddH_2O	double-distilled H_2O
DIC	differential interference contrast
DMSO	dimethyl sulfoxide
EDTA	ethylenediaminetetraacetic acid
EF1α	elongation factor 1 alpha
EPCR	endothelial protein C receptor
FACS	fluorescence-activated cell sorting
FBS	fetal bovine serum
G6PD	glucose-6-phosphate dehydrogenase
GMFI	geometric mean fluorescence intensity
Hb	hemoglobin
HBSS	Hank’s balanced salt solution
IC_{50}	half maximal inhibitory concentration
ICAM-1	intracellular adhesion molecule 1
IgG	immunoglobulin G
KAHRP	knob-associated histidine-rich protein
KO	knockout
LB	Luria broth
LOD	logarithm of odds
MTDR	MitoTracker® Deep Red FM
MTG	MitoTracker® Green FM
NCBI	National Center for Biotechnology Information

NTS	N-terminal segment
PAGE	polyacrylamide gel electrophoresis
PAM	protospacer adjacent motif
PBS	phosphate-buffered saline
pCas9	plasmid expressing Cas9
pCGT	plasmid expressing the CRSIPR guide RNA and template
PECAM-1	platelet endothelial cell adhesion molecule 1
PEXEL	*Plasmodium* export element
PfCRT	*P. falciparum* chloroquine-resistance transporter
PfEMP1	*P. falciparum* erythrocyte membrane protein 1
PHIST	*Plasmodium* helical interspersed sub-telomeric
PNEP	PEXEL-negative exported proteins
pRBC	parasitized red blood cell
PTEX	*Plasmodium* translocon for export
QTL	quantitative trait locus
RBC	red blood cell
RIFIN	repetitive interspersed family protein
SDS	sodium dodecyl sulfate
SG	SYBR® Green I
SMART	simple modular architecture research tool
SNP	single-nucleotide polymorphism
SOC	super optimal broth with catabolite repression
STEVOR	subtelomeric, variable open reading frames protein
SV40-NLS	simian virus 40 nuclear localization signal
TBE	Tris-borate-EDTA
TBS	Tris-buffered saline
TE	Tris-EDTA
TEMED	N, N, N’, N’-tetraethylenediamine
TPCK	tosyl phenylalanyl chloromethyl ketone
uRBC	uninfected red blood cell
VCAM-1	vascular cell adhesion molecule 1
v/v	volume per volume
w/v	weight per volume

In this, O Nature, yield I pray to me.
I pace and pace, and think and think, and take
The fever'd hands, and note down all I see,
That some dim distant light may haply break.

The painful faces ask, can we not cure?
We answer, No, not yet; we seek the laws.
O God reveal thro' all this thing obscure
The unseen, small, but million-murdering cause.

–"Indian Fevers" by Sir Ronald Ross

Introduction

1.1 Malaria

Malaria is a tropical infectious disease caused by protozoan parasites of the genus *Plasmodium*. The disease, which has been a significant source of morbidity and mortality for millennia, is responsible for an estimated 124 to 283 million malaria episodes each year, of which up to 755,000 result in death[1]. This burden is shouldered exclusively by the tropical climate regions of South America, Asia, and Africa, the last of which disproportionally experiences the majority of severe cases and death, primarily in children under 5 years old[1]. This occurrence can be largely attributed to the intense and widespread transmission of the most lethal of the 5 *Plasmodium* species that cause disease in humans, *Plasmodium falciparum*.

1.1.1 ***Plasmodium falciparum*** **life cycle**

Though the parasites responsible for malaria have ancient origins and likely spread from gorillas to humans thousands of years ago in Africa[2–4], it was not until the French military surgeon Laveran's studies in the 1880s that the parasite was first identified in human blood[5]. More than a decade later, the mode of *Plasmodium* transmission via mosquitoes was demonstrated in birds by the British military surgeon Ross[6,7] and in humans by the Italian physicians Grassi, Bignami, and Bastianelli[8]. The mosquito species responsible were further shown to be those specifically belonging to the genus *Anopheles*[9,10], which are capable of transmitting the causative parasites of human malaria–*P. vivax*, *P. ovale*, *P. malariae*, *P. knowlesi*, and the most virulent species, *P. falciparum*[11,12].

Like all species of *Plasmodium*, the life cycle of *P. falciparum* can be divided into distinct sexual and asexual phases (Figure 1.1). The sexual phase begins with the commitment of an asexual form to develop into a female macrogametocyte or a male microgametocyte prior to reinvasion[13]. This development occurs over the course of 8 to 12 days, with gametocytes progressing through 5 morphologically identifiable stages before being ready to infect the anopheline vector[14,15]. When a female *Anopheles* mosquito takes a blood meal from a *P. falciparum*-infected individual, the haploid gametocytes are ingested into the mosquito midgut where fertilization occurs. This leads to the formation of a diploid zygote that subsequently develops into an ookinete. It is at this point in the life cycle that genetic recombination occurs, giving rise to much of the *P. falciparum* genetic diversity observed in endemic regions[16]. The ookinete then exits the midgut to form an oocyst, initiating the production of thousands of sporozoites over the next 10 to 14 days. Once fully-formed, the sporozoites migrate to the mosquito salivary glands and wait for the anopheline to take a blood meal[17].

Upon probing and biting another human, the mosquito injects sporozoite-laden saliva into the subcutaneous tissue. Within minutes, the generally small dose of infective sporozoites migrate into the bloodstream, travel to the liver, and traverse multiple hepatocytes before invading one for further development[18]. This invasion process is primarily mediated by the binding of the circumsporozoite protein and the thrombospondin-related adhesive protein to heparin sulfate proteoglycans on hepatocytes[19,20]. Once inside their chosen cells, sporozoites begin the process of differentiation, resulting in the production of tens of thousands of merozoites over the course of 5 to 7 days. After this symptomless period, merozoites rupture out of the infected hepatocytes and into the hepatic sinuses, where they encounter and invade circulating RBC host cells. While all *Plasmodium* parasites generally adhere to this developmental timeline, *P. vivax* and *P. ovale* are capable of persisting asymptomatically as hypnozoites, leading to relapse infections months to years after the initial infection[21,22].

The egress of invasion-competent merozoites into the bloodstream initiates the continuous asexual phase of the *P. falciparum* life cycle, which causes the clinical symptoms that characterize malaria[23]. Freed merozoites recognize RBCs through the interaction of parasite surface receptors, such as the reticulocyte binding protein homologs, the erythrocyte binding antigens, and other merozoite surface proteins, with RBC surface receptors, such as basigin, sialic acid, and the glycophorins[24,25]. This recognition prompts the merozoite to attach and reorient itself so that an irreversible tight junction can be formed between its apical end and the RBC membrane. Apical organelles, including rhoptries, micronemes, and dense granules, as well as molecular motors aid the parasite as it forces its way into the RBC, enveloping itself in a portion of the RBC membrane that ultimately becomes a parasitophorous vacuole[26]. This vacuole, while separating the parasite from the RBC cytosol, presents an additional membrane that the parasite must overcome in order to modify its RBC environment.

Within the RBC, merozoites become ring-stage forms, so named for their ring-like appearance in Giemsa-stained blood smears[5]. The continued development of parasites relies on nutrient uptake from the bloodstream, mediated through the plasmodial surface anion channel[27], and the catabolism of hemoglobin for amino acids, with the exception of isoleucine, to sustain growth and preserve the osmotic balance of the RBC environment[28,29]. To overcome the problem of toxic heme accumulation resulting from hemoglobin digestion, parasites effectively inactivate the compound by crystallizing it into a stable form called hemozoin, a process commonly disrupted by chloroquine and related antimalarials[30]. As the parasite progresses from the ring stage to the trophozoite stage over the course of 24 hours, it extensively remodels its RBC environment to enable pRBC cytoadherence to the microvascular endothelium. This sequestering behavior, which accounts for the presence of only ring-stage parasites and gametocytes on diagnostic blood smears, pulls pRBCs out of circulation in order to avoid clearance by the spleen[31].

The parasite continues to mature from the trophozoite stage to the schizont stage, where several rounds of mitotic replication produce 16 to 40 new daughter merozoites[32,33].

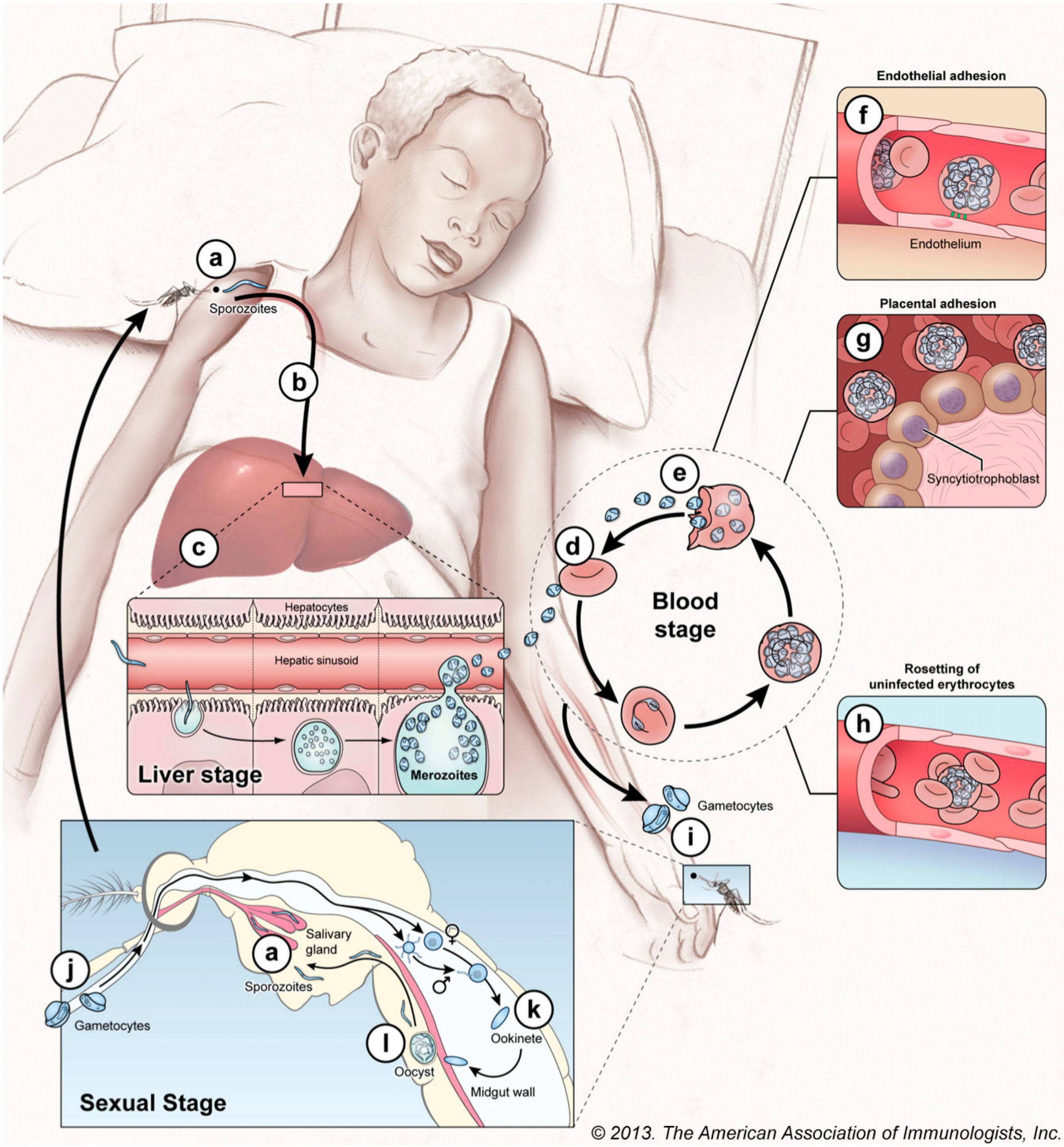

© 2013. The American Association of Immunologists, Inc.

Figure 1.1: Complete life cycle of *P. falciparum*. The life cycle of *P. falciparum* parasites occurs in 3 distinct stages across 2 radically different hosts. Parasite behavior during the asexual blood stage is responsible for the clinical symptoms that characterize malaria. This figure is reproduced from [34].

All of these merozoites, like the original one they developed from, are equipped to recognize and invade new RBCs upon egress from the pRBC at the end of the approximately 48-hour intraerythrocytic cycle, thus perpetuating the asexual phase. This expansion from 1 parasite to at least 16 results in an exponential increase in parasite density over the course of infection. Prior to egress, the daughter merozoites in some schizonts fully commit to either male or female gametocytogenesis, beginning the transformation upon reinvasion of a new RBC and initiating the sexual phase[35]. The commitment to gametocytogenesis is likely triggered by a variety of possible factors, including inhospitable host conditions[36] and parasite-derived microvesicles[37,38].

1.1.2 Malaria morbidity and mortality

The clinical symptoms of malaria are the direct consequence of infection with at least 1 of the 5 *Plasmodium* species that propagate in humans. In regions of malaria endemicity (Figure 1.2), individuals are constantly at risk of naturally acquiring infections through exposure to *P. falciparum*-infected *Anopheles* mosquitoes. The rate at which individuals are bitten, termed the entomological inoculation rate[39–41], directly influences the number of individuals that harbor parasites in a given population, termed the parasite prevalence rate[42,43]. These rates, in turn, are directly influenced by regional climate, vector species prevalence[44], proximity to larval habitats[45], individual attractiveness to mosquitoes[46], and epidemiological control measures, such as the usage of bed nets[47]. To understand the global burden of malaria, parasite prevalence rates in the under-10 age group are used to classify regions as hypoendemic if <10%, mesoendemic if 10 to 49%, hyperendemic if 50 to 75%, and holoendemic if >75%[48]. Individuals in regions of intense malaria transmission may be bitten by multiple infected mosquitoes, though not every infectious bite will result in a clinical episode of malaria[49]. Individuals who are bitten and remain asymptomatic may still

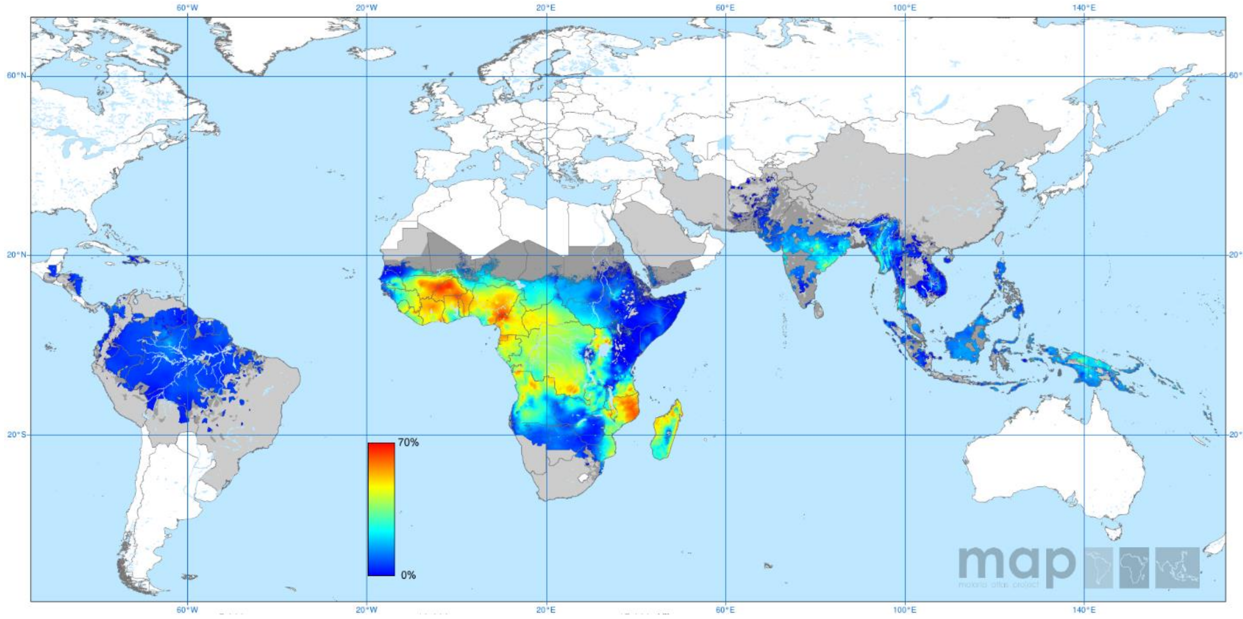

Figure 1.2: Global endemicity of *P. falciparum* in 2010. The parasite prevalence rate of 2- to 10-year old children in the general population in 2010 was estimated globally and mapped to accurately determine the endemicity of *P. falciparum* malaria. This figure was originally generated as part of the Malaria Atlas Project[50].

present with low levels of circulating parasites, potentially serving as a reservoir of sexual stage parasites for continued transmission[51,52].

If enough *P. falciparum* sporozoites are injected by an infected mosquito, and if those sporozoites reach the liver and produce merozoites, then an uncomplicated malaria infection may result. The simple presence of parasitemia is not itself associated with symptoms, but as parasites begin to multiply exponentially, symptoms may appear[53]. However, the correlation between parasite density and morbidity is not always clear, as very high circulating parasitemias do not necessarily result in a more severe disease state[54,55]. An individual with uncomplicated malaria generally experiences fever, chills, headache, and fatigue, all of which are accompanied by the detection of pRBCs in peripheral blood[56]. Occasionally, gastrointestinal symptoms such as vomiting and diarrhea may occur, and symptoms such as anemia or splenomegaly are common in infections that are able to persist. The paroxysms that have historically characterized malaria as a tertian fever may be seen in individuals suffering from *P. falciparum* infection, though they are most commonly associated with *P. vivax* infection today due to the greater developmental synchronicity of parasites in those infections[57,58].

Approximately 2% of uncomplicated malaria episodes progress to severe disease, the most notable manifestations being cerebral malaria[59], severe malarial anemia[60], and respiratory distress[61]. Although each of these conditions have their own associated clinical features, their occurrence in an infected individual is not mutually exclusive[62]; a fact that is considered in a recently developed severe malaria scoring system[63]. General symptoms of severe malaria can include shock, prostration, hypoglycemia, intense vomiting, jaundice, renal insufficiency, hyperpyrexia, and hemoglobinuria[56]. Cerebral malaria is qualitatively diagnosed using the Blantyre and Glasgow coma scales for children and adults, respectively. Ocular, motor, and verbal responsiveness are measured on a 0 to 5 scale ranging from unconscious to normal, with a diagnosis of cerebral malaria generally being made if a score is ≤ 2[56]. Severe malarial anemia is defined by the World Health Organization as the presence of a hemoglobin level <5 g/dL and may be further accompanied by secondary jaundice or renal failure[56]. Respiratory distress is characterized by hyperventilation and labored breathing, both of which result from metabolic acidosis and possibly vascular congestion due to mass parasite sequestration[64].

The progression to severe manifestations of malaria has been associated with factors such as age and malaria transmission intensity[65,66], with the most common observation being that children under 10 years old present most frequently with severe disease[67]. The risk of developing severe malaria generally decreases with age, but malaria-naïve adults and adults returning to endemic regions after several years away remain at risk[68]. Furthermore, recent reports of *P. vivax* infections meeting some of the World Health Organization criteria for severe malaria suggest that the condition may not be *P. falciparum*-

specific and could pose a greater threat in malaria-endemic regions outside of Africa[69–72]. Of the *P. falciparum* malaria episodes that progress to severe disease, only a small proportion result in death, though most individuals with severe malaria would die without medical intervention[56]. The general presence of acidosis, coma, convulsions, elevated blood urea nitrogen levels, and underlying chronic illnesses have all been associated with an increased risk of death[73,74].

In addition to uncomplicated and severe malaria, women become particularly susceptible to a unique manifestation of the disease during pregnancy[75]. This pregnancy-associated malaria mostly affects primigravidae, placing the mother at risk of anemia and hypertension, and placing the infant at risk of spontaneous abortion *in utero*, low birth weight, and immunologically mediated hemolysis due to increased sensitivity to *P. falciparum* antigens[76,77].

Individuals infected with *Plasmodium* parasites are generally diagnosed by microscopic evaluation of a Giemsa-stained peripheral blood smear[56]. In resource-poor settings, rapid diagnostic tests specific for histidine-rich protein 2 or lactate dehydrogenase released by blood-stage parasites can serve as an effective diagnostic substitute[56,78,79]. Once blood-stage parasites are observed or a positive rapid test is obtained, antimalarial drugs capable of radically curing infections are typically administered. These include relatively modern compounds such as chloroquine, sulfadoxine, primaquine, and artemisinin, as well as the much older therapeutic quinine[80]. With the emergence and subsequent spread of chloroquine-resistant *P. falciparum* parasites in the 1960s[81], strategies have been developed to decrease the likelihood of generating resistance against additional drugs. This is largely through the application of combination-therapy for malaria treatment, where 2 drugs with different mechanisms of action are used simultaneously so that parasites developing resistance to the first compound will retain susceptibility to the second compound[82].

To reduce malaria morbidity and mortality at the population level, vector control strategies such as insecticide-treated bed net distribution[83], indoor residual spraying of pesticides[84], and mosquito breeding habitat elimination[85] have been highly effective. Additionally, efforts to develop a protective *P. falciparum* malaria vaccine have seen recent success with the completion of initial phase III clinical trials with the candidate subunit vaccine RTS,S[86]. Though RTS,S has shown 30 to 50% protection when paired with the AS01 adjuvant[87], a recent whole organism vaccine, PfSPZ, based on the radiation-attenuated sporozoite-approach developed in the 1960s[88,89] has shown 100% protection with intravenous-administration in some groups following a homologous parasite challenge[90].

1.1.3 Pathogenesis of *Plasmodium falciparum* malaria

The pathogenesis of *P. falciparum* malaria involves both parasite- and host-derived components, enabling parasites to proliferate and cause disease while simultaneously evading the host immune system. At a very fundamental level, high circulating parasite densities can lead to the development of hypoglycemia due to *P. falciparum* metabolizing 30 to 75 times more plasma glucose than uRBCs[91,92]. The accumulation of lactic acid, a byproduct of glucose consumption, can result in acidosis and potentially lead to severe respiratory distress associated with mortality[93,94]. The rate of parasite multiplication is influenced by a number of factors, including the mean corpuscular hemoglobin concentration of RBCs, heritable parasite traits governing multiplication, and RBC selectivity[33]. In particular, the development of high parasitemias and severe malaria have each been associated with a lack of RBC selectivity among parasites[95], though these observations are not always consistent[96]. RBC-unselective behavior, as determined by the decreased occurrence of multiply-infected RBCs relative to what would be expected from a random Poisson distribution, results in rapidly expanding parasitemias due to merozoites invading any and all RBCs rather than a select subset[97]. The presence of multiply-infected cells, while generally suggestive of RBC-selective behavior, can also be explained by parasite rosetting behavior, where the pRBC surrounds itself with uRBCs that daughter merozoites can immediately enter upon egress[98]. This process is mediated by the binding of uRBC complement receptor 1 and heparin sulfate by the primary parasite virulence factor PfEMP1[99].

PfEMP1 is responsible for the parasite's primary pathological behavior and survival strategy– cytoadherence. The recognition and binding of host microvascular endothelial cell receptors such as ICAM-1, VCAM-1, EPCR, and CD36 by PfEMP1 enables pRBCs to fall out of circulation as they mature[31]. This behavior prevents parasites from reaching the spleen, which is capable of recognizing and "pitting" the parasites[100,101]. Within the splenon, the functional unit of splenic RBC filtration, the rigid pRBC is forced through interendothelial slits that mechanically squeeze the parasite out of the RBC and allow the formerly-infected RBC to return to circulation, frequently with parasite-generated proteins still present. In individuals with intact spleens[102], pRBC cytoadherence leads to the mass sequestration of parasites in the post-capillary venules of major organs such as the kidneys, heart, liver, lungs, brain, and placenta[103,104]. Sequestration in the latter organs, which seem mediated by specific variants of PfEMP1[105,106], can lead to the development of severe respiratory distress, cerebral malaria, and pregnancy-associated malaria, respectively. In each case, high parasite densities and the host inflammation response can occlude microvessels and significantly restrict blood flow[107–109]. Additionally, the binding of pRBCs to endothelial cells can stimulate the downstream release of inflammatory cytokines, the upregulation of additional adhesion receptors, and the loss of microvascular integrity[110].

An additional severe manifestation of malaria, severe malarial anemia, results from the significant destruction of both pRBCs and uRBCs. Splenic clearance and macrophage phagocytosis are responsible for eliminating pRBCs[102,111], though these processes alone cannot explain the observed drop in hemoglobin levels that occur during severe malaria episodes. Multiple studies have demonstrated that up to 10 times as many uRBCs are destroyed during an infection[112–114], which could potentially be the result of non-specific macrophage phagocytosis, splenic clearance, or accelerated RBC aging due to an environment of oxidative stress and inflammation. Furthermore, the pro-inflammatory state during severe malaria infection may lead to impaired erythropoiesis and the failure to replenish the rapidly destroyed RBCs[115]. Public health efforts to reduce the mortality of severe malarial anemia by increasing baseline hemoglobin levels through broad iron supplementation in malaria endemic regions have unexpectedly resulted in an increased susceptibility to developing malaria symptoms[116]. This suggests that iron-deficiency anemia protects against infection, and that the spike in serum iron levels that accompanies iron supplementation may supply the parasite with the otherwise unavailable iron necessary for DNA replication[117], pyrimidine synthesis[118], and heme production[119].

1.1.4 Protection from malaria

The innate and adaptive branches of the human immune system, as well as heritable genetic polymorphisms, provide protection from *P. falciparum* malaria at virtually every stage of the parasite life cycle in humans. The moment an individual is inoculated with sporozoites from an infected mosquito, dermal mast cells at the site of the bite respond by degranulating, which leads to the extravasation of fluid, neutrophil influx, and the generation of a general inflammatory response[120]. Repeated exposure to mosquito bites, a common occurrence in malaria-endemic regions, predisposes individuals to develop IgE responses to both parasite antigens and mosquito salivary gland components[121]. Furthermore, a study examining *P. yoelii* infection in mice demonstrated that pre-exposure to bites from uninfected mosquitoes is protective against infection[122]. While at the subcutaneous injection site or within the bloodstream, naturally-developed or vaccine-induced antibodies against sporozoite antigens such as the circumsporozoite protein are able to neutralize the parasite, inhibit hepatocyte entry, and prevent the development of malaria symptoms, though very high antibody titers are necessary to do so[123–126].

Sporozoites that reach the liver and successfully infect hepatocytes become shielded from circulating antibodies. However, resident hepatic CD8+ T-cells can recognize and destroy parasites in an interferon-γ-dependent manner[127]. The high degree of protection achieved with the experimental PfSPZ vaccine is thought to result from potent CD8+ T-cell induction rather than the traditional stimulation of antibody production[128]. Parasites that escape destruction and are able to release merozoites into the bloodstream are thought to trigger natural killer cell activation as inferred by increased levels of soluble granzymes, interferon-γ, and several interleukins[129].

Once in the bloodstream, the immune system has multiple mechanisms for reducing the parasite burden and ultimately clearing the infection. Circulating antibodies against some merozoite surface proteins block RBC invasion and promote the phagocytosis of free merozoites, which in turn can lead to the production of additional types of anti-merozoite antibodies[130–134]. Merozoites that successfully invade RBCs must remove themselves from circulation as they develop since the RBC-filtering capacity of the spleen effectively excises and destroys parasites[101]. As parasites cytoadhere and sequester, circulating anti-PfEMP1 antibodies efficiently block the parasite from binding endothelial receptors[102,135–138], sending the parasites to the spleen for destruction or flagging them for phagocytosis by activated monocytes[111,139,140]. Parasites that fully mature and rupture release not only merozoites but also DNA-coated hemozoin crystals, which have been shown to radically enhance the innate immune response by directly presenting malarial DNA to Toll-like receptor 9[141].

Naturally-acquired, protective immunity to *P. falciparum* malaria is a slow process that is both age- and exposure-dependent[142–144]. Though sterilizing immunity never develops, the susceptibility to severe and uncomplicated malaria gradually decreases with continuous parasite exposure to a point where asymptomatic parasitemia is generally the only consequence of infection[143]. This progression is thought to be the result of the immune system better controlling parasite density[145], as adults that develop high parasite densities during infection tend to experience disease progression at a rate similar to young children[146]. The contribution of antibodies to parasite density control and malaria protection has been observed with passive antibody transfer[147–149] and longitudinal studies examining invasion-blocking antibodies[150,151]. Further examination of antibodies against the intraerythrocytic form of the parasite have demonstrated that those targeting PfEMP1 play a crucial role in mediating protective immunity[152–156]. Furthermore, anti-VAR2CSA antibodies are strongly implicated in protection from pregnancy-associated malaria, as the level of VAR2CSA-specific antibodies within multigravidae correlate with the number of pregnancies they have experienced[157–160]. The unique expression patterns and high sequence diversity of PfEMP1 contribute to the exposure-dependence of protective immunity development since repeated infections gradually present more and more variants to the immune system for protective antibody production[161].

In addition to classical immunity, some heritable polymorphisms naturally provide protection against severe manifestations of malaria. An estimated 7% of the world's population carries 1 or more hemoglobin mutations[162], which include the well-characterized hemoglobins S, C, and E, as well as many other polymorphisms. A recent systematic review and meta-analysis[163] definitively showed that hemoglobin genotypes AS, CC, AC, and homozygous and heterozygous α-thalassaemia significantly protect against severe malaria. The mechanism of this protection is likely multifactorial, but emphasis has been placed on the inability of the parasite to produce normally formed and distributed knob structures, resulting in less surface-displayed PfEMP1 and decreased cytoadherence[164–166]. Additional well-characterized mutations include Duffy antigen receptor for chemokines negativity, which generally prevents *P. vivax* infection simply due to the absence of the crucial merozoite recognition and invasion receptor[167–169], and G6PD deficiency, which likely results in an increased cell-mediated immune response against oxidatively-stressed pRBCs[54,170]. Interestingly, a recent study of *P. falciparum* malaria episodes has shown that G6PD deficiency reduces the risk of cerebral malaria but increases the risk of severe malarial anemia[171], suggesting that the proposed malaria-protective effects of the mutation may not significantly improve the outcome of *P. falciparum* infection as predicted for *P. vivax* infection[172].

1.2 *Plasmodium falciparum* erythrocyte membrane protein 1

PfEMP1 is the primary virulence factor of *P. falciparum* during its blood-stage development due to its central role in mediating the cytoadherence of pRBCs to the human microvasculature[173,174].

1.2.1 PfEMP1 structure and diversity

PfEMP1 consists of a family of 200-350 kDa hypervariable surface antigens encoded by approximately 60 *var* genes per haploid genome[175]. Though considerable diversity exists among family members, each variant possesses the same general structure[176] (Figure 1.3). A generally conserved, intracellular acidic terminal segment (ATS) domain is involved in the binding of RBC spectrin, RBC actin, knob-associated histidine-rich protein (KAHRP)[177], and PHIST domains of other parasite proteins[178], all of which anchor PfEMP1 to the erythrocyte cytoskeleton and properly orient the protein in pRBC surface knobs. The ATS domain is joined to the extracellular hypervariable region by a transmembrane domain that may be involved in protein trafficking[179]. A series of multiple adhesive sub-domains, comprised exclusively of DBL and CIDR domains, are joined to the transmembrane domain and capped at the N-terminal end with a semi-conserved head structure consisting of an NTS domain and a DBL1-type domain[176,180]. This semi-conserved N-terminal region appears to contain sequence features signaling the export of PfEMP1 beyond the parasitophorous vacuole[181,182].

Significant sequence variation among subdomains within the hypervariable extracellular region has led to the development of a classification system for DBL and CIDR domains, as well as the overall structure of complete PfEMP1 variants. Guided by sequence similarities, DBL domains have been divided into the 6 classes α, β, γ, δ, ε, and ζ, and CIDR domains have been divided into the 4 classes α, β, γ, and δ[180]. The various combinations of

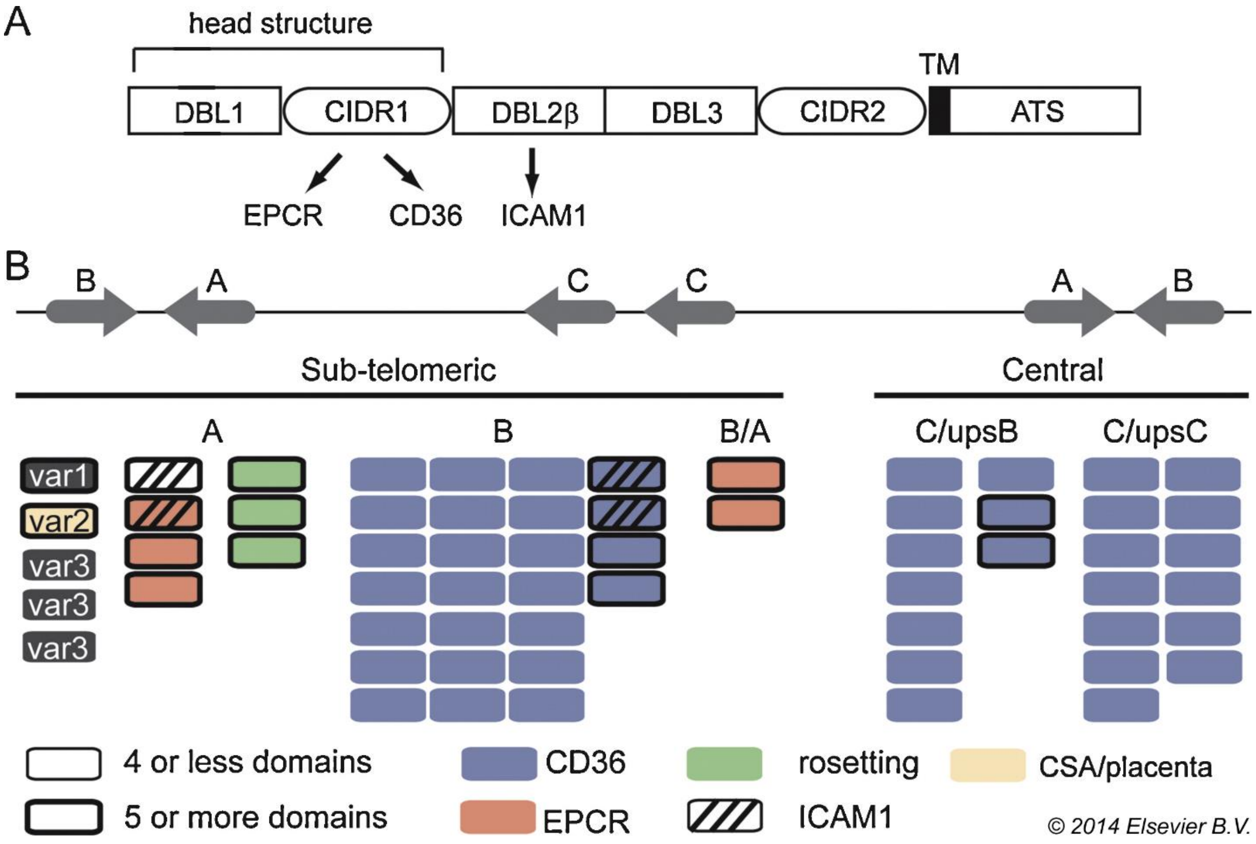

Figure 1.3: Schematic of PfEMP1 structure and genome organization. PfEMP1 variants are composed of a general structure (A) consisting of a relatively conserved ATS domain, a transmembrane domain, a hypervariable region with at least 1 DBL/CIDR subdomain, and a semi-conserved N-terminal head structure with DBL1, CIDR1, and N-terminal segment (NTS) domains. CIDR1 domains of group A and B/A variants have been shown to bind EPCR, while those of group B and C variants do not bind EPCR but do bind CD36. The binding of ICAM-1 has been mapped to DBLβ subdomains. The *var* genes encoding PfEMP1 have been broadly grouped into 3 groups, each with distinct genomic positions (B). Using the 3D7 reference genome, the predicted binding properties of each encoded PfEMP1 variant are shown. This figure is reproduced from [183].

these sub-domains in PfEMP1 variants have revealed 31 different architectural types in a study of 3 parasite lines, with consistently observed features such as CIDR1 domains following DBL1 domains[184]. Taking subdomain composition and adjacent non-coding regions into account, complete PfEMP1 variants have been organized into 3 major groups, A, B, and C, as well as 2 intermediate groups, B/A and B/C, that represent transitions between the major groups[185]. The increased availability of additional genome sequence data from a broad range of *P. falciparum* parasite lines has led to the further refinement of the general classification system, with the most recent study identifying 628 conserved minimal PfEMP1 building blocks[186]. Additionally, 21 conserved PfEMP1 subdomain compositions have been identified and termed "domain cassettes," which are predicted to confer specific receptor binding phenotypes, such as the binding of EPCR by domain cassettes 8 and 13[186,187]. Cytoadherence studies of subdomains and PfEMP1 variants *in vitro* have contributed means of classification based on functionality, such as the specific binding of ICAM-1 by DBLβ[188].

A PfEMP1 classification system has clear advantages for the general study of the protein family, but its specific applications may be limited given that the individual domains of most PfEMP1 variants possess less than 50% protein sequence identity between parasite isolates[184]. Furthermore, minimal sequence overlap in the DBLα domain has been reported in several studies, highlighting the extreme diversity of PfEMP1[189–192]. Despite such high sequence diversity, malaria-protective and cross-reactive anti-PfEMP1 antibodies are rapidly and sequentially acquired against common PfEMP1 subdomains during initial infections in both children[153,193–196] and malaria-naïve adults[197]. The presence of conserved epitopes on these subdomains results in the production of antibodies protective against severe disease, but the extreme sequence diversity of PfEMP1 likely explains why sterilizing immunity is never achieved and how *P. falciparum* parasites are able to persist in the presence of a primed host immune system[198].

1.2.2 *var* gene regulation and expression

The *var* genes that encode PfEMP1 range in size from 8 to 15 kb, with a highly diverse 5' exon, an approximately 1 kb intron, and a relatively conserved 1 to 1.5 kb second exon. Each *P. falciparum* chromosome, excluding chromosome 14, contains at least 1 member of the *var* gene family, with the genes generally being found after *P. falciparum*-specific repeat sequences at the subtelomeric ends of chromosomes[199–201]. In addition to subtelomeric *var* genes, chromosomes 4, 7, 8, and 12 contain internal clusters of *var* genes that seem generally more conserved across parasite lines, unlike those at the subtelomeres[202]. The location of *var* genes at the subtelomeres and near repetitive sequences enables ectopic recombination to occur during meiosis and possibly mitosis, providing ample opportunity for *P. falciparum* PfEMP1 diversity to expand[203–205]. Regardless of the chromosomal location of *var* genes, all are capable of being expressed[180,202,206].

The unique regulation of *var* gene expression permits only 1 gene to be transcribed per reinvasion cycle, resulting in a single PfEMP1 variant being displayed on the pRBC surface[207,208]. However, the possibility of 2 simultaneously expressed *var* genes has been reported in a subclone of the laboratory line 3D7[209], though it is unclear how frequently this behavior may occur or how representative it is of *P. falciparum* during infection. All *var* genes, regardless of transcription status, are physically located at the nuclear periphery in telomeric clusters[203,210,211]. The activation of *var* gene transcription, regulated in part by epigenetic modification via chromatin-altering proteins such as the histone lysine methyltransferase PfSETvs[212–214], results in the repositioning of genes from “silent” clusters to transcriptionally active locations[215,216]. Additionally, active *var* gene promoters are capable of associating with particular genes within clusters[217]. A recent study examining the role of perinuclear filamentous actin in *var* gene regulation has implicated the polymerization of actin in the repositioning and activation of *var* genes, suggesting that a motor protein such as myosin may contribute to *var* regulation and PfEMP1 expression[218]. Once *var* genes are activated, transcription occurs soon after invasion and becomes undetectable 20 hours after invasion[219].

The effects of mutually exclusive *var* gene expression can be seen beyond a single reinvasion cycle, since maturing parasites are able to impart a “memory” of the expressed

PfEMP1 variant to daughter merozoites[220]. However, to persist in the presence of an adaptive immune system, switching between *var* genes across generations must be regulated to evade the immune response but also to avoid depleting the reservoir of PfEMP1 variants presented[174]. Several studies have examined switching rates in both *in vitro* and *ex vivo* parasites[220–227], resulting in initially calculated switch rates ranging from 1 to 18%, but possibly as high as 100%[220,226,228,229]. Interestingly, it has been demonstrated that *P. falciparum* may express all PfEMP1 variants at the population level during the early stages of an infection[230] and subsequently modify its behavior toward the expression of a single dominant variant as the infection progresses[226]. The selection and expression of a dominant *var* gene has been shown to follow a non-random, highly-structured switching pattern that both responds to immune-mediated selection pressure and avoids needlessly revealing the entire limited PfEMP1 variant repertoire[227]. However, the organized and coordinated expression of *var* genes *in vivo* seems impacted by the cultivation of parasites *in vitro*, where the expression of a single dominant *var* gene in the original *ex vivo* parasite population gives way to the expression of many *var* genes without clearly dominating variants over successive *in vitro* generations[223,226,231]. Interestingly, this is not the case with many long-term laboratory-adapted parasite lines, including A4, HB3, and 3D7, which appear to stably express a particular subset of *var* genes and can be cultured *in vitro* for many generations without switching from the dominant variant[227,229,232].

1.2.3 Contribution of PfEMP1 to malaria pathogenesis

The DBL and CIDR domains of PfEMP1 mediate binding to a variety of general and organ-specific endothelial receptors, enabling parasites to bind at many sites within the body with varying degrees of affinity. The frequently observed cytoadhesion to the ubiquitous receptor CD36 is mediated by CIDRα domains of group B and C, but not A, *var* genes[233]. In contrast, the binding of ICAM-1 is mediated by DBLβ domains from all 3 *var* gene groups[188,234,235]. The specific binding of other receptors, including VCAM-1, thrombospondin, P-selectin, E-selectin, and PECAM-1, regularly occurs in some parasite lines but is overall less defined[236–238]. The wide-range of subdomains that compose a given PfEMP1 variant likely act synergistically to aid parasite adhesion under intravascular blood flow conditions. It seems that pRBCs are initially slowed by temporary rolling adhesion to ICAM-1, VCAM-1, thrombospondin, and P-selectin, and become statically anchored to the vessel wall by adhesion to CD36[239–241], except in the brain where adhesion is mediated by EPCR[106,242]. Furthermore, the binding of CD36 initiates actin recruitment and receptor clustering, potentially explaining the role CD36 binding plays in static cytoadherence[243].

While the composition of PfEMP1 variants enables the binding of many host receptors and the persistence of uncomplicated malaria, only a few specific PfEMP1-receptor interactions have been associated with the development of specific disease manifestations. A study of African children with severe malaria demonstrated a significant association between pRBC cytoadhesion to heparin sulfate and severe disease[244]. Recent studies of severe and cerebral malaria found an association with the PfEMP1 domain cassettes 8 and 13[187,245], which was further refined to the specific binding of EPCR by the CIDRα1 subdomain of cassette 8[106]. The well-characterized PfEMP1 variant VAR2CSA has been shown to bind CSA on placental syncytiotrophoblasts, resulting in pregnancy-associated malaria[246]. Lastly, PfEMP1-mediated rosetting has been associated with severe malaria in Africa[247–249], likely mediated by the binding of the DBLα sub-domain to complement receptor 1[99], type A and B blood group antigens[250,251], and heparin sulfate-like molecules[252,253].

PfEMP1 begins to appear on the pRBC surface at about 12 hours after invasion, reaching saturating levels after 24 hours and persisting until reinvasion occurs[254]. The protein is oriented at electron-dense, pRBC surface knob structures of parasite origin. These knobs, which tightly bind the ATS domain of PfEMP1 and aid pRBC cytoadherence[255], are structurally composed primarily of the parasite proteins KAHRP and PfEMP3, and the RBC protein spectrin[256]. The surface display of PfEMP1, though absolutely essential to parasite survival, directly exposes the protein to the human immune system for at least 36 hours. Consequently, it has been repeatedly demonstrated that a proportion of naturally-acquired, blood-stage immunity is directed against PfEMP1[153,154,198,257], forcing the parasite to develop immune evasion strategies to persist. At the genetic sequence level, the frequent recombination and rearrangement of extremely diverse *var* genes continuously produces new PfEMP1 variants to which the immune system has never been exposed[205]. At the transcription level, individual parasites express only 1 *var* gene at a time[258], and it has been further demonstrated that *ex vivo* parasites generally coordinate the expression of a single or small group of dominant *var* genes at the population level[226,259]. This unique expression pattern and the ordered switching from one *var* gene to another enables the parasite to evade the immune system through antigenic variation[260,261], which minimizes the loss of PfEMP1 variants to immune recognition by expressing the fewest variants possible and switching once an immune response is generated. This pathogenic behavior explains in part why repeated exposure to *P. falciparum* is necessary to generate protective, though not sterilizing, immunity to malaria.

1.3 Protein trafficking in *Plasmodium falciparum*

Unlike intracellular bacteria, most intracellular protozoa, and virtually all viruses, *P. falciparum* has evolved to thrive in a very unusual host cell environment. Mature RBCs are small, highly deformable, devoid of organelles and vesicular trafficking pathways, and continuously monitored by the spleen. This environment naturally poses considerable obstacles to parasite survival, all of which are further complicated by the fact that *P. falciparum* must rely on components and systems that it is largely responsible for manufacturing and organizing. In spite of this, *P. falciparum* has developed a highly successful strategy of thoroughly modifying its RBC environment through the export of effector proteins, many of which play crucial roles in transporting PfEMP1 and orienting it at the pRBC surface.

1.3.1 Parasite-generated trafficking structures

Since RBCs are devoid of organelles and protein export systems that are generally hijacked by intracellular pathogens, *P. falciparum* manufactures its own unique set of trafficking structures, chiefly Maurer's clefts. Maurer's clefts were first described in 1902[262] and have since been extensively studied using advanced microscopy techniques. Electron microscopy and tomography have revealed these organelles to be Golgi-like stacks of membrane-limited vacuoles with electron-dense coats[263–265]. The structures are generally located throughout the RBC cytosol and appear to associate with the RBC membrane. Size, morphology, number, and location of Maurer's clefts seem to vary across parasite lines[266], with some, such as 3D7[267], producing single slender lamella and others, such as HB3[268], producing stacks of multiple lamellae. The contrasting appearance of these Maurer's clefts is intriguing, though studies addressing their functionality have not been completed. Whole-cell imaging and lipid dye experiments have revealed that Maurer's clefts are associated with a vast interconnected lipid network within the RBC cytosol that potentially connects the parasitophorous vacuole, other Maurer's clefts, and the RBC membrane[269–272]. However, Maurer's clefts remain as distinct structures[273], likely originating from the parasitophorous vacuolar membrane and only later associating with other lipid channels deployed by the parasite[274].

Most proteins exported out of the parasite arrive at a Maurer's cleft[275], even if that is not their final destination. Known exceptions include membrane-associated histidine-rich protein 2[276], heat shock protein 40[277], and heat shock protein 70-x[278]. The transient association of PfEMP1[179] and other proteins with Maurer's clefts suggests that the structures may function as a protein sorting center in the cytosol. To perform this role, Maurer's clefts appear to leave the parasite within 2 to 4 hours after invasion and migrate through the cytosol to positions at the inner leaflet of the RBC membrane[279]. The ordered movement of the structures suggests that they are anchored to the erythrocyte cytoskeleton, seemingly by skeleton binding protein 1[280,281], with actin involvement being unlikely since cytochalasin D treatment does not impact Maurer's cleft migration[282]. However, actin has been shown to tether the structures to the intracellular side of parasite-induced knobs[283]. The direct observation of vesicles on these filaments, and their disruption in HbS and HbC RBCs, demonstrates that actin and associated transport proteins may play a significant role in the final stages of PfEMP1 surface display. Further evidence of the involvement of Maurer's clefts in PfEMP1 display comes from the disruption of proteins critical to the formation of Maurer's clefts, which does not impact parasite viability *in vitro* but does impact surface PfEMP1 levels[284]. This suggests that the role of Maurer's clefts in sorting exported proteins is more important for parasite virulence than parasite development and propagation. Interestingly, when Maurer's cleft function is compromised, some PfEMP1 still appears on the pRBC surface, suggesting the existence of an alternative trafficking pathway that bypasses Maurer's clefts[284]. Despite being essential for PfEMP1 trafficking, the precise role of Maurer's clefts other than transiently holding PfEMP1 is still under investigation.

In addition to sending out Maurer's clefts, the parasite deploys a lipid-rich tubulovesicular network throughout the RBC cytosol[264]. Unlike Maurer's clefts, this network has been poorly characterized, though it has been shown to contain the common Golgi marker sphingomyelin synthase[272,285]. This initially suggested that the tubulovesicular network could serve a secretory function, but later experiments disrupting the network through sphingomyelin synthase inhibition demonstrated that protein export was unaffected[286]. It is likely that the tubulovesicular network is not involved in PfEMP1 export but rather in the import of some extracellular nutrients and lipids critical for parasite development[287,288].

1.3.2 PEXEL-mediated trafficking

The discovery of a conserved amino acid sequence associated specifically with exported proteins provided an essential missing piece in the understanding of protein trafficking in *P. falciparum*[181,182]. This PEXEL motif consists of the residues RxLxE/Q/D and initiates protein cleavage by the aspartic protease Plasmepsin V in the parasite endoplasmic reticulum[289–291], resulting in an N-acetylated xE/Q/D N-terminal sequence[292–294]. A further examination of the residues comprising the PEXEL motif revealed that altering the arginine or leucine residues prevents recognition and cleavage[291,293,295], though altering the E/Q/D residue only results in inefficient export across the parasitophorous vacuolar membrane. Additionally, the insertion of an extra residue before the last E/Q/D residue still permits recognition and cutting[295,296].

After cleavage, N-acetylated proteins exit the lumen of the endoplasmic reticulum, enter the parasite cytoplasm, and travel to protein export sites at the parasite plasma membrane in what is still a poorly understood process, though association with phosphatidylinositol-3-phosphate may be involved[297]. Once at the parasite plasma membrane, proteins are secreted into the parasitophorous vacuole and recognized by a currently unknown mechanism for export into the RBC cytosol. Protein transport across the parasitophorous vacuolar membrane is mediated by PTEX, a multi-subunit pore complex consisting of the proteins EXP2, HSP101, PTEX150, TRX2, and PTEX88[298,299]. Within the complex, EXP2 is predicted to form the transmembrane pore across the parasitophorous vacuolar membrane and is positioned directly above the structurally supportive PTEX150 subunit and HSP101, which is responsible for unfolding proteins prior to transport. These 3 components are essential and lead to severe developmental defects if conditionally knocked out[298,300]. The functions of the TRX2 and PTEX88 subunits are not entirely clear, though knocking out either subunit results in parasites that develop at a significantly slower rate compared to wild-type parasites[301,302].

PTEX is initially expressed during the late blood stage and stored in the dense granules of merozoites. Within 10 minutes of invasion, the complex is secreted into the parasitophorous vacuole and immediately begins exporting proteins into the RBC cytosol[299,303]. Once exported proteins have entered the cytosol, chaperones such as heat shock protein 40 and heat shock protein 70-x may refold proteins or stabilize their unfolded state as they are guided to Maurer's clefts for sorting[181,277,278]. Although PfEMP1 variants do not contain PEXEL motifs or process through the PTEX export pathway, many of the 463 predicted PEXEL-containing proteins aid in the export and display of PfEMP1[295,304]. In a recent study, pharmacological inhibition of Plasmepsin V activity resulted in a nearly 50% decrease in the surface PfEMP1 levels of VAR2CSA-expressing parasites derived from 3D7[305]. Although PfEMP1 display was clearly impacted, it remains unclear as to how so much of the protein was still able to arrive at the pRBC surface without PEXEL-containing protein involvement.

1.3.3 PNEP trafficking

PEXEL-mediated export serves as the primary protein trafficking pathway of *P. falciparum*. However, a group of PEXEL-negative proteins (PNEPs) are produced and exported out of the parasite during development. These PNEPs lack an N-terminal hydrophobic signal sequence, a PEXEL motif, or any other conserved export sequences[306], and are not processed by Plasmepsin V or N-acetylated[295]. Though some PEXEL-like motifs have been proposed for PNEPs such as membrane-associated histidine-rich protein 2[276], a commonly conserved sequence has yet to be identified across PNEPs, among which are the PfEMP1 variants. Without a common signal sequence, it is difficult to estimate how many PNEPs may be produced or if PNEPs process through the same trafficking pathway as PEXEL-containing proteins. Interestingly, PNEP export is sensitive to brefeldin A treatment, suggesting that vesicular trafficking from the endoplasmic reticulum to the parasite membrane is necessary for PNEP export[307–309].

1.3.4 Known components of the PfEMP1 trafficking pathway

The export of the PNEP protein PfEMP1 is a complex process involving both PEXEL and PNEP proteins, as well as a variety of parasite- and RBC-derived structures. The overall PfEMP1 trafficking pathway is poorly defined, although it has been demonstrated that the process initiates with transmembrane domain-mediated entry into the endoplasmic reticulum[310,311]. To proceed forward, the semi-conserved head structure, transmembrane domain, and cytoplasmic tail are known to be required[179,312]. Predicted host cell-targeting motifs consisting of the amino acid sequences KDVLE in *Pf3D7_1200400* and KELLD in *Pf3D7_1240600* have been shown to bind phosphatidylinositol-3-phosphate-enriched regions of the endoplasmic reticulum to enter budding vesicles[297,313]. However, the absence of this lipid at the erythrocyte membrane[314] suggests that these vesicles do not transition across the parasitophorous vacuolar membrane.

The process of translocating such a large protein as PfEMP1 across the parasite and parasitophorous vacuolar membranes remains unclear, though recent co-localization studies have demonstrated that PfEMP1 does not co-localize with the PTEX complex[303]. Given that PfEMP1 transiently localizes to Maurer's clefts prior to surface display, it was hypothesized that PfEMP1 was not exported but rather preloaded into the structures before they migrated away from the parasite. However, this possibility was rejected given the recent observation that Maurer's clefts are deployed into the RBC cytosol 2 hours after invasion[279], and thus 2 hours before PfEMP1 expression begins[274,315]. It has also been observed that PfEMP1 remains bicarbonate-extractable during trafficking[316], suggesting that the protein is carried to Maurer's clefts as a soluble chaperoned complex rather than a membranous structure.

Despite knowing very little about the PfEMP1 trafficking pathway, several critical components have been identified. The PNEPs skeleton binding protein 1[281], membrane-associated histidine-rich protein 1[317], and Pf332[318] have been directly implicated in PfEMP1 export. A large-scale gene disruption study showed that 6 previously unknown PEXEL-containing genes, 5 of which have unknown functions, were involved in PfEMP1 export[319]. When most of these genes were disrupted, PfEMP1 accumulated at Maurer's clefts but did not appear of the pRBC surface. Like the initial stages of PfEMP1 export, the transfer of PfEMP1 from Maurer's clefts to pRBC surface knobs is also poorly understood. However, one study suggests that actin tethered to Maurer's clefts may provide a support structure for vesicular transport of PfEMP1 to the RBC membrane[283]. Another study has demonstrated that whatever complex PfEMP1 is transferred in fuses with cholesterol-rich microdomains within the RBC membrane[320].

The proper trafficking of PfEMP1 and its associated proteins is essential to pRBC cytoadherence and parasite survival *in vivo*. However, there seems to be some natural variation among field isolates and *in vitro* culture-adapted lines concerning this process. A study of 14 *ex vivo* field isolates from Ghanaian children revealed considerable variation in the density of pRBC surface knobs[321]. The same variation was observed among 10 *in vitro* culture adapted lines selected for VAR2CSA expression. Although surface PfEMP1 levels were not measured for the parasites in that study, the reduced density[164,166] or total loss of knobs[322] has been previously shown to significantly reduce, but not eliminate, surface PfEMP1 levels. This would presumably result in decreased pRBC cytoadherence, placing the parasite at a survival disadvantage. Interestingly, the majority of parasites obtained from symptomatic, splenectomized hosts do not form pRBC surface knobs[323–325], suggesting that knob formation and cytoadherence may actually be disadvantageous in the absence of splenic pressure.

It remains unclear as to how some parasites naturally produce more knobs and if this leads to greater amounts of surface-displayed PfEMP1 or more severe disease. Of particular interest is the laboratory-adapted parasite line 3D7, which has been shown to produce knobs at equivalent densities to those of other laboratory-adapted parasite lines[321] (Fairhurst lab, personal communication). However, studies examining PfEMP1 directly in knob-positive 3D7[326] and A4[322] parasites demonstrated that most PfEMP1 in 3D7 remains intracellular while most PfEMP1 in A4 is displayed on the pRBC surface. This suggests that 3D7 likely possesses a natural defect in trafficking and displaying PfEMP1, but the export component responsible has yet to be identified. Interestingly, the reduced surface PfEMP1 levels of 3D7 do not prevent the parasite from causing disease in humans, though it remains unclear if the parasite is less virulent than isolates that display higher surface PfEMP1 levels[90].

The current understanding of PfEMP1 trafficking has been greatly expanded over the past decade, though there is still much that remains undefined. High resolution and 3D imaging studies of pRBCs have provided novel insights into spatial and temporal aspects of PfEMP1 trafficking[267,274,283], but the earliest and least-understood processes occurring within the parasite itself remain difficult to interrogate. Directed[273,281,284] and broad[319] gene knockout strategies have been highly successful in identifying trafficking components, though these approaches are limited to genes that are non-essential for parasite survival. With widely-available genetic data for many routinely-used laboratory-adapted parasite lines, this limitation can be uniquely addressed by applying a phenotype-to-genotype approach. A previous study using this strategy further clarified the role of ring-exported protein 1 in the ultrastructure of Maurer's clefts based on observations made in the D10 parasite line[327].

Given the observation that 3D7 likely possesses a natural defect in PfEMP1 trafficking, a phenotype-to-genotype approach could be similarly applied to identify the genetic determinant(s) of the impaired trafficking phenotype and potentially reveal novel components of the PfEMP1 export pathway. Unlike D10, which has naturally lost a 55 kb region on the right arm of chromosome 9 containing 22 genes including ring-exported protein 1[328–330], 3D7 does not present with any obvious gene candidates. A comparison of the 3D7 genome with that of a PfEMP1 trafficking-competent line such as A4 would yield so many differences that the results would be relatively uninformative. However, a comparison with other genetically-similar parasite lines, such as recombinant progeny, could identify a reasonable number of candidate genes or polymorphisms for further study. Fortunately, a genetic cross had been conducted between 3D7 and the presumably trafficking-competent line HB3[331], providing a unique opportunity to identify potentially novel components of the PfEMP1 export pathway.

The work presented in this thesis aimed to do just that by first establishing surface PfEMP1 level phenotypes for HB3, 3D7, and 16 genetic cross progeny (chapter 2), and then associating those phenotypes with available full-genome data in QTL analysis (chapter 3). The identified candidate gene was then used in allele-exchange transfection experiments in an effort to establish a causal link with the impaired trafficking of PfEMP1 in 3D7 (chapter 4).

This thesis concludes with a discussion of the implications of this work and its contribution to the current understanding PfEMP1 trafficking (chapter 5).

2 Measuring parasitized erythrocyte surface PfEMP1 levels among progeny from an HB3 x 3D7 genetic cross

2.1 Introduction and aims

The trafficking and display of PfEMP1 on the surface of mature pRBCs is essential to *P. falciparum* survival *in vivo*. Immense pressure from the human spleen has selected for the characteristic PfEMP1-mediated microvasculature cytoadherence of this parasite, while the unrelenting host immune system has driven it to employ antigenic variation of PfEMP1 as an effective survival strategy. While much research has been conducted on the contribution of PfEMP1 to *P. falciparum* pathogenesis and the complex role of the protein at the host-parasite interface (discussed in section 1.2), it has been widely and commonly assumed that, although the particular variant may differ, all parasites naturally display the same amount of PfEMP1 on the pRBC surface.

Research addressing the protective effects of hemoglobinopathies such as HbS and HbC has established that PfEMP1 levels on the pRBC surface can be significantly impacted by the host RBC environment. However, when this variable is controlled for, only experiments utilizing genetically altered, isogenic parasite lines report any differences in surface PfEMP1 levels among parasites. This molecular manipulation approach is very effective when clear targets are known, but to identify completely novel components of the PfEMP1 trafficking and display pathway, *in vitro*-adapted parasite lines possessing natural variation in surface PfEMP1 levels provide powerful experimental resources. Specifically, the association of clearly defined phenotypes with corresponding genetic data from highly similar parasite lines, such as the parents and progeny of a genetic cross, can reveal potentially causative links between genotypes and phenotypes in a quantitative, statistically measurable way.

Guided by the general hypothesis that the trafficking of PfEMP1 from the parasite to the pRBC surface is controlled at the genetic level, and the specific hypothesis that 3D7 harbors 1 or more genetic determinants of impaired PfEMP1 trafficking, the aim of this chapter is to first establish and characterize the natural difference in surface PfEMP1 levels between the *P. falciparum* laboratory lines HB3 and 3D7. Following the demonstration of robust, clearly different parental phenotypes, this chapter describes the phenotyping and characterization of surface PfEMP1 levels among progeny from an HB3 x 3D7 genetic cross. The resulting phenotypes are subsequently combined with genomic data and used in QTL analysis, as discussed in chapter 3.

2.2 Materials and methods

2.2.1 *In vitro* parasite culture

Continuous *in vitro* culture of *P. falciparum* was first achieved in 1976[332] and has been subsequently modified and refined into the modern culturing method described here. Whole blood was obtained from healthy O+ donors and stored in 40 ml aliquots at 4°C for up to 4 weeks. When uRBCs were needed, stored blood was centrifuged at 3000 rpm for 10 minutes to pack the erythrocytes and enable the removal of buffy coat leukocytes and plasma. The remaining erythrocytes were washed 3 times with cold incomplete parasite culture medium (Table 2.1), suspended to 50% hematocrit, and stored at 4°C for up to 2 weeks.

Cryovials of preserved parasites were transferred directly from -80°C or liquid nitrogen storage to a 37°C incubator for 30 minutes. Once equilibrated to 37°C, 0.2x cryovial volumes of a pre-warmed 12% NaCl solution was added dropwise over 2 minutes. The mixture was left undisturbed for 5 minutes before 6x cryovial volumes of a pre-warmed 1.8% NaCl solution was added dropwise over 5 minutes. The mixture was left undisturbed for another 5 minutes before 6x cryovial volumes of a pre-warmed 0.9% NaCl and 0.18% glucose solution was added dropwise over 5 minutes. The thawed and equilibrated cells were spun at 1500 rpm for 5 minutes, resuspended in pre-warmed incomplete parasite culture medium, and spun at 1500 rpm for 5 minutes again. Washed uRBCs were added to the recovered pRBCs to obtain a final packed cell volume of 500 µl. The cells were then suspended in pre-warmed complete parasite culture medium (Table 2.1) at 1% hematocrit, gassed with a mixture of 1% O_2, 3% CO_2, and 96% N_2, and placed in a 37°C incubator. After 48 hours, the culture medium was changed and parasitemia was determined.

For all experiments, asexual blood-stage parasites were continuously cultured at 37°C in complete parasite culture medium at 1% hematocrit in a low oxygen environment of

1% O_2, 3% CO_2, and 96% N_2. To monitor parasite growth and development, small aliquots from cultures were pelleted, thinly smeared on glass slides, fixed with methanol, and stained with a 0.45 µm filtered solution of concentrated Giemsa stain diluted 1:9 in pH 7.2 PBS. Stained slides were viewed at 1000x magnification under oil immersion, and approximately 500 total cells across multiple viewing fields were counted. Parasitemia was determined by dividing the number of viable parasites by the total cell count and multiplying by 100. To maintain healthy parasite populations and avoid gametocyte production, cultures were limited to parasitemias of approximately 5% or less. The frequency of culture medium replenishment was determined based on parasitemia, with higher parasitemia cultures receiving more frequent medium changes, but typically occurred every other day. At the earliest possible opportunity, parasites were preserved and archived as described below to ensure that lines were not permanently lost due to microbial contamination or cross-contamination with other parasite lines. To avoid long-term culture-induced changes and to minimize the likelihood of *var* gene switching, parasites were generally cultured for up to 1 month before being neutralized and discarded.

To preserve and archive pRBCs for future experiments, methods for cryopreserving plasma-depleted RBCs have been successfully adopted to maintain the viability of ring-stage parasites but not mature or extracellular forms[333–336]. In preparation for freezing and long term storage at -80°C or in liquid nitrogen, synchronous ring-stage parasites were grown to approximately 5% parasitemia. For each stabilate, 300 µl of packed pRBCs were transferred to a 50 ml Falcon™ tube and slowly mixed with 100 µl of pre-warmed Glycerolyte 57 solution (Table 2.2). The mixture was left undisturbed for 5 minutes before adding 400 µl of pre-warmed Glycerolyte 57 solution dropwise over 4 minutes. The 800 µl mixture, now at the appropriate 5:3 ratio of Glycerolyte 57 solution to pRBCs, was then transferred to a sterile 1 ml screw-cap cryovial and stored at -80°C. For parasite stabilates stored in liquid nitrogen, cryovials at -80°C were relocated the following day. If a single

Incomplete Parasite Culture Medium	
RPMI-1640 with $NaHCO_3$ and L-glutamine	500 ml
1.0 M HEPES buffer	12.5 ml
45.0% D-(+)-glucose solution	2.2 ml
1.0 M NaOH	1 ml
10 mg/ml gentamicin solution	1.25 ml
Complete Parasite Culture Medium	
Incomplete Parasite Culture Medium	450 ml
62.5 mg/ml hypoxanthine solution	0.4 ml
Pooled, heat-inactivated human serum	50 ml

Table 2.1: *In vitro* parasite culture medium components.

Glycerine	57 g
Sodium lactate	1.6 g
Potassium chloride	30 mg
Sodium phosphate monobasic (monohydrate)	51.7 mg
Sodium phosphate dibasic (anhydrous)	124.2 mg
ddH_2O	Volume up to 100 ml
Phosphoric acid	Adjust to pH 6.8

Table 2.2: Glycerolyte 57 solution components per 100 ml of ddH_2O.

parasite line was to be used in multiple experiments across several weeks or months, large volumes of pRBCs were cultured and cryopreserved at the same time in an effort to minimize stabilate-to-stabilate variation as cryovials were thawed for each experiment.

Unlike parasites obtained directly from infected individuals[337–339], parasite populations maintained in continuous *in vitro* culture tend to become asynchronous[332,340], requiring frequent stage synchronization through various *in vitro* methods[341,342]. One of these methods exploits the activation of the Plasmodial surface anion channel (PSAC) beginning at approximately 16 hours post-invasion, which permits the unregulated uptake of sorbitol by pRBCs, ultimately resulting in cell lysis and parasite death if suspended in an isotonic sorbitol solution[343–345] (Desai lab, personal communication). To tightly synchronize cultures, pRBCs consisting of mostly ring-stage parasites were suspended in a pre-warmed, isotonic solution of 5% sorbitol and left undisturbed at 37°C for 30 minutes. pRBCs were then washed once with pre-warmed incomplete parasite culture medium and returned to 37°C under typical culturing conditions. Growth was monitored periodically until schizonts began rupturing, at which point pRBCs were again subjected to the above sorbitol-lysing process. Following the second sorbitol treatment, pRBCs were returned to typical culturing conditions for approximately 14 hours. pRBCs were then subjected to a third and final round of sorbitol lysis to obtain a highly synchronous parasite population ranging in age from 14 to 16 hours post-invasion (Figure 2.1).

Parasites maintained in *in vitro* culture for long periods of time are susceptible to a spontaneous break in chromosome 2, resulting in an accelerated life cycle and the complete loss of parasite-induced pRBC surface knobs[346–348]. To avoid the inclusion of knob-negative parasites in any experiments, cultures were routinely subjected to Plasmion® floatation, which isolates knob-positive pRBCs based on their delayed sedimentation rate relative to knob-negative pRBCs and uRBCs[349–353]. Cultures were first centrifuged at 1800 rpm for 5 minutes to pellet the cells. After removing and discarding the supernatant, 500 µl of packed cells were resuspended in a mixture of 2.5 ml Plasmion® and 1.5 ml incomplete parasite culture medium. The resuspended cells were transferred to a 15 ml Falcon™ tube, which was then placed upright in a 37°C incubator and left undisturbed for 30 to 45 minutes. After knob-negative pRBCs and uRBCs had clearly settled at the bottom of the tube, the top 3 ml of the cell suspension were carefully transferred to a new tube containing incomplete parasite culture medium. The isolated knob-positive pRBCs were centrifuged at 1500 rpm for 5 minutes, resuspended in complete parasite culture medium, and brought to the appropriate packed cell volume with fresh uRBCs before being returned to *in vitro* culture.

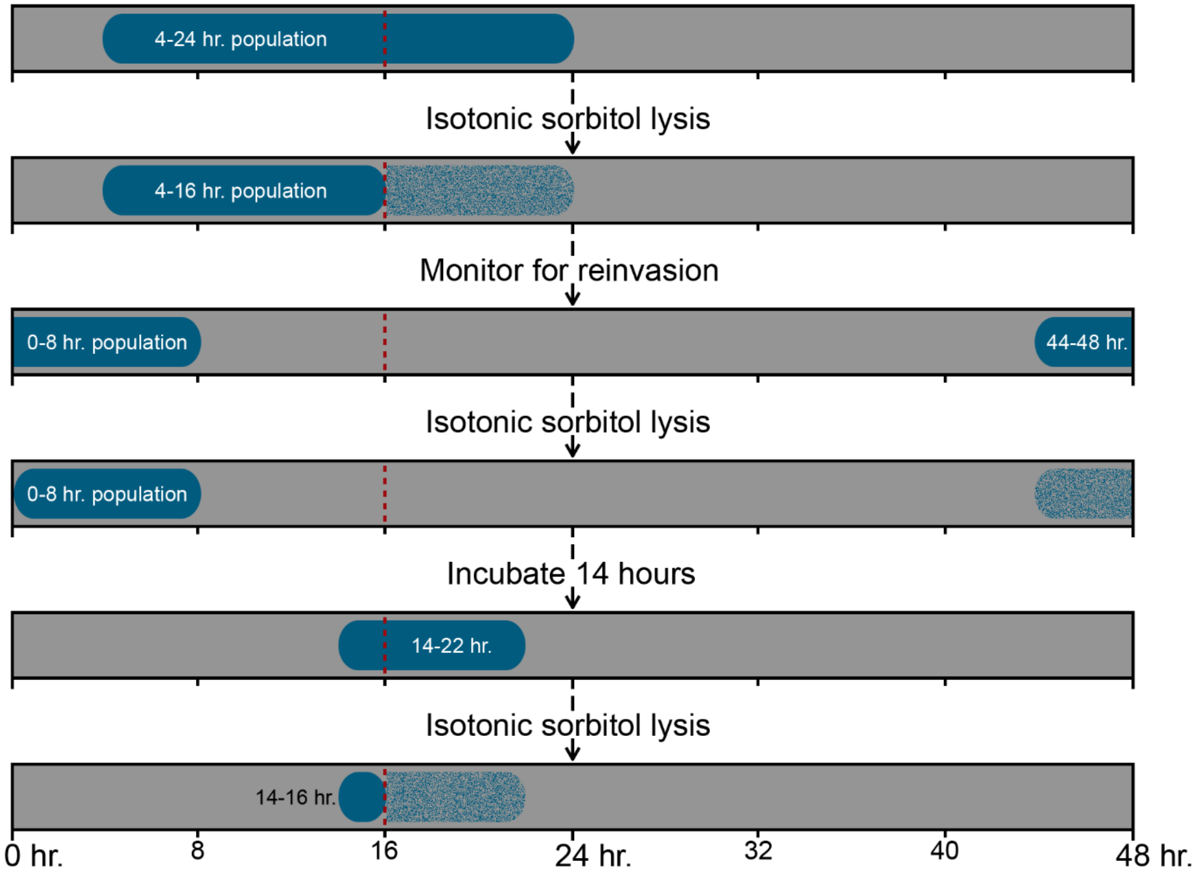

Figure 2.1: Schematic representation of parasite stage synchronization *in vitro* by isotonic sorbitol lysis. Highly synchronous trophozoite populations were obtained after 3 rounds of isotonic sorbitol treatment, which selectively lyses parasites more than 16 hours old without affecting parasites less than 16 hours old.

2.2.2 Parasite lines

To explore differences in pRBC surface display of PfEMP1, the *in vitro* culture-adapted parasite lines HB3 and 3D7 were used extensively and specifically selected for 2 reasons. First, previously published experiments showed that 3D7 produces a large amount of PfEMP1 but does not display the vast majority of it on the pRBC surface, unlike the parasite line A4[322,326]. This suggested that 3D7 possesses an inherent defect in the trafficking and surface display of PfEMP1 rather than the production of PfEMP1. Second, a genetic cross was performed using HB3 and 3D7 as the parental lines. The cross progeny, and the accompanying genetic data, provide a rich resource for genotype-phenotype association studies.

Clone HB3 was isolated on January 27th, 1983, by microscopic selection from cultures of the Honduras I/CDC strain obtained on January 25th, 1980[354]. Clone 3D7 was isolated in 1985 by limiting dilution from cultures of the NF54 strain obtained in 1981 from a patient living near Schipol Airport, Amsterdam, who had never left the Netherlands[331,355,356]. Occasionally, the parasite line A4 was included in experiments as a positive control. Clone A4 was isolated in 1992 by microscopic selection from cultures of the ITO4 clone originally derived from the preceding lines ITO, IT 4/25/5, and, ultimately, the Ituxi 084 strain isolated in Brazil on July 25th, 1979[221,231,357].

The first *P. falciparum* genetic cross was completed in 1985 using HB3 and 3D7[331], yielding 113 progeny clones, 89% of which displayed non-parental genotypes[358]. From this subset, 55 independent recombinant clones are currently available for use, and 16 were selected for initial genotyping using 9 independently inherited, dimorphic genes located across multiple chromosomes (Table 2.3). Of these clones, full genome sequences were obtained for 14 by the Wellcome Trust Sanger Institute according to protocols established by the Malaria Genomic Epidemiology Network Consortium[359]. The remaining 2 progeny were SNP-mapped using the PFSANGER Genechip® as previously reported[360].

Cryopreserved parasite stocks obtained from the original parental HB3 and 3D7 clones were available for use in the Newbold laboratory. To confirm their identity and to monitor for cross-contamination, the clones were initially and periodically genotyped by PCR-amplifying the genes for MSP1, MSP2, and GLURP[361]. All 18 progeny in Table 2.3 were obtained from the Ranford-Cartwright laboratory since those stabilates were closest in generational-age to the original cross progeny stabilates prepared in 1985. The cryopreserved progeny were thawed and placed in *in vitro* culture according to the procedures described in section 2.2.1. During the thawing process, significant pRBC

Chromosome:	2	7	9	10	3	4	8	12	14
Gene:	MSP1	STARP	MSP2	GLURP	C3M85	POLYα	TA17	TA48	CAL
Fully Sequenced Progeny									
XP4	HB3	HB3	HB3	3D7	HB3	HB3	HB3	3D7	3D7
XP5	HB3	HB3	HB3	3D7	HB3	3D7	HB3	3D7	3D7
XP8	HB3	3D7	HB3	HB3	3D7	HB3	HB3	3D7	3D7
XP9	HB3	HB3	HB3	HB3	HB3	HB3	HB3	3D7	3D7
XP52	HB3	HB3	HB3	3D7	3D7	HB3	HB3	HB3	HB3
X2	HB3	3D7	3D7	3D7	3D7	HB3	HB3	HB3	3D7
X4	HB3	HB3	HB3	HB3	HB3	HB3	HB3	3D7	3D7
X5	HB3	3D7	HB3	3D7	HB3	HB3	HB3	3D7	HB3
X6	3D7	HB3	HB3	HB3	HB3	HB3	HB3	HB3	3D7
X10	HB3	HB3	HB3	HB3	3D7	3D7	3D7	3D7	HB3
X12	HB3	HB3	HB3	3D7	3D7	HB3	3D7	3D7	HB3
X30	HB3	3D7	3D7	3D7	HB3	3D7	3D7	3D7	HB3
X33	HB3	HB3	3D7	3D7	HB3	HB3	HB3	HB3	HB3
X35	3D7	HB3	NP	HB3	3D7	HB3	HB3	3D7	HB3
X39*	3D7	3D7	HB3	HB3	3D7	HB3	HB3	HB3	HB3
SNP-Mapped Progeny									
XP25	3D7	HB3	HB3	3D7	HB3	3D7	HB3	HB3	3D7
X44	HB3	HB3	NP	HB3	3D7	3D7	HB3	HB3	HB3

Table 2.3: Sequenced and SNP-mapped progeny from the HB3 x 3D7 genetic cross. After clonal populations of the collected progeny were obtained by limiting dilution, parasites were classified using genotypes across 9 genes with dimorphic alleles unique to each parent. Some progeny possess non-parental (NP) genotypes, indicating that a cross-over event occurred within that particular gene. Progeny XP9 and X4 have the same 9 alleles, though full-genome sequences have confirmed that they are genetically distinct clones. While most of the progeny have been fully sequenced, SNP data for the non-sequenced clones XP25 and X44 are available from a SNP-chip with 3,597 unique genome-wide markers. *Clone X39 did not survive the cryovial thawing process, so it was excluded from the experiments described in this thesis.

lysis occurred, likely due to either the age of the stabilates or their cryopreservation using different methods, resulting in the loss of clone X39. For the remaining 16 progeny, healthy cultures were expanded to large volumes so that multiple parasite stabilates could be cryopreserved from a single culture, minimizing variation when freshly thawed stabilates were required for experiments.

2.2.3 Trypsin treatment and protein extraction

Localizing PfEMP1 in mature blood-stage parasites relies on the trypsin sensitivity of surface-displayed PfEMP1[281,322,326], the trypsin-inaccessibility of intracellular PfEMP1[362,363], and the separation of membrane-bound proteins from free intracellular proteins through differential detergent extraction[254,364,365].

Highly synchronous cultures of trophozoites approximately 27-29 hours post-invasion were subjected to Plasmion® floatation as described in section 2.2.1 to obtain pRBC pellets of at least 80% parasitemia. Cells were washed once with incomplete parasite culture medium before being equally divided into 2 tubes for trypsin or mock treatment. For trypsin-treated pRBCs, cells were suspended in 10x pellet volumes of a pre-warmed 1 mg/ml solution of TPCK-treated trypsin (Sigma T1426) in incomplete parasite culture medium. For mock-treated pRBCs, cells were suspended in 10x pellet volumes of a pre-warmed 2 mg/ml solution of Type II-O, partially purified ovomucoid trypsin inhibitor (Sigma T9253) in incomplete parasite culture medium. Both tubes were incubated at 37°C for 5 minutes before adding 10x pellet volumes of a pre-warmed 2 mg/ml solution of trypsin inhibitor in incomplete parasite culture medium. Both tubes were then incubated at room temperature for 5 minutes before being washed once with 20x pellet volumes of a pre-warmed solution of 1x Roche cOmplete EDTA-free protease inhibitor cocktail in incomplete parasite culture medium.

For differential detergent extraction of PfEMP1, trypsin- and mock-treated pRBC pellets were extracted in 10x pellet volumes of a 4°C solution of 1% Triton™ X-100 in NET solution (150 mM NaCl, 50 mM Tris pH 8.0, 5 mM EDTA) containing 1x Roche cOmplete EDTA-free protease inhibitor cocktail. Tubes were allowed to incubate on ice for 5 minutes before being centrifuged at 13,000 rpm for 5 minutes in a 4°C refrigerated centrifuge. The supernatants were collected as the "Triton-soluble fractions" and immediately placed on dry ice for 5 minutes before being stored at -80°C. The remaining pellets were washed once with the same volume of 1% Triton™ X-100 solution to ensure that any remaining Triton™ X-100-soluble proteins would not contaminate the next fraction. The pellets were then subjected to further extraction using 10x original pellet volumes of a room temperature solution of 2% SDS in TSA solution (150 mM NaCl, 20 mM Tris pH 8.0, 0.02% w/v NaN_3) containing 1x Roche cOmplete EDTA-free protease inhibitor cocktail. Parasite DNA was sheared by repeated passage through a 25 gauge needle. The tubes were then centrifuged at 13,000 rpm for 10 minutes at room temperature. The supernatants were collected as the "Triton-insoluble fractions" and immediately placed on dry ice for 5 minutes before being stored at -80°C.

2.2.4 SDS-PAGE and Western blotting

To analyze and quantify PfEMP1 from differential detergent extracts, proteins were first separated according to size by denaturing and reducing SDS-PAGE using a modified method of Laemmli[366]. Stock solutions for polyacrylamide gel preparation were formulated according to Table 2.4 and stored at 4°C until use. A gel was prepared by first assembling a glass gel cassette, mixing a separating gel using the volumes in Table 2.5, and pouring the mixture into the cassette. To prevent drying and uneven settling, the still-liquid separating gel was overlaid with a solution of 25% v/v Solution A in ddH_2O including 1% v/v SDS. Once the separating gel had polymerized and become solid, the overlay solution was removed and replaced with a stacking gel prepared using the volumes in Table 2.5. While the stacking gel was still liquid, a plastic gel comb was carefully inserted to create individual sample lanes. Once the stacking gel had polymerized and become solid, the comb was removed and the cassette was submerged in a Bio-Rad Mini-PROTEAN® 3 electrophoresis chamber filled with running buffer consisting of ddH_2O with 25 mM Tris, 192 mM glycine, and 0.1% v/v SDS.

Differential detergent extracts were thawed on ice before being diluted with an equal volume of 2x Laemmli sample buffer consisting of ddH_2O with 62.5 mM Tris-HCl pH 6.8, 25% v/v glycerol, 2% v/v SDS, 0.01% v/v bromophenol blue, and 5% v/v β-mercaptoethanol. Diluted samples were then incubated at 95°C for 10 minutes, chilled on ice for 1 minute, and centrifuged at 13,000 rpm for 1 minute to remove precipitated, insoluble protein. The denatured and reduced samples, along with a full-range molecular weight marker, were loaded onto the previously prepared polyacrylamide gel and run at 150 volts for approximately 90 minutes or until the blue sample dye had just run off of the gel. Gels that were not used in Western blotting were submerged for 1 hour in a protein fixation and staining solution consisting of ddH_2O with 20% v/v methanol, 10% v/v glacial acetic acid, and 0.05% w/v Coomassie Brilliant Blue G-250. Stained gels were then washed overnight with the same solution, excluding Coomassie Brilliant Blue G-250, and imaged.

Gels that were further used in Western blotting were first equilibrated for 20 minutes in Western transfer buffer consisting of ddH_2O with 25 mM Tris, 192 mM glycine, and 20% v/v methanol. An equilibrated gel was then placed on a 0.45 µm pore size nitrocellulose membrane and sandwiched between 2 pre-wetted sheets of Whatman 3MM filter paper followed by 2 fiber pads. The wet transfer sandwich was placed in a cassette, submerged in a Bio-Rad Mini Trans-Blot® electrophoretic transfer cell filled with pre-cooled Western transfer buffer, and run at 90 volts for approximately 90 minutes. The protein-containing membrane was then rinsed twice in TBS including 0.1% v/v Tween® 20 and submerged for 1 hour at room temperature in 0.22 µm-filtered Western blocking buffer consisting of TBS with 0.1% v/v Tween® 20 and 5% w/v non-fat dried milk powder. After blocking, the membrane was rinsed twice in TBS including 0.1% v/v Tween® 20.

Extracted PfEMP1, regardless of variant, was detected using a polyclonal rabbit antibody developed against the highly-conserved ATS domain of the protein[254,367]. Prior to use in Western blotting, the anti-ATS antibody was pre-adsorbed twice on intact uRBCs and

	Solution A	Solution B	Solution C (ProtoGel)
1 M HCl	48 ml	48 ml	-
Tris	36.3 g	6 g	-
TEMED	0.23 ml	0.48 ml	-
Acrylamide	-	-	30% solution volume
Bisacrylamide	-	-	0.8% solution volume
ddH_2O	Volume up to 100 ml	Volume up to 100 ml	-

Table 2.4: SDS-PAGE gel preparation solution components per 100 ml of ddH_2O.

	5% Running Gel	10% Running Gel	Stacking Gel
Solution A	2.5 ml	2.5 ml	-
Solution B	-	-	0.95 ml
Solution C	1.7 ml	3.3 ml	1.25 ml
10% v/v SDS	0.1 ml	0.1 ml	0.075 ml
10% w/v APS	0.1 ml	0.1 ml	0.075 ml
ddH_2O	5.3 ml	4.0 ml	5.0 ml

Table 2.5: SDS-PAGE gel components.

twice on ghosted uRBCs to reduce any non-specific binding signal. 50 µl of antibody were mixed with 50 µl of packed uRBCs in a 1.5 ml Eppendorf tube and placed on a tube inverter for 30 minutes. The mixture was then centrifuged at 10,000 rpm for 30 seconds to pellet the cells. The supernatant was removed and added to another 50 µl of packed uRBCs to repeat the pre-adsorption process. While the second tube was being inverted, 200 µl of packed uRBCs were washed three times with 200 µl of ghosting solution consisting of 5 mM NaH_2PO_4 in ddH_2O, yielding approximately 100 µl of uRBC ghosts. Once the second pre-adsorption mixture finished inverting, the tube was centrifuged as before so that the supernatant could be removed and added to 50 µl of uRBC ghosts. The same pre-adsorption process then repeated for both uRBC ghost rounds, resulting in a final pre-adsorbed antibody volume of approximately 40 µl.

The pre-adsorbed antibody was diluted 1:650 with TBS including 0.1% v/v Tween® 20 and added to the blocked membrane, which was then incubated at room temperature for

1 hour in a 50 ml Falcon™ tube on a horizontal tube roller. Following the primary antibody incubation, the membrane was rinsed twice with TBS including 0.1% v/v Tween® 20 and washed 8 times over 12 minutes with the same solution. A secondary antibody consisting of donkey-derived anti-rabbit IgG conjugated to horseradish peroxidase was diluted 1:50,000 with TBS including 0.1% v/v Tween® 20 and added to the blocked membrane, which was again incubated at room temperature for 1 hour while spinning. Following the secondary antibody incubation, the membrane was rinsed and washed as before and placed protein-side up on a smooth piece of plastic wrap. Room-temperature Amersham™ ECL™ Prime detection reagents were freshly mixed and added to the membrane, which was then incubated for 5 minutes at room temperature to detect the presence of horseradish peroxidase. Following the incubation, the membrane was lightly dried, placed in a clear plastic sleeve, and imaged by exposing to Fujifilm Super RX medical x-ray film.

2.2.5 Flow cytometry

Flow cytometry offers a rapid, high-throughput, and sensitive method for directly quantifying pRBC surface-displayed PfEMP1[154,368,369]. This approach relies on measuring the intensity of clearly distinguishable fluorescent signals to discern pRBCs from uRBCs and to determine both the presence and amount of pRBC surface-displayed PfEMP1. To phenotype HB3, 3D7, and the genetic cross progeny, a 2-color, 3-layer flow cytometry protocol was developed (Figure 2.2).

Since pRBCs and uRBCs have virtually indistinguishable side scatter versus forward scatter profiles (Figure 2.3, upper panels), the DNA-binding dye SG (Invitrogen™ S-7563) was used to specifically identify pRBCs given that enucleated uRBCs do not contain any DNA of their own (Figure 2.3 lower panels). Thus, SG-positive cells are exclusively pRBCs and show signal intensities that correlate directly with parasite developmental stage[370,371]. SG, which was supplied at 10,000x concentration in DMSO, was diluted to 50x in HBSS and

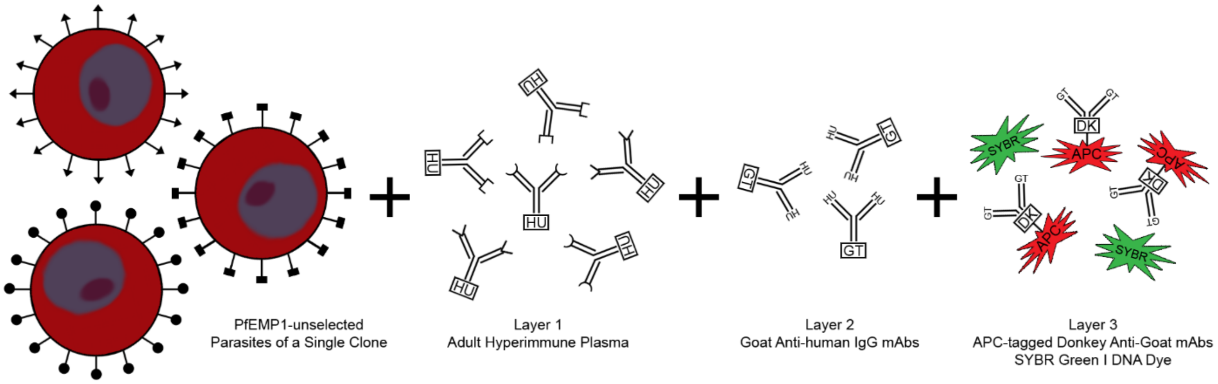

Figure 2.2: Schematic representation of 2-color, 3-layer flow cytometry protocol. PfEMP1-unselected 27-29 hour-old trophozoites were first probed with PfEMP1-reactive pooled plasma obtained from Malian adults. A goat anti-human secondary layer was then added, followed by a donkey anti-goat tertiary layer conjugated to APC. SG was included to clearly distinguish pRBCs from uRBCs.

stored at 4°C in the dark for up to 1 month. Titrations of SG determined that a 1:500 dilution of the 50x solution, or final sample concentration of 0.1x, provided optimal separation of pRBCs from uRBCs. HBSS was specifically selected as a flow cytometry dye and sample buffer since it contains significantly less phosphate than other buffers, generally resulting in greater intracellular retention of DNA-binding dyes.

The detection of surface-displayed PfEMP1 was accomplished using a 3 antibody layer approach, which provides greater signal intensity and resolution compared to 1 and 2 layer approaches[372,373]. The primary antibody layer consisted of hyperimmune plasma pooled from 4 adults who had spent their entire lives in a malaria-hyperendemic area of Mali[374]. The pool components, chosen from screens of 16 Malian adult plasmas, pooled Kenyan adult plasma, pooled Gambian adult plasma, and lyophilized therapeutic plasma, were specifically selected for the breadth and intensity of their reactivity against HB3 and 3D7. Hyperimmune plasma was used instead of a PfEMP1 variant-specific antibody to ensure that all parasite lines would be detected regardless of which PfEMP1 variant was being expressed or how often *var* gene switching occurred. Additionally, the characteristically poor cytoadherence of 3D7[375,376], and the possibility of progeny clones expressing PfEMP1 variants that do not bind common cell receptors or that bind multiple receptors[377], greatly reduced the feasibility and potential success of panning parasites on endothelial cell lines to obtain the single PfEMP1 variant-expressing parasite populations necessary for specific antibody-based detection. The primary Malian plasma pool layer was followed by a secondary antibody layer consisting of an affinity isolated, goat-derived IgG antibody (Sigma I2136) specifically targeting the conserved Fc fragment of human IgG. This secondary layer was followed by a tertiary antibody layer consisting of an affinity isolated, donkey-derived $F(ab')_2$ antibody fragment (Thermo Scientific 31980) specifically targeting the heavy and light chains of goat IgG. This final antibody layer was conjugated to APC and pre-adsorbed against human IgG to ensure that there would be low to no cross-reactivity with the primary antibody layer. The APC fluorophore was specifically selected due to its relatively high quantum yield of 0.68 and its negligible fluorescence emission overlap with SG (Figure 2.4), resulting in flow cytometry data that do not require signal compensation or further manipulation.

Each individual FACS experiment consisted of 3 genetic cross progeny and a standard HB3 control (Table 2.6), all of which were analyzed 1 cycle after thawing. To ensure consistency across experiments, every HB3 control originated from a single culture that was cryopreserved at once in multiple vials. Prior to cryopreservation and after thawing, each grouping of parasite lines was maintained in the same batch of uRBCs in an effort to minimize potential bias caused by the host RBC.

To prepare samples for FACS analysis, highly synchronous cultures of approximately 27-29 hour-old trophozoites were diluted to a parasitemia between 1% and 2% with the same uRBCs used in culturing. Two aliquots of 30 µl of packed pRBCs were obtained from each diluted culture and trypsin treated or mock treated as described in section 2.2.3. The aliquots were then washed twice with pre-warmed FACS wash buffer, consisting of HBSS

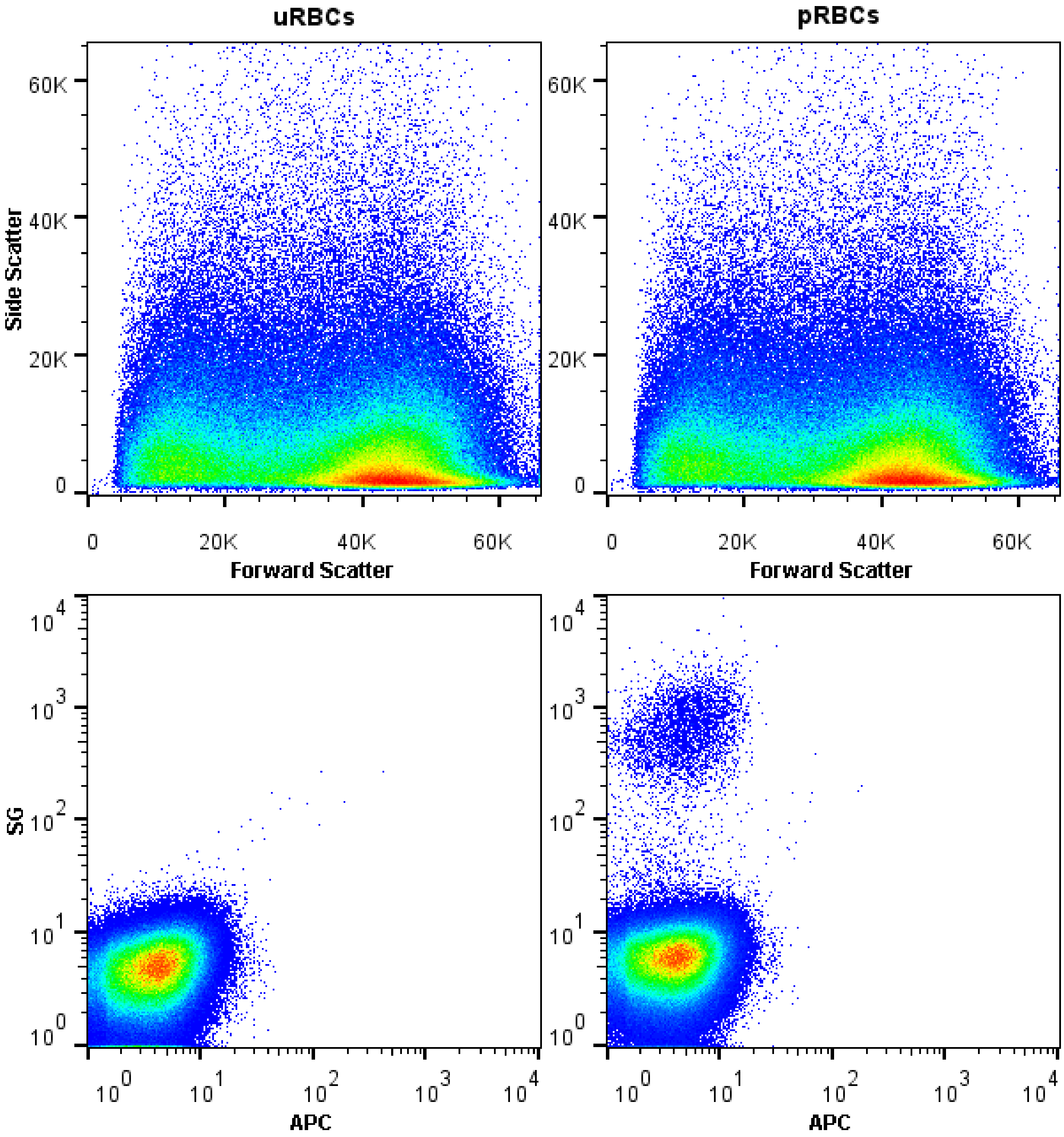

Figure 2.3: Flow cytometry plots of SG stained uRBCs and pRBCs. Since *P. falciparum* does not significantly increase the size of its host RBC during development, the flow cytometry measurements of forward scatter, an indicator of cell size, and side scatter, an indicator of cell granularity, are unable to distinguish pRBCs from uRBCs. The inclusion of the DNA-specific fluorescent dye SG results in the clear separation of pRBCs from uRBCs. SG scatterplots are shown with an APC x-axis, the partner fluorophore in the 2-color, 3-layer flow cytometry protocol.

with 2% v/v FBS, and resuspended to a final hematocrit of 10% in FACS wash buffer. From those resuspensions, 25 µl aliquots were added to 25 µl aliquots of either 1:3 pooled Malian plasma in FACS wash buffer or 1:3 pooled European serum in FACS wash buffer to give a final sample plasma/serum concentration of 1:6 and a final hematocrit of 5%. Samples were incubated at 37°C for 30 minutes and then washed 3 times with 500 µl of FACS wash buffer. During the final wash aspiration, 25 µl of buffer was left with each pRBC pellet so that the subsequent addition of 25 µl of secondary antibody at 1:1000 in FACS wash buffer would result in a final antibody concentration of 1:2000 and a final hematocrit of 5%. Samples were once again incubated at 37°C for 30 minutes and then washed 3 times with 500 µl of FACS wash buffer. The same final aspiration procedure was followed so that the addition of 25 µl of tertiary antibody at 1:500, including SG at 0.2x, in FACS wash buffer would result in a final antibody concentration of 1:1000, a final SG concentration of 0.1x, and a final hematocrit of 5%. Samples were incubated a final time at 37°C for 30 minutes and then washed 3 times with 500 µl of FACS wash buffer. After the final aspiration, cells were resuspended in 1100 µl of FACS wash buffer containing 1% v/v paraformaldehyde and transferred to flow cytometry tubes for analysis 1 hour later. FACS sample components are detailed in Table 2.7.

Each antibody layer was titrated against HB3 and 3D7 to find the optimal saturating concentration (Figure 2.5), ensuring that any differences in fluorescence signal intensity among parasite lines were truly due to different surface PfEMP1 levels and not an unavailability of antibody. With all antibody layers at saturating levels, the APC-signal intensity should correspond directly to the amount of PfEMP1 displayed on the pRBC surface. While it is possible for the plasma pool to contain IgG against other families of pRBC surface antigens, such as RIFIN and STEVOR, it has been overwhelmingly demonstrated that the natural blood-stage antibody response is primarily directed against PfEMP1[153,154,198,257].

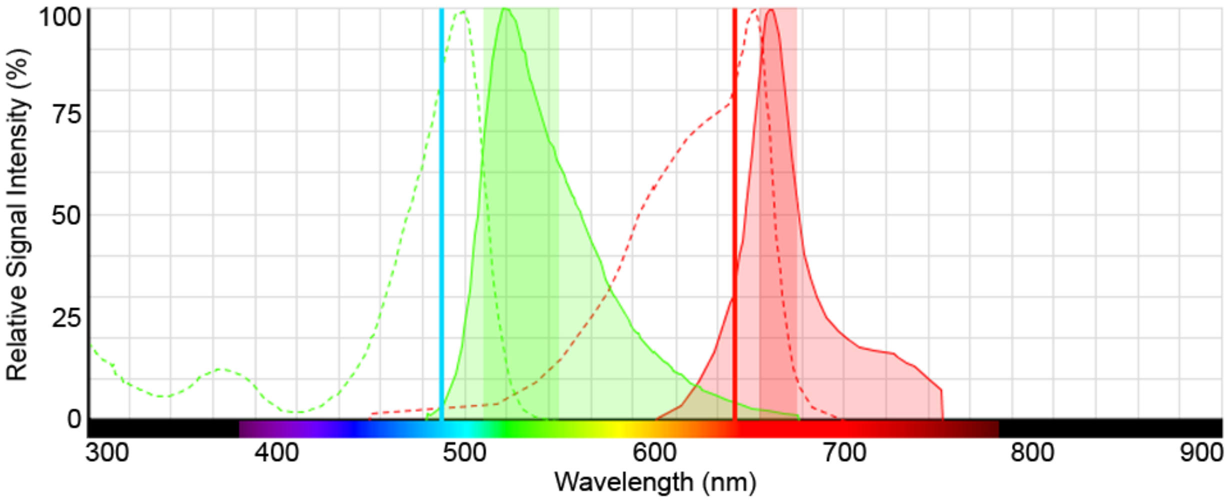

Figure 2.4: Fluorescence spectra for SG and APC. SG (green) and APC (red) have largely non-overlapping excitation (dashed curve) and emission (solid curve) spectra. SG was excited with a 488 nm laser (solid blue bar) and detected through a 530/40 band-pass filter (shaded green bar), while APC was excited with a 642 nm laser (solid red bar) and detected through a 665/20 band-pass filter (shaded red bar). Spectra were generated using the Life Technologies™ Fluorescence SpectraViewer.

Sample	Sample Type	Trypsin	SG	1° Malian	1° European	2° Ab	3° Ab
1	HB3 Unstained	No	-	-	-	-	-
2	HB3 SG Only	No	+	-	-	-	-
3	HB3 APC Only	No	-	+	-	+	+
4-6	HB3 Negative Control	No	+	-	+	+	+
7-9	HB3 Mock-treated	No	+	+	-	+	+
10-12	HB3 Trypsin-treated	Yes	+	+	-	+	+
13-15	X# Negative Control	No	+	-	+	+	+
16-18	X# Mock-treated	No	+	+	-	+	+
19-21	X# Trypsin-treated	Yes	+	+	-	+	+
22-24	X## Negative Control	No	+	-	+	+	+
25-27	X## Mock-treated	No	+	+	-	+	+
28-30	X## Trypsin-treated	Yes	+	+	-	+	+
31-33	X### Negative Control	No	+	-	+	+	+
34-36	X### Mock-treated	No	+	+	-	+	+
37-39	X### Trypsin-treated	Yes	+	+	-	+	+

Table 2.6: Sample summary for an each individual FACS experiment. An HB3 control and 3 different progeny (X#, X##, X###) were prepared for every FACS experiment. Each sample type was run in triplicate, excluding standard compensation controls.

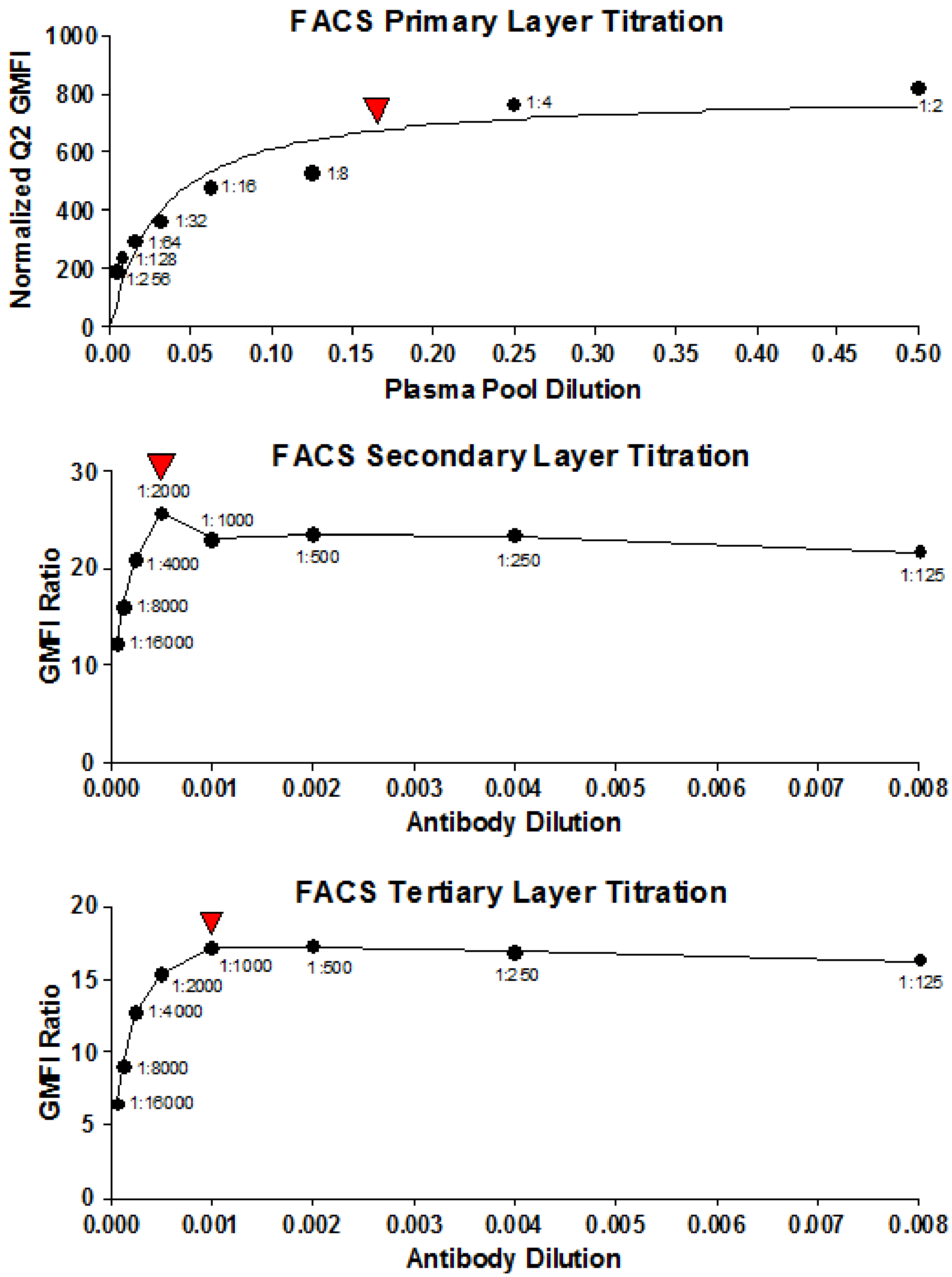

Figure 2.5: Titration curves of FACS antibody layers. The primary layer titration is expressed as fluorescence intensity and is fitted with a single-site binding curve. The secondary and tertiary layer titrations are expressed as ratios of the pRBC GMFI to the uRBC GMFI in order to account for the proportional APC signal shift demonstrated in Figure 2.7. Red markers indicate the concentrations used in the optimized FACS assay.

Component	Concentration	Composition
1° Antibody layer	1:6	Pooled Malian plasma or pooled European serum
2° Antibody layer	1:2000	Goat anti-human IgG, Fc-specific
3° Antibody layer	1:1000	Donkey anti-goat IgG, APC-conjugated
DNA stain	0.1x	SYBR® Green I
Wash buffer	N/A	HBSS with 2% v/v FBS
Fixation buffer	N/A	HBSS with 2% v/v FBS, 1% v/v paraformaldehyde

Table 2.7: 2-color, 3-layer FACS assay components.

Fixed FACS samples were analyzed using a single 9-parameter Beckman Coulter CyAn ADP Analyzer equipped with 405 nm, 488 nm, and 642 nm solid-state lasers. SG and APC were excited and detected using the parameters described in Table 2.8 and visually represented in Figure 2.4. The flow cytometer was calibrated weekly, and voltages for each experiment were set based on unstained control samples. 300000 ungated events were collected for each stained sample at a rate of 1000 to 3000 events per second. All data were acquired using Summit version 4.3.02 software and later processed using FlowJo version 7.6.5 or version 10.0. Raw sample data were processed by first applying a doublet-exclusion gate based on event pulse width, followed by a uRBC-exclusion gate on the resulting sub-population of singlets. The remaining SG-positive, pRBC-only populations were gated as either ‘Plasma Positive’ or ‘Plasma Negative’ using contour plots, APC signal histograms, and criteria based on the APC signal intensity of the pRBC population in non-immune pooled European serum-incubated samples (Figure 2.6). The GMFI in the APC channel was determined for both populations and used in further analysis.

Inherent errors in pipetting the exact volumes of 2° and 3° antibodies needed for each FACS sample produced varying global population shifts in APC signal intensity across samples, meaning that a direct sample-to-sample comparison of APC signal intensities of plasma-positive pRBCs would be inaccurate. To circumvent this problem, a ratio of the

‘Plasma Positive’ population GMFI to the ‘Plasma Negative’ population GMFI within each sample was calculated (Figure 2.7). This ratio was then used to normalize each sample to the HB3 control included in each experiment. Normalized sample ratios reflected PfEMP1 surface expression phenotypes and were used to categorize the progeny.

2.2.6 Advanced microscopy

To discern key morphological features of pRBCs, cells were directly visualized using immunofluorescence confocal microscopy and scanning electron microscopy. Confocal microscopy is routinely used to observe antibody-bound, surface-displayed[164,165,378] and intracellular[379] PfEMP1. This application, though not as quantitative or high-throughput as flow cytometry, enables visual confirmation of scatterplot data and offers insights into the clustering and surface distribution of PfEMP1. Scanning electron microscopy provides images at a resolution high enough to observe knob structures on the surface of pRBCs without the use of stains or labels[164,256,380]. Since the presence and distribution of knobs directly affects the quantity of PfEMP1 displayed[322], this technique is able to provide essential confirmation of pRBC knob-positivity for any study of cell surface PfEMP1.

To collect immunofluorescence images by confocal microscopy, 27-29 hour-old trophozoites stained with SG and labeled with APC as described in section 2.2.5 were first suspended in the PBS-based fluorescence anti-fade mountant CitiFluor™ AF3. A wet mount microscopy slide was then prepared and sealed before immediate viewing on a Leica TCS SP II laser scanning spectral confocal microscope equipped with a 488 nm argon-krypton laser, a 633 nm helium-neon laser, and adjustable short-pass dichroic mirrors. All slides were viewed with a 63x/1.4 numeric aperature lens under the immersion oil-based fluorescence anti-fade solution CitiFluor™ AF87. SG and APC were excited and detected using the parameters described in Table 2.9. At the onset of each imaging experiment, laser voltages and channel gain values were manually adjusted based on the fluorescence of

Fluorophore	Max Excitation	Max Emission	Laser	Band-Pass Filter
SG	497 nm	520 nm	488 nm	530/40
APC	650 nm	660 nm	642 nm	665/20

Table 2.8: FACS fluorophore properties and instrument parameters.

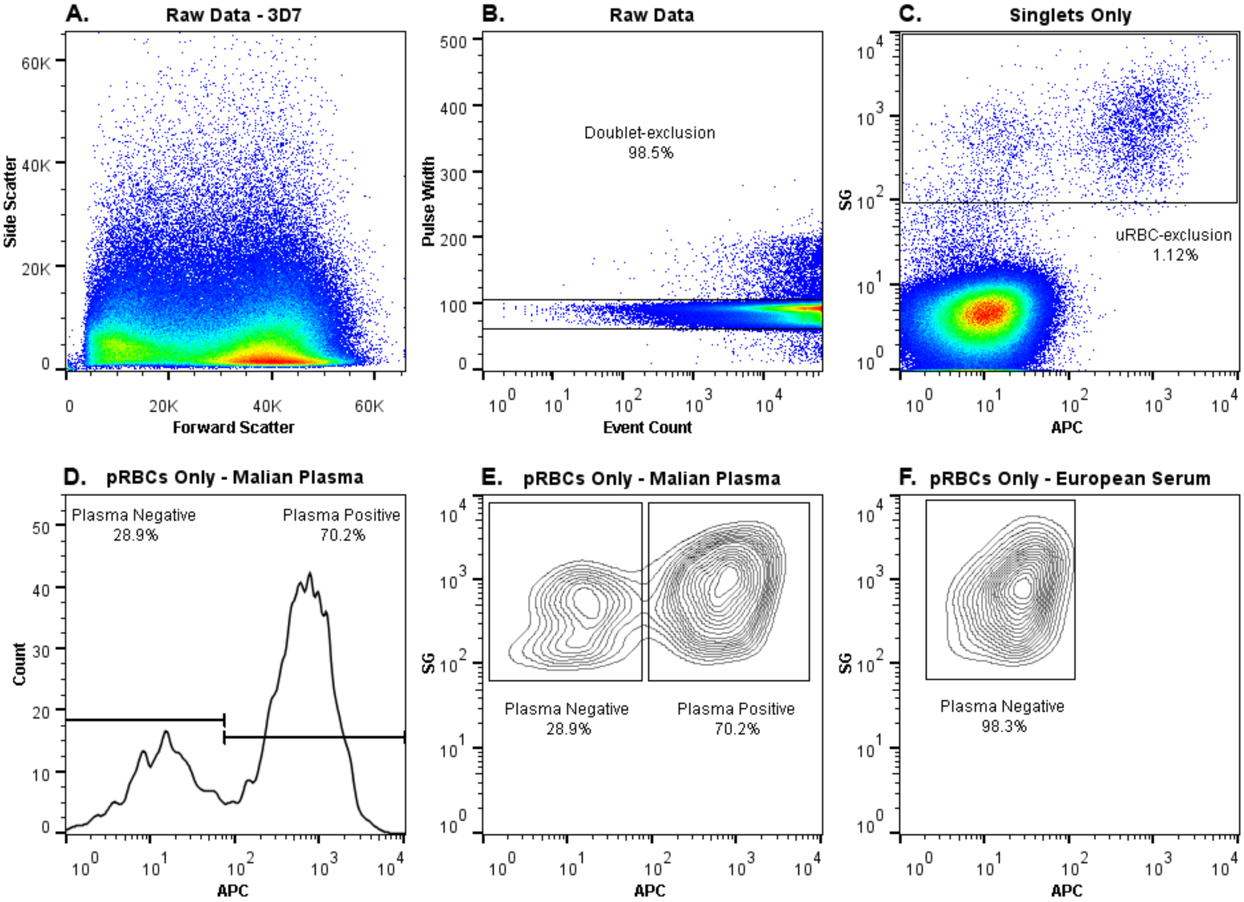

Figure 2.6: Gating strategy for FACS data. For all FACS samples, 300,000 raw events were initially collected (A). Pulse width-based (B) and SG-channel-based (C) gates were applied to exclude cell doublets and uRBCs, respectively, from analysis. The remaining pRBC-only populations were divided into plasma-negative and plasma-positive populations based on APC histograms (D), contour plots (E), and the position of pRBCs in the non-immune pooled European serum-treated negative control (F). An APC-channel GMFI ratio of the plasma-positive population to the plasma-negative population was developed and used in subsequent analysis.

untreated, plasma-positive HB3 pRBCs and remained unchanged throughout the course of the experiment. Once an individual pRBC containing a single parasite was identified, approximately 20 Z-sections of steps 512 x 512 pixels were captured beginning in the plane just above the pRBC and ending in the plane just below the pRBC. Captured images were processed, stacked, summed, and overlaid using ImageJ v1.47.

To collect high-resolution images by scanning electron microscopy, highly synchronous cultures of approximately 27-29 hour-old trophozoites were first subjected to Plasmion® floatation as described in section 2.2.1 to obtain pRBC pellets of at least 80% parasitemia. pRBCs were then washed once with 1 ml of cold HBSS and resuspended in 1 ml of the same cold HBSS. To best preserve pRBC morphology and reduce cell distortion by harsh fixation[381], 1 ml of cold HBSS with 2% v/v glutaraldehyde was slowly added dropwise to the resuspended pRBCs, resulting in a final glutaraldehyde concentration of 1% v/v. The cells were allowed to fix for 1 hour at 4°C before being washed once with 1 ml of cold HBSS and transferred to coverslips. Using a PELCO BioWave® Pro microwave set at 250 watts under a 15 inch mercury vacuum, cells were post-fixed first in 0.5% w/v osmium tetroxide in PBS, then in 1% v/v tannic acid in PBS, and finally in 1% w/v uranyl acetate in PBS. Cells were then dehydrated in a graded ethanol series for 1 minute under constant vacuum and dried to the critical point in a Bal-Tec CPD 030 dryer. Cells were coated with 75 ångströms of iridium in an ion beam sputter and imaged on a Hitachi SU8000 cold-emission scanning electron microscope. Images were processed in Photoshop® CS2, where a 1 µm x 1 µm box was drawn over a relatively flat portion of the pRBC in order to determine the approximate number of knobs per square µm on the cell.

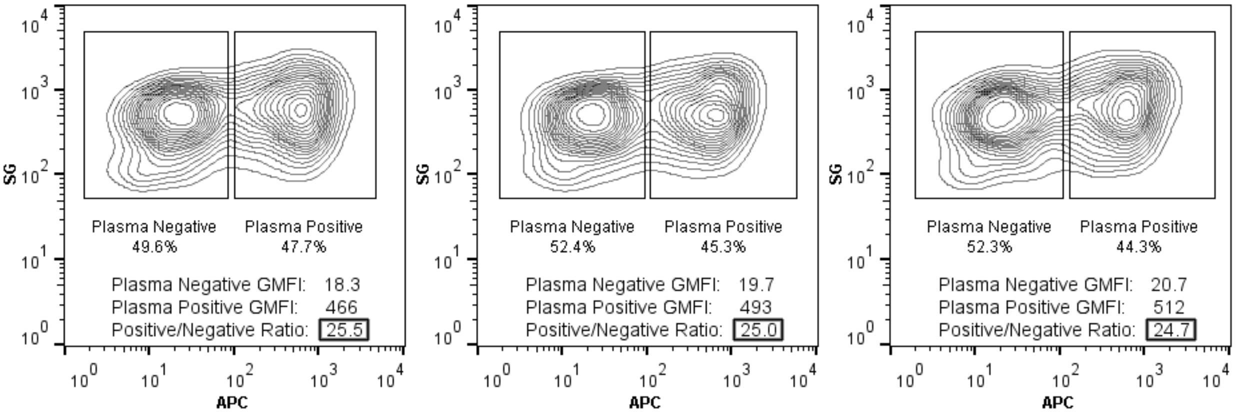

Figure 2.7: Shifting APC signal intensities among FACS technical replicates. Samples processed in triplicate typically possess different APC-channel GMFIs due to normal sample variation. However, increased concentrations of 2° and 3° antibodies result in a global, proportional increase in the APC-channel GMFIs of all populations. A GMFI ratio of ‘Plasma Positive’ to ‘Plasma Negative’ was used when comparing triplicates in order to account for the effects of any signal intensity shift.

Fluorophore	Max Excitation	Max Emission	Laser	Short-Pass Mirror
SG	497 nm	520 nm	488 nm	498-562 nm
APC	650 nm	660 nm	633 nm	640-721 nm

Table 2.9: Immunofluorescence confocal microscopy fluorophore properties and instrument parameters.

2.3 Results

2.3.1 Parental HB3 and 3D7 surface PfEMP1 phenotypes

To begin addressing the specific hypothesis that 3D7 harbors 1 or more genetic determinants of impaired PfEMP1 trafficking, previous observations regarding the low surface PfEMP1 levels of 3D7 relative to A4 (discussed in section 2.2.2) first needed to be confirmed and subsequently compared to the suspected PfEMP1 trafficking-competent parasite line HB3. The verification of distinct, contrasting parental surface PfEMP1 level phenotypes would support the phenotyping of HB3 x 3D7 genetic cross progeny for use in QTL analysis. The first attempt to accomplish this utilized the well-established method of differential detergent extraction and PfEMP1-detection by Western blotting with an anti-ATS antibody (sections 2.2.3 and 2.2.4). Representative blots of 3D7 and HB3, with an A4 positive control, are shown in Figure 2.8. As expected with A4, the Triton-insoluble, full-length PfEMP1 signal from trypsin-treated parasites was significantly weaker than the signal from mock-treated parasites, while the Triton-soluble, full-length PfEMP1 signal was similar in both trypsin-treated and mock-treated parasites. This indicated that extracellular, but not intracellular, PfEMP1 was digested with trypsin and therefore localized to the pRBC surface. With 3D7, a similar result was seen, with the most relevant difference being that the Triton-soluble, full-length PfEMP1 signal was similar in intensity to the Triton-insoluble, full-length PfEMP1 signal. This suggested that much of the PfEMP1 produced by 3D7 remained intracellular rather than appearing on the pRBC surface. With HB3, a highly unusual pattern was seen. Specifically, the Triton-insoluble, full-length PfEMP1 signal appeared to be trypsin-resistant while the Triton-soluble, full-length PfEMP1 signal appeared to be trypsin-sensitive. Since the localization of PfEMP1 to the pRBC surface relies on the trypsin sensitivity of Triton-insoluble PfEMP1 and the trypsin inaccessibility of Triton-soluble PfEMP1, the results for HB3 could not be used as initially planned. In an attempt to

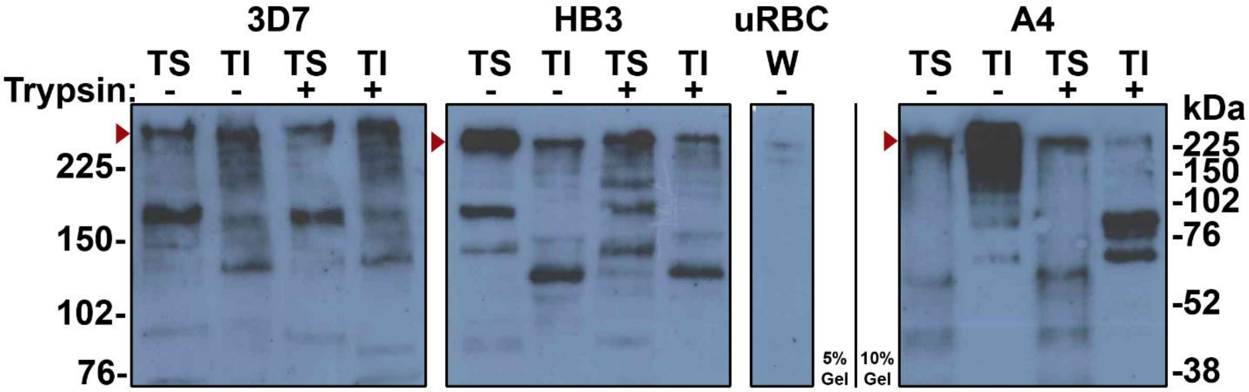

Figure 2.8: Anti-ATS Western blots of 3D7, HB3, and A4 differential detergent extracts. Triton-soluble (TS) and Triton-insoluble (TI) extracts from mock-treated or trypsin-treated 27-29 hour-old trophozoites were probed with an anti-ATS antibody that had been pre-adsorbed on uRBC ghosts. The position of full-length PfEMP1 is indicated by a red arrow, while trypsin cleavage fragments are generally located between 76 and 225 kDa. Non-specific antibody binding to the RBC heterodimer spectrin can be seen in whole cell (W) extracts from uRBCs. Membrane-anchored, surface-displayed PfEMP1 is expected in the TI fraction, and intracellular, trypsin-inaccessible PfEMP1 is expected in the TS fraction.

overcome the observed trypsin-resistance, the pRBC incubation step with trypsin was increased from 5 minutes to 10 minutes. However, the resulting change in the post-trypsinization supernatant from clear to light red suggested that cell lysis was occurring, which further complicated PfEMP1 localization since trypsin could access the previously-shielded intracellular pool.

The issues with PfEMP1 localization due to trypsin-resistance led to a shift from Western blotting to flow cytometry as the primary method for establishing parental surface PfEMP1 level phenotypes. While the notable advantage of detecting all PfEMP1 variants through the conserved ATS domain was lost, flow cytometry offered higher sample throughput and provided more quantitative data, all while eliminating potential sources of error such as the inadequate solubility of membrane proteins, the degradation of samples, or the inefficient transfer of PfEMP1 to membranes for probing.

Using the optimized 2-color, 3-layer FACS assay described in section 2.2.5, standard phenotypes were determined for HB3 and 3D7 to guide further phenotyping of the genetic cross progeny (Figure 2.9). Expectedly, not all pRBCs were recognized by the plasma pool. Possessing 2 distinct pRBC populations is characteristic of PfEMP1-unselected parasite lines, as some pRBCs likely express a subset of PfEMP1 variants that the plasma pool antibodies do not recognize. However, HB3 consisted of 3 distinct pRBC populations, 2 of which were recognized by the plasma pool. When both plasma-positive HB3 populations are included in the comparison against the single plasma-positive 3D7 population, the difference in the APC GMFI ratios is not large enough for use in QTL analysis (Figure 2.9 B). However, when only the brightest pRBC population is compared to 3D7, there is a 76.7% difference in the APC GMFI ratio. For QTL analysis to serve as a viable method of addressing the central hypothesis of this thesis, only the brightest pRBC population was used in establishing the surface PfEMP1 level phenotype of HB3.

Before the FACS assay could be confidently used to determine surface PfEMP1 level phenotypes, the pRBC age-specific reactivity of the hyperimmune plasma pool needed to be assessed. Highly synchronous 7-9 hour-old ring-stage pRBCs did not react at all with the plasma pool, while 27-29 hour old trophozoites and 37-39 hour old schizonts both reacted equally well (Figure 2.10). This result was consistent with previously reported data showing that PfEMP1 begins appearing on the pRBC surface at 12 hours post-invasion and saturates at 24 hours post-invasion[254].

Proceeding forward with highly synchronous 27-29 hour old trophozoites, the trypsin-sensitivity of the APC signal was evaluated. Interestingly, 3D7 parasites exhibited trypsin-sensitivity while HB3 parasites exhibited both trypsin-sensitivity and trypsin-resistance (Figure 2.9 A), supporting the Western blotting results described previously. In order to further understand the nature of the 2 HB3 populations, a FACS assay was performed using the hyperimmune plasma pool and its individual components against mock-treated and

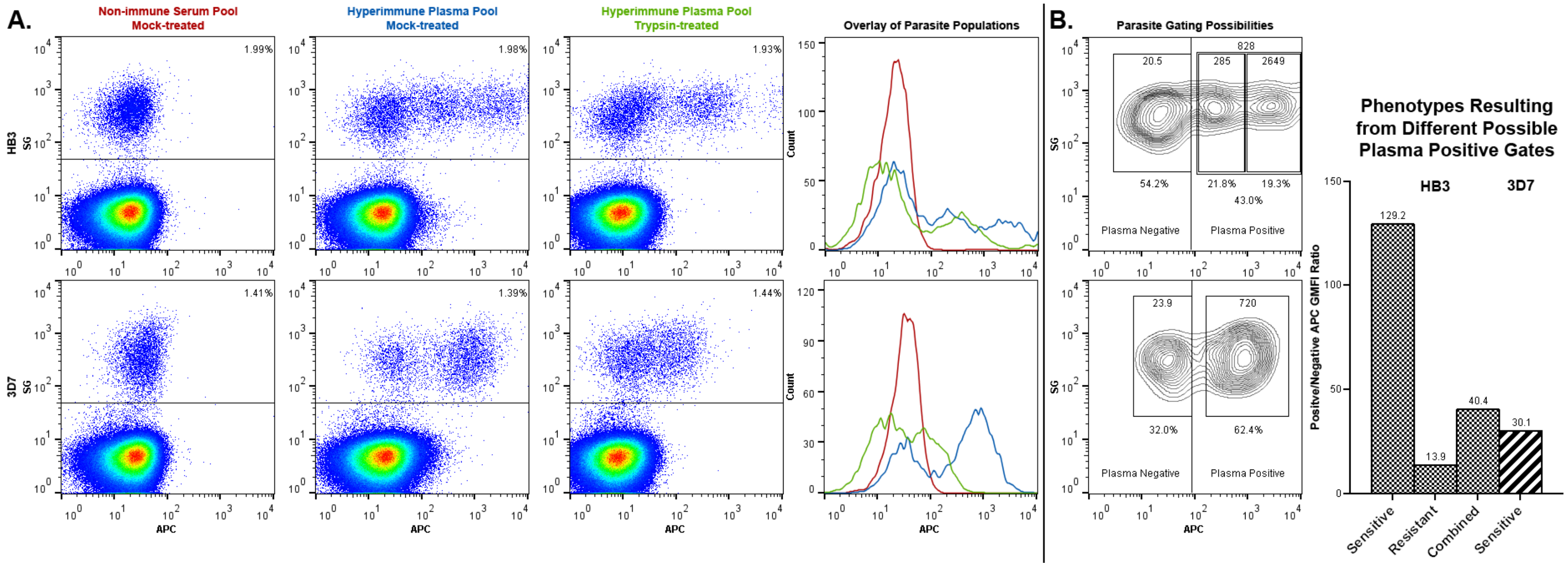

Figure 2.9: Standard FACS phenotypes established for HB3 and 3D7. pRBCs were either mock-treated or trypsin-treated before being incubated with non-immune pooled serum or hyperimmune pooled plasma (panel A). Both HB3 and 3D7 pRBCs did not react at all with the non-immune pooled serum but did react, albeit differently, to the hyperimmune pooled plasma. The single, trypsin-sensitive plasma positive population of 3D7 is typical of PfEMP1-unselected parasites, while the double, trypsin-resistant and trypsin-sensitive plasma positive populations of HB3 were unexpected. To establish the surface PfEMP1 level phenotypes for both parasite lines, a ratio was developed using the APC-channel GMFIs of the plasma positive and plasma negative populations (panel B). Since HB3 possessed multiple plasma-positive populations, three ratios were developed and compared to 3D7. Ultimately, only the bright, trypsin-sensitive population was considered in establishing the phenotype of HB3.

trypsin-treated HB3 pRBCs (Figure 2.11). The recognition profiles of each plasma sample varied, with plasma M01 being the only component that detected the trypsin-resistant population. Additionally, the residual bright population left after trypsinization could be attributed to a newly emergent population detected by plasma F07. This suggested that HB3 possessed 2 truly distinct plasma positive populations with distinct trypsin sensitivities.

To investigate whether the PfEMP1 of HB3 was susceptible to digestion by other proteases, a FACS assay using chymotrypsin and pronase E was performed (Figure 2.12). Digestion by chymotrypsin resembled digestion by trypsin in both HB3 and 3D7, though the plasma-positive populations of HB3 appeared slightly more resistant to chymotrypsin. Digestion by pronase E completely abolished the APC signal in both HB3 and 3D7. However, the post-digestion supernatant of pronase E-treated pRBCs resembled the supernatant of pRBCs incubated with trypsin for 10 minutes, effectively excluding pronase E as a trypsin-replacement for Western blotting. For subsequent FACS assays, trypsin was therefore included as the standard protease. Conveniently, the trypsin-sensitive and trypsin-resistant populations of HB3 served as internal indicators of trypsin activity, enabling the confident identification of trypsin-resistant PfEMP1 variants in subsequent FACS assays.

Trypsin-sensitivity, though expected for a protein as large as PfEMP1, was not essential to determine surface PfEMP1 level phenotypes for HB3 and 3D7 by FACS. However, knob presence and density have been previously shown to significantly impact surface-displayed PfEMP1[322], so it was necessary to confirm that both parasite lines were knob-positive. Images acquired by scanning electron microscopy clearly showed that knobs were present on HB3 and 3D7 pRBCs but not on knob-negative, KAHRP-KO 3D7 pRBCs[255] (Figure 2.13). Additionally, the knob distribution and density per µm^2 were not significantly different (p = 0.9) between HB3 and 3D7 as determined by a Mann-Whitney rank test. To reproduce previously published data and further observe the effects of knob-presence on surface PfEMP1 levels, HB3, 3D7, and KAHRP-KO 3D7 pRBCs were analyzed by FACS.

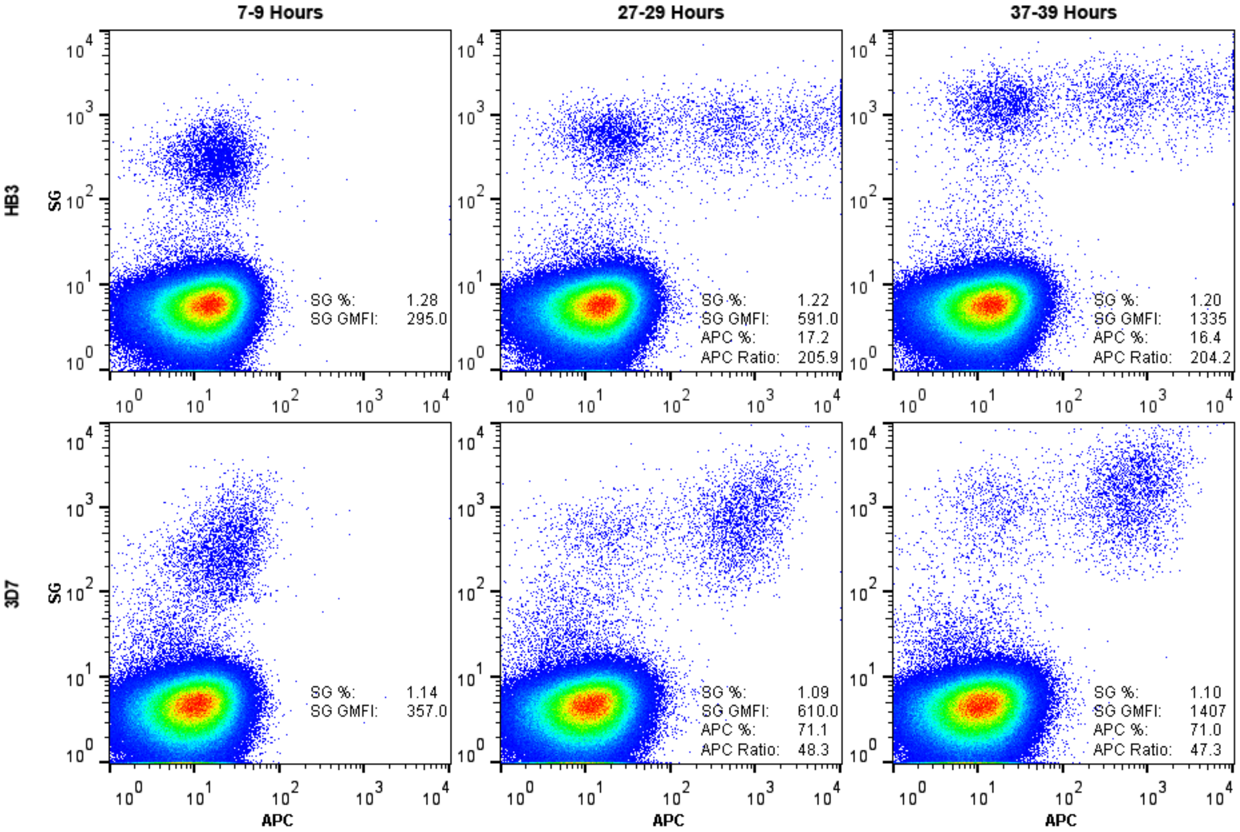

Figure 2.10: pRBC age-specific reactivity of the hyperimmune plasma pool. pRBCs collected at 3 different time points were incubated with the hyperimmune plasma pool to indirectly gauge PfEMP1-specific recognition. Parasites were only recognized after PfEMP1 had been displayed on the cell surface, which reaches saturating levels after 24 hours. The plasma positive parasitemia and APC GMFI ratio did not significantly increase between 27-29 hours and 37-39 hours. The increase in SG GMFI across time points is directly attributable to the increased DNA content of the parasite as it develops.

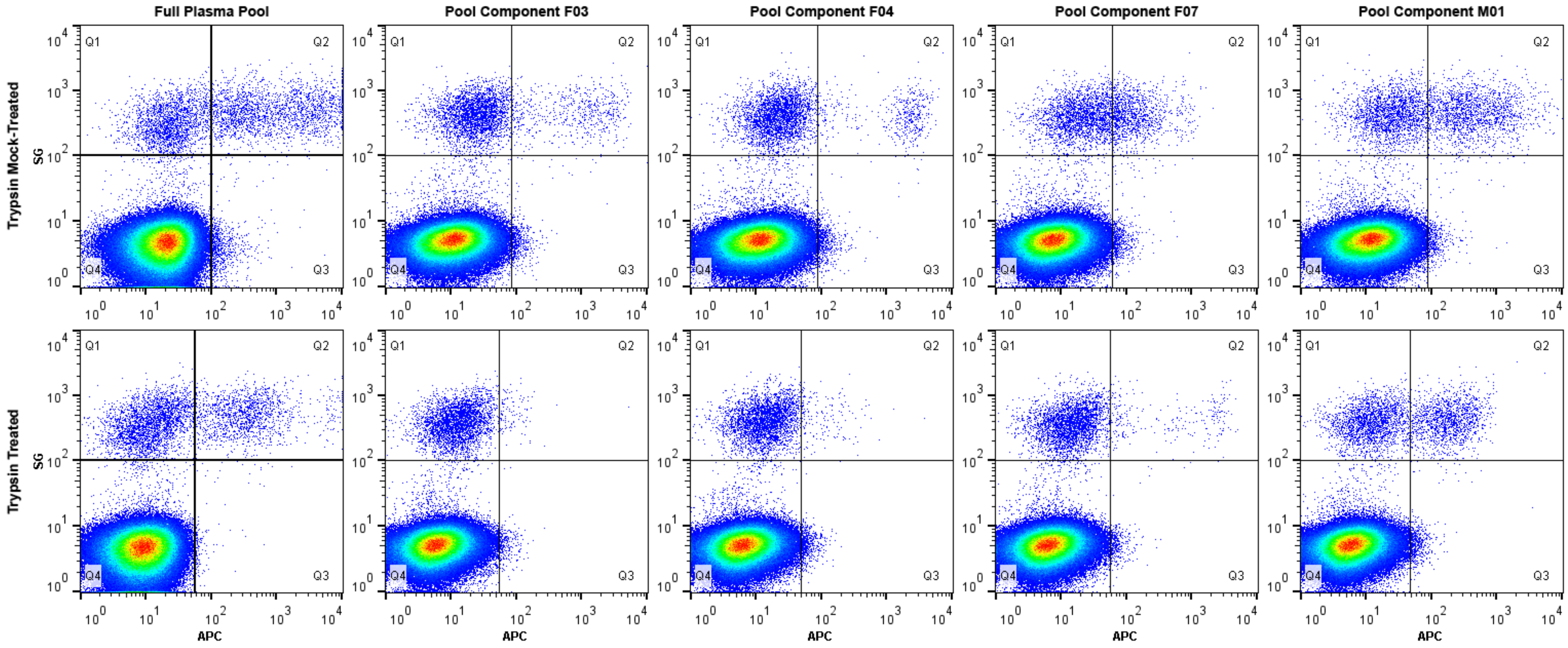

Figure 2.11: Antibody recognition and trypsin-sensitivity of HB3 using the components of the hyperimmune plasma pool. HB3 pRBCs were mock-treated or trypsin-treated before being incubated with the hyperimmune plasma pool and its individual components. A trypsin-sensitive, plasma positive population is recognized by each plasma sample, though the APC-channel signal intensity with F07 is much lower than with the other plasmas. M01 uniquely recognizes a trypsin-resistant, plasma positive population, which solely accounts for the resistance seen with the plasma pool. Taken together, the resistance seen with M01, the sensitivity seen with F03 and F04, and the post-trypsinization population seen with F07, all suggest that HB3 possesses distinct trypsin-sensitive and trypsin-resistant plasma positive populations.

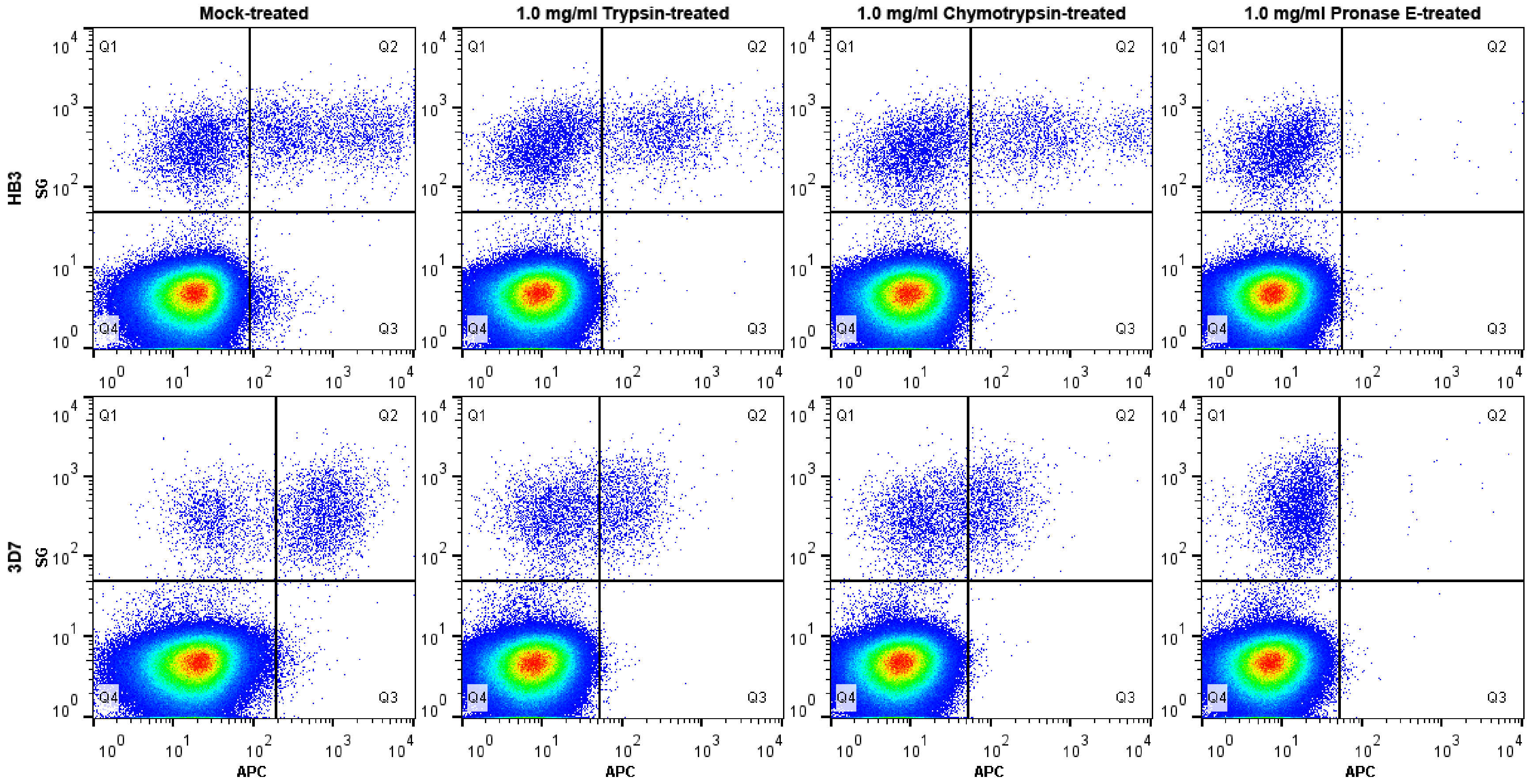

Figure 2.12: Protease-sensitivity of HB3 and 3D7. pRBCs were either mock-treated or treated with 1.0 mg/ml trypsin, chymotrypsin, or pronase E before being incubated with the hyperimmune plasma pool. The PfEMP1 of 3D7 parasites was digested equally well by trypsin and chymotrypsin, though only pronase E digestion was able to fully reduce the plasma positive APC signal to plasma negative levels. The PfEMP1 of HB3 exhibited reduced sensitivity to chymotrypsin compared to trypsin, but only pronase E was able to fully digest the trypsin-resistant PfEMP1 variants.

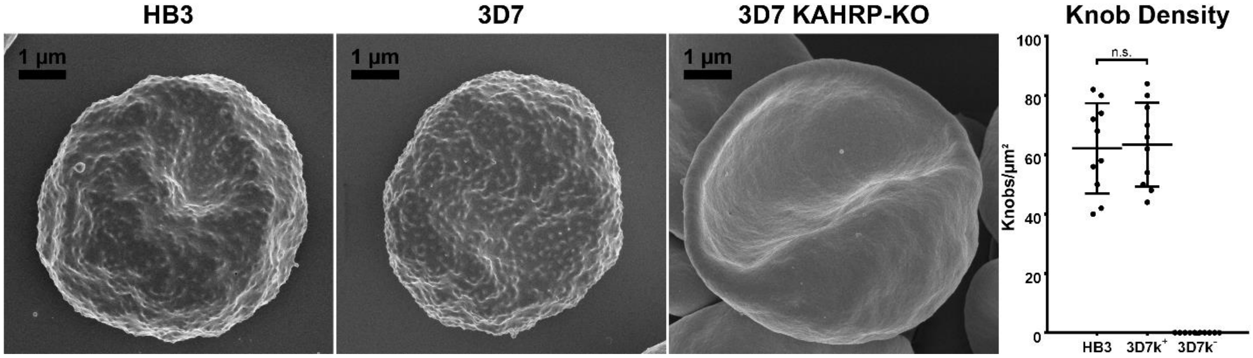

Figure 2.13: Knob distribution on HB3, 3D7, and 3D7 KAHRP-knockout pRBCs. Scanning electron micrographs of HB3, 3D7, and 3D7 KAHRP-knockout pRBCs show that both the HB3 and 3D7 lines used in this thesis are knob-positive and possess comparable knob densities per µm^2 (n = 10).

As expected, the loss of knobs in 3D7 resulted in a 50% decrease in surface-displayed PfEMP1 (Figure 2.14 B).

It has also been reported that parasites maintained in medium containing serum-replacements such as AlbuMAX® II display less PfEMP1 on the pRBC surface[320,382]. While serum-supplemented medium was exclusively used for all parasite cultures mentioned in this chapter, an experiment using 0.5% w/v AlbuMax® II-supplemented medium was performed to determine if the differences in surface PfEMP1 levels between HB3 and 3D7 could possibly be serum-related (Figure 2.14 A). Similar to what has been published previously, there was a 10% decrease in PfEMP1 surface levels across all parasite lines tested.

Direct visual confirmation of the differences in surface PfEMP1 levels between HB3 and 3D7 was obtained by examining FACS samples under confocal microscopy. While both parasite lines displayed the characteristic punctate fluorescence pattern of knob-anchored PfEMP1 (Figure 2.15), the overall APC signal of HB3 pRBCs was significantly brighter than that of 3D7 pRBCs. Other features such as cell size, morphology, and SG staining appeared similar between the 2 parasite lines.

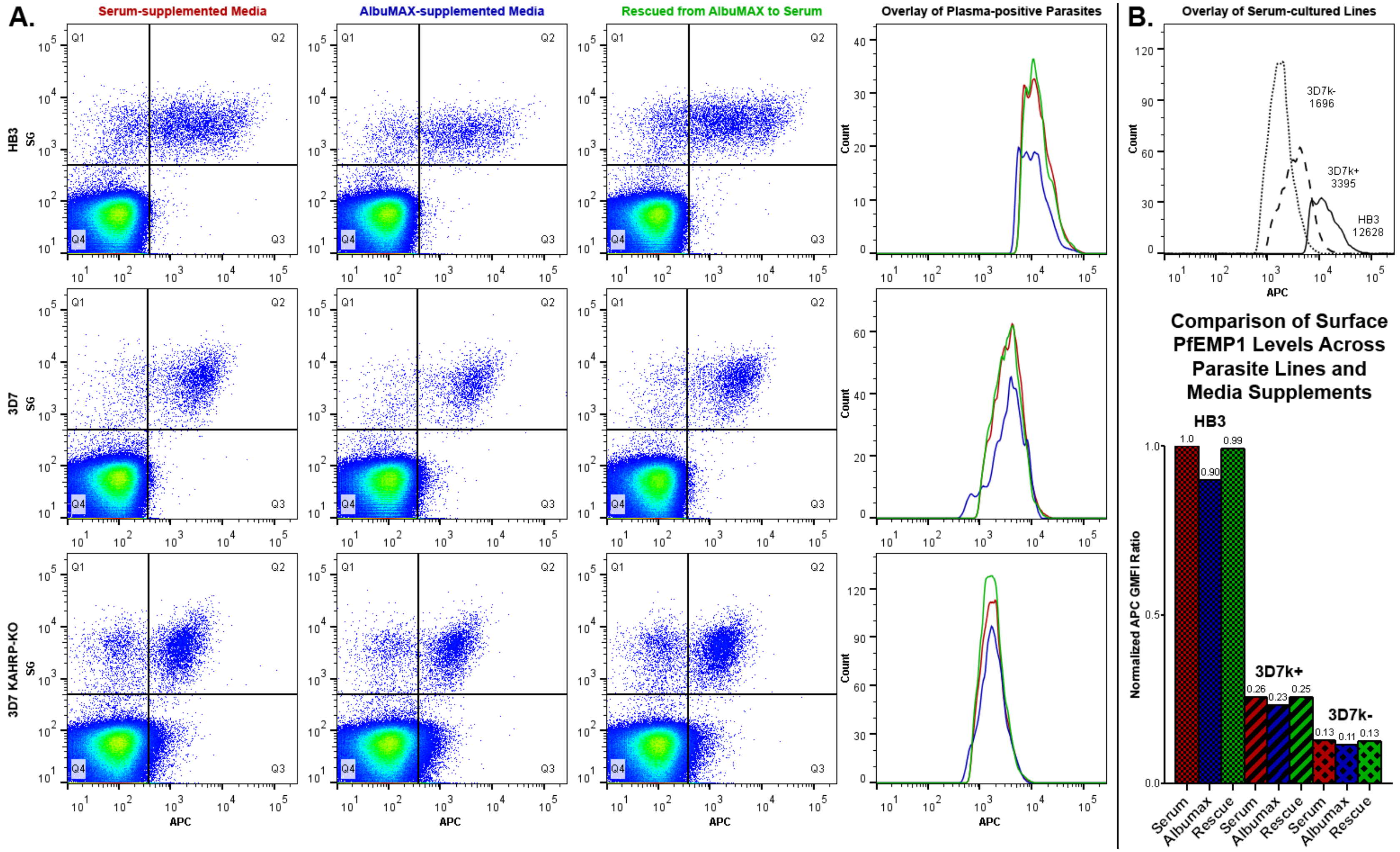

Figure 2.14: Effects of medium supplements and parasite knobs on surface-displayed PfEMP1 levels. HB3, 3D7, and 3D7 KAHRP-knockout pRBCs were cultured in 10% serum-supplemented and 0.5% w/v AlbuMAX® II-supplemented medium (panel A). Culturing with AlbuMAX® II instead of serum resulted in a rescuable 10% decrease in surface PfEMP1 levels. The loss of pRBC surface knobs in 3D7 resulted in a 50% decrease in surface PfEMP1 levels (panel B).

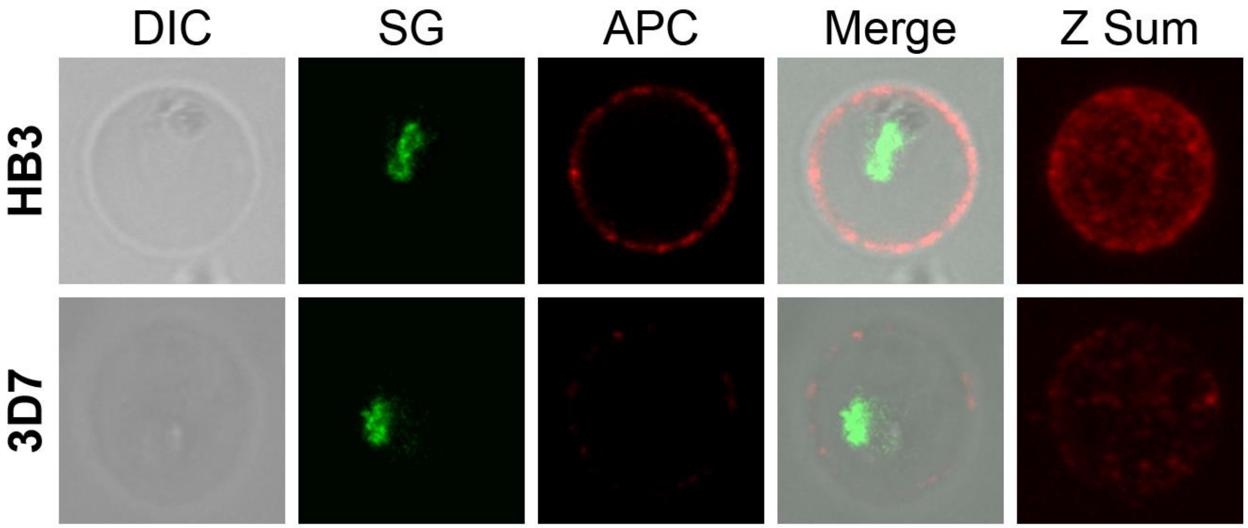

Figure 2.15: HB3 and 3D7 surface-displayed PfEMP1 by confocal microscopy. FACS-prepared HB3 and 3D7 trophozoites were imaged by confocal microscopy using consistent laser voltages and signal gain adjustments. Cells containing single parasites showed similar SG signal intensities but vastly different APC signal intensities, supporting observations made by flow cytometry. The summation of 20 Z-stacks reveals the cell-wide distribution and punctate appearance of knob-anchored PfEMP1.

2.3.2 Progeny surface PfEMP1 phenotypes

With well-characterized, clearly distinct parental phenotypes, the progeny from the HB3 x 3D7 genetic cross could be confidently phenotyped for use in further genetic analysis. The same optimized 2-color, 3-layer FACS assay described in section 2.2.5 was used to establish phenotypes for 16 genetically distinct progeny (Figure 2.16). A range of progeny phenotypes were observed, including clones possessing phenotypes beyond those of both parents. At the most extreme ends, clone X44 appeared 37% brighter than HB3, while clone X35 appeared 13% dimmer than 3D7. Overall, the non-bimodal distribution of the progeny phenotypes was characteristic of a complex, multi-locus genotype-phenotype association. Due to limiting amounts of hyperimmune plasma, biological replicates could not be performed for each of the progeny. However, an effort to determine the robustness of the observed phenotypes was made by re-phenotyping select progeny possessing phenotypes

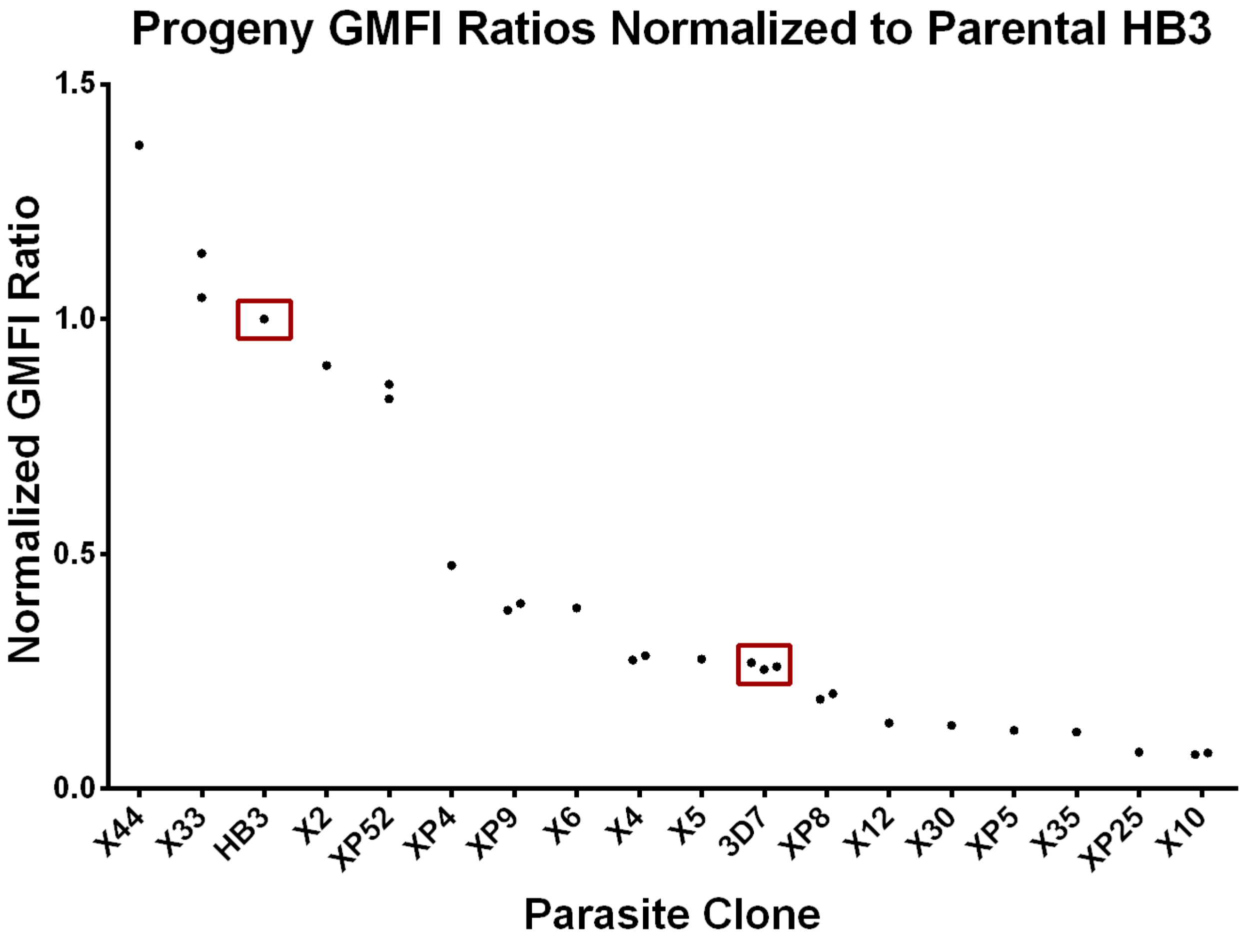

Figure 2.16: Normalized GMFI Ratios determined by FACS for HB3, 3D7, and 16 progeny from an HB3 x 3D7 genetic cross. Progeny analyzed by FACS and normalized to an internal HB3 control possess a range of phenotypes. Parental HB3 and 3D7 phenotypes (red boxes) differ by 75%, with most of the progeny phenotypes falling in between. Each point represents a single biological replicate.

that spanned the general distribution. Of these biological replicates, the greatest difference observed was an 8.26% reduction in the normalized GMFI ratio of X33. The remaining replicates showed reductions of 3.57% for XP52, 3.73% for XP9, 5.78% for XP8, 4.65% for X10, and an increase of 3.44% for X4. This suggested that the observed phenotypes were generally stable and reproducible.

As with HB3 and 3D7, all of the progeny were mock-treated and trypsin-treated prior to FACS processing. The subsequent FACS results revealed a range of parasite

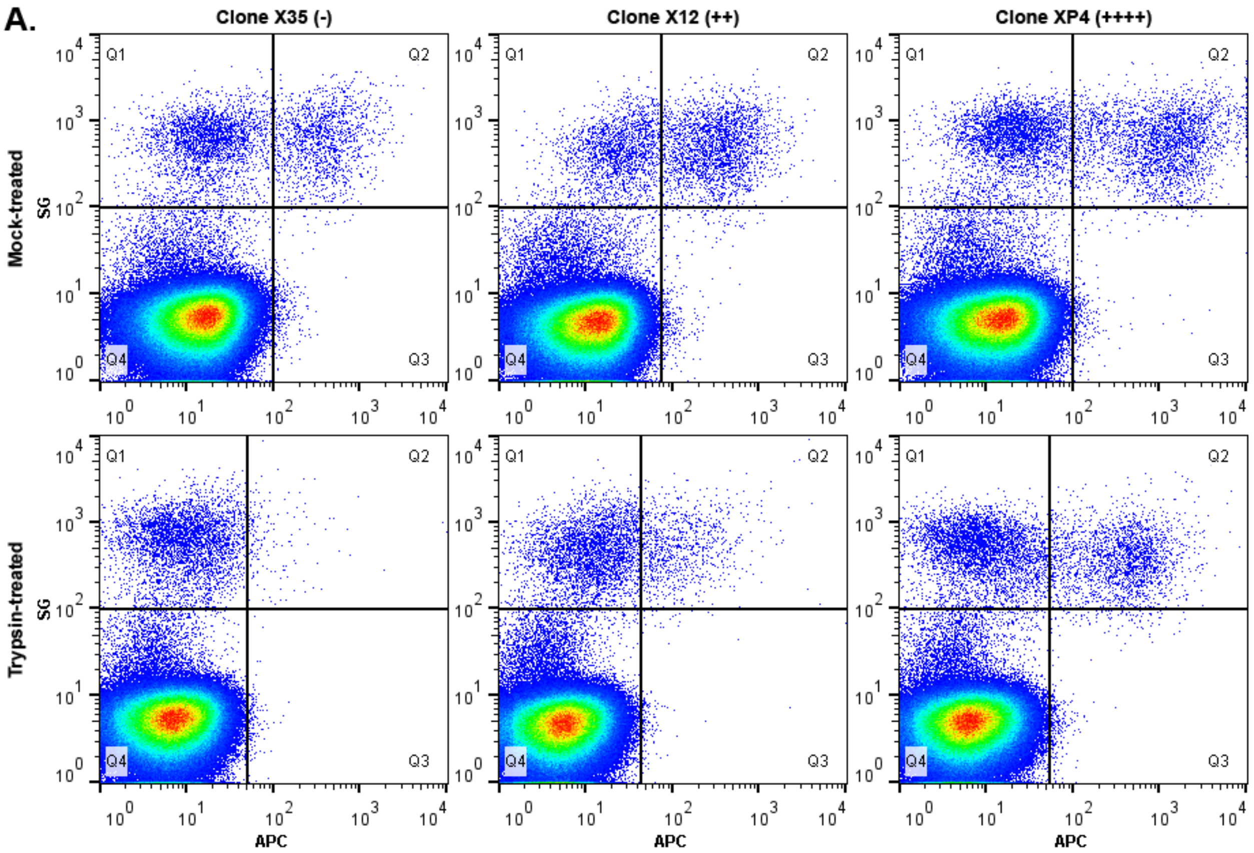

B.

Parasite Clone	HB3*	3D7	XP4	XP5	XP8	XP9	XP25	XP52	X2
Plasma positive %	14.3	70.7	37.4	74.6	45.1	34.3	47.2	28.8	64.7
Trypsin resistance	-	+	++++	++	-	++++	++	-	++++

Parasite Clone	X4	X5	X6	X10	X12	X30	X33	X35	X44
Plasma positive %	46.4	63.9	46.8	74.3	51.1	49.4	65.9	31.5	37.8
Trypsin resistance	-	-	-	+	++	++++	+	-	+

Figure 2.17: Variation in trypsin sensitivity and pRBC recognition among phenotyped progeny. The 16 progeny phenotyped by FACS possessed a range of trypsin profiles, examples of which can be clearly seen in clones X35, X12, and XP4 (panel A). The degree of trypsin resistance among the progeny was qualified from fully sensitive (-) to fully resistant (++++) (panel B). The percent of plasma positive pRBCs is listed to demonstrate the breadth of PfEMP1 recognition by the hyperimmune plasma pool. For HB3, only the most APC-positive plasma positive population was considered.

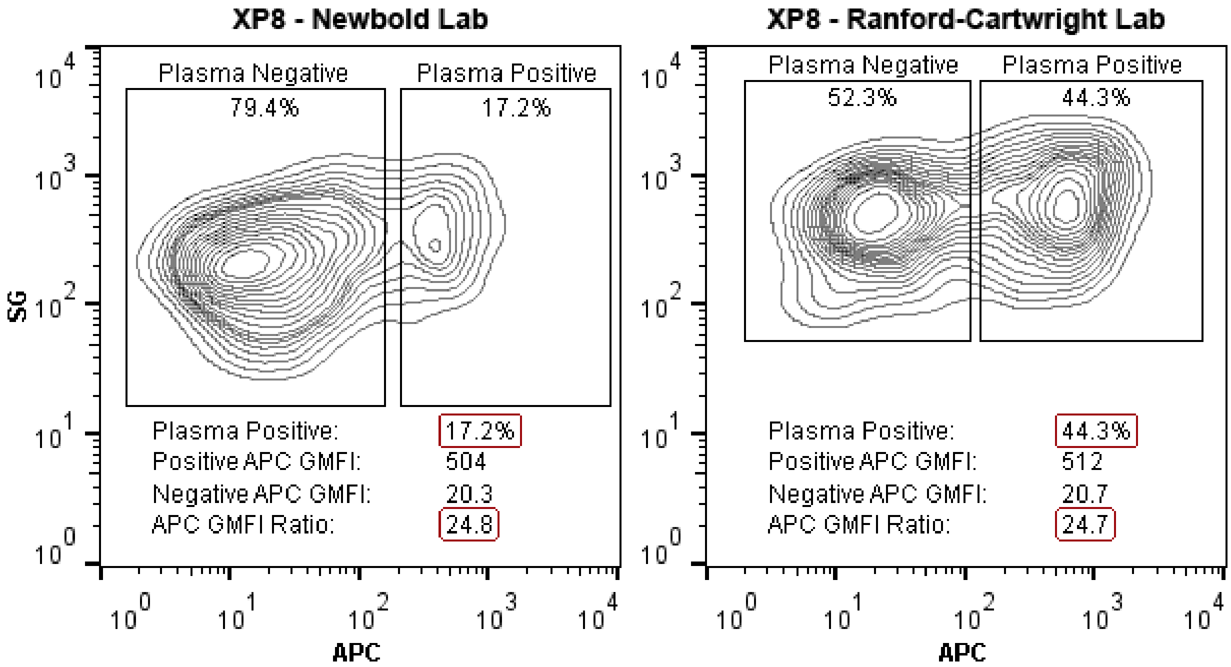

Figure 2.18: Impact of plasma positive pRBC percentage on the APC GMFI ratio. Cryovials of progeny clone XP8 were obtained from the Ranford-Cartwright laboratory and the Newbold laboratory, which had obtained the clone from the Ranford-Cartwright laboratory several years prior. The hyperimmune plasma pool recognized each sample differently, likely due to natural PfEMP1 variant switching, but the APC GMFI ratio used to establish the phenotype of XP8 was unaffected.

sensitivities to trypsin (Figure 2.17 A). For each FACS assay, the standard HB3 internal control responded to trypsinization as described above, indicating that the trypsin was active and that any resistant progeny were truly resistant. The trypsin profiles of the progeny were qualified using a scale ranging from completely sensitive (-) to completely resistant (++++) (Figure 2.17 B). Unlike HB3, all of the progeny segregated into only 2 populations with varying degrees of pRBC recognition by the hyperimmune plasma pool. In cases of resistant progeny, such as XP4 and X30, the single plasma positive population was used to establish the surface PfEMP1 level phenotype of that clone even though it was fully trypsin resistant. The proportion of pRBCs recognized did not appear to have an impact on the calculated GMFI ratio (Figure 2.18).

2.4 Discussion

The first aim of this chapter was to establish and characterize the natural difference in surface PfEMP1 levels between the *P. falciparum* lines HB3 and 3D7. The initial attempt to accomplish this relied on probing differential detergent extracts from trypsin- and mock-treated pRBCs with an anti-ATS antibody via Western blotting in order to quantify relative levels of intracellular and surface-displayed PfEMP1. This was an attractive approach since an antibody specific to the highly conserved ATS domain of PfEMP1 would recognize most variants of the protein. Additionally, the decrease in molecular weight of surface-displayed PfEMP1 after trypsinization allowed for the specific localization of PfEMP1 to the pRBC surface while still providing insights into the overall amount of PfEMP1 produced by the parasite and the efficiency of the PfEMP1 trafficking process.

In agreement with previous findings[254,322,367], A4 parasites clearly displayed the majority of their expressed PfEMP1 on the pRBC surface, as evidenced by the relatively minimal Triton-soluble PfEMP1 band and the overwhelmingly trypsin-sensitive Triton-insoluble PfEMP1 band (Figure 2.8). The unaltered intensity of the Triton-soluble PfEMP1 band suggested that some PfEMP1 remains intracellular and unexposed to trypsin, which remains extracellular. Furthermore, the nearly complete elimination of the Triton-insoluble full-length PfEMP1 band after trypsinization suggested that all of that PfEMP1 is surface-displayed and trypsin-sensitive. It was thus concluded that, of the PfEMP1 produced by A4, most is trafficked and displayed on the pRBC surface.

Unlike A4 parasites, 3D7 parasites appeared to display only a small portion of their expressed PfEMP1 on the pRBC surface, as evidenced by the relatively small difference in the Triton-soluble and Triton-insoluble PfEMP1 bands and the imperceptible change in the Triton-insoluble full-length PfEMP1 band after trypsinization (Figure 2.8). Generally, Triton-soluble PfEMP1 is intracellular and Triton-insoluble PfEMP1 is surface-displayed. The small band intensity difference between these fractions suggested that a significant amount of the PfEMP1 expressed by 3D7 remains intracellular. Additionally, the appearance of a faint trypsin cleavage product in the Triton-insoluble fraction after trypsinization suggested that either most of the surface-displayed PfEMP1 of 3D7 was trypsin-resistant or most of the Triton-insoluble PfEMP1 was not surface-displayed but rather remained intracellular within Triton-insoluble structures, such as the parasite itself or Maurer's clefts. While either of these possibilities could account for the Western blotting results, a previous report assessing the trypsin-sensitivity, chymotrypsin-sensitivity, and CD36-adherence of 3D7 and several isogenic knockouts concluded that the protease-sensitive PfEMP1, though appearing at unexpectedly low levels, is representative of the amount of PfEMP1 displayed on the surface of 3D7 pRBCs[326].

The Western blotting results for HB3 were entirely unexpected due to the unusual trypsinization pattern observed (Figure 2.8). Normally, the strong PfEMP1 band in the Triton-soluble fraction compared to the relatively weak band in the Triton-insoluble fraction would suggest that most of the PfEMP1 produced by HB3 remained intracellular. However, the significant decrease in the full-length PfEMP1 band intensity in the Triton-soluble fraction after trypsinization, as well as the appearance of a trypsin cleavage product between 150 and 225 kDa, suggested that either trypsin was entering the pRBC and accessing the intracellular PfEMP1 pool or surface-displayed PfEMP1 in HB3 was Triton-soluble. Since cell membranes are expected to be insoluble in Triton™ X-100[383], the trypsin-sensitive PfEMP1 of HB3 was either integrated into a Triton-soluble part of the pRBC membrane or it was not anchored to the pRBC membrane as predicted for PfEMP1[324,384]. Previous studies of the integral RBC membrane protein band 3 have demonstrated Triton™ X-100 solubility of up to 60% of the total band 3 fraction[385–387], which at the very least allows for the possibility of other membrane proteins, such as PfEMP1, to be partially Triton-soluble. The interpretation of the blot was further complicated by the fact that the intensity of the Triton-insoluble PfEMP1 band was unaltered by trypsinization, suggesting that HB3 possessed a trypsin-resistant PfEMP1 variant. Trypsin-resistant PfEMP1 variants have been reported previously[236,388–390], and the potential expression of at least 1 such variant by HB3 would prevent the accurate localization of PfEMP1 to the pRBC surface, effectively eliminating Western blotting as a phenotyping method. Given that neither A4 nor 3D7 showed changes in the PfEMP1 band intensity in the Triton-soluble fractions after trypsinization, it was concluded that HB3 possessed 2 distinct surface-displayed PfEMP1 populations— 1 Triton-soluble and trypsin-sensitive, and 1 Triton-insoluble and trypsin-resistant. Consequently, Western blotting ceased to be a viable method for establishing surface PfEMP1 level phenotypes.

The inability to specifically localize surface-displayed PfEMP1 by Western blotting led to a focus on flow cytometry as a means of phenotyping HB3, 3D7, and the genetic cross progeny. This approach provided the distinct advantage of directly detecting PfEMP1 that had been naturally displayed on the pRBC surface by the parasite, thus providing the most true-to-life assessment possible. The most significant disadvantage of flow cytometry was the necessary reliance on a hyperimmune plasma pool rather than a specific, broadly reactive antibody to detect PfEMP1, resulting in the potential caveat that plasma-positive pRBCs were positive due to the expression of plasma-reactive antigens other than PfEMP1. Though it has been overwhelmingly demonstrated that the natural blood-stage antibody response is primarily directed against PfEMP1[153,154,198,257], FACS experiments were designed and optimized in an attempt to reduce the uncertainty that antigens other than PfEMP1 were being detected. The pRBC age-specific response demonstrated in Figure 2.10 clearly excluded ring-stage surface antigens as antibody targets, and the generally consistent APC GMFI ratio as parasites matured from trophozoites to schizonts suggested that other variable surface antigens such as RIFIN and STEVOR were unlikely to be contributing to the plasma recognition of pRBCs.

Two previously reported characteristics of surface-displayed PfEMP1 were assessed in Figure 2.14 to provide indirect evidence of PfEMP1 detection by the hyperimmune plasma pool. First, the loss of pRBC surface knobs in a 3D7 KAHRP-knockout, as confirmed in Figure 2.13, resulted in a 50% decrease in the normalized APC GMFI ratio. This result was consistent with flow cytometry experiments using knob-positive and knob-negative A4 parasites probed with a monoclonal antibody specific to a single A4 PfEMP1 variant[322]. Additionally, Figure 2.13 showed that any difference in surface PfEMP1 levels between HB3 and 3D7 could not be attributed to the absence of pRBC surface knobs. Second, the use of AlbuMAX® II as a serum-replacement in complete parasite culture medium resulted in a repeatable 10% decrease in the normalized APC GMFI ratios of HB3, 3D7, and a 3D7 KAHRP-knockout. This result was similar to the nearly 20% decrease seen with monoclonal antibody-probed A4 parasites in 1 study[320], though a subsequent study reported a decrease as large as 80%[382]. The variation observed among different parasite lines is not unusual given their different genetic backgrounds and the wide range of culturing methods and experimental techniques practiced among different laboratories.

Confident that the hyperimmune plasma pool was specifically detecting PfEMP1, surface PfEMP1 level phenotypes were established for HB3 and 3D7 (Figure 2.9).This was straightforward for 3D7 given that the pRBCs segregated into a single plasma negative population and a single plasma positive population. However, the presence of 2 distinct plasma positive populations in HB3 complicated the establishment of a phenotype. When the individual plasma pool components were tested against HB3 (Figure 2.11), it was clear that plasmas F03, F04, and M01 all recognized the same bright, trypsin-sensitive population, while only M01 recognized the dimmer, trypsin-resistant population. The frequent recognition of the bright population, coupled with its PfEMP1-characteristic response to trypsin, led to its selection as the only plasma positive population of HB3. Additionally, the phenotype determined by including only the bright positive population was significantly different than the phenotype of 3D7 (Figure 2.9 B), providing the clearly different parental phenotypes necessary for QTL analysis. The disparity in the surface PfEMP1 levels of HB3 and 3D7 was further seen in confocal microscopy images clearly showing the characteristic cell-wide distribution of PfEMP1 clusters (Figure 2.15).

The large difference in parental phenotypes, though explainable by 3D7 displaying less PfEMP1 on the pRBC surface, could also be explained by a low-avidity antibody reacting against the particular PfEMP1 variant expressed by 3D7 or a high-avidity antibody reacting against the particular PfEMP1 variant expressed by HB3. In either of those cases, the APC signal intensity of the plasma positive pRBC population would not be truly representative of the amount of PfEMP1 on the pRBC surface. Unfortunately, without using a monoclonal antibody specifically targeting a single PfEMP1 variant, as described above for A4 parasites, the secondary explanation cannot be adequately excluded. An indirect way of addressing the issue of antibody avidity relies on the composition of the hyperimmune plasma pool. By including multiple plasma samples, the pool not only recognizes a broad range of PfEMP1 variants, but it also decreases the likelihood that an unusually low- or high-avidity antibody would solely define the plasma positive pRBC population. This is demonstrated for HB3 in Figure 2.11, where the dim plasma-positive population recognized by plasmas F07 and M01 can be considered anomalous and excluded given that a bright plasma-positive population is recognized by plasmas F03, F04, and M01. Ultimately, the plasma positive population considered in establishing the phenotype of HB3, though important in providing a solid rationale for phenotyping the genetic cross progeny, would not directly impact the normalized phenotype distribution of the progeny if all parasite lines were normalized to HB3 in the same way.

The second aim of this chapter was to determine the natural differences in surface PfEMP1 levels among progeny from an HB3 x 3D7 genetic cross. Having excluded Western blotting as a viable method and having thoroughly examined relevant aspects of the flow cytometry approach, phenotypes were established for 16 of the progeny (Figure 2.16). Fortunately, all of the plasma reactivity profiles of the progeny resembled 3D7 rather than HB3, examples of which are seen in Figure 2.17 A. This greatly simplified the development of APC GMFI ratios since there were only single plasma positive populations to consider. Surprisingly, trypsin-resistant plasma positive populations were common among the progeny (Figure 2.17 B), which suggested that the phenomenon may be far more common among *P. falciparum* lines than previously considered. Alternatively, the trypsin-resistant populations may actually be trypsin-sensitive, but flow cytometry is unable to detect this since the antibodies recognizing those PfEMP1 variants could be binding epitopes that remain attached to the pRBC surface after trypsinization. Regardless of the explanation, the sensitivity or resistance of pRBCs to trypsin appeared to have no impact on the APC GMFI ratio or the phenotypic distribution of the progeny.

As seen with HB3 and 3D7, the hyperimmune plasma pool did not consistently recognize the same proportion of pRBCs among the different progeny (Figure 2.17 B). Given that the clones likely express different PfEMP1 variants at the individual pRBC or population level, this observation was not surprising. With antibody layers at saturating concentrations (Figure 2.5), the APC signal intensity should provide an accurate measure of surface-displayed PfEMP1 whether 1% of pRBCs are recognized or 100%. Figure 2.18 clearly supports this assertion, which is additionally verified by the robustness of the select biological replicate phenotypes shown in Figure 2.16. The variable recognition of pRBCs was interesting, though it was not considered in any further way when finalizing the progeny phenotypes.

3 Identifying genetic polymorphisms associated with impaired PfEMP1 trafficking to the infected erythrocyte surface

3.1 Introduction and aims

The rapid expansion of DNA sequencing technologies over the past decade has provided invaluable resources for experimentally understanding complex behaviors in *P. falciparum*. Detailed SNP libraries and high-coverage genome sequences have been generated for many laboratory-adapted and field-isolated parasites, offering a previously unattainable level of insight into parasite biology. The explosive rate of genomic data accumulation, though an undeniable benefit to the malaria scientific research community, has far outpaced the rate at which parasite phenotype data has been accumulated and interrogated. Of the approximately 5,500 putative coding regions identified in the *P. falciparum* genome, over 50% encode proteins of unknown function. Furthermore, only 2% of the coding regions have been experimentally disrupted to establish causative genotype-phenotype associations. The inherent difficulties of manipulating parasites in the laboratory certainly contribute to the low association of known genes with unknown phenotypes, but the large deficit in the current knowledge of gene-function relationships can be mostly attributed to the difficulties of associating known phenotypes with unknown genes.

Quantitative trait loci analysis is a powerful tool capable of reducing complex parasite phenotypes to their most basic genetic elements through the statistical association of quantitative phenotypes with genotypes. This technique takes advantage of the recombination and segregation of parental alleles during meiosis, which results in haploid progeny possessing genotype combinations unlike each other and the original parents. As long as a clearly defined phenotype exists between the parental lines, QTL analysis can be easily applied to genotyped progeny that have been assessed for the same parental phenotype.

With clear surface PfEMP1 level phenotypes for HB3, 3D7, and many of their progeny, the aim of this chapter is to identify any genetic polymorphisms associated with the impaired trafficking of PfEMP1 in 3D7. This is directly addressed by performing QTL analysis using the phenotype data described in chapter 2 and pre-existing parasite genomic data. Following the identification of potential gene candidates, the second aim of this chapter is to thoroughly characterize any genes of interest in order to best select which candidate to pursue in subsequent genetic manipulation and phenotyping experiments.

3.2 Materials and methods

3.2.1 QTL analysis

Genetic linkage analysis provides a robust means of determining the genetic loci responsible for *P. falciparum* phenotypes that are complex or lack obvious candidate genes. Though this approach is confined to parasites involved in experimental genetic crosses, the completion of 4 unique crosses to date[331,391,392] (Wellems Lab, personal communication) enables the pursuit of a wide range of phenotype-genotype associations. With the parents and progeny of a genetic cross available, linkage analysis can be applied if a clearly segregating parental phenotype exists, the same phenotype has been measured in the progeny, and genetic maps of each progeny clone identifying regions of the genome inherited from each parent have been generated. Through the use of statistical methods[393–396], observed phenotypes can be associated with genetic maps to determine maximum likelihood estimates and logarithm of odds (LOD) scores for the entire genome, highlighting regions with the highest probability of containing the genetic locus responsible for the phenotype of interest.

The simplest form of linkage analysis involves a phenotype of interest that is bimodally distributed between the parents and progeny of a genetic cross[358]. Since each progeny phenotype would align exactly with 1 of the 2 parental phenotypes, the presence of a single inherited gene or SNP, e.g. the K76T mutation in PfCRT[397], would be responsible for the phenotype of interest, e.g. chloroquine resistance. For more complex phenotypes that are likely influenced by multiple genetic loci, such as PfEMP1 trafficking, the phenotype of interest would be unimodally distributed, resulting in progeny that possess non-parental phenotypes that could exceed or fall in between those of either parent. In that case, phenotypes must be quantified and associated using a statistical method known as quantitative trait loci (QTL) analysis[398]. Briefly, this strategy utilizes interval mapping where, assuming a normal “bell curve” distribution of phenotypes, each location in the genome is sequentially posited as the location of the putative QTL[399,400]. The known genetic map markers, genotyped as either AA or AB depending on which parent the marker was inherited from, are then used to calculate the probability that a putative QTL possesses the AA or AB genotype. The quantitative phenotypes are then considered in weighing the probability that a putative QTL with the appropriate genotype is responsible for the phenotypic distribution or segregation of progeny clones.

The surface PfEMP1 level phenotypes established for HB3, 3D7, and 16 genetic cross progeny (chapter 2) (Table 3.1) resulted in a phenotype distribution that was somewhat bimodal, but still demonstrated enough variation from the parental phenotypes to be considered for QTL analysis instead of simple linkage analysis. Having already satisfied 2 of the 3 requirements necessary to perform QTL analysis, only genetic inheritance maps for each of the progeny clones needed to be developed. Using previously obtained full-genome sequences and SNP maps (section 2.2.2), over 7000 SNP markers were first analyzed across the progeny to exclude markers that did not contribute any segregation information, such as those inherited in a large region of DNA that was not separated by recombination in any of the progeny. The resulting 3597 genome-wide SNP markers were used to construct the genetic maps of the progeny (Figure 3.1). Table 3.2 lists the number of SNPs distributed on each chromosome.

Identifying QTL in *P. falciparum* continues to rely on statistical analysis methods originally designed for diploid organisms[399,401,402]. Fortunately, the haploid progeny of a *P. falciparum* cross are genetically equivalent to the diploid progeny of a cross using recombinant inbred lines[403]. Treating the HB3 x 3D7 genetic cross as such, the phenotype values in Table 3.1 were associated with the genotype data composing the genetic map in Figure 3.1 using the statistical computing software R version 3.0.1[404] and the add-on package R/qtl version 1.27-10[405]. A 1-dimensional genome scan with a single QTL model

Parasite Clone	Phenotype Value
HB3	1.00
3D7	0.27
XP4	0.48
XP5	0.12
XP8	0.20
XP9	0.39
XP25	0.08
XP52	0.86
X2	0.90
X4	0.27
X5	0.28
X6	0.39
X10	0.08
X12	0.14
X30	0.14
X33	1.14
X35	0.12
X44	1.37

Table 3.1: HB3-normalized surface PfEMP1 level phenotypes for QTL analysis.

was performed using the “scanone” function in order to identify any QTL specifically associated with the phenotype of interest. A LOD score of 3, equivalent to a 1000 to 1 odds of association, served as the initial threshold for the exclusion of unlikely QTL associations[358]. LOD scores greater than 3 were further examined and assessed for significance. This was accomplished using the “scanoneperm” function to initiate a 10000 random permutation test in order to establish a genome-wide distribution of maximum likelihood LOD scores. Single-marker effect plots were generated for significant or near-significant QTL using the function “effectplot” in order to determine the percentage of phenotypic variance explained by the QTL. The genomic locations of QTL responsible for at least 50% of the phenotypic variance were further refined using the “refineqtl” function, which narrows the width of the significant LOD score peak by successively searching for a 1.5 LOD score decrease in each direction away from the peak. This results in the reduction

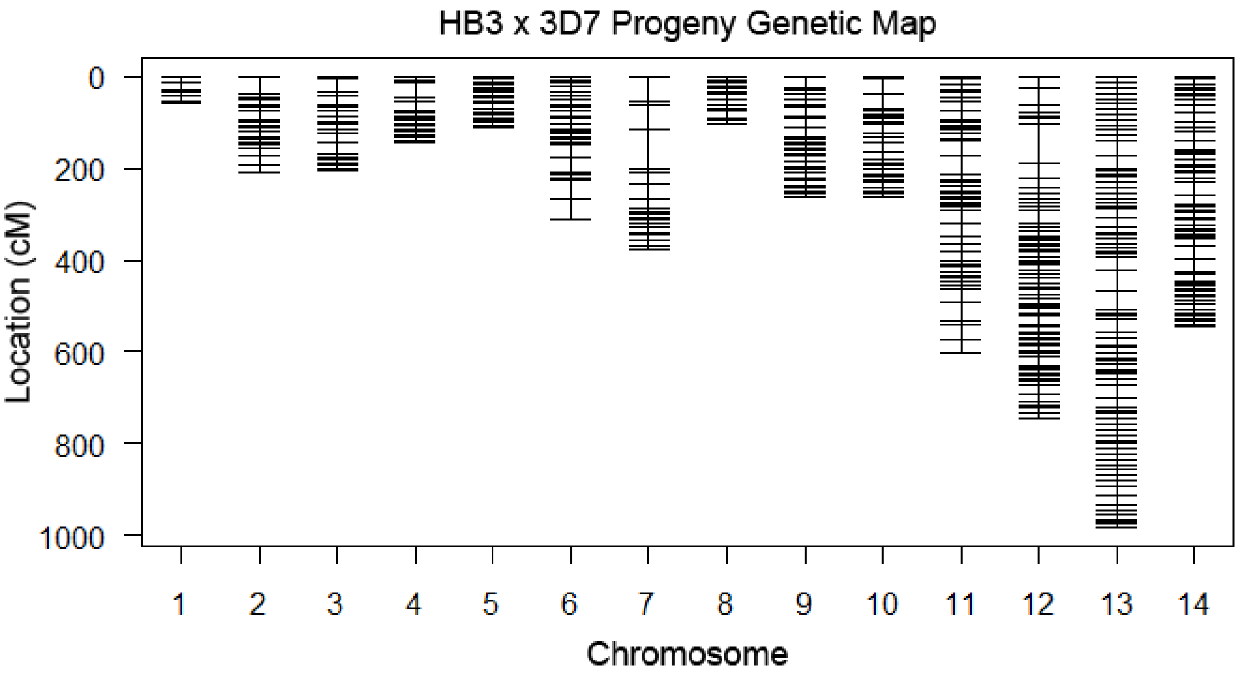

Figure 3.1: Genetic marker map developed for the phenotyped HB3 x 3D7 genetic cross progeny. 3597 SNP markers located across the entire genome were selected for use in QTL analysis. Some chromosomes, such as chromosome 5, were extensively covered due to either high rates of recombination or high SNP frequencies, while others, such as chromosome 7, contained largely stable regions.

Chromosome	1	2	3	4	5	6	7	8	9	10	11	12	13	14
Markers	70	159	152	242	239	246	37	27	297	294	315	454	388	677

Table 3.2: Genetic map SNP marker distribution across *P. falciparum* genome.

of a broad peak spanning multiple markers to a single sharp peak bounded by the markers with the highest probability of containing the physical location of the QTL. The refined genomic regions containing the QTL of interest were then examined to determine which candidate genes to characterize for further genetic manipulation experiments. The entire QTL analysis workflow is summarized in Figure 3.2.

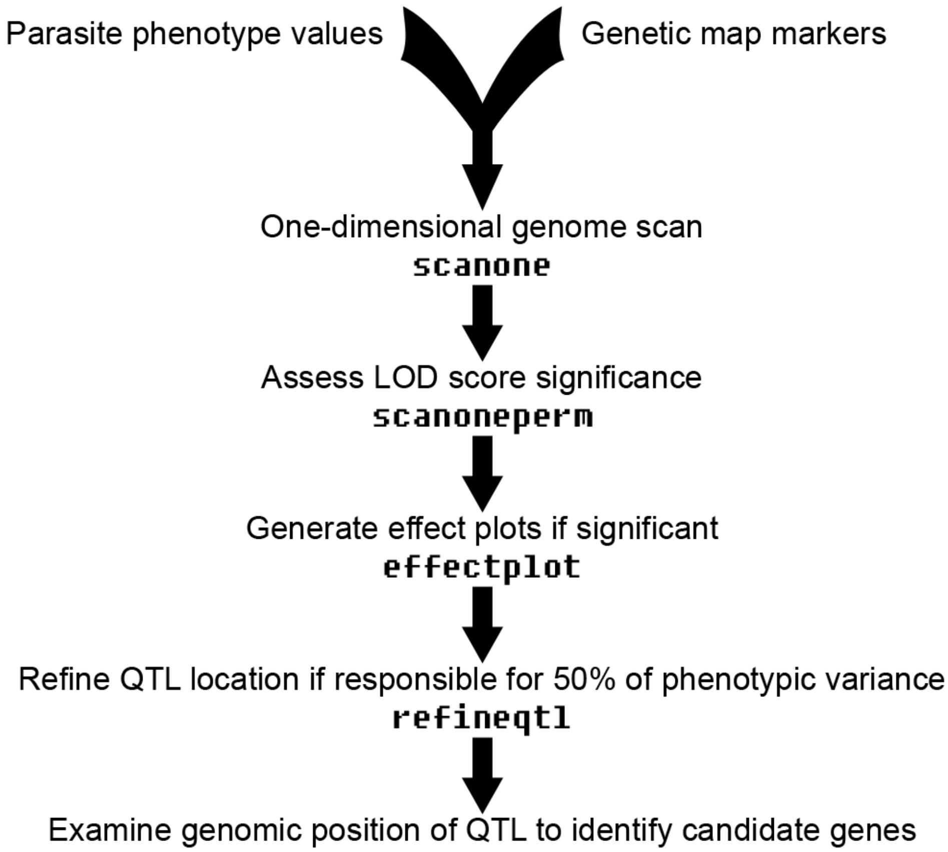

Figure 3.2: QTL analysis workflow using R/qtl. Each step in the QTL analysis workflow is described above the R/qtl syntax used to execute that function. QTL were successively excluded at each step in the analysis process so that only the most likely QTL would be considered for future genetic manipulation experiments.

3.2.2 Candidate gene characterization

Each gene identified within significant loci determined by QTL analysis was initially examined for several key features, though all were considered for further characterization if necessary. First, basic features such as putative or known function, *Plasmodium* homologs, and known non-synonymous SNPs, as well as practical experimental considerations such as gene size and number of exons, were identified using version 3 of the annotated 3D7 reference genome[175] as accessed with PlasmoDB version 13.0[406] and the genome analysis tool Artemis version 15.0.0[407,408]. Of particular interest were genes found only in *P.*

falciparum since PfEMP1 and many of its trafficking components are not found in any other *Plasmodium* species.

Protein sequences, also available through PlasmoDB, were submitted to InterPro version 49.0[409], UniProt[410,411], and the NCBI Conserved Domain Database[412–414] to identify conserved protein domains and potential active sites. This information was used to classify proteins of interest as being more or less likely to contribute to protein trafficking pathways based on sequence similarity to other proteins with known functions. For example, a gene of unknown function predicted to contain a conserved F-actin binding domain would be considered a highly attractive candidate since actin has been previously implicated in the display of PfEMP1 on the pRBC surface[283]. Any conserved domains identified within candidate proteins were assessed using SMART[415,416] to better understand domain function, evolution, and architecture. Sequences were also analyzed for the presence of parasite-specific motifs that might suggest a role in PfEMP1 trafficking. The PEXEL signal[181,182,293] has been shown to direct *P. falciparum*-produced proteins out of the parasite and into the RBC cytosol, and so candidate genes encoding this motif would be well worth pursuing since many previously identified trafficking pathway components possess PEXEL signals[319].

In addition to providing DNA and protein sequence data, PlasmoDB aggregates gene expression data from both the sexual and asexual stages of the *P. falciparum* life cycle. These transcriptome data were used to determine the likelihood that candidate genes were expressed during the blood-stages in a manner consistent with the trafficking of PfEMP1, meaning that genes expressed exclusively during the late trophozoite and schizont stages would be considered less attractive candidates than those expressed during the early stages of development when PfEMP1 is being produced and exported.

3.3 Results

3.3.1 QTL analysis

To address the aim of this chapter, the surface PfEMP1 level phenotypes established in chapter 2 were combined with pre-existing genomic data in QTL analysis to identify genetic determinants responsible for the impaired trafficking of PfEMP1 in 3D7. A 1-dimensional genome scan searching for single, non-interacting QTLs revealed 2 peaks exceeding the LOD score threshold of 3 (Figure 3.3). These QTLs were located on the distal end of chromosome 12 and the proximal end of chromosome 14 (Figure 3.4). The statistical significance of the QTLs was assessed using LOD score significance thresholds produced from a 10000 random permutation test (Figure 3.5). A LOD score of 5.24 would have a *p* value of 0.05, and a LOD score of 4.88 would have a *p* value of 0.10. Consequently, the chromosome 14 locus (*p* = 0.46) was discarded, and the chromosome 12 locus (*p* = 0.075) was further pursued. Even though the *p* value was not at or below the 0.05 threshold, obtaining such a near-significant *p* value with only 16 progeny phenotypes was well worth pursuing instead of reevaluating the progeny phenotypes.

Using the chromosome 12 QTL, an effect plot was generated to estimate the effect the QTL had on the phenotype of interest (Figure 3.6). Of the 16 progeny phenotyped, only 2 did not segregate based on both marker genotype and phenotype value. X33 possessed the 3D7 allele but the HB3 phenotype, and X6 possessed the HB3 allele but the 3D7 phenotype. Given these discordant progeny, the effect of the QTL was estimated to explain 52% of the phenotypic variance, exceeding the threshold of 50%. The physical location of the chromosome 12 QTL was then refined to the specific markers most likely containing the QTL (Table 3.3). The identified QTL-bordering markers SNP_NGS_12_1901003 and SNP_10K_12_1907861 spanned a 39.4 cM region, with the QTL c12.loc702 located somewhere in between. A scan of version 3.0 of the annotated 3D7 reference genome

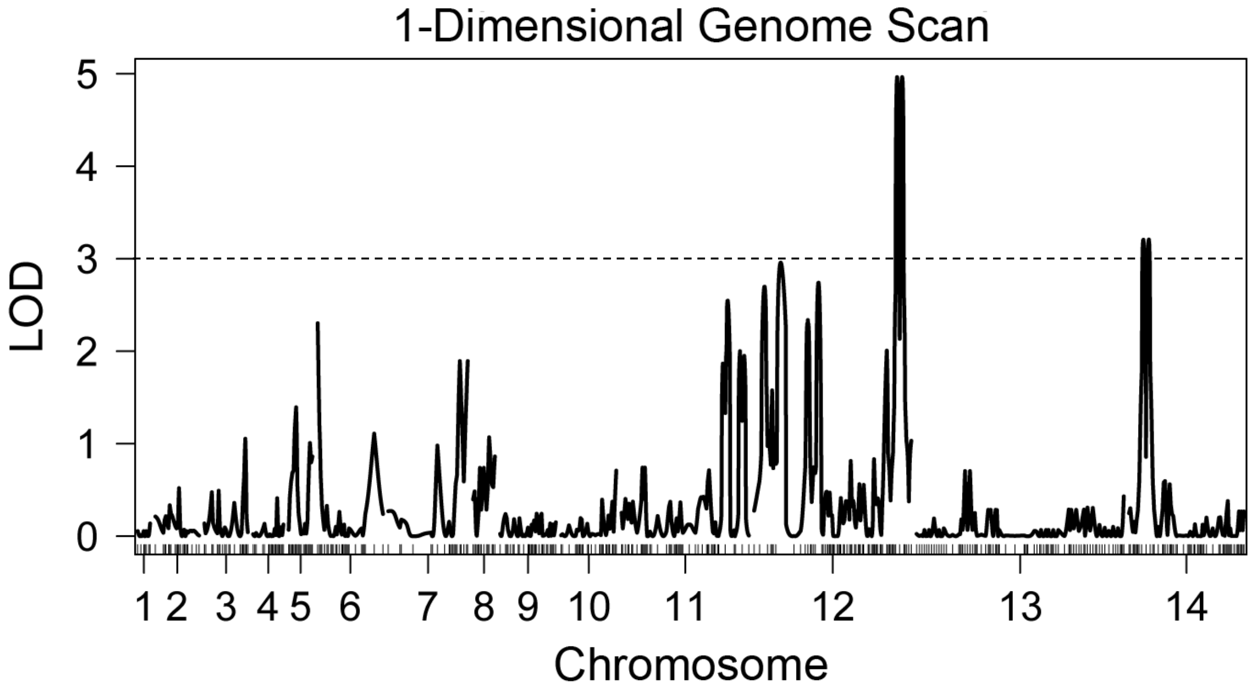

Chromosome	Marker Position (cM)	LOD Score
12	740.4	4.963
14	112.1	3.207

Figure 3.3: 1-dimensional genome scan performed using R/qtl. The association of PfEMP1 surface level phenotypes with genome-wide SNP markers produced 2 major peaks exceeding the LOD score threshold of 3.

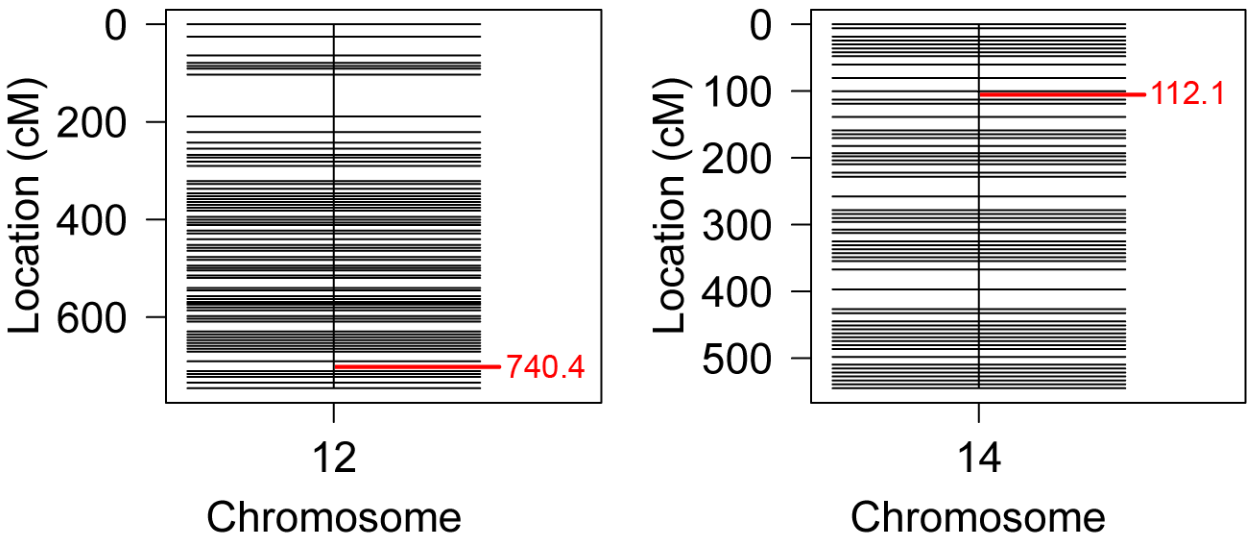

Figure 3.4: Approximate QTL locations on chromosomes 12 and 14. The locations of the 2 QTLs with LOD scores over 3 are shown on each SNP-marked chromosome.

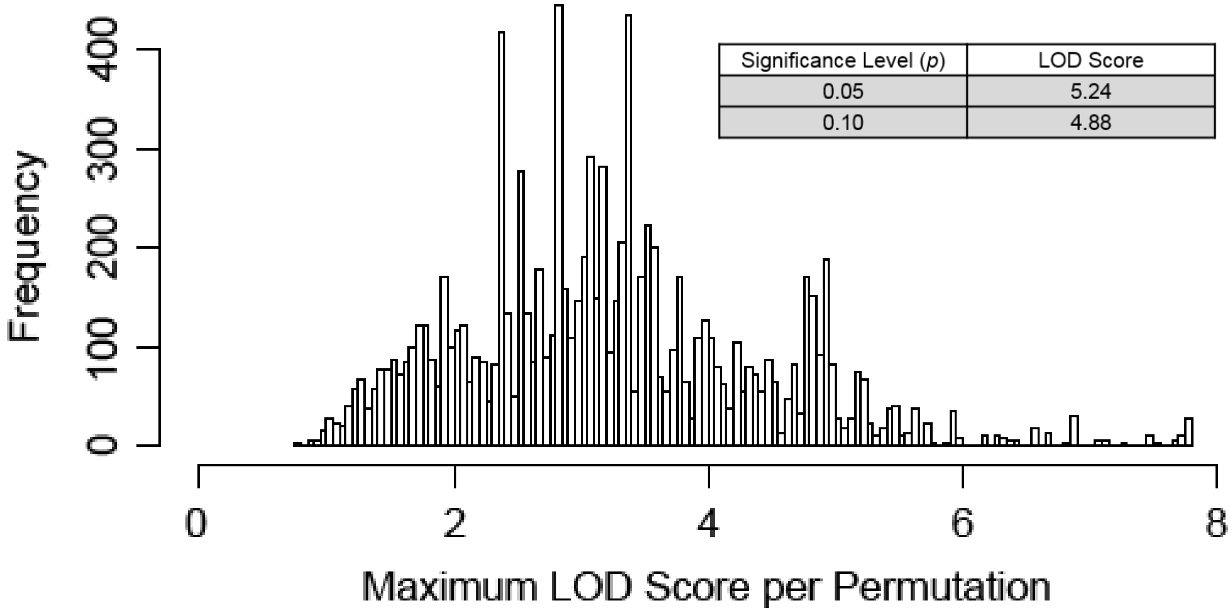

Significance Level (*p*)	LOD Score
0.05	5.24
0.10	4.88

Figure 3.5: Random permutation analysis to establish LOD score significance. The phenotype values were randomly shuffled relative to the marker genotypes 10000 times to obtain a frequency distribution of the maximum LOD score for each permutation. For each QTL analysis experiment, a LOD score of 5.24 would be expected 5% of the time, and a LOD score of 4.88 would be expected 10% of the time.

identified the chromosome 12 base positions of the above markers as 1901003 and 1907003, respectively, providing a 6000 bp region to further examine for candidate genes.

3.3.2 Candidate gene characterization

Having identified and refined a single, near-significant QTL on chromosome 12 accounting for approximately half of the phenotypic variance seen in the progeny, the 6000 bp region estimated to contain the QTL was examined for potential genes of interest. Surprisingly, only a single gene, *Pf3D7_1245600*, was located in this region (Figure 3.7), effectively eliminating the process of candidate gene selection. *Pf3D7_1245600* is a predicted protein-coding gene spanning bases 1900249 to 1905066 in version 3.0 of the 3D7 reference genome, possessing syntenic orthologs in every species of *Plasmodium* sequenced to date.

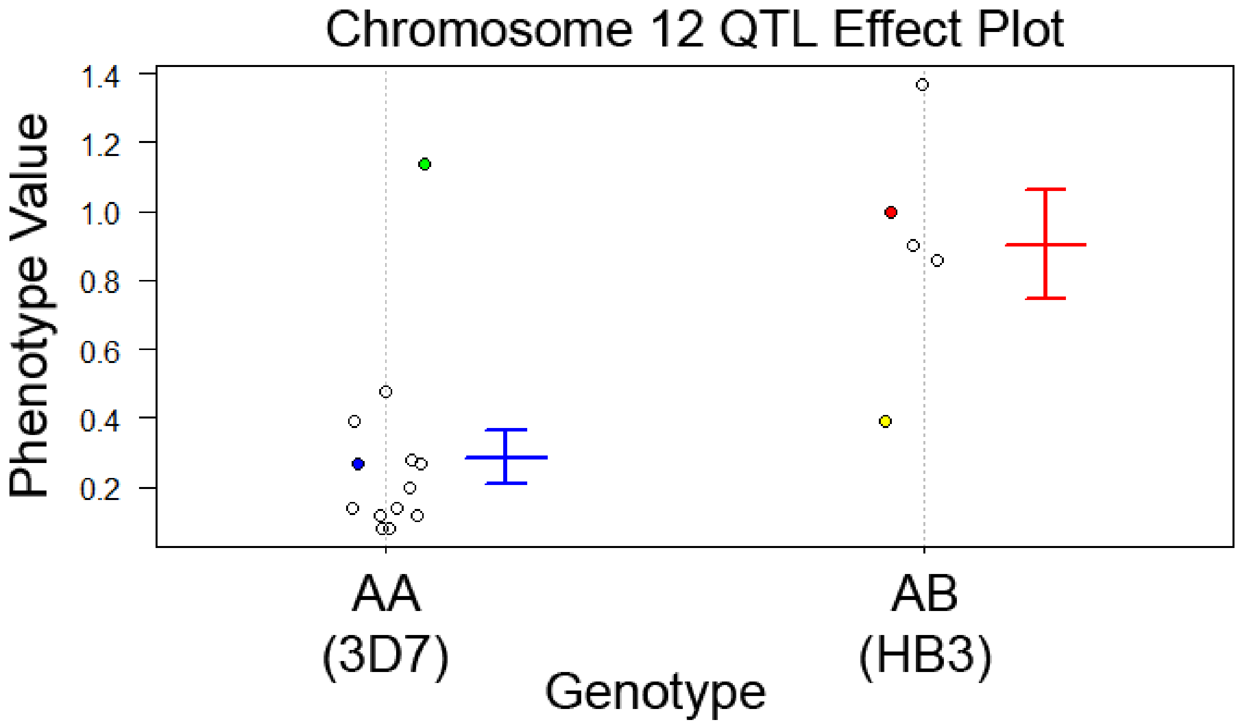

Figure 3.6: Chromosome 12 QTL effect plot. To determine the effect of the chromosome 12 QTL on the phenotypic variance, an effect plot was generated showing the phenotype value versus the chromosome 12 genotype. 3D7 (blue dot) and HB3 (red dot) serve as reference points. Of 16 progeny, only X33 (green dot) and X6 (yellow dot) are discordant.

Marker Name	Position (cM)	LOD Score	Size (cM)	Position (bp)
SNP_NGS_12_1901003	708.9891	2.602	39.4	1901003
c12.loc702	740.3740	4.963		unknown
SNP_10K_12_1907861	748.3740	2.602		1907003

Table 3.3: Results from the refinement of the chromosome 12 QTL. Using the “refineqtl” function, the physical location of the chromosome 12 QTL was localized to position 740.3740 cM, which is bounded by the markers at positions 708.9891 and 748.3740 cM. This translated to a 6000 bp region from chromosome 12 base 1901003 to 1907003.

The 4818 bp single exon gene is likely to encode a kinesin based on sequence homology as predicted by the Pfam database[417], with E-values of 9.8e-60 for the catalytic kinesin motor domain and 1.6e-16 for the microtubule binding region. A scan of known non-synonymous SNPs in the HB3, 3D7, and progeny sequences revealed the presence of 1 definite SNP at

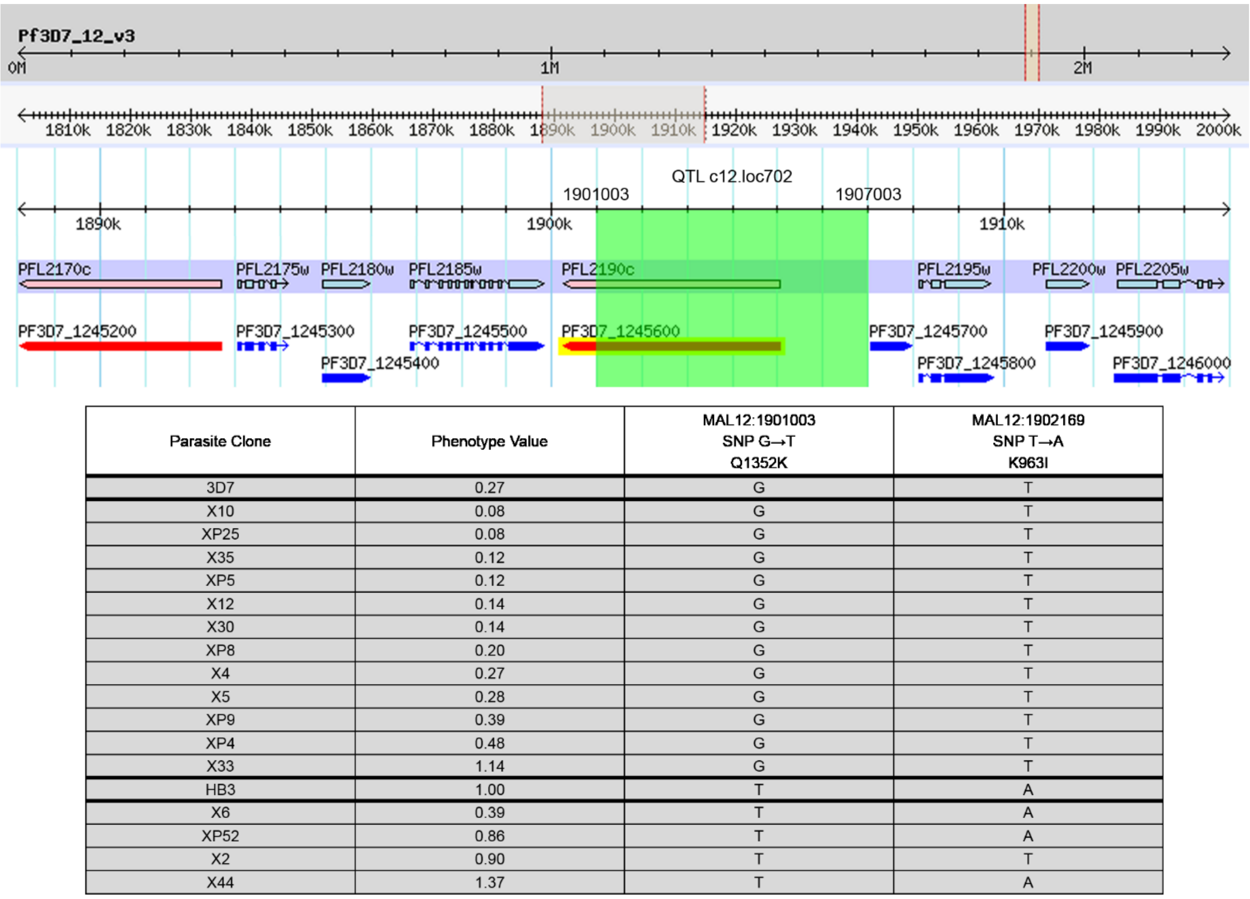

Parasite Clone	Phenotype Value	MAL12:1901003 SNP G→T Q1352K	MAL12:1902169 SNP T→A K963I
3D7	0.27	G	T
X10	0.08	G	T
XP25	0.08	G	T
X35	0.12	G	T
XP5	0.12	G	T
X12	0.14	G	T
X30	0.14	G	T
XP8	0.20	G	T
X4	0.27	G	T
X5	0.28	G	T
XP9	0.39	G	T
XP4	0.48	G	T
X33	1.14	G	T
HB3	1.00	T	A
X6	0.39	T	A
XP52	0.86	T	A
X2	0.90	T	T
X44	1.37	T	A

Figure 3.7: Genomic position of QTL c12.loc702 as shown in PlasmoDB and parasite SNP table. QTL c12.loc702 was refined to the area between bases 1901003 and 1907003, a 6000 bp region (green) containing the uncharacterized protein coding gene *Pf3D7_1245600*. Protein coding genes (grey band) are shown above the list of all predicted genes. The graphical representation of the annotated genome was generated by PlasmoDB. HB3, 3D7, and the phenotyped progeny were examined for non-synonymous SNPs in the region estimated to contain the QTL (table).

base 1901003 and 1 potential SNP at base 1902169 (Figure 3.7), though poor sequence coverage and mixed base-calling suggest that the latter is not an actual SNP. A further analysis of SNP data available in PlasmoDB indicated that there are 237 total SNPs, 197 of which are non-synonymous, across 203 *P. falciparum* lines. A comparison of SNP presence across nearby genes, other known or putative kinesins, and highly polymorphic genes is shown in Table 3.4.

		SNPs					
Gene ID	Name/Function	Total	NS	NC	STOP	S	NS/S
Pf3D7_1245600	Kinesin	237	197	0	4	36	5.47
Pf3D7_1245500	Unknown	230	20	198	3	9	2.22
Pf3D7_1245400	Mito. Ribo. L3	12	7	0	2	3	2.33
Pf3D7_1245300	UBC12	61	3	57	0	1	3.0
Pf3D7_1245200	Unknown	168	124	1	1	42	2.95
Pf3D7_1245800	Clathrin AP180	138	33	89	2	14	2.36
Pf3D7_1245900	Unknown	8	7	0	0	1	7
Pf3D7_1246000	Unknown	87	17	63	1	6	2.83
Pf3D7_1246100	ALAS	54	8	37	0	9	0.89
Pf3D7_0111000	Kinesin-8	283	111	121	7	44	2.52
Pf3D7_0317500	Kinesin-5 (EG5)	230	146	37	3	44	3.32
Pf3D7_0319400	Kinesin-8	168	122	0	0	46	2.65
Pf3D7_1245100	Kinesin-13 (KLP8)	189	110	48	2	29	3.79
Pf3D7_0724900	Kinesin-19	118	87	0	8	23	3.78
Pf3D7_1211000	Kinesin-7	187	95	41	2	49	1.94
Pf3D7_0806600	Kinesin-like	175	52	107	2	14	3.71
Pf3D7_1146700	Kinesin-like	185	45	130	1	9	5.0
Pf3D7_0930300	MSP1	339	301	0	4	34	8.85
Pf3D7_0206800	MSP2	189	178	0	6	5	35.6
Pf3D7_1133400	AMA1	97	89	0	1	7	12.71
Pf3D7_1035300	GLURP	171	130	0	0	41	3.17

Table 3.4: SNP overview of *Pf3D7_1245600* in context with other *P. falciparum* genes. Using 203 SNP data sets available through PlasmoDB, a table was developed to show the total SNP number, non-synonymous (NS) number, non-coding (NC) number, stop codon-generating (STOP) number, synonymous (S) number, and the NS/S SNP ratio for *Pf3D7_1245600*, the 8 protein coding genes immediately up and downstream, the 8 other predicted kinesins, and 4 known polymorphic genes.

A translation of the predicted gene sequence resulted in a 1605 amino acid protein with an estimated molecular weight of 188.2 kDa. A search of the protein did not reveal the presence of a PEXEL motif, but submissions to InterPro, UniProt, and the NCBI Conserved Domain Database revealed the presence of a highly conserved, 328 residue KISc catalytic ATPase motor domain most similar to that of the human kinesin-like protein KIF20B (Figure 3.8). KIF20B is a vertebrate-specific, N-type kinesin belonging to the microtubule-dependent

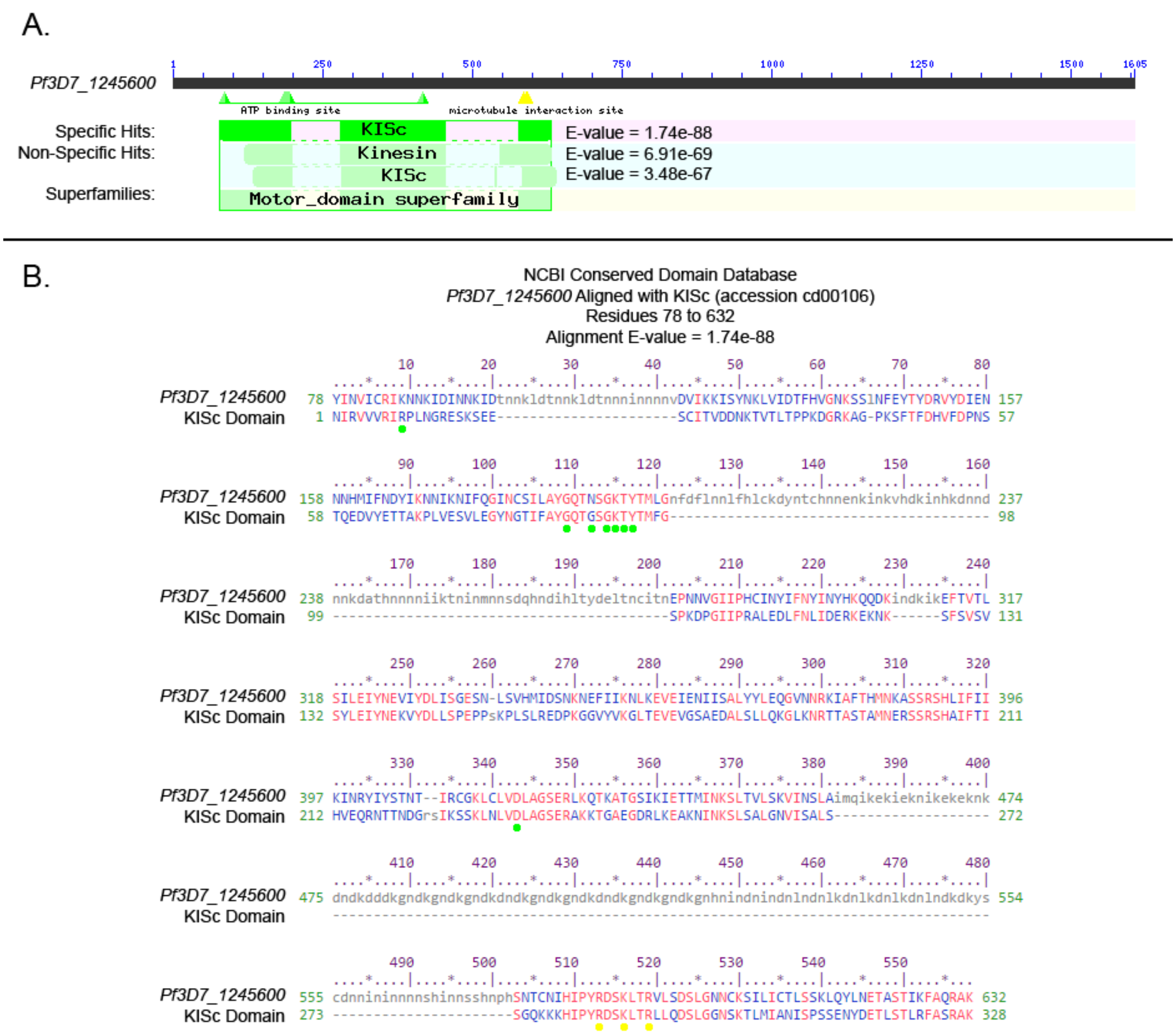

NCBI Conserved Domain Database
Pf3D7_1245600 Aligned with KISc (accession cd00106)
Residues 78 to 632
Alignment E-value = 1.74e-88

```
                          10        20        30        40        50        60        70        80
                  ....*....|....*....|....*....|....*....|....*....|....*....|....*....|....*....|
Pf3D7_1245600  78 YINVICRIKNNKIDINNKIDtnnkldtnnkldtnnninnnnvDVIKKISYNKLVIDTFHVGNKSSlNFEYTYDRVYDIEN 157
KISc Domain     1 NIRVVVRIRPLNGRESKSEE----------------------SCITVDDNKTVTLTPPKDGRKAG-PKSFTFDHVFDPNS 57

                          90       100       110       120       130       140       150       160
                  ....*....|....*....|....*....|....*....|....*....|....*....|....*....|....*....|
Pf3D7_1245600 158 NNHMIFNDYIKNNIKNIFQGINCSILAYGQTNSGKTYTMLGnfdflnnlfhlckdyntchnnenkinkvhdkinhkdnnd 237
KISc Domain    58 TQEDVYETTAKPLVESVLEGYNGTIFAYGQTGSGKTYTMFG--------------------------------------- 98

                         170       180       190       200       210       220       230       240
                  ....*....|....*....|....*....|....*....|....*....|....*....|....*....|....*....|
Pf3D7_1245600 238 nnkdathnnnniiktninmnnsdqhndihltydeltncitnEPNNVGIIPHCINYIFNYINYHKQQDKindkikEFTVTL 317
KISc Domain    99 -----------------------------------------SPKDPGIIPRALEDLFNLIDERKEKNK------SFSVSV 131

                         250       260       270       280       290       300       310       320
                  ....*....|....*....|....*....|....*....|....*....|....*....|....*....|....*....|
Pf3D7_1245600 318 SILEIYNEVIYDLISGESN-LSVHMIDSNKNEFIIKNLKEVEIENIISALYYLEQGVNNRKIAFTHMNKASSRSHLIFII 396
KISc Domain   132 SYLEIYNEKVYDLLSPEPPsKPLSLREDPKGGVYVKGLTEVEVGSAEDALSLLQKGLKNRTTASTAMNERSSRSHAIFTI 211

                         330       340       350       360       370       380       390       400
                  ....*....|....*....|....*....|....*....|....*....|....*....|....*....|....*....|
Pf3D7_1245600 397 KINRYIYSTNT--IRCGKLCLVDLAGSERLKQTKATGSIKIETTMINKSLTVLSKVINSLAimqikekieknikekeknk 474
KISc Domain   212 HVEQRNTTNDGrsIKSSKLNLVDLAGSERAKKTGAEGDRLKEAKNINKSLSALGNVISALS------------------- 272

                         410       420       430       440       450       460       470       480
                  ....*....|....*....|....*....|....*....|....*....|....*....|....*....|....*....|
Pf3D7_1245600 475 dndkdddkgndkgndkgndkdndkgndkgndkdndkgndkgndkgnhnindnindnlndnlkdnlkdnlkdnlndkdkys 554
KISc Domain       --------------------------------------------------------------------------------

                         490       500       510       520       530       540       550
                  ....*....|....*....|....*....|....*....|....*....|....*....|....*....|....*...
Pf3D7_1245600 555 cdnnininnnnshinnsshnphSNTCNIHIPYRDSKLTRVLSDSLGNNCKSILICTLSSKLQYLNETASTIKFAQRAK 632
KISc Domain   273 ----------------------SGQKKKHIPYRDSKLTRLLQDSLGGNSKTLMIANISPSSENYDETLSTLRFASRAK 328
```

Figure 3.8: NCBI Conserved Domain Database results for *Pf3D7_1245600*. The predicted protein sequence of *Pf3D7_1245600* was scanned for the presence of conserved domains in order to better understand its potential function (A). An alignment was created using the top specific hit (B). ATP binding sites (green dots) and microtubule interaction sites (yellow dots) are noted to show the conservation of critical active site residues.

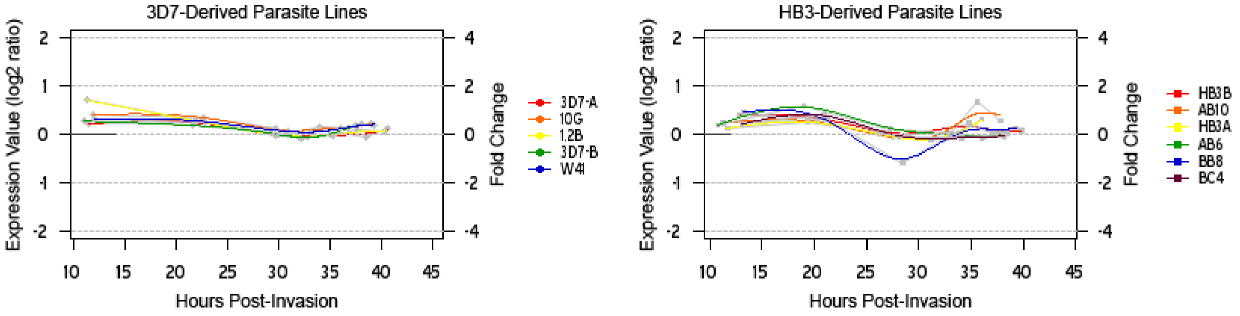

Figure 3.9: Blood-stage transcriptome results for *Pf3D7_1245600* as shown on PlasmoDB. Previously reported transcriptome data available through PlasmoDB were used to visualize *Pf3D7_1245600* expression throughout blood-stage development. Neither HB3- nor 3D7-derived parasite lines showed large changes in transcription, though the slight changes seen in HB3-derived lines are consistent with the timing of PfEMP1 production and trafficking.

Kinesin-6 family broadly associated with mitotic spindle assembly and cytokinesis[418–420]. The homology with KIF20B suggested that *Pf3D7_1245600* is a Kinesin-6 protein, 1 of 3 present in *P. falciparum*[421]. An examination of blood-stage transcription profiles of *Pf3D7_1245600* in HB3- and 3D7-derived parasite lines[422] showed generally consistent expression of the gene throughout parasite development (Figure 3.9), though HB3-derived lines did possess slight variations in expression consistent with the timing of PfEMP1 production and trafficking.

3.4 Discussion

The aim of this chapter was to identify any genetic polymorphisms associated with the impaired trafficking of PfEMP1 in 3D7. To address this, a QTL analysis was conducted using the surface PfEMP1 level phenotypes described in chapter 2 and pre-existing genotype data for HB3, 3D7, and 16 unique genetic cross progeny. A 1-dimensional genome scan revealed 2 QTL with LOD scores exceeding 3 (Figure 3.3). Both of those peaks appeared as doublets, suggesting the presence of 2 immediately adjacent QTL. However, a more likely explanation is the absence of specific markers in some of the progeny genetic maps, or the inclusion of SNPs that are poorly covered and are thus inconsistently labeled among the progeny (Figure 3.7). Though significance testing (Figure 3.5) determined that neither QTL was significant according to the widely-accepted threshold of $p = 0.05$, the near-significant chromosome 12 QTL possessing a p value of 0.075 was very promising given that only 16 progeny were included in the analysis. Recently reported experiments applying QTL analysis to the understanding of 4-aminoquinoline drug resistance[423], channel-mediated nutrient uptake[27], and hemoglobin catabolism[424] have relied on 32, 34, and 34 unique phenotyped progeny, respectively, to identify significant QTL. It is possible that the significance of the chromosome 12 QTL would increase with the inclusion of additional phenotyped progeny in the analysis.

An effect plot generated for the chromosome 12 QTL (Figure 3.6) was used to calculate an explained phenotypic variance of 52%, with only 2 progeny harboring discordant genotype-phenotype pairings. Given the large number of genes already known to contribute to PfEMP1 trafficking[304], it was unlikely that a single QTL would explain 100% of the phenotypic variance. If that were the case, the surface PfEMP1 level phenotype distribution would have been distinctly bimodal, enabling simple linkage analysis to be performed instead of QTL analysis. Refinement of the chromosome 12 QTL resulted in a

39.4 cM region spanning 6000 bp (Table 3.3). This approximate map unit size of 152 bp/cM was highly unexpected given that the most recent estimation of *P. falciparum* recombination rates using a GB4 x 7G8 genetic cross established an average map unit size of 9600 bp/cM when highly recombinogenic regions were included and 12800 bp/cM when they were excluded[360]. A similar average map unit size of 11000 bp/cM has been roughly established for the HB3 x 3D7 cross used in this thesis (Ranford-Cartwright Lab, personal communication). Since chromosome crossover events are not distributed randomly and uniformly throughout the genome, a map unit size as small as 152 bp/cM can be explained by the occurrence of recombination "hotspots"[425]. The location of the chromosome 12 QTL at the distal end of the chromosome rather than in the middle (Figure 3.4) places it in a position more likely to undergo recombination. If recombination "hotspots" are nearby, then it is entirely possible that some of the phenotyped progeny resulted from a crossover event just upstream or downstream of the QTL.

The 6000 bp region identified after QTL refinement contains a single gene, *Pf3D7_1245600*, predicted to encode a kinesin (Figure 3.7). Though the gene is not *P. falciparum*-specific as would be expected for a component of the PfEMP1 trafficking pathway, the fact that its putative protein product belonged to a class definitively known for intracellular transport was very promising. A search of parental and progeny SNPs identified at least 1 definitive non-synonymous SNP between HB3 and 3D7 (Figure 3.7), providing a potential genetic determinant of impaired PfEMP1 trafficking to pursue further. 203 SNP data sets available through PlasmoDB were used to assess the occurrence of *Pf3D7_1245600* SNPs in the context of nearby genes, other predicted kinesins, and highly polymorphic genes (Table 3.4). At 237 total SNPs, 197 of which are non-synonymous, *Pf3D7_1245600* has more SNPs than any genes in its immediate region, and more non-synonymous SNPs than any other predicted kinesin. This high level of polymorphism was unexpected for a gene encoding such a conserved protein. Furthermore, kinesins commonly reside within cells, which would effectively shield them from potentially selective pressure from the human immune system.

An in-depth analysis of conserved protein domains in *Pf3D7_1245600* revealed the presence of a highly conserved, N-terminal KISc motor domain most similar to that of the human kinesin-like protein KIF20B (Figure 3.8). Like KIF20B, *Pf3D7_1245600* is predicted to be a Kinesin-6, the family most associated with mitotic spindle assembly and cytokinesis[426]. Structurally, Kinesin-6 proteins consist of homodimers, each with a globular motor domain head that binds microtubules and hydrolyzes ATP for movement, a coiled stalk, and a globular tail that binds cellular cargo. The dimerization of the protein enables the globular heads to effectively function as feet, enabling the protein to “walk” toward the plus-end of microtubules. In contrast to the human genome, which encodes 45 kinesins, the *P. falciparum* genome only encodes 9 kinesins from 6 different families[421]. Even though *Pf3D7_1245600* would not be expected to traffic PfEMP1 based on known functions of other Kinesin-6 proteins, the complete absence of any parasite homologs of Kinesin-1, the family most associated with transporting cellular cargo over vast distances, maintains the possibility that *Pf3D7_1245600* performs classically uncharacteristic functions, such as protein export, in *P. falciparum*. Transcriptome data from HB3-derived parasites is at least suggestive of this possibility considering that the timing of *Pf3D7_1245600* during the blood-stages lines up more closely with the expression and export of PfEMP1 than the production of merozoites during schizogony (Figure 3.9).

Despite their known roles in organizing cellular compartments and transporting various forms of cellular cargo, kinesins have never been studied as agents of protein trafficking in *P. falciparum*. The inclusion of *PfI0260c*, a putative dynein, in a recent systematic gene disruption study[319] is the closest examination yet of microtubule-dependent motor proteins and protein export. Though disruption of *PfI0260c* did not result in a decrease in pRBC surface PfEMP1 levels, further analysis of motor protein contribution to protein export should not be ignored. To advance this largely unexplored area of research, the potential involvement of *Pf3D7_1245600* in PfEMP1 trafficking, supported by QTL analysis and bioinformatics characterization, needs to be confirmed through *P. falciparum* genetic manipulation experiments.

4 Impaired PfEMP1 trafficking in genetically modified parasite lines

4.1 Introduction and aims

Kinesins are highly conserved motor proteins responsible for a multitude of cellular functions, from organelle movement to cell division to vesicle transport. Despite *P. falciparum* possessing 10 putative kinesins, this family of proteins is extremely understudied in parasites. The little research that has been conducted only indirectly implicates kinesins, by way of microtubules, in functions such as liver stage development, merozoite invasion, and schizont segmentation. Given the essential and well-defined role kinesins play in transporting cellular cargo in humans and many other organisms, it seems unusual that members of the protein family have not been pursued in *P. falciparum* as potential contributors to the trafficking and display of PfEMP1.

The seeming lack of interest in *P. falciparum* kinesins is partly due to their unlikely potential as antimalarial drug targets. With few exceptions, the extremely high sequence homology of kinesins across species practically ensures that compounds disrupting *P. falciparum* kinesin function would also disrupt human kinesin function. Knowing this, exploring the role of kinesins in essential parasite functions is still a worthwhile endeavor that would undoubtedly expand the current understanding of *P. falciparum* pathogenesis and potentially reveal other, more easily exploitable pathways or therapeutic targets.

Following the results of the QTL analysis described in chapter 3, the primary aim of this chapter is to establish a causal relationship between the identified gene *Pf3D7_1245600* and the trafficking of PfEMP1. This aim is directly addressed by first determining the genomic sequence variation of the putative kinesin between HB3 and 3D7, and subsequently using that information in CRISPR-Cas9-driven allele-exchange transfection experiments to effectively reverse the surface PfEMP1 level phenotypes of HB3 and 3D7 described in chapter 2. The aim of this chapter is also indirectly addressed through the chemical manipulation of microtubules, the structures most commonly associated with kinesins such as *Pf3D7_1245600*.

4.2 Materials and methods

4.2.1 *In vitro* parasite culture

P. falciparum was maintained and manipulated in continuous *in vitro* culture as described in section 2.2.1.

4.2.2 Parasite lines

The *in vitro* culture-adapted parasite lines HB3 and 3D7 were used exclusively since the contrasting surface PfEMP1 phenotypes of those clones ultimately led to the implication of *Pf3D7_1245600* in the trafficking of PfEMP1 to the pRBC surface (chapters 2 and 3). Detailed descriptions of HB3 and 3D7 can be found in section 2.2.2.

4.2.3 DNA extraction and PCR

To begin experimentally confirming the results of the QTL analysis (Chapter 3), genomic DNA from parental HB3 and 3D7 pRBCs was extracted from *in vitro* cultures using a QIAGEN® QIAamp® DNA Blood Mini Kit. First, synchronous cultures of approximately 40-44 hour-old schizonts were subjected to Plasmion® floatation as described in section 2.2.1. Approximately 1 ml of the enriched schizont suspension was then centrifuged at 13,000 rpm for 10 seconds to pellet the cells before being transferred to -20°C to directly freeze and lyse the pRBCs. Lysates were then thawed at room temperature, diluted in PBS to 200 µl final volume, and processed with the QIAamp® kit according to the manufacturer's instructions. The resulting purified genomic DNA was eluted in DNAse- and RNAse-free ddH_2O and stored at -20°C long-term or 4°C short-term. A NanoDrop 1000 spectrophotometer was used to quantify DNA and determine sample purity. Since *in vitro* cultures only contain the uRBC portion of whole blood, most of the genomic DNA obtained should belong to *P. falciparum*.

Pf3D7_1245600 was initially amplified from HB3 and 3D7 genomic DNA by PCR for sequence confirmation[427,428]. Since the full 4818 bp gene was too large for fluorescent dye-terminator cycle sequencing, 6 oligonucleotide primer pairs were designed to amplify the gene in 6 overlapping fragments ranging in size from 911 bp to 1033 bp, with the additional option of amplifying the full-length gene using the first forward primer and last reverse primer (Figure 4.1). Primers were designed by hand using version 3.0 of the annotated 3D7 reference genome viewed with the genome analysis tool Artemis version 15.0.0[175,407,408]. Primer target specificity was evaluated using the NCBI BLAST® program[429,430], and hairpin loop formation, self-dimerization, and hetero-dimerization were assessed using the IDT® OligoAnalyzer 3.1 tool. Lyophilized primers were resuspended in DNAse- and RNAse-free ddH_2O to 50 µM concentrations and stored at -20°C long-term or 4°C short-term. PCR reactions were prepared using the Invitrogen™ AccuPrime™ *Pfx* SuperMix solution containing a high-fidelity polymerase with 3’ to 5’ exonuclease activity. The 1.1x concentration master mix was diluted to 1x concentration with the addition of primers at a final reaction concentration of 300 nM and genomic DNA at a final reaction concentration of approximately 2 ng/µl. All reactions were carried out in a Bio-Rad DNA Engine® Peltier Thermal Cycler. Each reaction was initiated by a polymerase activation step of 95°C for 5 minutes, followed by 36-40 cycles of DNA denaturation at 95°C for 30 seconds, primer annealing at 50°C for 30 seconds, initial polymerase extension at 62°C for 30 seconds, and full polymerase extension at 65°C for 1 minute. A final polymerase extension step of 65°C for 2 minutes was included after the last cycling step, followed by an indefinite sample hold at 4°C (Figure 4.1 C). To amplify full-length *Pf3D7_1245600*, the same protocol was followed, except that the cycled extension step lasted 5 minutes instead of 1 minute, and the final extension step lasted 10 minutes instead of 2 minutes.

PCR reaction products were size-separated and visualized by gel electrophoresis using either freshly-made 0.5-2% w/v agarose gels containing ethidium bromide or precast

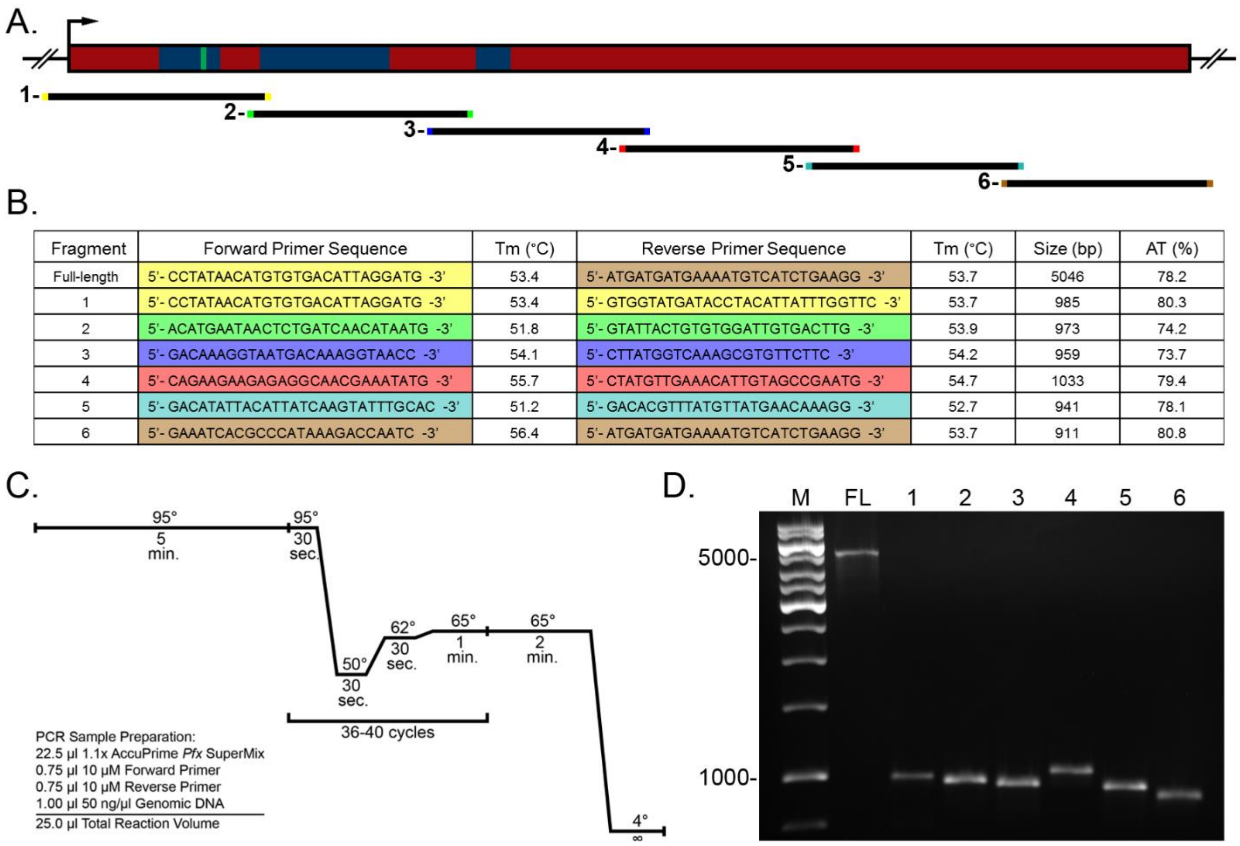

Fragment	Forward Primer Sequence	Tm (°C)	Reverse Primer Sequence	Tm (°C)	Size (bp)	AT (%)
Full-length	5'- CCTATAACATGTGTGACATTAGGATG -3'	53.4	5'- ATGATGATGAAAATGTCATCTGAAGG -3'	53.7	5046	78.2
1	5'- CCTATAACATGTGTGACATTAGGATG -3'	53.4	5'- GTGGTATGATACCTACATTATTTGGTTC -3'	53.7	985	80.3
2	5'- ACATGAATAACTCTGATCAACATAATG -3'	51.8	5'- GTATTACTGTGTGGATTGTGACTTG -3'	53.9	973	74.2
3	5'- GACAAAGGTAATGACAAAGGTAACC -3'	54.1	5'- CTTATGGTCAAAGCGTGTTCTTC -3'	54.2	959	73.7
4	5'- CAGAAGAAGAGAGGCAACGAAATATG -3'	55.7	5'- CTATGTTGAAACATTGTAGCCGAATG -3'	54.7	1033	79.4
5	5'- GACATATTACATTATCAAGTATTTGCAC -3'	51.2	5'- GACACGTTTATGTTATGAACAAAGG -3'	52.7	941	78.1
6	5'- GAAATCACGCCCATAAAGACCAATC -3'	56.4	5'- ATGATGATGAAAATGTCATCTGAAGG -3'	53.7	911	80.8

Figure 4.1: *Pf3D7_1245600* PCR amplification and cycle sequencing strategy. The full-length *Pf3D7_1245600* gene was divided into 6 overlapping fragments of approximately 1,000 bp each for PCR amplification and cycle sequencing (A and B). The developed PCR protocol (C) was used successfully to amplify all 6 fragments and the full-length gene (D).

1.2% E-Gels® containing SYBR Safe™. To prepare agarose gels, 0.5-2 g of UltraPure™ agarose was added to 100 ml of TBE buffer in a Pyrex® bottle and microwaved at 700 watts for 2 minutes. The molten solution was swirled several times before being microwaved again at 700 watts for 30 seconds. 1 µl of a 10 mg/ml solution of the DNA-binding, fluorescent dye ethidium bromide was then added, resulting in a final dye concentration of 100 ng/ml. The agarose solution was allowed to briefly cool at room temperature before being poured into a plastic gel cassette to solidify. A plastic well comb was inserted into the gel before solidification. Once solid, the comb was removed and the gel was submerged in an electrophoresis tank filled with TBE buffer. Care was taken to ensure that the gel was positioned with the wells closest to the negative electrodes. DNA samples were diluted 1:6 with 6x DNA loading dye consisting of ddH_2O with 10 mM Tris-HCl, 60 mM EDTA, 0.03% v/v bromophenol blue, 0.03% v/v xylene cyanol FF, and 60% v/v glycerol. The diluted DNA samples, along with a DNA size ladder, were loaded onto the submerged gel and run at 60 volts until the dye front was at least half-way down the gel. Gels were then removed and imaged using a Syngene G:BOX F3 imaging system running GeneSys version 1.3.1.0 software. To visualize PCR products using precast 1.2% E-Gels® containing SYBR Safe™, 20 µl of each PCR reaction was loaded directly onto the E-Gel®. If a PCR reaction contained less than 20 µl, it was brought to 20 µl using DNAse- and RNAse-free ddH_2O. It was not necessary to dilute DNA samples with loading dye prior to running. Loaded E-Gels® were inserted into the accompanying PowerBase™ gel runner and run using the "30 Minutes" setting. E-Gels® were imaged as described above.

When DNA needed to be purified for further use, a QIAGEN® QIAquick® PCR Purification Kit or Gel Extraction Kit was used. For gel extraction, DNA samples were first size-separated on a 0.5-1% w/v agarose gel as described above. The gel was then transferred to an ultraviolet light box and the appropriate DNA bands were excised using clean razor blades. Gel extracts were weighed in 1.5 ml Eppendorf tubes and processed with the QIAquick® Gel Extraction Kit according to the manufacturer's instructions. For PCR purification, DNA could be directly processed with the QIAquick® PCR Purification Kit immediately after PCR amplification. The PCR purification kit was also used to purify DNA that had been digested with restriction enzymes or fused with the In-Fusion® HD cloning system. In all cases, the purified DNA was eluted in DNAse- and RNAse-free ddH_2O and stored at -20°C long-term or 4°C short-term. A NanoDrop 1000 spectrophotometer was used to quantify DNA and determine sample purity.

Following sequence confirmation of *Pf3D7_1245600*, fragments were amplified from HB3 and 3D7 genomic DNA by PCR for CRISPR-Cas9-driven allele-exchange transfection experiments (Figure 4.2). As described further in section 4.2.5, the CRISPR-Cas9 system requires at least 2 plasmids encoding a Cas9 endonuclease that induces a double-strand break at a specific DNA sequence, a guide RNA that directs Cas9 genome cutting, and a repair sequence that serves as a template for repairing, and introducing polymorphisms to, the cut endogenous locus. The downstream use of the *Pf3D7_1245600* fragments required specially designed primers to make the amplicons compatible with the ligase-independent In-Fusion® HD Plus cloning system[431,432]. In-Fusion® primers consisted of the typical gene-specific segment of normal primers but with an additional 15 bp or larger homology sequence appended to the 5' end. This sequence was generally designed to complement specific restriction-enzyme digestion sites within the vector into which the amplified fragment would ultimately be inserted (Figures 4.2 and 4.3). In-Fusion® primers were designed by hand and assessed as described above for use in first linking PCR fragments together and then fusing the linked products into vector backbones for transfection (Figure 4.3 B and C).

Using different primer combinations, 4 separate fragments of *Pf3D7_1245600* were amplified with In-Fusion® homology regions appended to both ends of the fragments. The single upstream fragment was labeled “Silent Mutation F” and the 3 adjacent downstream fragments were labeled “Silent Mutation R1/2/3” depending on the size. For Silent Mutation F, a 16 bp PciI homology sequence was appended to the 5' end of the fragment, and a 15 bp Silent Mutation R1/2/3 homology sequence was appended to the 3' end of the fragment. Just upstream of the 3' homology sequence, 3 synonymous SNPs were introduced via PCR-mediated site-directed mutagenesis[433] to ultimately prevent the CRISPR-Cas9 template plasmid from being recognized and degraded by the Cas9 nuclease. For each Silent Mutation R1/2/3, a 16 bp PciI homology sequence was appended to the 3' end of the fragment so that the fully linked *Pf3D7_1245600* fragments could be fused into a PciI cut site in either orientation. All 4 fragments were amplified using the reagents and cycling conditions described above and shown in Figure 4.1 C. Even though the primers used for

A.

Component	Forward Primer Sequence	Tm (°C)	Reverse Primer Sequence	Tm (°C)	Size (bp)	AT (%)
Silent Mutation F	5'- GCAGGAAAGAACATGTATTCTTTAGCTATCATGCAGATAAAGG -3'	61.9 (53.3)	5'- CTTAACCATTTTAGCTCTCTGTGCGAATTTTATTGTTGATGCCGT -3'	64.2	567	70.9
Silent Mutation R1	5'- GCTAAAATGGTTAAGGCCAAACC -3'	54.9	5'- CCTTTTGCTCACATGTCAAAAGAAGATGATATCTTTGGTTATGTG -3'	62.3 (53.1)	297	74.4
Silent Mutation R2	5'- GCTAAAATGGTTAAGGCCAAACC -3'	54.9	5'- CCTTTTGCTCACATGTGGAATGTTTATTTTATCTCCTTGAGCATC -3'	63.3 (54.6)	1059	75.7
Silent Mutation R3	5'- GCTAAAATGGTTAAGGCCAAACC -3'	54.9	5'- CCTTTTGCTCACATGTGACACGTTTATGTTATGAACAAAGG -3'	62.8 (52.7)	2235	77.7
In-Fusion Product FR1	5'- GCAGGAAAGAACATGTATTCTTTAGCTATCATGCAGATAAAGG -3'	61.9 (53.3)	5'- CCTTTTGCTCACATGTCAAAAGAAGATGATATCTTTGGTTATGTG -3'	62.3 (53.1)	849	72.2
In-Fusion Product FR2	5'- GCAGGAAAGAACATGTATTCTTTAGCTATCATGCAGATAAAGG -3'	61.9 (53.3)	5'- CCTTTTGCTCACATGTGGAATGTTTATTTTATCTCCTTGAGCATC -3'	63.3 (54.6)	1611	74.1
In-Fusion Product FR3	5'- GCAGGAAAGAACATGTATTCTTTAGCTATCATGCAGATAAAGG -3'	61.9 (53.3)	5'- CCTTTTGCTCACATGTGACACGTTTATGTTATGAACAAAGG -3'	62.8 (52.7)	2787	76.4

B.

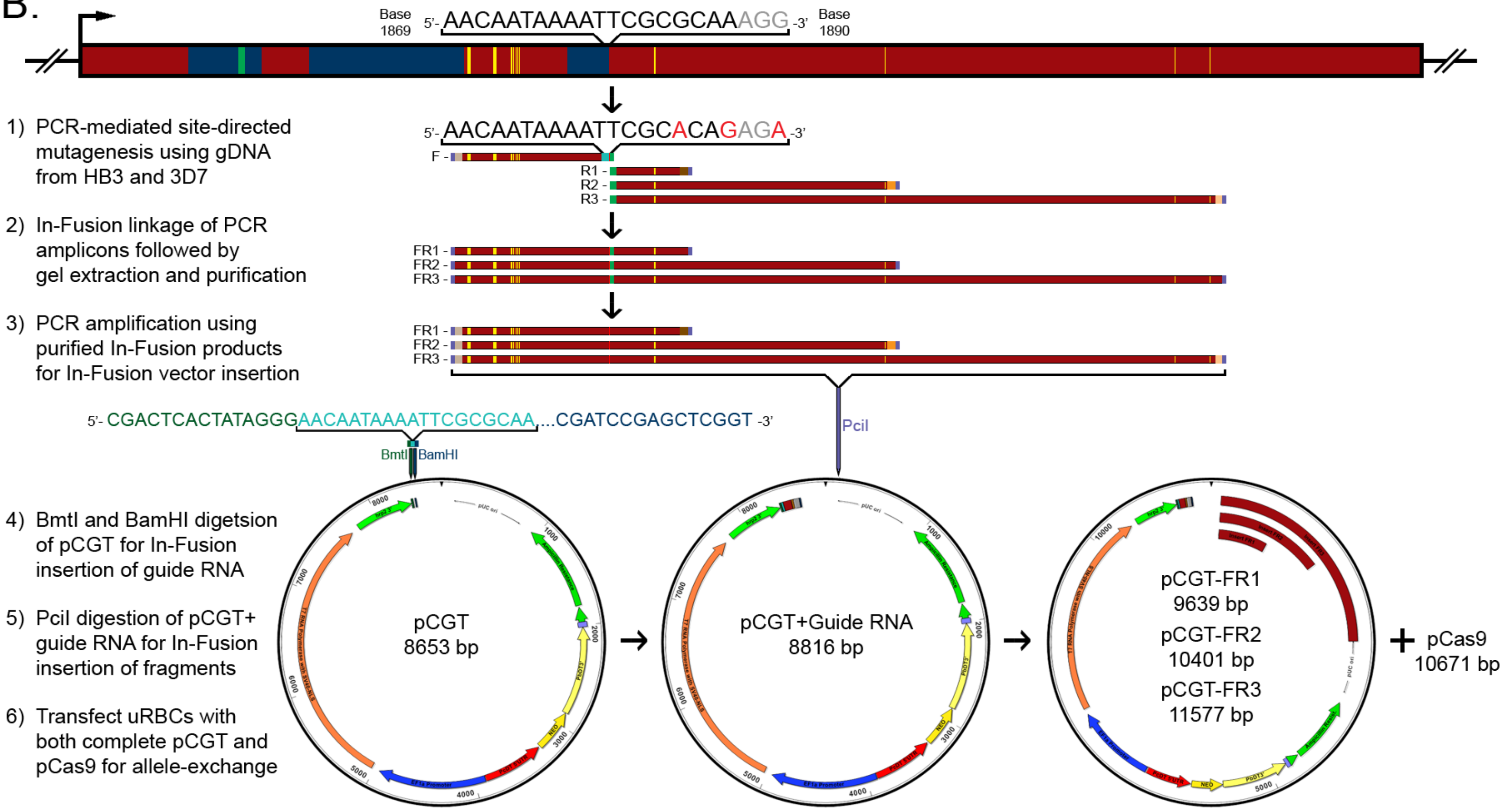

1) PCR-mediated site-directed mutagenesis using gDNA from HB3 and 3D7

2) In-Fusion linkage of PCR amplicons followed by gel extraction and purification

3) PCR amplification using purified In-Fusion products for In-Fusion vector insertion

4) BmtI and BamHI digetsion of pCGT for In-Fusion insertion of guide RNA

5) PciI digestion of pCGT+ guide RNA for In-Fusion insertion of fragments

6) Transfect uRBCs with both complete pCGT and pCas9 for allele-exchange

Figure 4.2 *(left)*: *Pf3D7_1245600* fragment amplification and plasmid construction for CRISPR-Cas9-driven allele-exchange transfections. Multiple primers (A) with In-Fusion® homology regions were used to amplify the "Silent Mutation" and "In-Fusion Product" fragments. Gene-specific primer Tm values, shown in parentheses, were used in determining the PCR primer annealing temperature. Assembling the complete pCGT plasmid involved 6 main steps (B). Fragments of *Pf3D7_1245600* containing all of the identified sequence differences between HB3 and 3D7, shown in yellow, were first amplified from both HB3 and 3D7 genomic DNA. 3 synonymous SNPs, shown in red, were introduced into the target RNA recognition sequence, shown in black, and PAM motif, shown in gray, to prevent plasmid degradation by the Cas9 nuclease. The target RNA sequence, shown in light blue, was fused into the BmtI- and BamHI-digested pCGT plasmid. The *Pf3D7_1245600* fragments were fused together, gel purified, and PCR-amplified before being inserted into the PciI-digested pCGT plasmid containing the guide RNA sequence. These completed plasmids were combined with the pCas9 plasmid for use in parasite transfection experiments.

amplification were predicted to have Tm values much higher than the sequencing primers the cycling conditions were designed for, only the gene-specific region of the primer was considered in determining the appropriate annealing temperature. The high Tm of the Silent Mutation F reverse primer was predicted to be much lower due to the region of incompatibility with the genomic sequence of *Pf3D7_1245600*.

The 4 Silent Mutation PCR fragments were PCR purified as described above and joined by the In-Fusion® HD Plus cloning system (Figure 4.3 B). The Silent Mutation F fragment was added to each Silent Mutation R fragment in a 2:1 molar ratio, as calculated by the In-Fusion® Molar Ratio Calculator tool, up to a maximum total volume of 16 µl. If the volume of the combined fragments was less than 16 µl, then DNAse- and RNAse-free ddH$_2$O was added to bring the volume to 16 µl. 4 µl of 5x In-Fusion® HD Enzyme Premix (Clontech 638909) was then added to each mixture, resulting in a final sample volume of 20 µl at 1x enzyme concentration. The tubes were incubated at 50°C for 15 minutes and placed on ice. The In-Fusion® reactions were then size-separated on a 1.5% agarose gel, extracted, and gel purified as described above. The extracted, purified products were labeled “In-Fusion Product FR1/2/3” based on which Silent Mutation R fragment was included. Using the same PciI-homology primers, PCR reagents, and cycling conditions described above, the low quantities of purified In-Fusion Product FR1/2/3 were used as templates to PCR amplify large amounts of each fragment for later In-Fusion® insertion into the pCGT plasmid (Figure 4.2).

While the repair template fragments were being assembled and amplified, the chimeric guide RNA sequence was developed for later insertion into the pCGT plasmid. The presence of engineered BmtI and BamHI cut-sites next to the T7 promoter in the pCGT plasmid (Figure 4.2 B) meant that the In-Fusion® system could be potentially utilized as described above to integrate the complete guide RNA sequence (Figure 4.3 A). Accordingly, a 15 bp BmtI homology sequence was appended to the 5’ end of the forward primer and a 15bp BamHI homology sequence was appended to the 5’ end of the reverse primer (Figure 4.4). The forward primer also contained an appended 19 bp target-specific crRNA sequence, followed by an 18 bp PCR template-specific sequence that would position the crRNA sequence immediately upstream of the tracrRNA sequence, thus creating the chimeric guide RNA. An existing TOPO® TA cloning vector containing the tracrRNA sequence, a T7 terminator sequence, and a BamHI cut-site was used as the PCR DNA template for the forward and reverse guide RNA primers shown in Figure 4.4. The complete guide RNA sequence was amplified using the reagents and cycling conditions described above and shown in Figure 4.1 C, with the only exception being that the annealing temperature was lowered from 50°C to 45°C for the first 10 cycles.

In addition to performing PCR amplifications of *Pf3D7_1245600* and the corresponding CRISPR-Cas9 guide RNA, regions of intact plasmids were PCR amplified during plasmid development and after pRBC transfection to confirm the presence of the

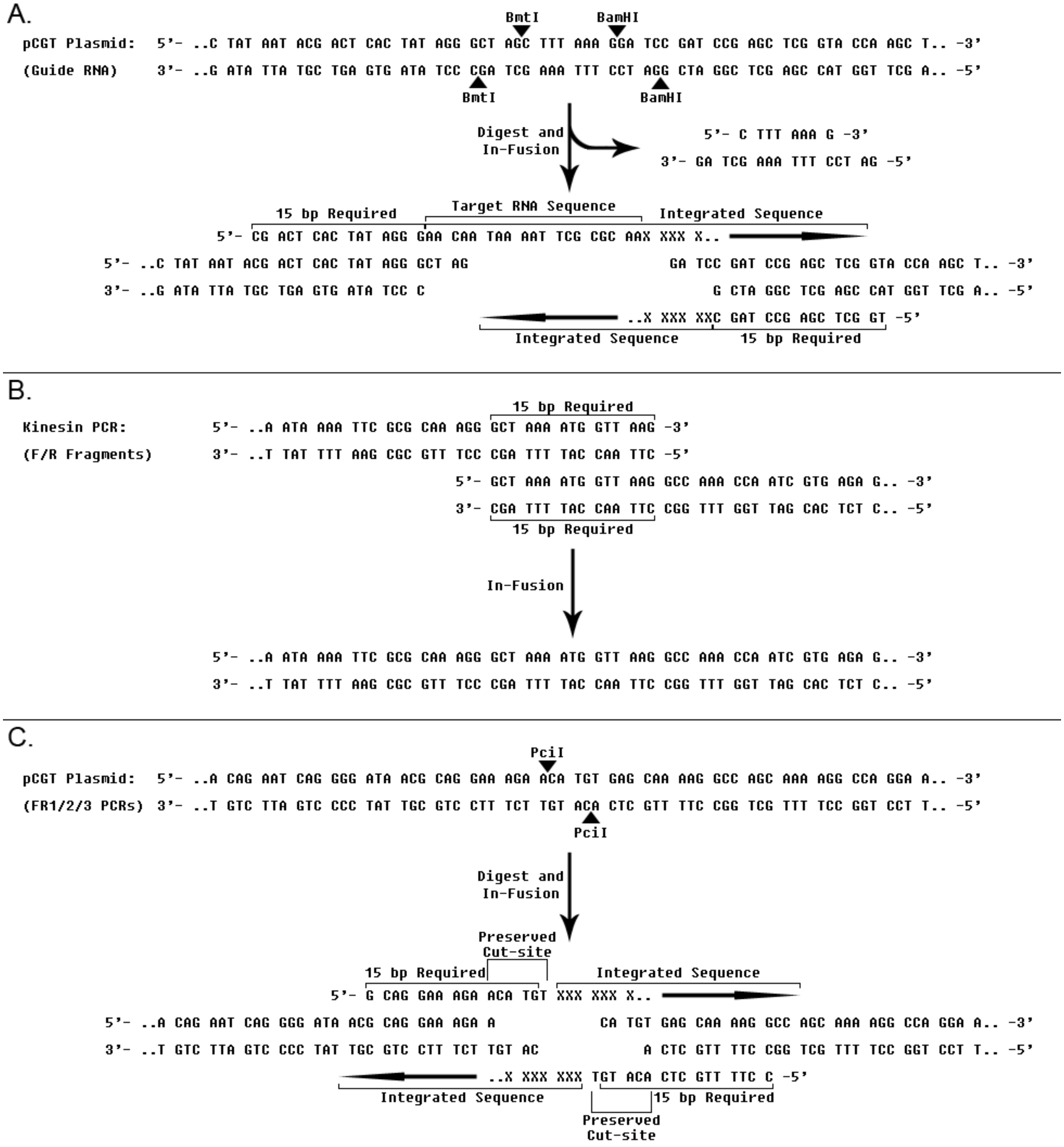

Figure 4.3: Utilized applications of the In-Fusion® HD Plus cloning system. The ligase-independent In-Fusion® system was used to insert the CRISPR-Cas9 guide RNA into the pCGT backbone (A), fuse “Silent Mutation F” with each “Silent Mutation R” (B), and insert each “In-Fusion Product FR” into the pCGT backbone already containing the guide RNA (C).

Primer	Sequence	Tm (°C)	Size (bp)	AT (%)
Guide RNA In-Fusion F	5'- CGACTCACTATAGGGAACAATAAAATTCGCGCAAGTTTTAGAGCTAGAAATA -3'	64.3 (40.2)	209	52.6
Guide RNA In-Fusion R	5'- ACCGAGCTCGGATCGGCATATATTAATGATCCTTCC -3'	64.0 (45.9)		

Figure 4.4: Guide RNA structure and amplification. The target-specific crRNA was appended to the scaffolding tracrRNA by PCR amplification from a TOPO® TA vector containing the scaffolding tracrRNA, T7 terminator, and downstream BamHI cut-site. BmtI and BamHI homology sequences were appended to the ends of the full-length guide RNA fragment for later insertion into the pCGT plasmid using the In-Fusion® system.

plasmids in drug-resistant bacteria and parasites. The pCGT + guide RNA plasmid obtained from transformed bacteria (section 4.2.5) was PCR-screened using the vector-specific gRNA forward primer 5’-CTAGTGGATCGAAGTATATGAG-3’, the gRNA-specific reverse primer 5’- CTTGAAAAAGTGGCAC-3’, and the same reagents and cycling conditions described above. The amplification of a 708 bp fragment indicated that the guide RNA had been successfully fused into the pCGT vector. The complete pCGT + repair template plasmid obtained from transformed bacteria (section 4.2.5) was PCR-screened using the ‘Silent Mutation F’ primer pair and the same reagents and cycling conditions described above. The amplification of a 567 bp fragment indicated that the repair templates had been successfully fused into the pCGT + guide RNA vector. The pCas9 plasmid obtained from transfected parasites (section 4.2.8) was PCR-screened using the Cas9 nuclease sequence-specific forward primer 5’- GCCGTCGTTGGAACTGCTTTG-3’, the reverse primer 5’- TGTAGACCCCATTGTGAGTAC-3’, and the same reagents and cycling conditions described above. The amplification of an 1181 bp fragment indicated that the pCas9 plasmid was being successfully maintained and replicated. All PCR products were size separated on a 1.2% E-Gel® to confirm fragment sizes.

4.2.4 DNA sequencing and analysis

Due to the low cost of commercial DNA sequencing and the difficulty of obtaining reliable results from the extremely AT-rich sequences characteristic of *P. falciparum*, all sequencing was outsourced to Macrogen USA Corporation. There, Sanger cycle sequencing was performed using the BigDye® Terminator v3.1 system[434,435] and analyzed with an Applied Biosystems™ 3730XL DNA Analyzer. All submitted samples were first purified using a QIAGEN® QIAquick® PCR Purification Kit or Gel Extraction Kit as described in section 4.2.3 and subsequently diluted in DNAse- and RNAse-free ddH$_2$O to concentrations of 30 ng/µl for purified PCR products and 180 ng/µl for purified plasmids. The individual primers included with submitted samples were diluted in DNAse- and RNAse-free ddH$_2$O to concentrations of 5 µM.

All 6 overlapping PCR fragments shown in Figure 4.1 were sequenced in the forward and reverse directions at least twice with the same primers used for the initial amplifications from genomic DNA (Figure 4.1 B). This provided 4x coverage of the entire *Pf3D7_1245600* gene for both HB3 and 3D7. The “In-Fusion Product FR1/2/3” fragments shown in Figure 4.2 B were sequenced in the forward and reverse directions at least twice with the same primers used to amplify the original PCR Fragment 3 from genomic DNA (Figure 4.1B). This provided 4x coverage of the In-Fusion®-linked region containing the synonymous SNPs generated by PCR-mediated site-directed mutagenesis for both HB3 and 3D7. The guide RNA fused into the pCGT vector background (Figure 4.4) was sequenced in the forward direction twice using the vector-specific, upstream gRNA primer described in section 4.2.3. This provided 2x coverage of the inserted guide RNA sequence. The *Pf3D7_1245600*-derived FR1/2/3 inserts in all pCGT plasmids obtained from the DNA minipreps described in section 4.2.5 were sequenced at least twice using several forward and reverse primer combinations spanning the entire insert. Those primers are the same ones shown in Figure 4.1 B and Figure 4.2 A, with the exception of a pCGT vector-specific forward primer with the sequence 5’-ACCGAGCTCGGATCGGCATATATTAATGATCCTTCC-3’. All of the sequencing template and primer combinations are listed in Table 4.1.

DNA sequence chromatograms were processed using Sequencher™ version 5.1 and assembled using the DNASTAR® Lasergene® Core Suite version 12.0.0 programs SeqBuilder™ and MegAlign™. Raw chromatogram sequences were trimmed at the 5’ and 3’ ends until the first and last 25 bases contained less than 3 ambiguities with a base-calling confidence less than 25%. To resolve sequence ambiguities that were not excluded by end trimming, all of the reads collected over a particular ambiguity were compared. The base-calling confidence of each read was examined and used to develop an average sequence over the ambiguity. A judgment call was then made to maintain, alter, or exclude the ambiguous base for the final consensus sequence. If a judgment call could not be made, new sequences were obtained using different primers and compared to the ambiguous sequence as before. Consensus sequences were ordered and assembled using the overlapping homology regions of individual fragments and aligned to version 3.0 of the 3D7 reference genome by the CLUSTAL W method[436]. Consensus DNA sequences were translated into protein sequences and aligned to each other by the CLUSTAL W method.

4.2.5 Plasmid construction and cloning

The stable expression of altered or tagged alleles in *P. falciparum* has provided essential insights into the functions of genes and consequences of SNPs, leading to the identification of genetic determinants responsible for phenotypes such as drug-resistance[437], nutrient-uptake[438], and parasite virulence[319]. The recent application of the bacterial CRISPR-Cas system[439] to genome editing[440] has dramatically increased the efficiency and specificity of genetic manipulation in many organisms, including *P. falciparum*[441,442]. This system relies on 3 essential components– the Cas9 double-stranded DNA endonuclease, a genome target-specific crRNA with an immediately adjacent PAM site, and a scaffolding tracrRNA.

	PCR Fragment						In-Fusion FR1/2/3			Miniprep pCGT plasmid		
Primer	1	2	3	4	5	6	FR1	FR2	FR3	pCGT-FR1	pCGT-FR2	pCGT-FR3
F1	■											
R1	■											
F2		■										
R2		■								■	■	■
F3			■				■	■	■			
R3			■				■	■	■		■	■
F4				■							■	■
R4				■								■
F5					■							■
R5					■							■
F6						■						■
R6						■						
F123 Mut.										■	■	■
F-pCGT										■	■	■
F-gRNA										■	■	■

Table 4.1: DNA sequencing sample and primer matrix. Each DNA sample was sequenced at least twice using multiple primers to provide thorough coverage of *Pf3D7_1245600* and the derived products. The individual forward (F) and reverse (R) primers used to sequence each DNA sample are indicated by black boxes.

The crRNA and tracrRNA components can be expressed as a single guide RNA chimera, which results in vectors that only require the introduction of an oligonucleotide corresponding to the genome target sequence. When co-expressed, the Cas9 nuclease recognizes the endogenous genome sequence complementing the guide RNA sequence and induces a double-strand break between the target sequence and the PAM site.

Transfecting parasites with a plasmid expressing the Cas9 nuclease and a guide RNA can efficiently generate gene knockouts since site-specific genome cutting will occur. However, to achieve allele-exchange in parasites, a double-strand break repair template must also be included. The CRISPR-Cas9 strategy developed for exchanging the *Pf3D7_1245600* alleles of HB3 and 3D7 utilized the 2 plasmids pCas9 and pCGT. The Cas9 nuclease is encoded on pCas9, and the guide RNA and repair template are encoded on pCGT. This arrangement ensured that the Cas9 nuclease would not be able to cut the endogenous *Pf3D7_1245600* locus without the repair template being present. Furthermore, PCR-mediated site-directed mutagenesis (section 4.2.3) was used to introduce 3 synonymous SNPs into the region of the repair template sequence corresponding to the guide RNA and PAM sequences. This ensured that the Cas9 nuclease would not recognize and cut the pCGT plasmid or the successfully repaired genome sequence.

Since the successful integration of a foreign sequence into the endogenous locus is potentially dependent on the size of the repair template[443], 3 repair templates of varying sizes (Figure 4.2) were generated for insertion into the pCGT plasmid (section 4.2.3). Though each template possessed the same 5’ cluster of sequence discrepancies seen between HB3 and 3D7, the larger templates possessed additional discrepancies toward their 3’ ends. This provided the additional advantage of being able to narrow down the causative SNP(s) to the 5’ or 3’ end depending on which transfectants showed phenotypic changes. With 3 different repair templates and 2 parasite lines, 6 unique pCGT plasmids were developed for co-transfection with the same pCas9 plasmid.

Plasmid pCas9 was previously derived from plasmid pDC[444], where the *PfCRT* promoter was replaced with the strong *P. berghei EF1α* promoter that has been routinely used for constitutive protein expression in *Plasmodium*[445,446] (Figure 4.5 A). The complete sequence of the *Streptococcus pyogenes* Cas9 endonuclease was cloned into the AvrII and MluI restriction sites of pDC, placing it just after the *EF1α* promoter. Expression of pCas9 produces the Cas9 endonuclease and also confers resistance to WR99210 by providing the human dihydrofolate reductase enzyme[447]. Plasmid pCGT was previously generated by cloning the complete T7 RNA polymerase sequence, including an SV40-NLS, from *E. coli* BL21 genomic DNA into the plasmid pCR 2.1 obtained from Invitrogen™ (Figure 4.5 B). The *EF1α* promoter was then cloned into the plasmid, placing it just before the polymerase

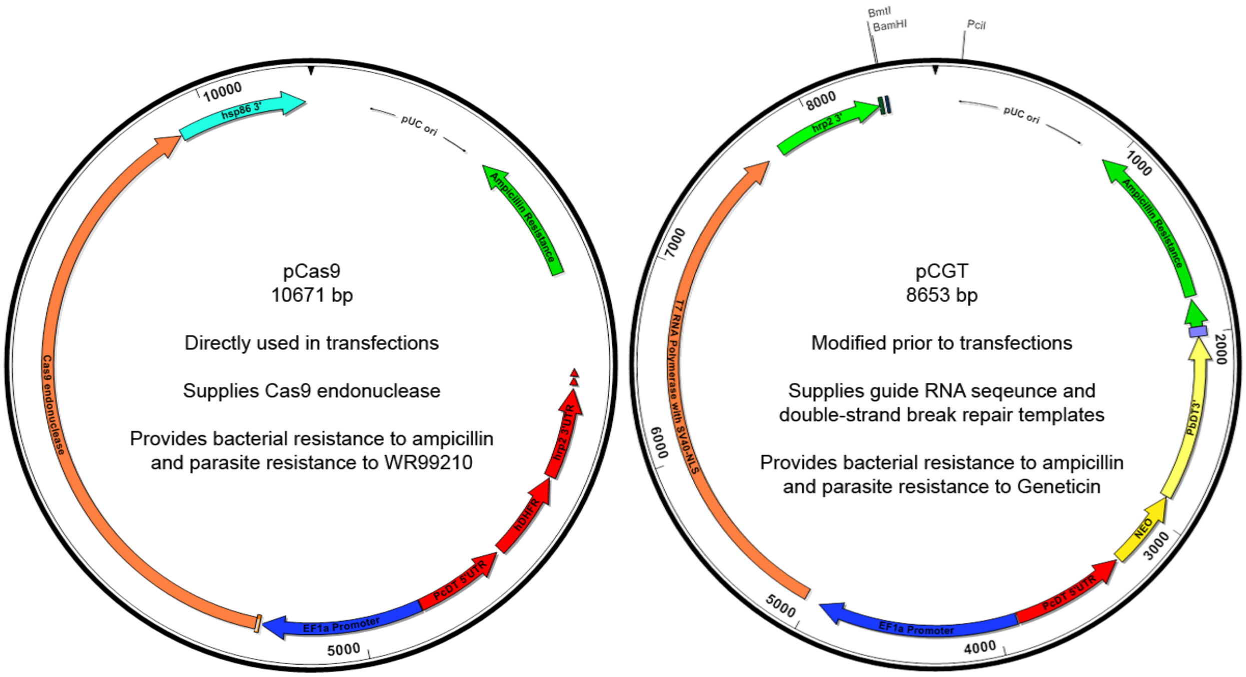

Figure 4.5: pCas9 and pCGT plasmid vectors used in CRISPR-Cas9-driven allele-exchange transfection. Plasmid pCas9 was directly used in parasite transfection experiments, while plasmid pCGT was modified prior to transfection by incorporating the Cas9 guide RNA sequence and the *Pf3D7_1245600* repair template.

sequence. A T7 promoter sequence was then cloned into the plasmid just before BmtI and BamHI cut-sites to allow for the insertion of a CRISPR-Cas9 guide RNA right after the promoter. A blasticidin-resistance cassette initially cloned into the plasmid was later replaced with a neomycin-resistance cassette, conferring resistance to Geneticin® by providing the neomycin phosphotransferase II enzyme from transposon Tn 5[448]. Both pCas9 and pCGT also contained the elements necessary to confer ampicillin-resistance to *E. coli* for the selection of positive transformants.

To prepare pCGT for transfection, the intact plasmid was first co-digested with the restriction endonucleases BmtI and BamHI. A mixture composed of 1 µl of a 10,000 units/ml BmtI solution (New England Biolabs® R0658S), 0.5 µl of a 20,000 units/ml BamHI solution (New England Biolabs® R0136S), 23.5 µl of ddH_2O, and 5 µl of 10x NEBuffer 3.1 (New

England Biolabs® B7203S) consisting of ddH_2O with 100 mM NaCl, 50 mM Tris-HCl, 10 mM $MgCl_2$, and 100 µg/ml BSA, was prepared on ice. 20 µl of purified pCGT plasmid was added to the mixture, resulting in a 50 µl reaction containing 200 units/ml of each endonuclease in a final buffer concentration of 1x. The mixture was placed in a 37°C incubator for approximately 14 hours to allow digestion to occur. Longer incubation times were avoided to minimize the occurrence of star activity[449]. The digested plasmid was then purified using a QIAGEN® QIAquick® PCR Purification Kit as described in section 4.2.3. The guide RNA sequence described in section 4.2.3 was mixed with the digested vector in a 2:1 molar ratio, as calculated by the In-Fusion® Molar Ratio Calculator tool, up to a maximum total volume of 8 µl. If the volume of the combined DNA was less than 8 µl, then DNAse- and RNAse-free ddH_2O was added to bring the volume to 8 µl. 2 µl of 5x In-Fusion® HD Enzyme Premix was then added to the mixture, resulting in a final sample volume of 10 µl at 1x enzyme concentration. The tube was incubated at 50°C for 15 minutes and placed on ice. While the tube was incubating, a tube containing 50 µl of high-efficiency, chemically-competent 10-beta *E. coli* cells (New England Biolabs® C3019H) was removed from -80°C storage and thawed on ice for 10 minutes. 3 µl of the completed In-Fusion® reaction was added to the *E. coli*, and the tube was gently flicked 4 times to mix. The mixture was then placed on ice for 30 minutes before being heat-shocked at exactly 42°C for precisely 30 seconds. The tube was immediately placed on ice for 5 minutes, after which the transformed cells were suspended in 950 µl of room-temperature SOC medium consisting of 2% w/v vegetable peptone, 0.5% w/v yeast extract, 10 mM NaCl, 2.5 mM KCl, 10 mM $MgCl_2$, 10 mM $MgSO_4$, and 20 mM glucose in ddH_2O. The tubes were then placed in a 37°C shaker for 60 minutes. After incubating, the tube was mixed by inversion, and 250 µl of the cell suspension was spread on a 37°C ampicillin selection plate containing a solidified mixture of 1% w/v tryptone, 0.5% w/v yeast extract, 0.17 M NaCl, 1.5% w/v agar, and 100 µg/ml ampicillin in ddH_2O.

Inoculated plates were incubated at 37°C overnight to allow successfully transformed bacteria to form colonies. Individual colonies were picked and transferred to numbered positions on a new 37°C ampicillin selection plate and incubated at 37°C overnight. Picked colonies were PCR-screened for the presence of the guide RNA insert using the reagents described in section 4.2.3 and intact bacteria as the DNA source. PCR-positive colonies were expanded to obtain large quantities of DNA for sequencing and downstream applications. A toothpick was touched to the appropriate numbered colony and dropped into a tube containing 5 ml of LB selection medium consisting of 1% w/v tryptone, 0.5% w/v yeast extract, 0.17 M NaCl, and 100 µg/ml ampicillin in ddH_2O. The tube was then incubated in a 37°C shaker overnight. Afterward, the tube was centrifuged at 4000 rpm for 5 minutes to pellet the bacteria. Plasmid DNA was obtained by processing the bacteria with a QIAGEN® QIAprep® Spin Miniprep Kit according to the manufacturer's instructions. The resulting purified plasmid DNA was eluted in DNAse- and RNAse-free ddH_2O and stored at -20°C long-term or 4°C short-term. Aliquots of the plasmid were submitted for sequence confirmation as described in section 4.2.4.

After the sequence of the inserted guide RNA had been confirmed, bacteria stocks were prepared for cryopreservation by first obtaining a 5 ml culture of bacteria as described above. The bacteria were then pelleted and resuspended in a 1x pellet volume of cryopreservation medium consisting of LB selection medium with 60% v/v glycerol. The bacteria mixture was transferred to a cryovial and stored at -80°C long-term. To grow bacteria from frozen stocks, the top of the frozen bacteria mixture was scraped with a wooden toothpick, which was then dropped directly into 5 ml of LB selection medium and incubated in a 37°C shaker overnight.

The sequence-confirmed pCGT + guide RNA plasmid was digested with the restriction endonuclease PciI. Similar to the first digestion, a mixture composed of 1 µl of a 10,000 units/ml PciI solution (New England Biolabs® R0655S), 24 µl of ddH_2O, and 5 µl of

10x NEBuffer 3.1 was prepared on ice. 20 µl of purified pCGT + guide RNA plasmid was added to the mixture, resulting in a 50 µl reaction containing 200 units/ml of endonuclease in a final buffer concentration of 1x. The mixture was placed in a 37°C incubator for approximately 14 hours to allow digestion to occur, after which the digested plasmid was purified using a QIAGEN® QIAquick® PCR Purification Kit as described in section 4.2.3. The single digested pCGT + guide RNA plasmid was used in 6 subsequent In-Fusion® reactions, each with a different repair template from either HB3 or 3D7. For each 10 µl reaction, the repair template was mixed with the digested vector in a 2:1 molar ratio and fused as described above. The reaction products were then used to transform *E. coli* as described above. Ampicillin-resistant colonies were screened for the presence of the repair template insert using the reagents described in section 4.2.3 and intact bacteria as the DNA source. PCR-positive colonies were expanded, processed with a QIAprep® Spin Miniprep Kit, and sequence-confirmed as described above.

After the sequence of the inserted repair templates had been confirmed, the pCGT plasmid was ready to use in transfection experiments. Before proceeding, frozen bacteria stocks were first prepared as described above. To obtain enough plasmid DNA to complete all of the planned transfections, the *E. coli* colonies expressing the sequenced plasmids were expanded by touching a toothpick to the appropriate colony and dropping it into a 2 L Erlenmeyer flask containing 1 L of LB selection medium. The flasks were then incubated in a 37°C shaker overnight. Afterward, the bacteria were pelleted by centrifugation at 4000 rpm for 15 minutes in a 4°C centrifuge. The bacteria pellets were then processed with an Invitrogen™ PureLink™ HiPure Plasmid Maxiprep Kit according to the manufacturer's instructions. Purified plasmid DNA was eluted in sterile TE buffer consisting of ddH_2O with 10 mM Tris-HCl and 0.1 mM EDTA, and stored at -20°C until its use in transfections.

While the pCGT plasmids were being prepared for transfections, a frozen stock of a previously transformed and sequenced *E. coli* colony containing the pCas9 plasmid was used to develop a 1 L culture as described above. Following the incubation, the bacteria were pelleted by centrifugation at 4000 rpm for 15 minutes in a 4°C centrifuge. The bacteria pellets were then processed with an Invitrogen™ PureLink™ HiPure Plasmid Maxiprep Kit according to the manufacturer's instructions. Purified plasmid DNA was eluted in sterile TE buffer and stored at -20°C until its use in transfections.

4.2.6 Asexual blood-stage pRBC transfection

P. falciparum transfection, from its earliest reported successes[255,450–452] to its widespread use as a routine step in parasite genetic manipulation[27,453,454], largely relies on blood-stage parasites to spontaneously uptake and express DNA from host erythrocytes[455]. This process has been traditionally achieved through the direct electroporation of early ring-stage pRBCs. However, the low efficiency frequently seen with this approach[456] can be significantly improved by pre-loading uRBCs with DNA via electroporation and introducing those cells to late-stage pRBCs[457]. Furthermore, the recent introduction and optimization of Nucleofector™ electroporation technology has increased the efficiency of cell loading while also significantly reducing the amount of DNA needed[458,459].

To prepare uRBCs for transfection, 10 µl of packed cells were added to 26 of the 32 available wells across both 16-well Nucleocuvette™ strips included with the Amaxa™ SE Cell Line 4D-Nucleofector™ X Kit S. Using Table 4.2 as a guide, 5 µg of the appropriate pCGT plasmid and 5 µg of the pCas9 plasmid were added to the wells. The volume in each well was then brought to 20 µl with the addition of the 4D-Nucleofector™ X Solution included with the kit. The prepared Nucleocuvette™ strips were inserted into a 4D-Nucleofector™ X Unit and pulsed using the CM-162 setting. Immediately after pulsing, 180 µl of pre-warmed complete parasite culture medium was added to each well before transferring the entire well contents to a flat-bottom 96-well plate. The plate was centrifuged for 2 minutes at 1500 rpm to pellet the electroporated uRBCs so that the supernatants could be removed. The cells

Plasmids	Parasite Line			
	Experimental Group		Control Group	
pCGT-HFR1 + pCas9	3D7	3D7	HB3	HB3
pCGT-HFR2 + pCas9	3D7	3D7	HB3	HB3
pCGT-HFR3 + pCas9	3D7	3D7	HB3	HB3
pCGT-3FR1 + pCas9	HB3	HB3	3D7	3D7
pCGT-3FR2 + pCas9	HB3	HB3	3D7	3D7
pCGT-3FR3 + pCas9	HB3	HB3	3D7	3D7
pCas9	HB3	3D7	None	None

Table 4.2: CRISPR-Cas9 transfection sample matrix. HB3 and 3D7 were each transfected with pCas9 and all 6 pCGT plasmids. Parasites receiving the non-identical *Pf3D7_1245600* allele would result in allele-exchanged lines, while parasites receiving the identical allele would serve as transfection and CRISPR-Cas9 editing controls. Parasites receiving the pCas9 plasmid alone would serve as controls and would be used for subsequent transfections with pCGT alone in the event that the double-transfections failed.

were then resuspended in 150 µl of pre-warmed complete parasite culture medium and placed at 37°C until the pRBCs were ready.

While the electroporation of uRBCs was occurring, highly synchronous HB3 and 3D7 schizonts preparing to reinvade within 1-2 hours were isolated by floatation in 5x pellet-volumes of pre-warmed ZeptoGel, a gelatin-based leukocyte isolation reagent that performs equally well to Plasmion® in floating knob-positive pRBCs. Great care was taken to obtain only the pRBC fraction of floated cells, as any uRBCs accidentally included with the pRBCs would effectively compete with the electroporated uRBCs for merozoites. This was accomplished by extracting only the top 1/3 volume of the total ZeptoGel suspension, which generally left a 1/3 volume buffer region above the settled uRBCs and knob-negative pRBCs. Isolated schizonts were washed once with pre-warmed complete parasite culture medium and resuspended in pre-warmed complete parasite culture medium to a concentration of 5 µl of packed schizonts per 150 µl. The 96-well plate containing the electroporated uRBCs was then removed from the incubator so that 150 µl of the HB3 and

3D7 schizont suspensions could be added to the appropriate uRBCs. The plate was maintained in a gassed culture chamber at 37°C, with medium changes occurring every 30 minutes for the first 2 hours and every 60 minutes for 6 subsequent hours. After a total of 8 hours in the 96-well plate, the contents of each well were transferred to 6-well plates for long-term culturing. A suspension containing 35 µl of packed uRBCs in 5 ml of pre-warmed complete parasite culture medium was added to each well, resulting in a final packed cell volume of 50 µl and a final hematocrit of 1%. Plates were maintained in a gassed culture chamber at 37°C, with medium changes occurring every day.

Once parasites had reinvaded 48 hours later, double-transfectants began receiving medium supplemented with Geneticin® (Gibco® 11811) and WR99210 (Sigma W1770), while single-transfectants began receiving medium supplemented with WR99210 alone. Geneticin® was included at a concentration of 200 µg/ml for HB3 and 250 µg/ml for 3D7. WR99210 was included at a concentration of 2 nM for both HB3 and 3D7. The drug concentrations used were initially determined based on previously published data[448,460], but a standard IC_{50} drug assay was later performed to further support the choice of concentrations used[461,462]. In a 96-well plate, 200 µl of 8055.6 µM Geneticin® in complete parasite culture medium and 200 µl of 64 nM WR99210 in complete parasite culture medium were added to 4 wells each. Every starting well was then serially diluted 1:2 in complete parasite culture medium across 9 additional wells. 100 µl of drug-free medium was added to the remaining 2 wells in each row. 100 µl of either HB3 or 3D7 pRBCs at 0.5% parasitemia and 4% hematocrit were added to each well so that both HB3 and 3D7 parasites were exposed to duplicate serial dilutions of each drug. With the addition of pRBCs, the drug concentrations ranged from 4027.8 to 7.87 µM for Geneticin® and 32 to 0.06 nM for WR99210. The plate was placed in a culture chamber and gassed before being incubated at 37°C for 72 hours. Afterward, the plate was removed from the chamber and placed directly at -80°C to lyse all of the cells. After completely freezing, the plate was allowed to completely thaw before the wells were mixed with 100 µl each of lysis solution consisting of ddH_2O with 20 mM Tris, 5 mM EDTA, 0.008% w/v saponin, 0.08% v/v Triton™ X-100, and 1.5x SG. The plate was incubated at room temperature for 60 minutes in the dark before analysis on a BMG Labtech FLUOstar OPTIMA microplate reader. The 497nm/520nm values were recorded for each well and processed by non-linear regression in GraphPad Prism® version 6.04 to obtain percent inhibition curves and IC_{50} values (Figure 4.6).

After 8 days of continuous drug pressure and daily medium changes, transfectants were diluted 1:2 with an equal volume of uRBCs in drug-free complete parasite culture medium and split into duplicate wells. One well continued to receive drug-supplemented medium while the other well received drug-free medium. The medium was changed every other day, and 5 µl of fresh uRBCs were added each week. Wells were checked for viable parasites at least once each week.

4.2.7 Viable transfectant screening by flow cytometry

The traditional and most widely practiced method of detecting viable, drug-selected parasites after transfection relies on the examination of Giemsa-stained thick- and thin-smears by microscopy[452,463,464]. While this approach is effective and provides information on parasite health and developmental stage, it is labor-intensive, time-consuming, and requires microscopists confident in identifying viable parasites at extremely low numbers among significant levels of post-transfection cell debris. To circumvent these issues, a rapid, high-throughput, and sensitive 2-color flow cytometry method was developed to monitor transfectants, enabling the clear detection of viable parasites at sub-microscopic levels[465].

As described in section 2.2.5, SG was used to distinguish pRBCs from uRBCs. Since SG indiscriminately stains DNA, regardless of parasite viability, the polarized mitochondria-specific, carbocyanine-based dye MTDR was included to specifically identify viable pRBCs (Figure 4.7). Of the available MitoTracker® dyes, MTDR was selected due to the minimal

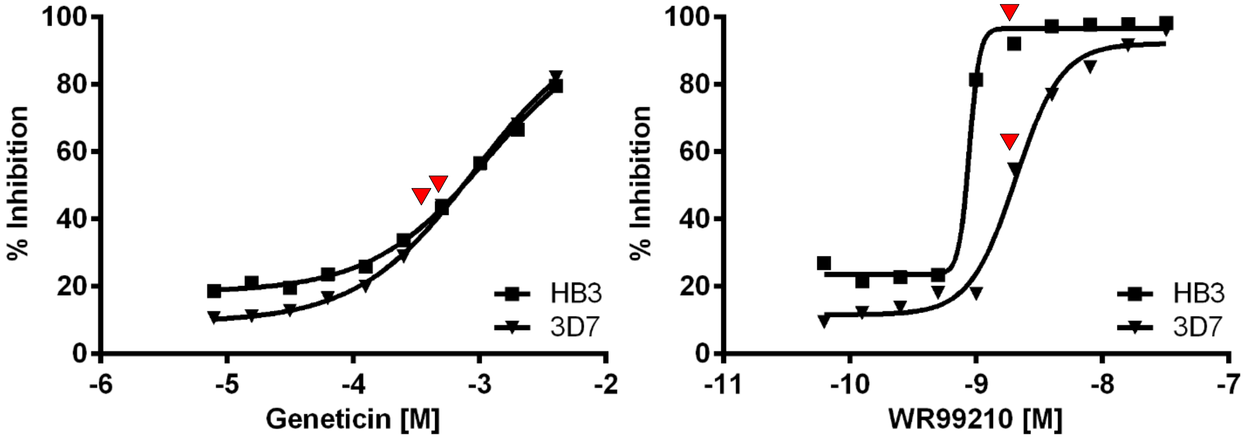

Geneticin		
Parasite	HB3	3D7
Log IC_{50}	-2.941	-3.052
Std. Error	0.094	0.072
Concentration	1145.51 μM	887.16 μM

WR99210		
Parasite	HB3	3D7
Log IC_{50}	-9.054	-8.687
Std. Error	0.134	0.039
Concentration	0.883 nM	2.056 nM

Figure 4.6: IC_{50} curves of the plasmid-selection drugs Geneticin® and WR99210 against wild-type HB3 and 3D7. Geneticin® concentrations ranging from 4027.8 to 7.87 μM and WR99210 concentrations ranging from 32 to 0.06 nM were added to wild-type HB3 and 3D7 pRBCs to develop IC_{50} curves for each drug against each parasite line. Percent inhibition curves and IC_{50} values were determined by non-linear regression analysis. Red arrows indicate the concentration of each drug used for each parasite line to select for pRBCs that stably expressed the transfected plasmids.

overlap with SG, eliminating the need for fluorescence spillover compensation of FACS data (Figure 4.8). MTDR was titrated prior to use to avoid non-specific organelle and cell staining due to an overabundance of free dye (Figure 4.9), which would have potentially resulted in nonviable parasites appearing in the viable parasite scatterplot quadrant. The accuracy and specificity of the FACS method was validated against the traditional microscopy method using available, pre-existing artemisinin-sensitive and artemisinin-resistant parasite field isolates that had been processed for the ring-stage survival assay[465,466] (Figure 4.10).

To prepare samples for FACS analysis, 3 μl of packed cells were obtained directly from each well of transfected parasites. The aliquots were then washed twice with pre-

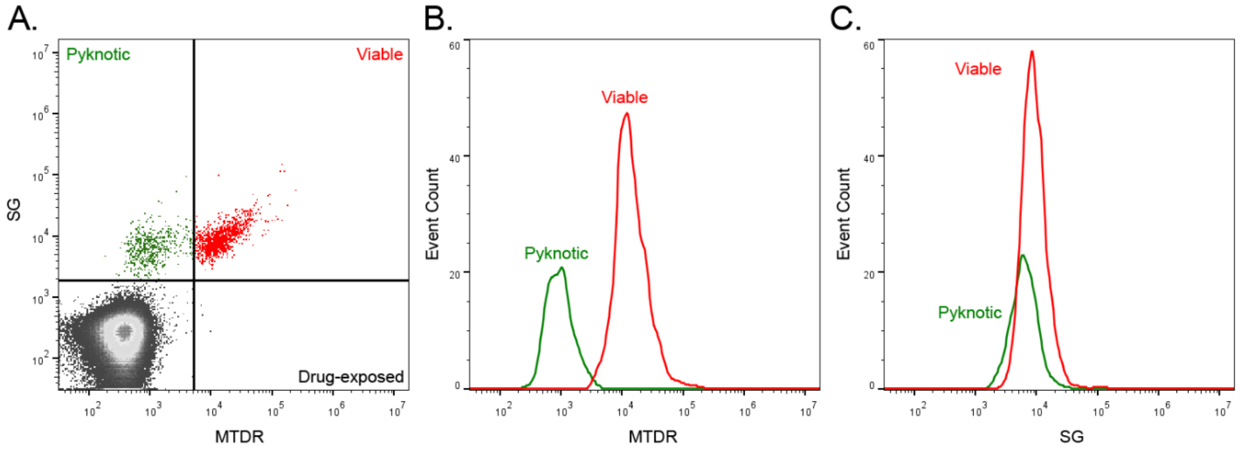

Figure 4.7: Viable and non-viable pRBC recognition by SG and MTDR. The viability of drug-treated parasites stained with SG and MTDR can be easily and rapidly assessed given the clear segregation of viable and non-viable pRBC populations (A). Histograms showing MTDR (B) and SG (C) staining of pRBCs demonstrate the inability of SG to specifically label viable cells, unlike MTDR.

warmed FACS wash buffer, consisting of HBSS with 2% v/v FBS, and resuspended to a final hematocrit of 10% in FACS wash buffer. From those resuspensions, 25 µl aliquots were added to 25 µl aliquots of FACS wash buffer containing 0.4x SG and 0.6 µM MTDR, resulting in a final SG concentration of 0.2x, a final MTDR concentration of 0.3 µM, and a final hematocrit of 5%. Samples were incubated at 37°C for 30 minutes and then washed 3 times with 500 µl of FACS wash buffer. After the final aspiration, cells were resuspended in 1100 µl of FACS wash buffer and transferred to flow cytometry tubes for immediate analysis. FACS sample components are detailed in Table 4.3.

FACS samples were analyzed using a single 6-parameter BD Biosciences Accuri™ C6 flow cytometer equipped with 488 nm and 640 nm solid-state lasers. SG and MTDR were excited and detected using the parameters described in Table 4.4 and visually represented in Figure 4.8. The flow cytometer was calibrated weekly, and voltages for each experiment were automatically adjusted based on standard fluorescent validation beads supplied by the manufacturer. 250000 ungated events were collected for each stained

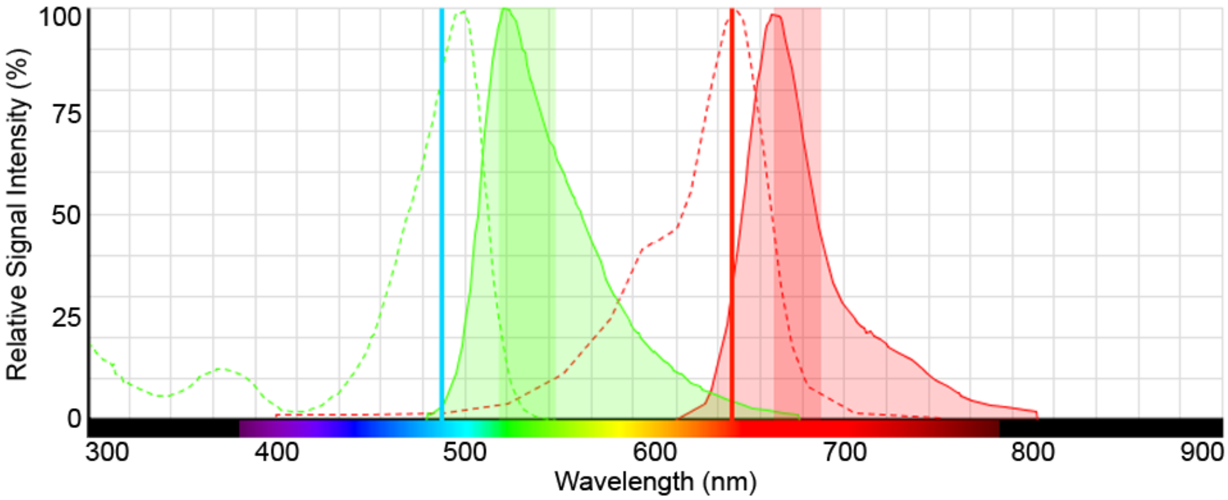

Figure 4.8: SG and MTDR fluorescence spectra. SG (green) and MTDR (red) have largely non-overlapping excitation (dashed curve) and emission (solid curve) spectra. SG was excited with a 488 nm laser (solid blue bar) and detected through a 533/30 band-pass filter (shaded green bar), while MTDR was excited with a 640 nm laser (solid red bar) and detected through a 675/25 band-pass filter (shaded red bar). Spectra were generated using the Life Technologies™ Fluorescence SpectraViewer.

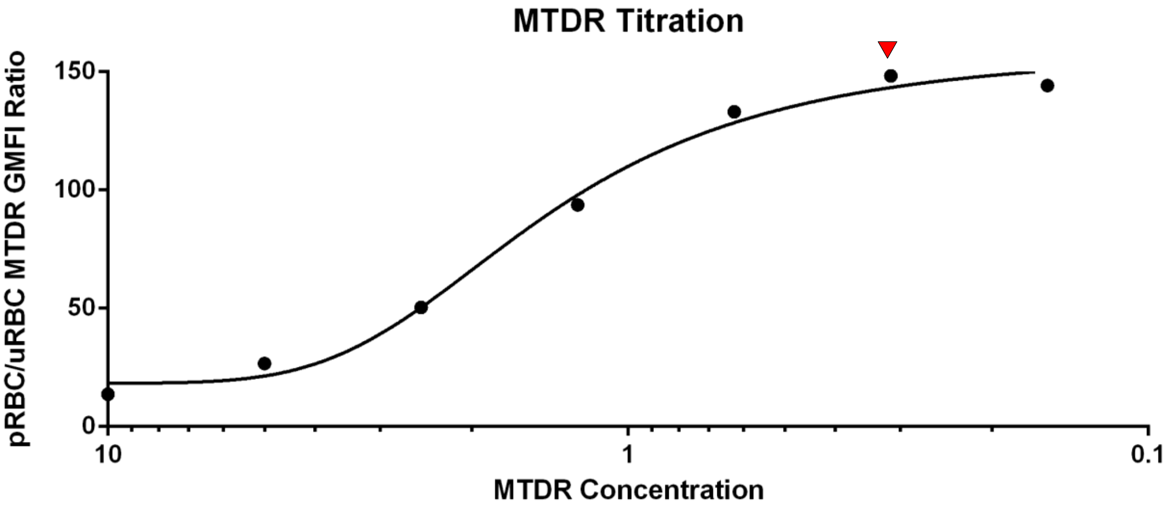

Figure 4.9: MTDR titration. A serial dilution of MTDR from 10 µM to 0.15625 µM was performed using a 1% parasitemia culture. A MTDR GMFI ratio was developed from the uRBC and pRBC populations to identify the dye concentration providing the greatest fluorescence signal separation. The data were fitted with a sigmoidal curve, R^2 value of 0.9924. The red arrow indicates the MTDR concentration used in further experiments.

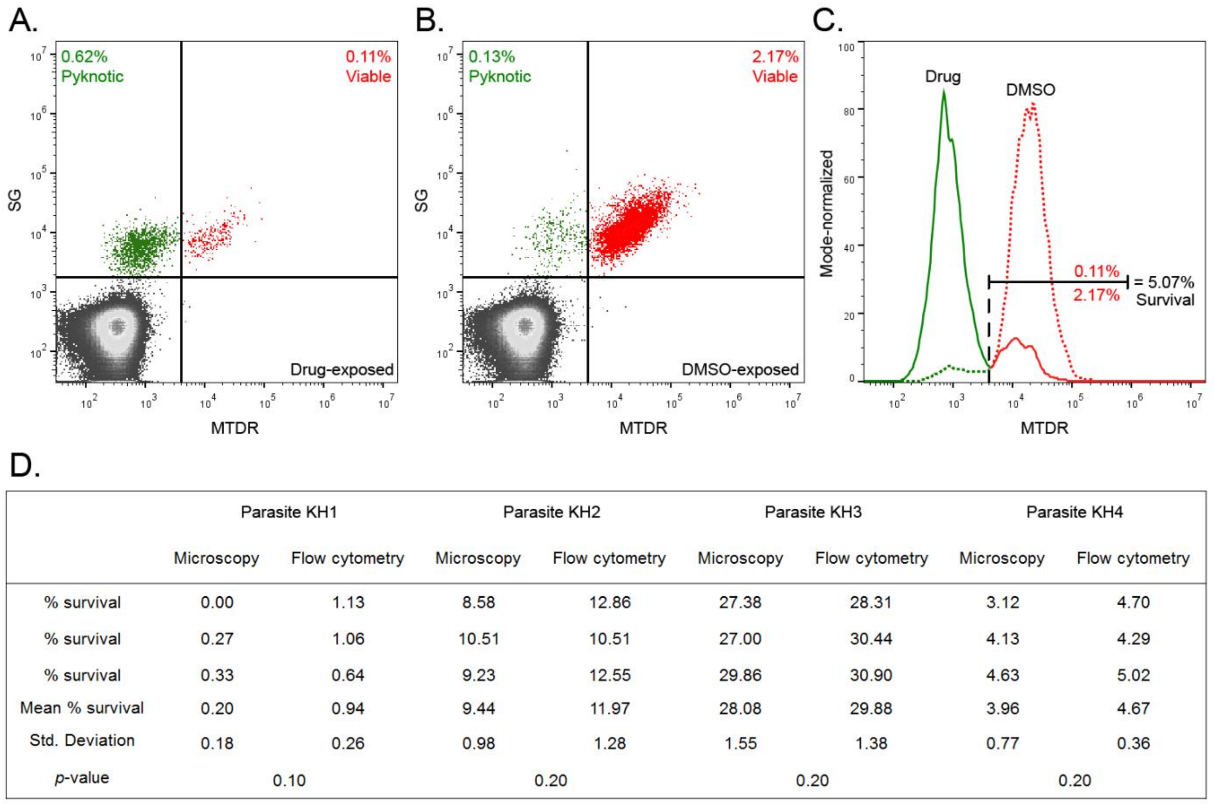

	Parasite KH1		Parasite KH2		Parasite KH3		Parasite KH4	
	Microscopy	Flow cytometry	Microscopy	Flow cytometry	Microscopy	Flow cytometry	Microscopy	Flow cytometry
% survival	0.00	1.13	8.58	12.86	27.38	28.31	3.12	4.70
% survival	0.27	1.06	10.51	10.51	27.00	30.44	4.13	4.29
% survival	0.33	0.64	9.23	12.55	29.86	30.90	4.63	5.02
Mean % survival	0.20	0.94	9.44	11.97	28.08	29.88	3.96	4.67
Std. Deviation	0.18	0.26	0.98	1.28	1.55	1.38	0.77	0.36
p-value	0.10		0.20		0.20		0.20	

Figure 4.10: Validation of FACS viability assay against traditional microscopy. Available, pre-existing parasite lines that had been processed for the ring-stage survival assay were analyzed by FACS and microscopy. The viable populations of artemisinin-treated (A) and DMSO-treated (B) parasites were used to calculate the percentage of parasites that survived artemisinin treatment (C). When compared to traditional microscopy (D), FACS-determined survival percentages were not significantly different.

Component	Concentration	Composition
DNA stain	0.2x	SYBR® Green I
Active mitochondria stain	0.3 µM	MitoTracker® Deep Red FM
Wash buffer	N/A	HBSS with 2% v/v FBS

Table 4.3: pRBC viability FACS assay components.

Fluorophore	Max Excitation	Max Emission	Laser	Band-Pass Filter
SG	497 nm	520 nm	488 nm	533/30
MTDR	644 nm	665 nm	640 nm	675/25

Table 4.4: Viability FACS fluorochrome properties and instrument parameters.

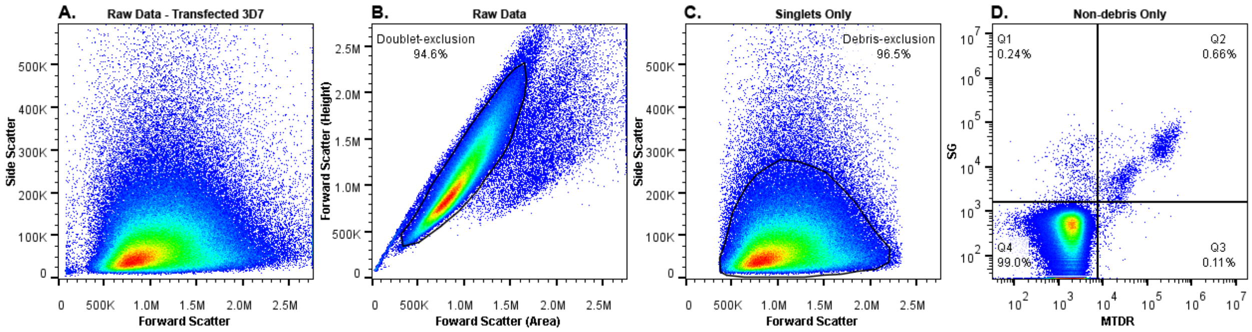

Figure 4.11: Gating strategy for viability FACS data. For all FACS samples, 250,000 raw events were initially collected (A). Forward scatter height versus area (B) and forward scatter versus side scatter (C) gates were applied to exclude cell doublets and cell debris, respectively, from analysis. The remaining populations were divided into 4 quadrants (D) to determine the percentage of viable pRBCs, located in Q2.

sample at a rate of 1000 to 3000 events per second. All data were acquired using CFlow® Sampler version 1.0.264.15 software and later processed using FlowJo version 10.0.7r2. Raw sample data was processed by first applying a doublet-exclusion gate based on the forward scatter height versus area scatterplot, followed by a debris-exclusion gate on the resulting sub-population of singlets. A quadrant gate was then applied to the SG versus MTDR scatterplot of the processed samples to determine the percentage of SG+/MTDR+ pRBCs (Figure 4.11). Once the percentage of SG+/MTDR+ pRBCs in a sample had exceeded 0.5%, the transfectant well was examined for parasites by Giemsa-stained thin smear and expanded for further use.

4.2.8 Expansion, manipulation, and phenotyping of transfectants

Upon confirmation of viable pRBCs by flow cytometry and microscopy, transfectant wells were expanded from 50 µl of packed cells at 1% hematocrit to 250 µl of packed cells at 1% hematocrit and transferred to a small flask for continued culture. Transfectants that had been split and cultured in drug-free medium were placed under drug selection pressure again to ensure that the detected parasites stably expressed the transfected plasmid. Drug-supplemented medium was changed daily until cultures reached 2% parasitemia, at which point knob-positive trophozoites and schizonts were isolated by ZeptoGel floatation as described in section 4.2.6. The floated pRBCs were added to 500 µl of fresh, packed uRBCs and cultured at 1% hematocrit under constant drug pressure. Once cultures reached 4-5% parasitemia, 300 µl aliquots of packed pRBCs were preserved by freezing according to section 2.2.1.

The pRBCs left in culture continued to be ZeptoGel-floated and diluted until stable growth under drug selection pressure was observed for at least 4 reinvasion cycles. Cultures were then loosely synchronized by sorbitol lysis, as described in section 2.2.1, before being ZeptoGel-floated a final time. Of the isolated knob-positive pRBCs, half were directly frozen for DNA extraction, as described in section 4.2.3, and half were returned to typical culture conditions. The extracted DNA was used to screen for the presence of the pCas9 plasmid, as described in section 4.2.3, and genotype pRBCs by amplifying and sequencing *Pf3D7_1245600* fragment 2, as described in sections 4.2.3 and 4.2.4, to monitor for any potential cross-contamination that might have occurred between HB3 and 3D7 due to culturing in well plates. Once the presence of pCas9 and the purity of the cultures was established, preliminary surface PfEMP1 level phenotypes of the transfectants were obtained by flow cytometry according to section 2.2.5, with the only exception being that FACS processed cells were analyzed on an Accuri™ C6 flow cytometer, as described in section 4.2.7.

4.2.9 Microtubule disruption assay

In addition to modifying the *Pf3D7_1245600* alleles of HB3 and 3D7 by CRISPR-Cas9 transfection, the role of the putative kinesin in PfEMP1 trafficking was indirectly assessed through the chemical manipulation of cellular microtubules. The association of kinesins with microtubules is a well-established and absolutely essential feature of virtually all cell types[467,468]. Without a microtubule network to act upon, kinesins remain inactive and are unable to fulfill their cellular transport roles[469]. By targeting microtubules with well-characterized polymerization inhibitors such as colchicine[470–472], kinesins can be indirectly rendered inactive, providing potential insights into their involvement in specific cellular processes.

A general microtubule disruption assay was developed and used with wild-type HB3 and 3D7 in 3 primary experiments (Figure 4.12). Each experiment began by first isolating schizonts preparing to reinvade within 1-2 hours by ZeptoGel floatation as described in section 4.2.6. The pRBCs were then added to 300 µl of packed uRBCs in 5 ml of complete parasite culture medium and incubated at 37°C for 2 hours. During the incubation, a 1 M solution of colchicine (Sigma C3915) in DMSO (Sigma D2650) was prepared and diluted in duplicate to a concentration of 1 mM for experiment 1 and 0.5 mM for experiments 2 and 3. All of the solutions were sterilized by passage through a 0.22 µm disk filter. After the 2 hour incubation, pRBCs were subjected to sorbitol lysis as described in section 2.2.1 to eliminate any schizonts that had yet to reinvade. The now 0-2 hour ring-stage pRBC population was resuspended in 5.7 ml of complete parasite culture medium, resulting in a 6 ml pRBC suspension at 5% hematocrit.

For experiment 1, the 1 mM colchicine solution was serially diluted 1:2 across 5 wells of a 6-well culture plate so that each well held 4 ml of colchicine-supplemented medium ranging in concentration from 1000 to 62.5 µM. The empty well was filled with 4 ml of complete parasite culture medium containing a volume of DMSO equivalent to the amount in the 1 mM colchicine well. 1 ml of the 6 ml pRBC suspension was added to each of the prepared wells, resulting in each well containing 5 ml of a 1% hematocrit pRBC suspension with colchicine concentrations of 800, 400, 200, 100, 50, and 0 µM. Plates were then placed in a culture chamber and gassed before being incubated at 37°C for 27 hours. Following the incubation, cells were harvested and processed for analysis on an Accuri™ C6 flow cytometer to determine surface PfEMP1 levels (section 2.2.5) and measure pRBC viability (section 4.2.7). All FACS data were processed as described in section 4.2.7.

For experiment 2, the 500 µM colchicine solution was diluted and added to 4 wells of a 6-well culture plate so that each well held 4 ml of colchicine-supplemented medium at concentrations of 500, 375, 250, and 125 µM. Of the 2 remaining wells, 1 was left empty while 1 was filled with 4 ml of complete parasite culture medium containing a volume of DMSO equivalent to the amount in the 500 µM colchicine well. 1 ml of the 6 ml pRBC suspension was added to each of the prepared wells, resulting in each well containing 5 ml of a 1% hematocrit pRBC suspension with colchicine concentrations of 400, 300, 200, 100, and 0 µM. Plates were then placed in a culture chamber and gassed before being incubated at 37°C for 27 hours. Following this first incubation, half of the cells in each well were harvested and processed for analysis on an Accuri™ C6 flow cytometer to determine surface PfEMP1 levels (section 2.2.5) and measure pRBC viability (section 4.2.7). The plates were then returned to the culture chamber and gassed before being incubated at 37°C for an additional 10 hours. Following this second incubation, the remaining cells in each well were harvested, processed, and analyzed as described above.

For experiment 3, 4 ml of the 500 µM colchicine solution were added to 2 wells of a 6-well culture plate. 4 ml of complete parasite culture medium containing a volume of DMSO equivalent to the amount in the 500 µM colchicine wells were added to 1 well. The remaining 3 wells were filled with 4 ml each of complete parasite culture medium. 1 ml of the 6 ml pRBC suspension was added to each of the prepared wells, resulting in each well containing 5 ml of a 1% hematocrit pRBC suspension, half of which also contained colchicine concentrations of 400 and 0 µM. Plates were then placed in a culture chamber and gassed before being incubated at 37°C for 6 hours. Following this first incubation, cells from 1 of the 400 µM colchicine wells, the DMSO well, and 2 of the untreated wells were transferred to 15 ml Falcon® tubes and pelleted by centrifugation at 1800 rpm for 5 minutes.

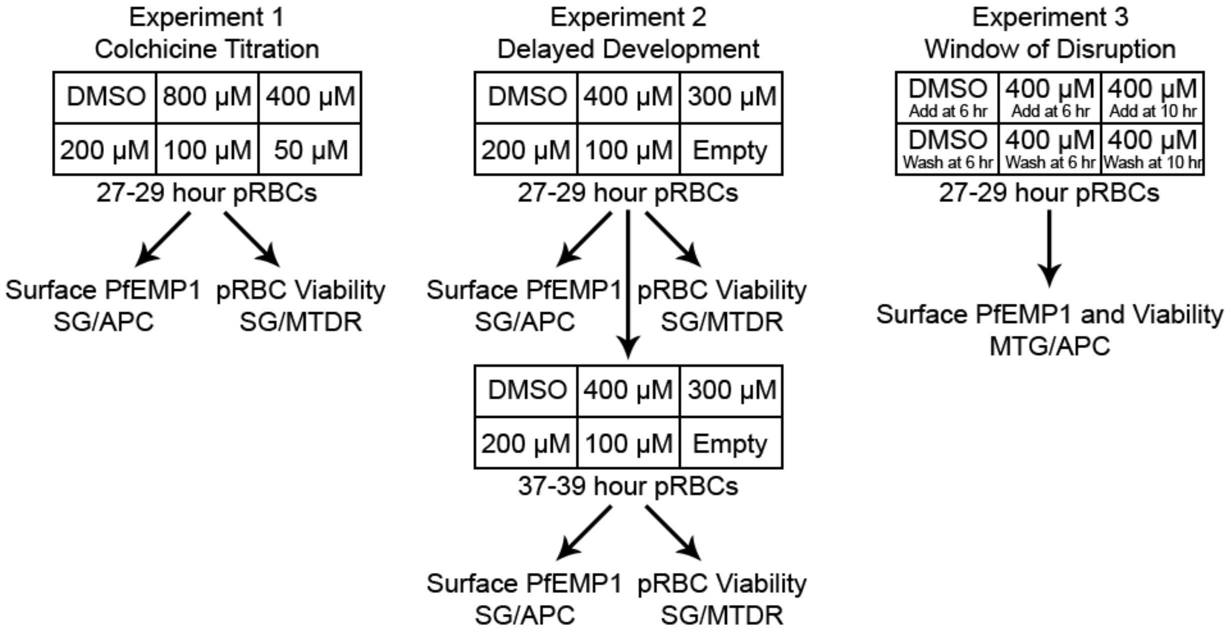

Figure 4.12: Schematic of microtubule disruption assay experiments. For each experiment, HB3 and 3D7 were cultured in individual 6-well plates in the presence of colchicine or DMSO. Experiment 1 established the range of colchicine most effectively impacting surface-displayed PfEMP1 levels. Experiment 2 used this narrowed range to examine the effect of colchicine on parasites that were incubated for an additional 10 hours in the presence of the drug. Experiment 3 used the highest concentration from experiment 2 to determine the effects of both removing colchicine from the medium and adding colchicine to the medium after 6 and 10 hours. Parasites from experiments 1 and 2 were analyzed for surface PfEMP1 levels and pRBC viability separately by FACS as described in sections 2.2.5 and 4.2.7. Parasites from experiment 3 were analyzed for surface PfEMP1 levels and pRBC viability simultaneously by FACS using a method modified from section 2.2.5, where the viability dye MTG was substituted in for SG.

After removing the supernatants, each sample was washed once by being resuspended in 5 ml of drug-free complete parasite culture medium and centrifuged again. The cells from the 400 µM colchicine and DMSO wells were resuspended in 5 ml of drug-free complete parasite culture medium and returned to the 6-well plate. The cells from the untreated wells were resuspended in 5 ml of either 400 µM colchicine-supplemented medium or medium supplemented with an equivalent volume of DMSO and returned to the 6-well plate. Plates were then returned to the culture chamber and gassed before being incubated at 37°C for 4 hours. Following this second incubation, the above washing process was repeated for the original 400 µM colchicine and untreated wells that were not disturbed after 6 hours. The washed cells from the 400 µM colchicine well were resuspended in 5 ml of drug-free complete parasite culture medium and returned to the 6-well plate. The washed cells from the untreated well were resuspended in 5 ml of 400 µM colchicine-supplemented medium and returned to the 6-well plate. Plates were then returned to the culture chamber and gassed before being incubated at 37°C for 17 hours. Following this final incubation, cells were harvested and processed for analysis on an Accuri™ C6 flow cytometer to simultaneously determine surface PfEMP1 levels and pRBC viability. This hybrid FACS preparation method followed the protocol described in section 2.2.5, with the only exception being that the DNA dye SG was replaced with the viability dye MTG. Since a final sample concentration of 0.3 µM was determined to be optimal for MTDR staining, the same final sample concentration was used for MTG staining. All FACS data were processed as described in section 4.2.7.

4.3 Results

4.3.1 *Pf3D7_1245600* sequence variation

To begin addressing the primary aim of establishing a causal relationship between *Pf3D7_1245600* and pRBC surface PfEMP1 levels, DNA sequences for the individual HB3 and 3D7 alleles first needed to be obtained and aligned in order to verify the presence of the previously known SNP between HB3 and 3D7 (section 3.3.2). The entire gene was successfully PCR-amplified in 6 overlapping fragments, as shown in Figure 4.1 D, and sequenced. The alignment of the resulting HB3 and 3D7 consensus DNA sequences, shown in Figure 4.13, verified the expected SNP at alignment position 4078 and revealed the presence of an additional 12 unexpected SNPs clustered between alignment positions 1560 and 1585, spanning 10 codons. Furthermore, 5 indels ranging in size from 3 to 12 bp were spaced throughout the gene in regions with highly repetitive sequences. Taking these into account, the total length of the HB3 allele became 4830 bp, 12 bp longer than the 3D7 allele. Translating the aligned DNA sequences into aligned protein sequences (Figure 4.14) verified the expected Q to K change at alignment position 1360 and further revealed that, between alignment positions 520 and 530, 6 of the 10 codons in the SNP cluster underwent non-synonymous changes. Interestingly, none of the SNPs or indels occurred in regions predicted to be highly conserved based on sequence homology with the KISc-type kinesin motor domain described in section 3.3.2.

4.3.2 CRISPR-Cas9-driven allele-exchange in HB3 and 3D7

Using the full DNA sequences of the HB3 and 3D7 alleles of *Pf3D7_1245600* described in section 4.3.1, the feasibility of CRISPR-Cas9-driven allele-exchange was assessed. Both alleles were first examined for any occurrence of the *S. pyogenes* Cas9 endonuclease PAM recognition sequence ‘NGG’. The selected site, shown in Figure 4.13,

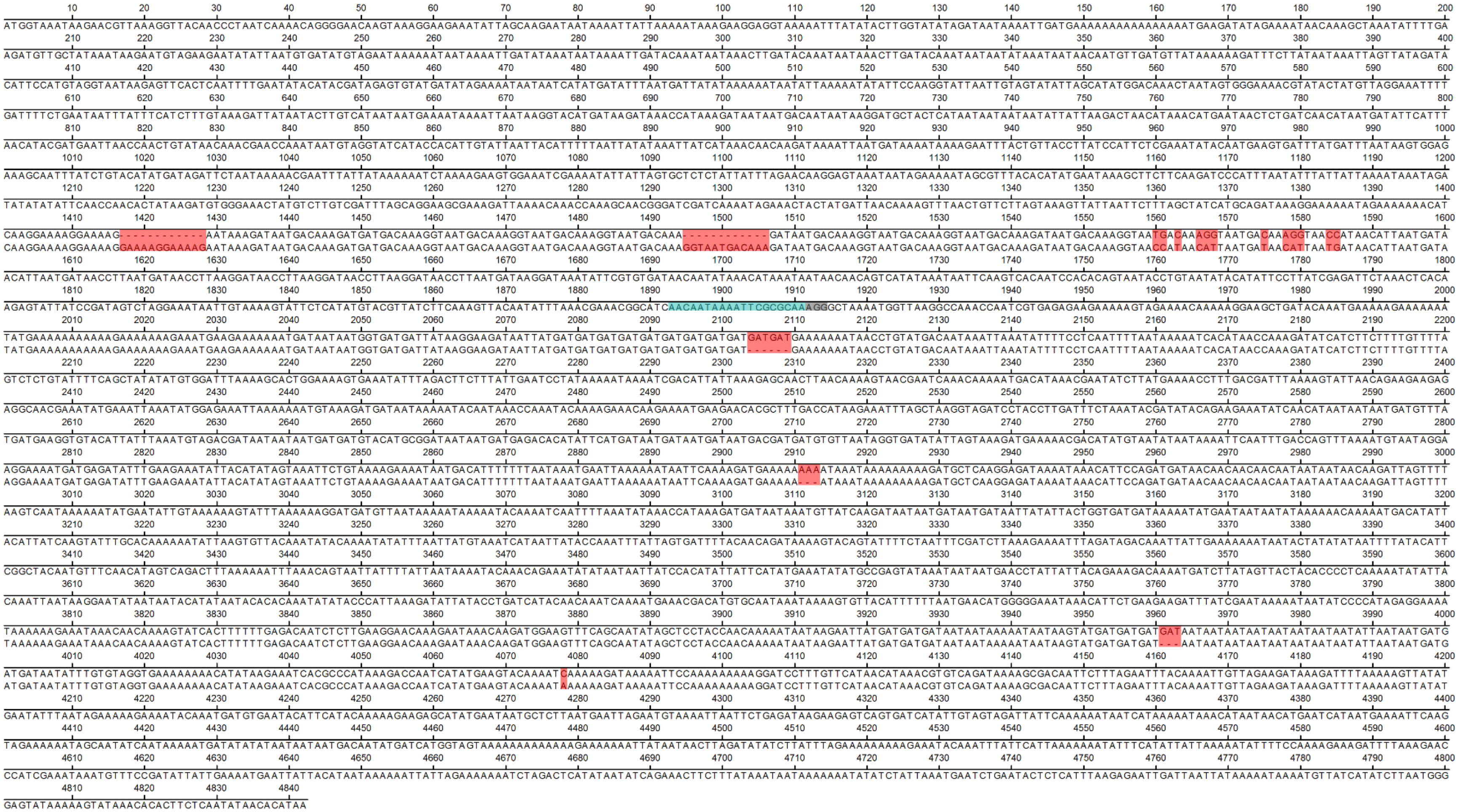

Figure 4.13: CLUSTAL W alignment of consensus HB3 and 3D7 *Pf3D7_1245600* DNA sequences. Aligned sequences are shown as a single consensus sequence when no mutations are present and as stacked 3D7 (top line) and HB3 (bottom line) sequences when differences (red) are present. The SNP at position 4078 had been previously identified, but the remaining SNPs and indels have not been reported. The CRISPR-Cas9 target RNA sequence (cyan) and PAM site (gray) were selected based on allelic sequence identity and proximity to sites of sequence difference.

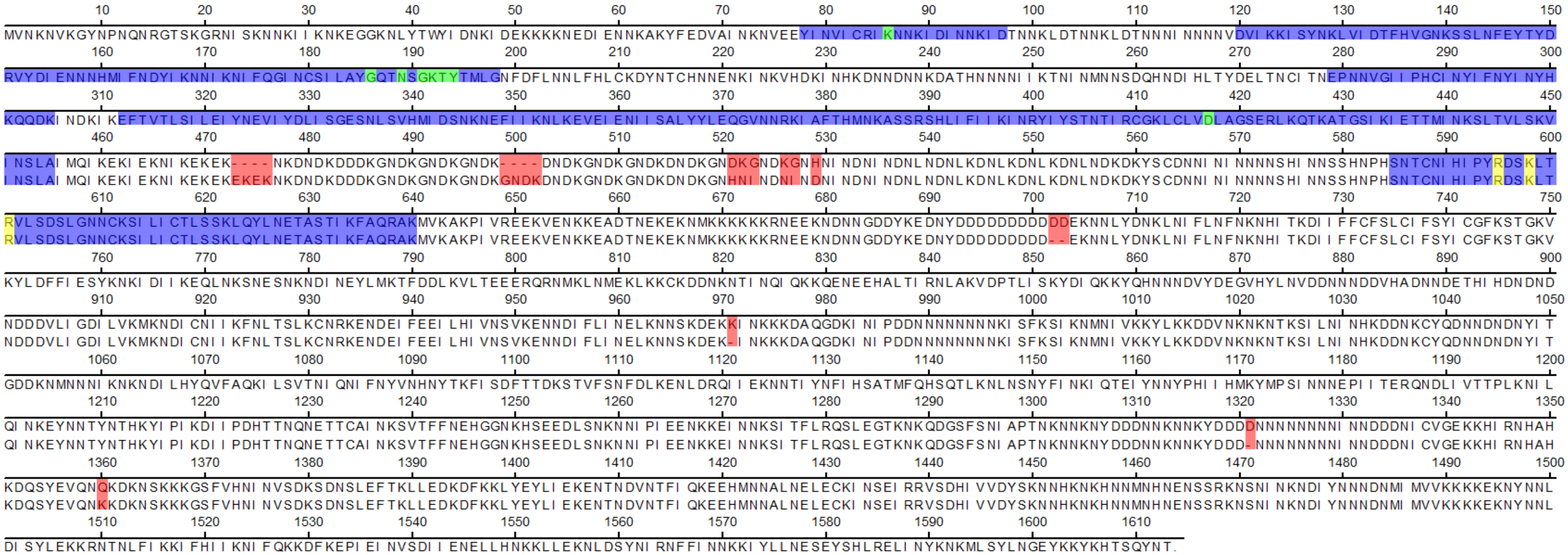

Figure 4.14: CLUSTAL W alignment of translated consensus HB3 and 3D7 *Pf3D7_1245600* DNA sequences. Aligned sequences are shown as a single consensus sequence when no mutations are present and as stacked 3D7 (top line) and HB3 (bottom line) sequences when differences (red) are present. Regions of sequence homology with the KISc-type kinesin motor domain are shown in blue. Residues predicted to be involved in the ATP hydrolysis active site are shown in green, and residues predicted to be involved in microtubule recognition and binding are shown in yellow. The non-synonymous change at position 1360 had been previously identified, but the remaining changes have not been reported.

met the criteria of being conserved between the 2 alleles and being as close as possible to the sites of sequence difference. To determine how specific the 19 bp target sequence immediately before the PAM site was to *Pf3D7_1245600*, a BLAST search (section 4.2.3) was performed against the entire *P. falciparum* reference genome using the full target sequence and adjacent PAM site. The E-value of 2×10^{-5} for *Pf3D7_1245600* was significantly smaller than the second highest E-value of 0.9 for a 14 bp site on chromosome 8. Furthermore, all of the non-specific BLAST results were predicted to bind only the 5' end of the target sequence and not the 3' PAM site, suggesting that non-specific cutting by would be extremely unlikely.

With a highly-specific, well-positioned Cas9 target sequence selected, the guide RNA needed to be amplified and fused into the pCGT plasmid prior to the insertion of any repair template sequences since each different repair template would utilize the same guide RNA sequence. The 209 bp guide RNA insert was successfully PCR-amplified (Figure 4.15 A) and fused into the pCGT vector backbone. Transformed *E. coli* were PCR-screened for a 708 bp fragment inclusive of the guide RNA insert (Figure 4.15 B), and any positive colonies were sent for sequence confirmation (Figure 4.15 C). Once the sequence had been confirmed, a single screened colony was expanded for 3 DNA miniprep extractions in order to obtain all of the pCGT + guide RNA plasmid necessary for further use.

Following the sequence confirmation of the pCGT + guide RNA plasmid, the *Pf3D7_1245600* repair template needed to be designed, amplified, and inserted into the vector. The full sequence alignment shown in Figure 4.13 was used to design a repair template containing all of the sequence differences identified between the HB3 and 3D7 alleles. Since the distance from the first indel at position 1417 to the last SNP at position 4078 spanned over 2500 bp, an allele-exchange strategy utilizing multiple repair templates was pursued. 3 templates of varying sizes containing various sequence differences were designed (Figure 4.2) to maximize the likelihood that the pCGT plasmid would be stably

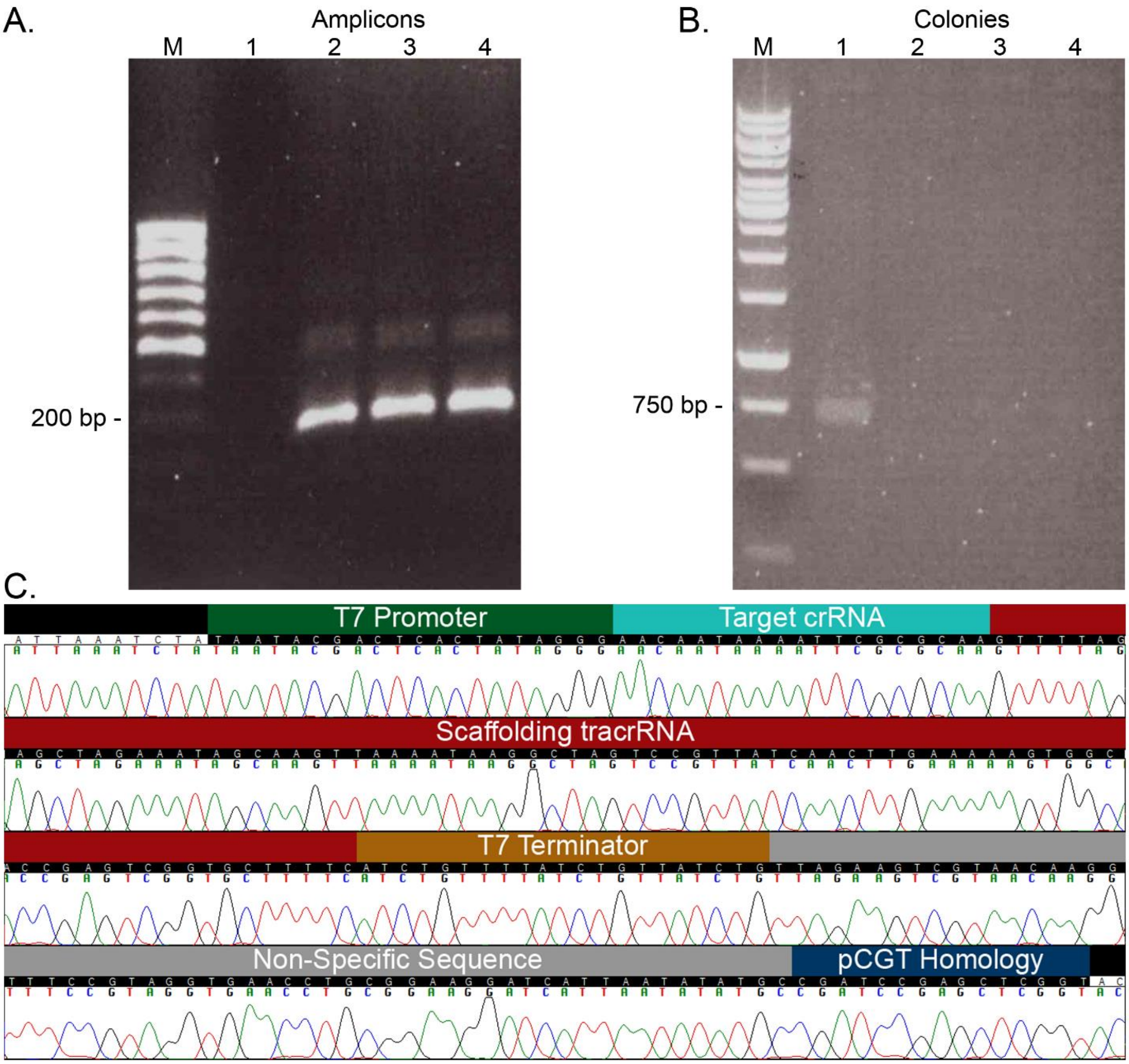

Figure 4.15: Amplification, screening, and sequencing of the pCGT guide RNA insert. The pCGT guide RNA was PCR-amplified (A) and size separated on an agarose gel (lanes 2-4) along with a DNA size marker (M) and a PCR contamination control (lane 1). After extracting the product, fusing it into the pCGT vector, and transforming *E. coli*, ampicillin-resistant colonies were PCR-screened (B) for the presence of the plasmid containing the insert (lanes 1-4) The clearly positive colony in lane 1 was sequenced (C) to confirm that the guide RNA had been correctly amplified and integrated. Regions are color-coded according to the schematic in Figure 4.4.

maintained and that the sequence differences would be successfully incorporated into the endogenous locus. Furthermore, each template was designed so that the target RNA and PAM site would contain 3 synonymous SNPs, effectively preventing Cas9 from cutting the pCGT plasmid or the repaired endogenous locus. Each repair template was successfully amplified in 2 fragments (Figure 4.16 A), fused together using the In-Fusion® system, and PCR-amplified as a single fragment (Figure 4.16 B). The single fragments were then fused into the pCGT + guide RNA vector and transformed into *E. coli*. Ampicillin-resistant colonies were PCR-screened for a 567 bp product (Figure 4.16 C), and any positive colonies were sent for sequence confirmation.

While the pCGT plasmids from each sequenced colony contained the 3 introduced synonymous SNPs (Figure 4.17), the overall accuracy of repair template replication varied among colonies (Figure 4.18). Omitted and added bases were frequently seen in the first colonies sequenced, ultimately leading to the sequencing of every FR1 colony, 4 FR2 colonies per parasite line, and every FR3 colony to find accurately replicated plasmids. For each of the 6 pCGT plasmids, a single colony containing the correct repair template sequence was identified and expanded to use as the source of the plasmids for transfection.

With large amounts of both the sequenced pCGT plasmids and the previously sequenced pCas9 plasmid, parasite transfection experiments could be initiated. Isolated wild-type HB3 and 3D7 pRBCs on the verge of reinvasion were added to transfected uRBCs (Figure 4.19 A) and monitored by Giemsa-stained thin smear for several hours afterward (Figure 4.19 B). Thin smears prepared the week following transfection showed significant amounts of debris and high gametocytemias in all transfectant cultures but not in routine cultures maintained in parallel (Figure 4.19 C). Transfectant screening by FACS (section 4.2.7) began 15 days after transfection and occurred every 10 days until either the viable parasitemia exceeded 0.5% or day 95 was reached without detecting any viable pRBCs. Drug-free and drug-supplemented cultures of HB3 and 3D7 pRBCs co-transfected with

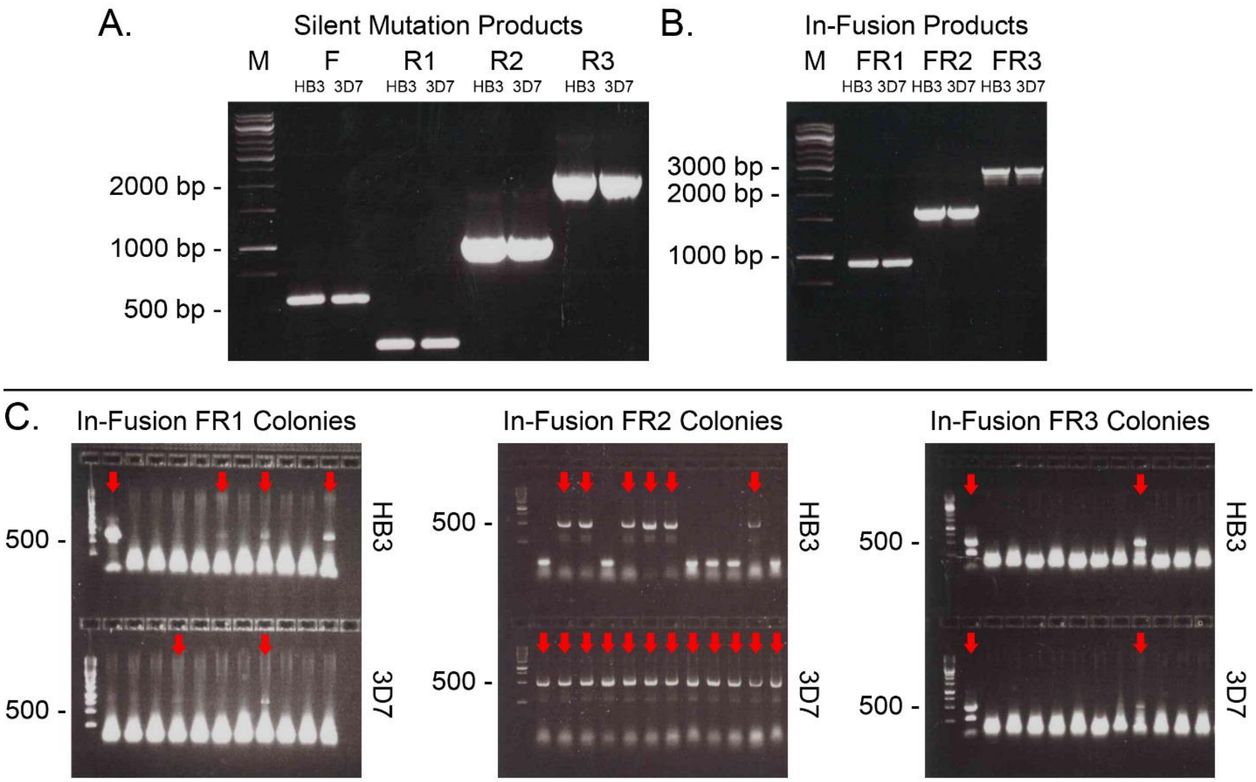

Figure 4.16: Amplification of *Pf3D7_1245600* repair templates and screening of colonies transformed with the complete pCGT plasmid. All 3 repair templates for HB3 and 3D7 were amplified in 2 separate fragments (A), a shared forward fragment and a unique reverse fragment of varying length. Each pair of fragments was fused together and amplified as a single fragment (B). Single fragments were fused into the pCGT + guide RNA plasmid and transformed into *E. coli*. Ampicillin-resistant colonies were screened for the presence of the repair template (C), and positive colonies (red arrows) were sequenced.

pCGT and pCas9 were monitored until day 95 and subsequently terminated since viable parasites were never detected in any of the culture wells. Giemsa-stained thick and thin smears were periodically prepared to manually search for parasites in case the collected FACS data were inaccurate, but the inability to find any viable parasites only further supported the validity of the FACS results. The failure to detect viable transfectants by either FACS or microscopy after 95 days of culturing suggested that the double-transfections completely failed. Without transfected, allele-exchanged parasites to phenotype and further characterize, the primary aim of this chapter, to establish a causal relationship between

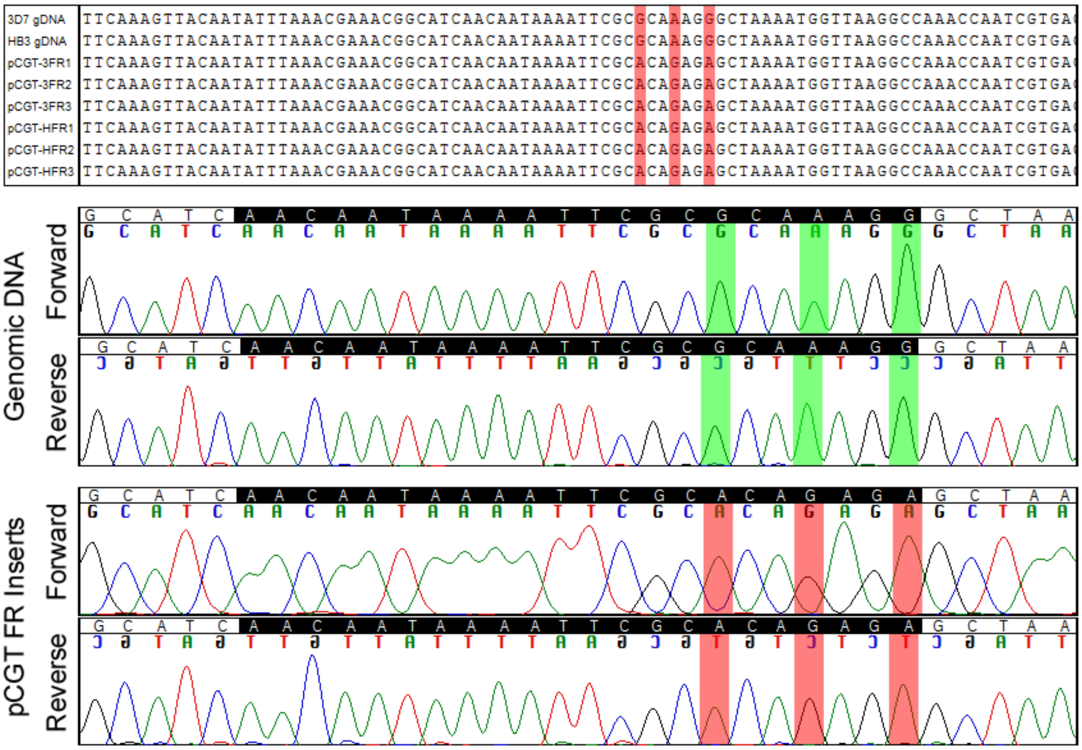

Figure 4.17: Cas9 target sequence and PAM site synonymous SNP confirmation. DNA sequences obtained for HB3, 3D7, and all 6 pCGT plasmids confirmed the presence of 3 synonymous SNPs introduced into the Cas9 target sequence and PAM site of the repair templates. For each sequence, overlapping forward and reverse reads were collected.

Pf3D7_1245600 and the trafficking of PfEMP1, could not be fulfilled.

HB3 and 3D7 pRBCs transfected with the pCas9 plasmid alone and switched to medium without WR99210 appeared 25 days after transfection (Figure 4.20 A). WR99210 was then returned to the medium at that point to eliminate any parasites that had failed to stably maintain and replicate the pCas9 plasmid. A large decrease in parasitemia was seen for both HB3 and 3D7 on day 35, though the cultures easily rebounded by day 45 (Figure 4.20 B). Transfected HB3 and 3D7 pRBCs continuously cultured in the presence of WR99210 appeared 35 days after transfection, and both had crossed the 0.5% viable parasitemia threshold by day 45. After expansion and several subsequent reinvasion cycles under constant drug pressure, both HB3 transfectant cultures were combined and both 3D7

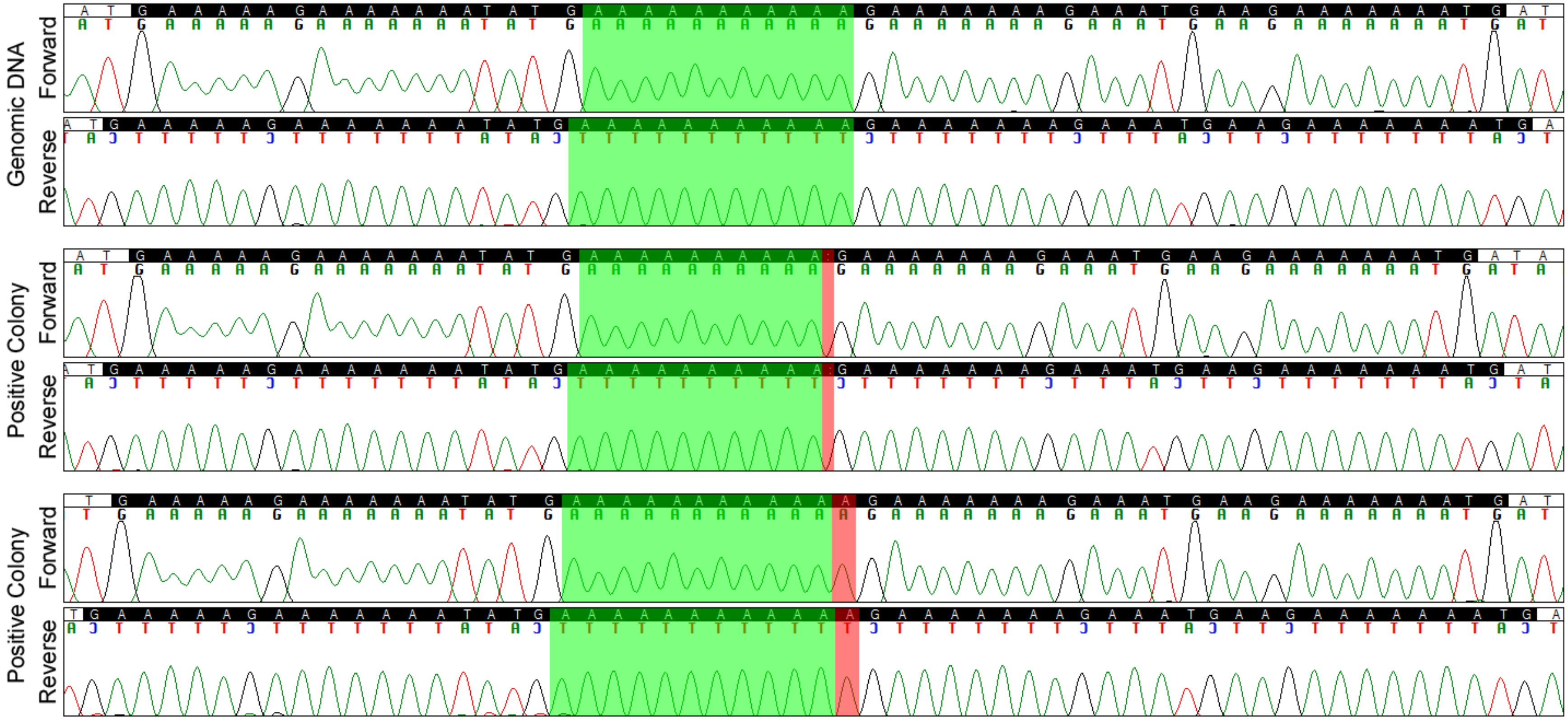

Figure 4.18: pCGT repair template replication errors in transformed *E. coli*. Ampicillin-resistant bacterial colonies that had been transformed with the complete pCGT plasmid were sequenced, revealing several replication errors in the repair template sequences. In a particularly repetitive, AT-rich region (top), *E. coli* would commonly omit a base (middle) or add an extra base (bottom). The resulting frameshifted sequences would effectively knock out *Pf3D7_1245600*.

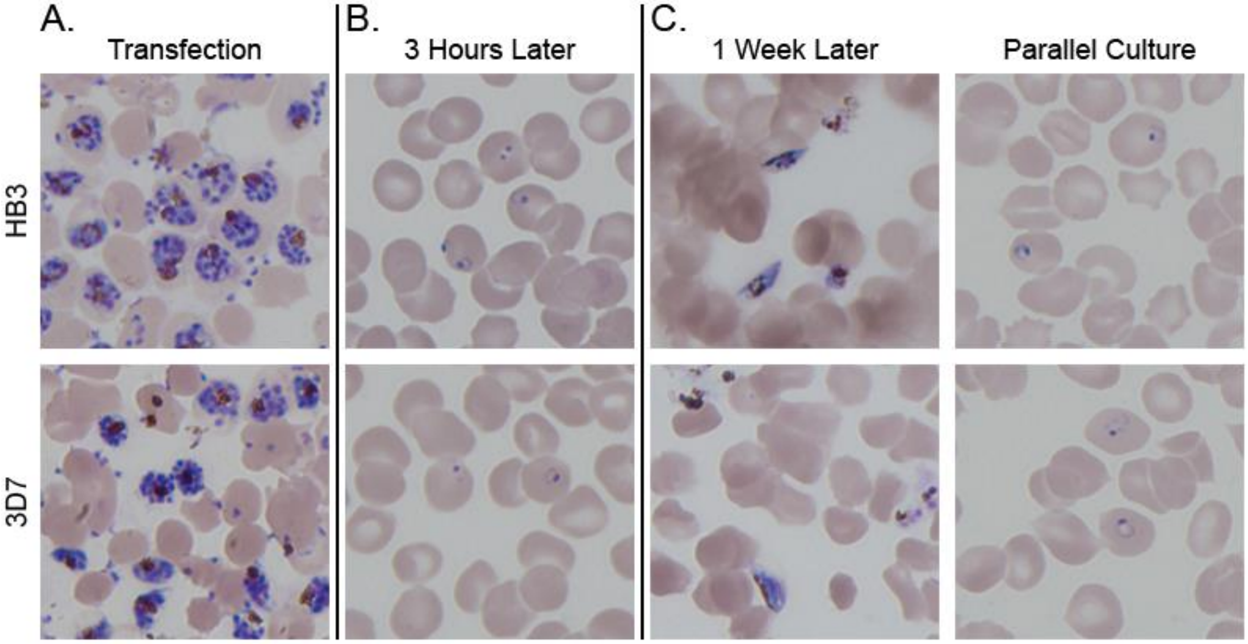

Figure 4.19: HB3 and 3D7 pRBCs examined at various early transfection time points. Isolated schizonts began reinvading soon after addition to transfected uRBCs (A). Rings appeared after 3 hours (B), indicating that reinvasion had successfully occurred. A week after transfection (C), cultures contained higher levels of debris and gametocytes compared to routine cultures maintained in parallel.

transfectant cultures were combined. Plasmid DNA was extracted from pRBCs and amplified to confirm the stable maintenance of the pCas9 plasmid (section 4.2.3). The presence of an 1181 bp fragment in both transfected parasite lines, but not in wild-type parasites, suggested that the pCas9 plasmid was being stably maintained (Figure 4.21 A). Transfectants with confirmed possession of pCas9 were analyzed by FACS (section 2.2.5) to verify the assumption that the presence of pCas9 alone would not impact the previously established surface PfEMP1 level phenotypes of HB3 and 3D7. Neither transfected parasite line showed significant changes in surface PfEMP1 levels (Figure 4.21 B).

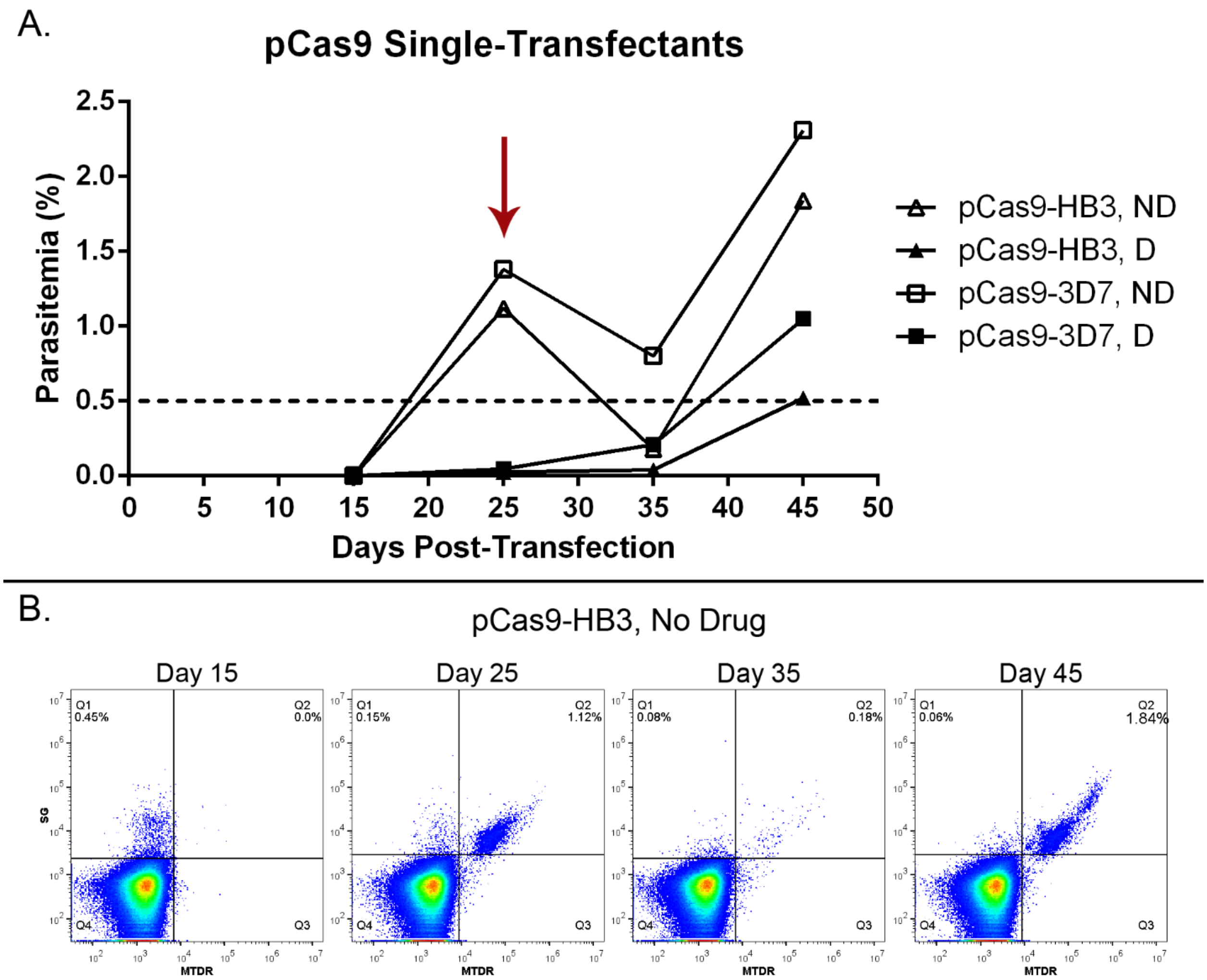

Figure 4.20: pCas9 single-transfectant screening by FACS. Parasites transfected with the pCas9 plasmid alone were monitored by FACS beginning 15 days after transfection (A). Transfectants cultured in drug-free medium (ND) appeared on day 25, so WR99210 was added back to the medium (red arrow), resulting in a drop in parasitemia. Parasites cultured in drug-supplemented medium (D) appeared on day 35. Example FACS screening results are shown for HB3 transfectants cultured in drug-free medium (B).

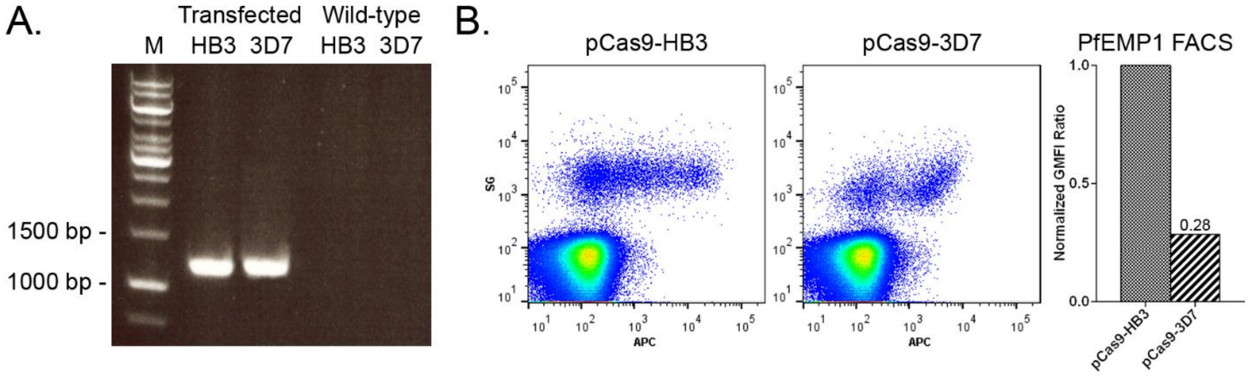

Figure 4.21: pCas9 amplification and PfEMP1 phenotyping using HB3 and 3D7 single-transfectants. An 1181 bp Cas9 gene-specific fragment was amplified from transfected, but not wild-type, HB3 and 3D7 to confirm the presence of pCas9 (A). The surface PfEMP1 levels of transfected parasites (B) suggested that pCas9 had no impact on the original parental phenotypes.

4.3.3 Microtubule disruption and surface PfEMP1 levels

Though *Pf3D7_1245600* could not be directly implicated in the trafficking of PfEMP1 to the pRBC surface due to the failure of the 2-plasmid transfections, the broader involvement of kinesins could be indirectly assessed through the disruption of microtubules. Colchicine potently inhibits the polymerization of microtubules by binding to the site of interaction between α- and β-tubulin subunits, effectively blocking their association. Titrating colchicine against wild-type HB3 and 3D7 pRBCs (section 4.2.9) resulted in a dose-dependent decrease in PfEMP1 expression in HB3 but not 3D7, with the most pronounced effect being seen at a colchicine concentration of 800 µM (Figure 4.22 A). The viability of parasites in the presence of colchicine was assessed by FACS (Figure 4.22 B), and the resulting data showed that both parasite lines remained largely viable even at the 800 µM concentration. However, the altered distributions of the viable parasite populations, combined with the dose-dependent decreases in the SG and APC GMFIs of normalized colchicine-treated plasma-positive parasites (Figured 4.22 C), suggested that colchicine was impairing parasite development and PfEMP1 display.

To further explore the potentially delayed development of colchicine-treated parasites, a second experiment was performed (section 4.2.9) using colchicine concentrations ranging from 0 to 400 µM and multiple sampling time points. Giemsa-stained thin smears prepared at 0-2 hour, 27-29 hour, and 37-39 hour time points showed a clear dose-dependent delay in parasite growth for both HB3 (Figure 4.23 A) and 3D7 (Figure 4.24 B), though the effects of colchicine were more pronounced in HB3. The impact of colchicine on parasite growth was further quantified using the FACS viability assay, confirming the observations made by microscopy (Figures 4.23 B and 4.24 B). Surprisingly, only the viability of HB3 parasites appeared to be impacted by the presence of colchicine, indicating that 3D7 may possess a higher tolerance for the drug.

The observation that colchicine delays parasite growth, combined with the fact that surface PfEMP1 levels do not saturate until approximately 24 hours after invasion, prompted an examination of surface PfEMP1 levels at the 27-29 hour and 37-39 hour time points to determine if the amount of surface PfEMP1 would eventually reach previously observed levels in the presence of colchicine. As seen in Figure 4.22 A, the surface PfEMP1 levels of HB3 parasites, but not 3D7 parasites, at the 27-29 hour time point were greatly affected by the presence of colchicine (Figure 4.25). After an additional 10 hours of incubation, increases in the number of plasma-positive parasites and the APC signal intensity of the population were observed for each colchicine-treated HB3 culture, but levels were still lower than those observed for the untreated control.

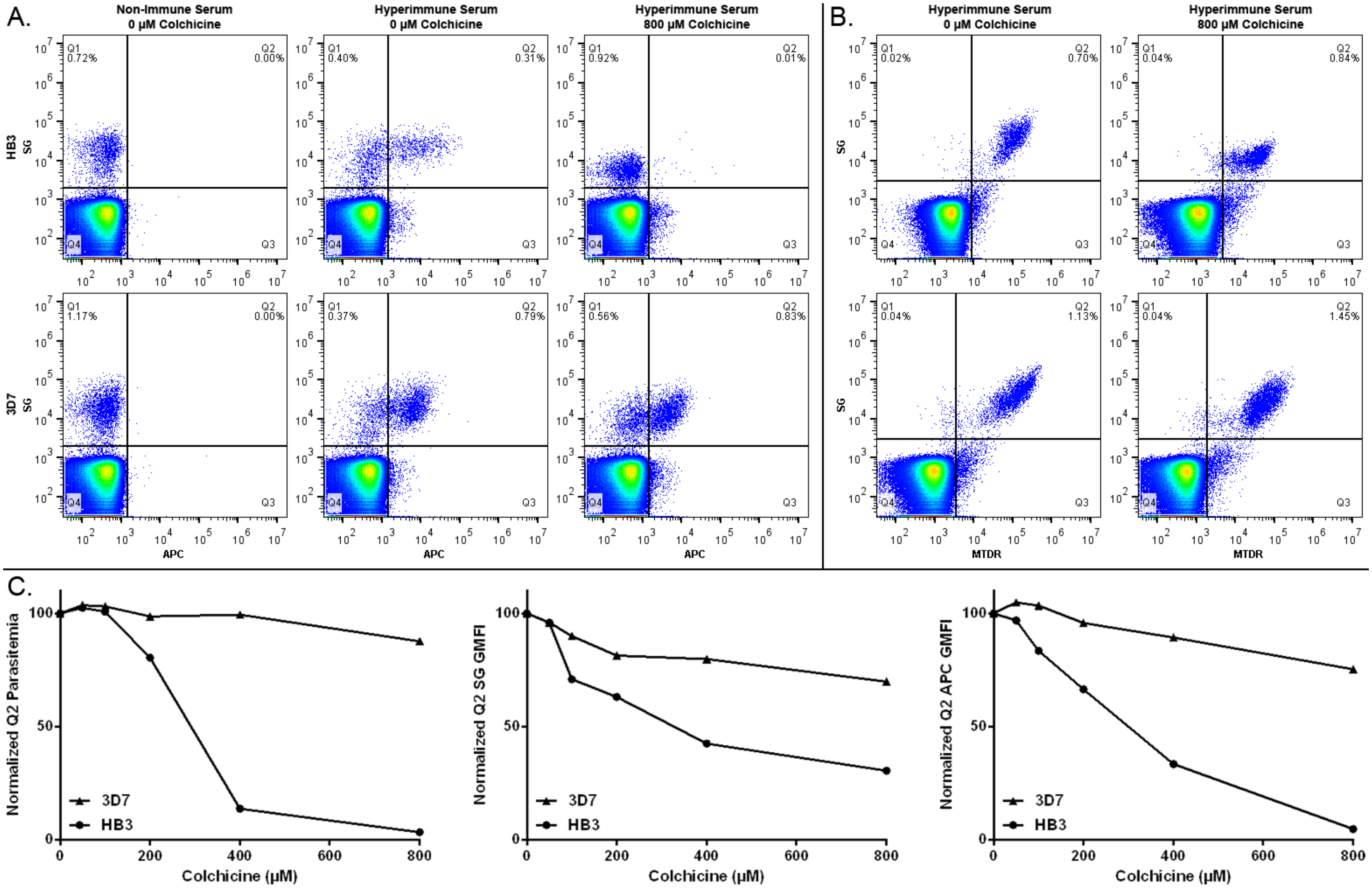A.
Non-Immune Serum
0 µM Colchicine
Hyperimmune Serum
0 µM Colchicine
Hyperimmune Serum
800 µM Colchicine
HB3
SG
3D7
SG
APC
Q1 0.72%
Q2 0.00%
Q1 0.40%
Q2 0.31%
Q1 0.92%
Q2 0.01%
Q1 1.17%
Q2 0.00%
Q1 0.37%
Q2 0.79%
Q1 0.56%
Q2 0.83%
Q3
Q4
B.
Hyperimmune Serum
0 µM Colchicine
Hyperimmune Serum
800 µM Colchicine
SG
MTDR
Q1 0.02%
Q2 0.70%
Q1 0.04%
Q2 0.84%
Q1 0.04%
Q2 1.13%
Q1 0.04%
Q2 1.45%
C.
Normalized Q2 Parasitemia
Normalized Q2 SG GMFI
Normalized Q2 APC GMFI
Colchicine (µM)
3D7
HB3
0
50
100
200
400
600
800

Figure 4.22 *(left)*: Effects of colchicine on surface PfEMP1 levels and pRBC viability of wild-type HB3 and 3D7 parasites. Untreated and colchicine-treated pRBCs were analyzed by FACS for surface PfEMP1 levels (A) and parasite viability (B). 800 µM colchicine produced a striking ablation of the plasma-positive population in HB3 but not 3D7, though both populations remained viable. The plasma-positive population in Q2 of each colchicine-treated sample was quantified and normalized to untreated controls (C) to observe the effects of colchicine on the number of plasma-positive parasites, the SG GMFI, and the APC GMFI. For each parameter, HB3 parasites were more affected by colchicine than 3D7 parasites.

Having confirmed that colchicine strongly reduces surface PfEMP1 levels in wild-type HB3 parasites, a final experiment was conducted (section 4.2.9) to establish a window of activity for colchicine since PfEMP1 transcription, translation, or trafficking could be specifically affected. Parasites exposed to 400 µM colchicine immediately after reinvasion for 6 or 10 hours would experience disrupted transcription and translation, but not trafficking, of PfEMP1. Parasites exposed to 400 µM colchicine after 6 or 10 hours of growth would experience disrupted trafficking, but not transcription or translation, of PfEMP1. Wild-type HB3 parasites (Figure 4.26) initially exposed to colchicine for 6 hours possessed surface PfEMP1 levels similar to the untreated control, while those exposed to colchicine for 10 hours possessed slightly decreased levels. HB3 parasites exposed to colchicine after 6 hours of growth possessed very low levels of surface PfEMP1, while those exposed to colchicine after 10 hours possessed levels similar to parasites that were only exposed to colchicine for an initial 10 hours. Giemsa-stained thin smears prepared from each FACS sample once again demonstrated that colchicine stunts the growth of HB3 parasites. Wild-type 3D7 parasites (Figure 4.27), regardless of the duration of 400 µM colchicine presence, showed virtually no changes in surface PfEMP1 levels. Giemsa-stained thin smears prepared from each FACS sample showed slight developmental delays due to colchicine.

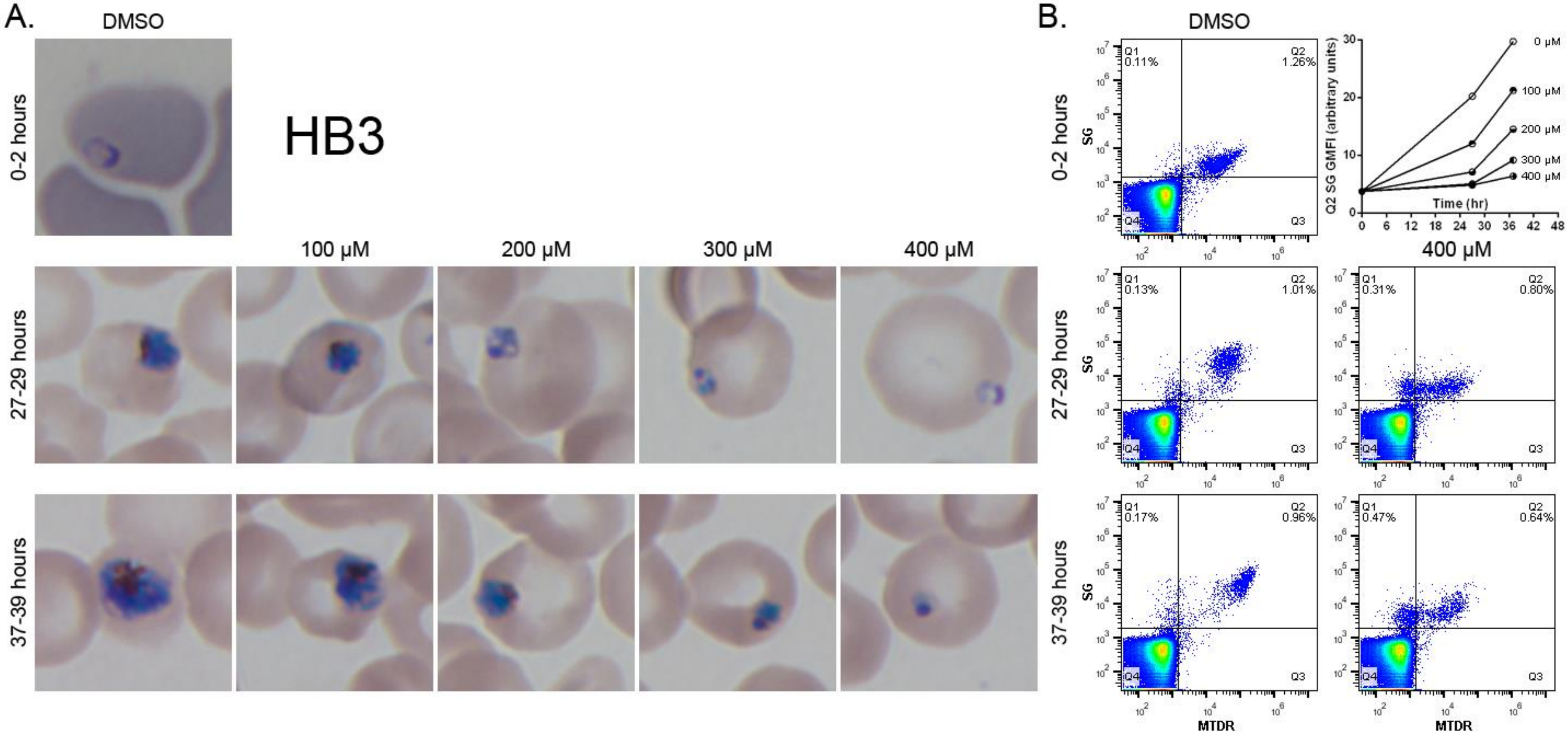

Figure 4.23: Effects of colchicine on wild-type HB3 parasite development and viability. Giemsa-stained thin smears prepared at 3 different time points (A) clearly showed a delayed growth effect with increasing concentrations of colchicine. The effect was quantified using the FACS viability assay (B), confirming that parasite development was strongly stunted due to the presence of colchicine. The increases seen in the SG GMFIs of viable parasites across time points showed that parasite growth was only delayed, not completely arrested. Even after 37 hours in the presence of colchicine, some parasites remained viable.

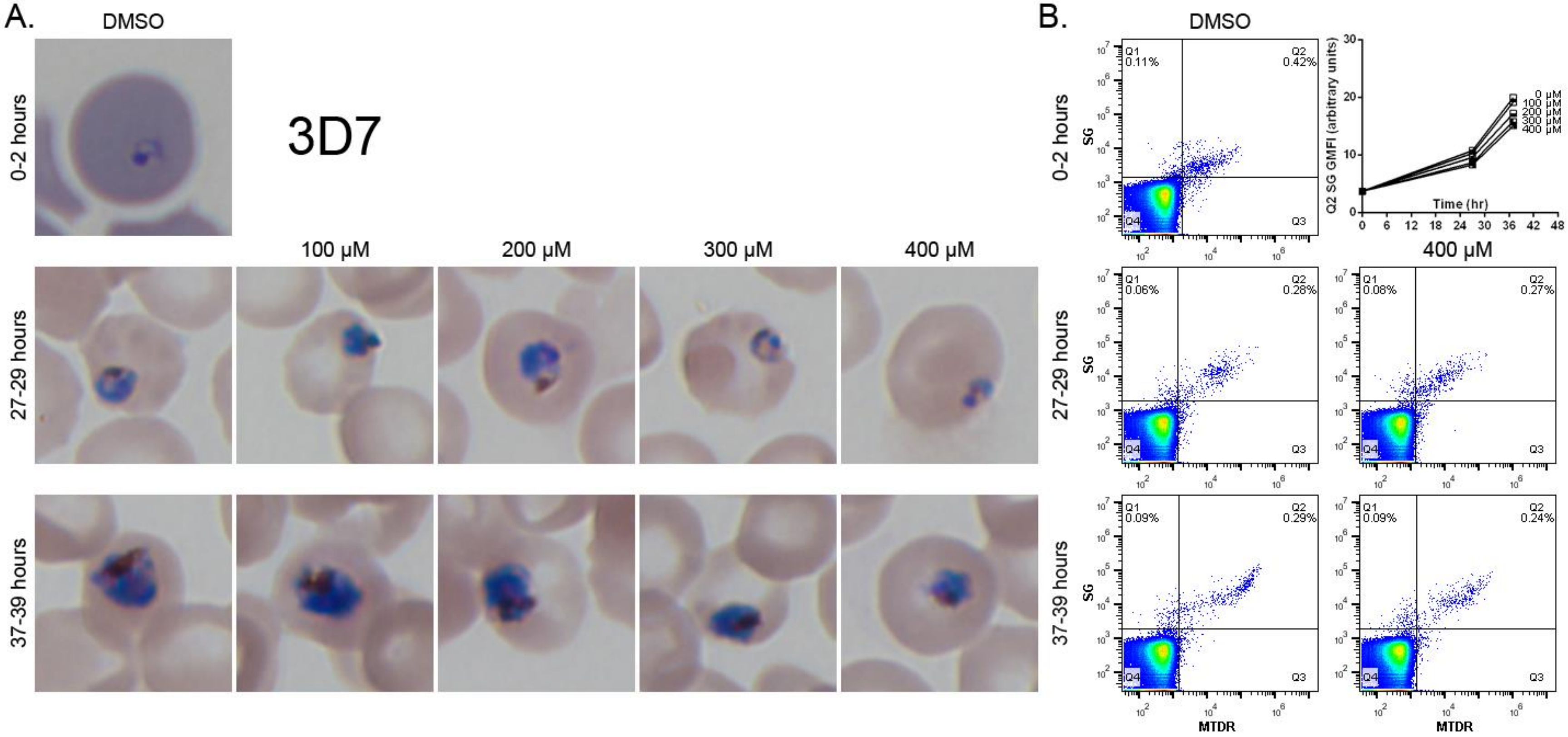

Figure 4.24: Effects of colchicine on wild-type 3D7 parasite development and viability. Giemsa-stained thin smears prepared at 3 different time points (A) clearly showed a delayed growth effect with increasing concentrations of colchicine. The effect was quantified using the FACS viability assay (B), confirming that parasite development was only slightly stunted due to the presence of colchicine. The increases seen in the SG GMFIs of viable parasites across time points showed that parasite growth was only delayed, not completely arrested. Even after 37 hours in the presence of colchicine, most parasites remained viable.

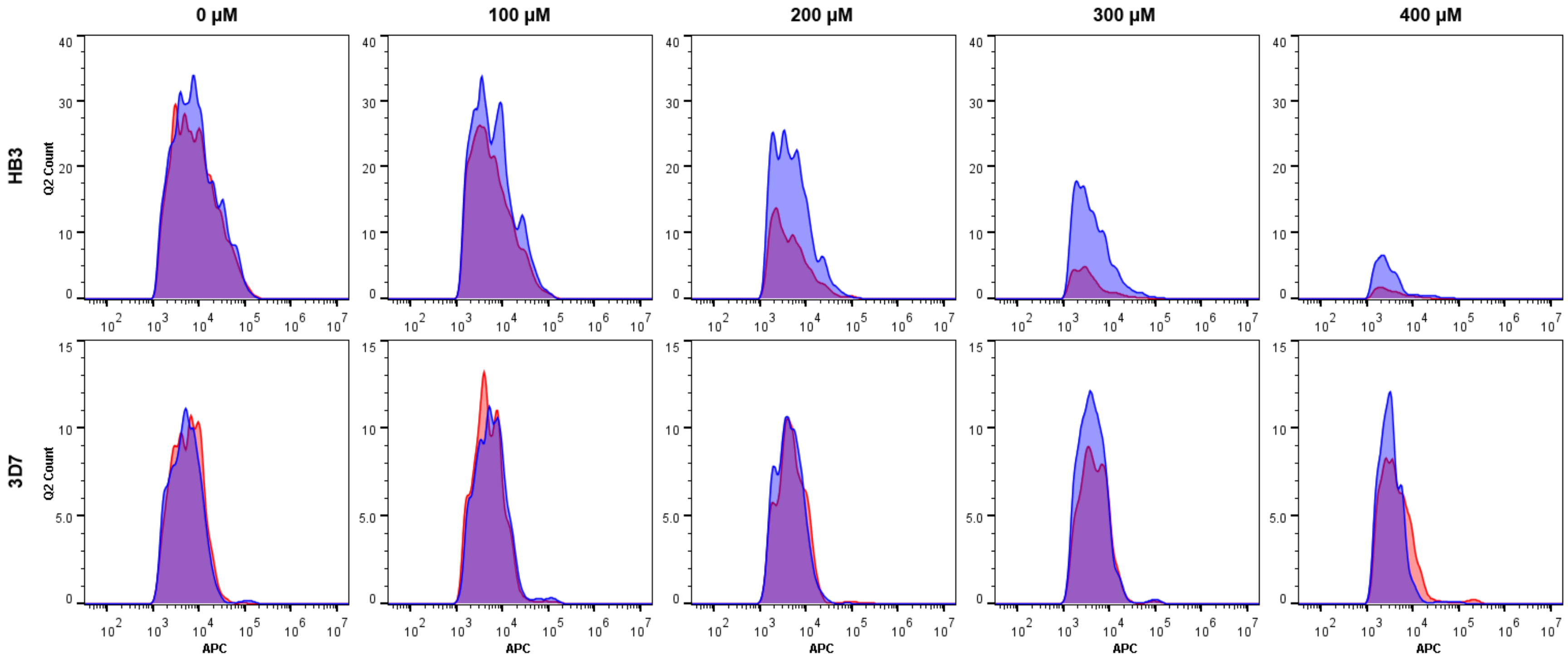

Figure 4.25: Surface PfEMP1 levels of colchicine-treated, plasma-positive parasites measured at 27-29 and 37-39 hours after invasion. Wild-type HB3 and 3D7 parasites cultured in the presence of varying concentrations of colchicine were analyzed by FACS at 27-29 hour (red) and 37-39 hour (blue) time points to observe changes in surface PfEMP1 levels. 3D7 parasites were largely unaffected by colchicine at the 27-29 hour time point, but slight increases in surface PfEMP1 levels were seen in the 300 and 400 µM cultures at the 37-39 hour time point. HB3 parasites were significantly affected by colchicine at both time points, though an increase in surface PfEMP1 levels was observed in each colchicine-treated culture at the 37-39 hour time point.

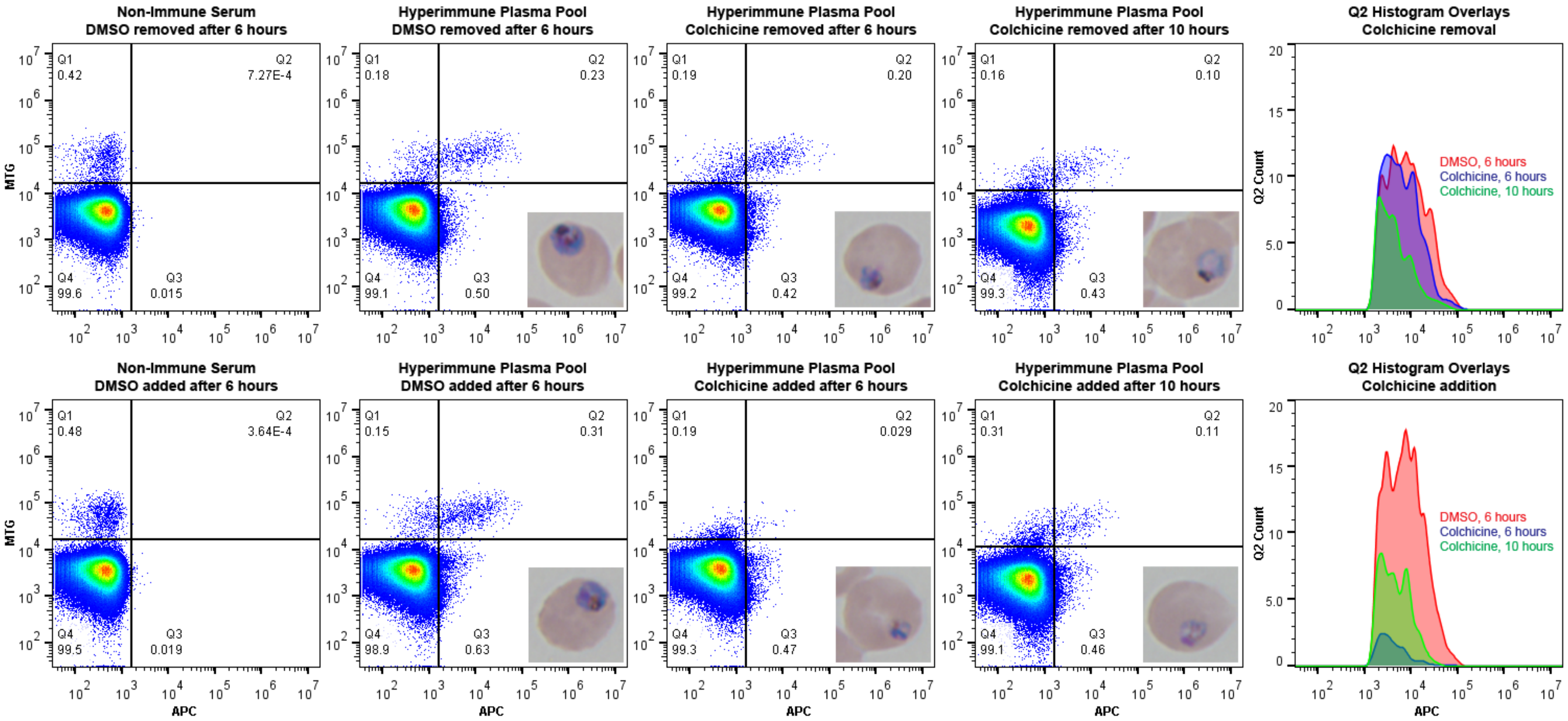

Figure 4.26: FACS analysis of wild-type 27-29 hour-old HB3 trophozoites exposed to 400 µM colchicine for various durations. Surface PfEMP1 levels were determined for viable parasites to establish a window of activity for colchicine. Scatterplots and Q2 histogram overlays showed that parasites initially exposed to colchicine still display PfEMP1 on the pRBC surface, though parasites exposed to colchicine after 6, but not 10, hours of growth display very little PfEMP1 on the pRBC surface.

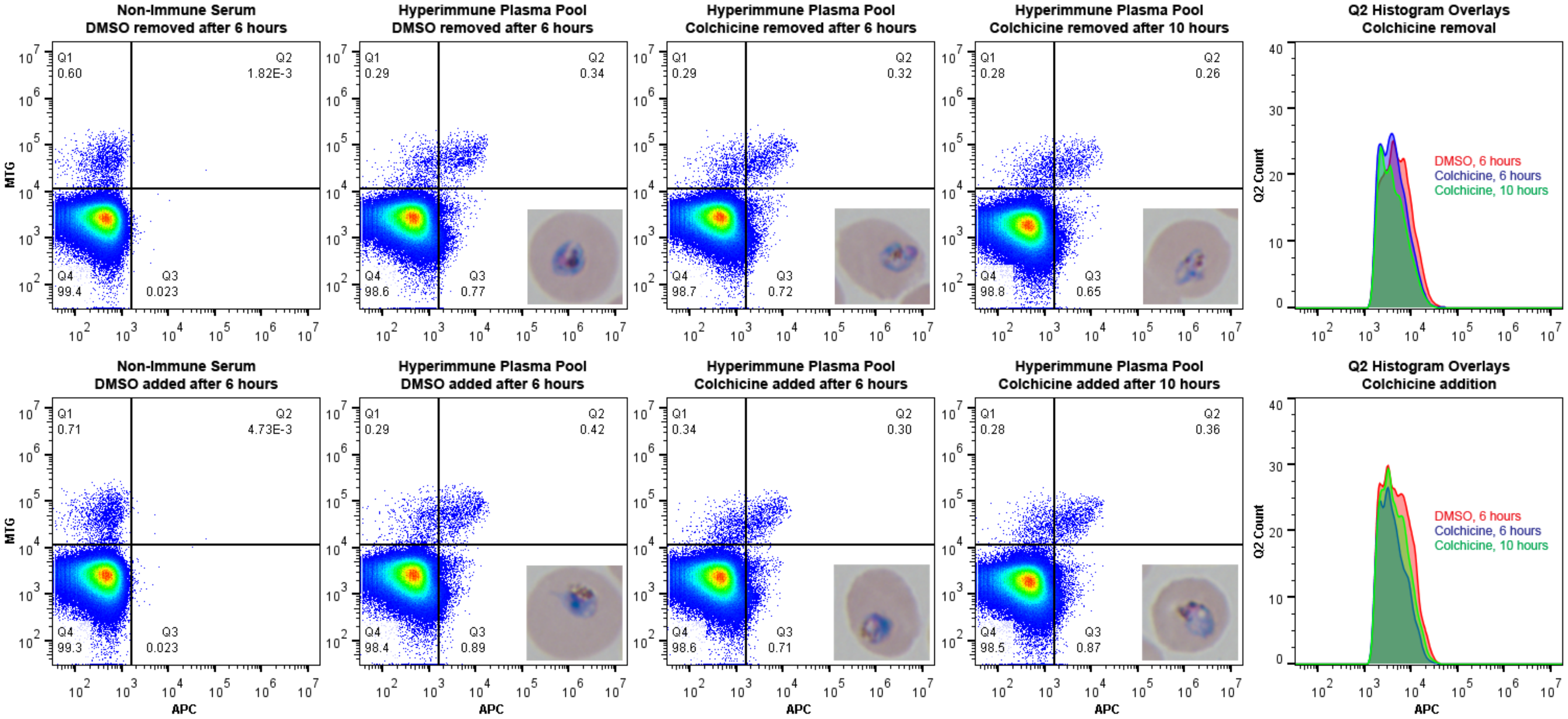

Figure 4.27: FACS analysis of wild-type 27-29 hour-old 3D7 trophozoites exposed to 400 µM colchicine for various durations. Surface PfEMP1 levels were determined for viable parasites to establish a window of activity for colchicine. Scatterplots and Q2 histogram overlays showed that all parasites, regardless of timing or duration of colchicine exposure, possess surface PfEMP1 levels similar to those of untreated control parasites.

4.4 Discussion

The primary aim of this chapter was to establish a causal relationship between the candidate gene *Pf3D7_1245600* and the trafficking of PfEMP1 to the pRBC surface. To begin addressing this aim, full DNA sequences were obtained for the HB3 and 3D7 alleles of the gene to investigate the possibility that a genetic polymorphism accounts for the differences in observed surface PfEMP1 levels. Individual sequences were obtained from 6 overlapping PCR amplicons spanning the entirety of *Pf3D7_1245600* (Figure 4.1), assembled using the homologous ends, and aligned to the 3D7 reference genome to identify any sequence differences between HB3 and 3D7 (Figure 4.13). The previously known SNP at genomic position MAL12:1901003, or alignment position 4078, was identified in addition to 5 indels and a cluster of 12 SNPs. When translated (Figure 4.14), these sequence differences resulted in 12 added and 7 substituted amino acid residues. Though none of these changes occurred in highly conserved regions predicted to be essential for kinesin function, the unexpected level of sequence difference between HB3 and 3D7 made *Pf3D7_1245600* an even more promising candidate for identifying the genetic determinant of impaired PfEMP1 trafficking in 3D7.

With full sequences available, a CRISPR-Cas9-driven allele-exchange strategy (Figure 4.2) was developed to effectively reverse the previously established surface PfEMP1 level phenotypes of HB3 and 3D7. The feasibility of the CRISPR-Cas9 genome-editing approach was assessed and pursued once a highly *Pf3D7_1245600*-specific 19 bp target RNA sequence and PAM site were identified near many of the allelic differences. The target RNA sequence was successfully amplified into a guide RNA fragment containing the Cas9 scaffolding RNA, the T7 terminator sequence, and In-Fusion® homology regions for insertion into the pCGT vector just after the T7 promoter sequence (Figures 4.4 and 4.15 A). The guide RNA fragment was then successfully fused into the pCGT vector, transformed into *E. coli*, extracted, and sequence confirmed (Figure 4.15 B and C). With the guide RNA in place, the only component necessary to complete the pCGT vector was the DNA double-strand break repair template.

Since any of the identified SNPs or indels could be solely or jointly responsible for the defective PfEMP1 trafficking in 3D7, every sequence difference needed to be exchanged between the parasite lines. A 2787 bp repair template was designed to accomplish this, though its significant size led to the development of 1611 bp and 849 bp repair templates incorporating fewer sequence differences but likely increasing the probability of successful allele-exchange. Additionally, multiple repair templates containing various sequence differences would further aid in the identification of the causative feature if all of the transfections were successful. Each repair template was initially PCR-amplified in 2 fragments, fused together, and re-amplified as a single fragment in order to introduce 3 synonymous SNPs by PCR-mediated site-directed mutagenesis (Figures 4.2 and 4.16). The successful incorporation of the SNPs (Figure 4.17) ensured that the pCGT vector and template-repaired endogenous locus would not be continuously recognized and cut by the Cas9 endonuclease. Each full-length repair template was fused into the pCGT + guide RNA vector, transformed into *E. coli*, and sequence-confirmed (Figures 4.16 C and 4.18). Though there were challenges in obtaining a transformed bacterial colony that had correctly replicated the entire repair template (Figure 4.18), 1 colony for each repair template was identified and expanded to obtain the complete pCGT vector for parasite transfections.

Using a previously constructed and sequence-confirmed pCas9 vector (section 4.2.5) and the constructed pCGT vectors, uRBCs were co-transfected and supplied to reinvading HB3 and 3D7 schizonts (Figure 4.19 A). Transfectants were examined 3 hours after reinvasion (Figure 4.19 B), and the presence of early ring-stage parasites in each culture well confirmed that reinvasion into the transfected uRBCs had occurred. Furthermore, a small proportion of the transfected uRBCs likely contained both pCas9 and pCGT, providing the parasites in those cells the ability to acquire resistance to WR99210 and Geneticin®. Transfectants were placed under continuous drug pressure after 48 hours using previously published concentrations that had been additionally verified by a standard IC_{50} assay (Figure 4.6). The concentrations of Geneticin® used were roughly at the IC_{50} value for both parasites, while the concentration of WR99210 used was at the IC_{50} value of 3D7 and the IC_{90} value of HB3. Even though HB3 parasites were more sensitive to WR99210, the expression of the human dihydrofolate reductase enzyme supplied by pCas9 would provide a 1000-fold increase in resistance[473], ensuring that parasites expressing the plasmid would survive in the presence of WR99210.

Cultures examined the week following transfection showed increased levels of cell debris and high gametocytemias (Figure 4.19 C), both of which are indicative of heavily stressed parasites. This was expected since the transfection process forces parasites briefly maintained at very high parasitemias to invade uRBCs damaged by electroporation. Even without applying heavy drug pressure, which transfectants later experience, the initial stresses of transfection result in significant parasite death and stress-induced gametocyte formation[474]. The FACS screening process began 15 days after transfection, continuing until day 95 for the double-transfectants. At that point, no viable parasites had been observed by FACS or Giemsa-stained smears, indicating that the double-transfections had failed. This could have occurred for several reasons, the most likely being that transfecting 2 plasmids at once is simply too inefficient with current *P. falciparum* transfection technologies. It is also possible that parasites acquired both plasmids and underwent Cas9 genome cutting, but the cut-site was improperly repaired or repaired with a template containing bacteria-derived replication errors such as those seen in Figure 4.18. If either of these scenarios occurred, then it would imply that *Pf3D7_1245600* is essential to parasite survival. This would not be entirely unexpected given the crucial roles kinesins perform in other organisms and cell types.

While the double-transfections failed, single-transfections with pCas9 alone succeeded for both HB3 and 3D7. Transfectants initially cultured in the presence of WR99210 but then cultured without it were detected by FACS 25 days after transfection (Figure 4.20 A). The addition of WR99210 back into the medium resulted in a decrease in parasitemia when measured on day 35, indicating that many of the detected parasites initially possessed pCas9 but subsequently lost it when no longer pressured by the presence of drug. A small proportion of parasites survived the renewed pressure and rebounded by day 45. Transfectants maintained under continuous WR99210 pressure were first detected by FACS 35 days after transfection and exceeded 0.5% parasitemia by day 45. After several additional replication cycles under continuous drug-pressure, HB3 cultures were combined and 3D7 cultures were combined since all parasites in each culture must have maintained pCas9 in order to survive so long. The presence of pCas9 was subsequently verified by PCR (Figure 4.21 A), and surface PfEMP1 levels measured by FACS clearly showed that pCas9 did not impact the previously observed HB3 and 3D7 phenotypes (Figure 4.21 B). This was fully expected since pCas9 was specifically designed so that a guide RNA sequence would not be available to direct Cas9 activity. Though the single-transfectants alone could not address the primary aim of this chapter, parasites already possessing pCas9 could easily be re-transfected with pCGT, dramatically increasing the likelihood of obtaining successful allele-exchange transfectants. Furthermore, the single-transfectants can serve as a resource for additional genetic manipulation studies given that transfection with only a single plasmid containing a guide RNA and a repair template would be necessary to achieve CRISPR-Cas9-driven genome editing.

Without *Pf3D7_1245600* allele-exchanged HB3 and 3D7 parasites available, the aim of this chapter could not be directly addressed. However, the manipulation of microtubules offered an opportunity to indirectly assess the role of kinesins in PfEMP1 trafficking (section 4.2.9). The potent microtubule inhibitor colchicine was used to disrupt microtubules in HB3 and 3D7 pRBCs after invasion of uRBCs had occurred. Surprisingly, the surface PfEMP1 levels of 3D7, but not HBS, pRBCs seemed largely unaffected by colchicine (Figure 4.22). Given that *Pf3D7_1245600* is predicted to harbor the genetic determinant of defective PfEMP1 trafficking in 3D7, it is possible that 3D7 has grown to rely on less efficient, non-kinesin-based pathways to export PfEMP1 to the pRBC surface. In that case, the disruption of microtubules would not be expected to have any effect on PfEMP1 trafficking. Alternatively, 3D7 may produce microtubules that are inherently resistant to colchicine disruption. An alignment of currently available HB3 and 3D7 sequences of the β-tubulin gene *Pf3D7_1008700* revealed the presence of 4 SNPs, though none were located in regions previously associated with colchicine binding[475,476]. With such a clear phenotype difference between HB3 and 3D7, colchicine inhibition of surface PfEMP1 display could serve as the phenotype for a future QTL experiment with the genetic cross progeny in order to implicate or exclude the SNPs of *Pf3D7_1008700*.

The scatterplot distribution of viable, colchicine-treated HB3 parasites (Figure 4.22 B) and the dose-dependent decrease in the normalized SG GMFI of colchicine-treated HB3 and 3D7 parasites (Figure 4.22 C) were of particular concern since the results suggested that colchicine was directly interfering with parasite development. If HB3 parasites were developmentally stunted, then the observed decreases in surface PfEMP1 levels may have simply been the result of parasites failing to reach the age at which PfEMP1 is normally displayed on the pRBC surface. To address this possibility, a second colchicine experiment was conducted, where parasites were examined at the usual 27-29 hour time point as well as 10 hours later. Figures 4.23 and 4.24 confirmed the observations made in the previous experiment and further showed that parasites continue to develop, albeit slowly, in the presence of colchicine. Surface PfEMP1 levels measured at each time point (Figure 4.25) once again showed a colchicine dose-dependent decrease with HB3, but not 3D7. Interestingly, PfEMP1 levels increased after an additional 10 hours of growth, suggesting that parasites would display normal levels of PfEMP1 on the pRBC surface if given enough time. This observation could be explained by a loss of colchicine activity considering that the plasma half-life of the drug is estimated to be 9 hours[477].

A final experiment was conducted to establish a window of colchicine activity in order to understand if PfEMP1 production, trafficking, or both were being affected by the loss of microtubules. Unlike previous experiments, MTG was substituted for SG so that only viable parasites would be used to establish surface PfEMP1 levels. As seen previously, 3D7 parasites were unaffected by colchicine regardless of the timing or duration of colchicine exposure (Figure 4.27). HB3 parasites initially exposed to colchicine for 6 or 10 hours made a near-complete recovery by the 27-29 hour time point (Figure 4.26). The decreased levels in 10 hour-treated parasites relative to 6 hour-treated parasites can be easily explained by the delayed growth parasites experienced during the additional 4 hours of colchicine exposure. The near recovery of both cultures suggested that PfEMP1 production was only marginally impacted. When colchicine was added after 6 hours of parasite growth, surface PfEMP1 levels resembled those of parasites continuously exposed to colchicine throughout the life cycle. However, this same effect was not seen when colchicine was added after 10 hours of parasite growth. One interpretation of these findings is that PfEMP1 production occurs primarily between 6 and 10 hours, meaning that parasites exposed to colchicine at 10 hours have already produced the majority of their PfEMP1 and are still able to export it if that process is microtubule-independent. Alternatively, the initial phase of PfEMP1 trafficking could occur between 6 and 10 hours, meaning that parasites have already produced the majority of their PfEMP1 but rely on microtubules, and by extension kinesins, to carry it to the parasite periphery for trafficking through the RBC cytoplasm. This interpretation is plausible given that neither microtubules nor *Pf3D7_1245600* are predicted to be exported out of the parasite, and that parasite-engineered proteins such as PfEMP1 must be relocated from the site of production to the parasitophorous vacuole for further transport to pRBC surface knobs. To truly refine the window of colchicine activity, a series of 1 hour removals and additions of the drug needs to be completed with HB3 pRBCs.

The results of the 3 microtubule disruption experiments provide the first examination of microtubules in the specific context of PfEMP1 display. The observation that colchicine broadly delays parasite development, particularly in HB3, certainly implicates microtubules in the general synthesis or transport of *P. falciparum* proteins, including PfEMP1. A similar conclusion was reached previously[478,479], where the synthesis of some parasite proteins was inhibited at the post-transcriptional level after trophozoites were exposed to the less toxic colchicine-derivative colcemid. The relationship of microtubules with protein synthesis is further supported by evidence in other organisms showing the association of ribosomes and mRNA translation complexes with microtubules and microtubule-dependent motor proteins[480–482].

Though the work in this thesis focused exclusively on post-translational aspects of PfEMP1, it would be interesting to consider the potential role of microtubules and kinesins in the regulation of *var* gene expression. Mutually-exclusive *var* gene expression has been experimentally disrupted by the pharmacological induction of filamentous actin formation, suggesting that actin polymerization is capable of relocating *var* genes to sites of active transcription[218]. The characterization of PfEMP1 variants expressed in untreated and colchicine-treated parasites of the same clone could reveal a similar role for microtubules in *var* gene expression or variant switching, especially if the depolymerization of the microtubule network enables the repositioning of chromosomes or the rearrangement of the genetic architecture contributing to mutually-exclusive *var* gene expression[216].

5 Conclusion

The virulence of *P. falciparum* can be largely attributed to the primary parasite virulence factor PfEMP1 due to the central role it plays in mediating pRBC cytoadherence to the microvascular endothelium. This falling out of circulation directly enables *P. falciparum* to survive and propagate in the human host by avoiding splenic clearance. Consequently, PfEMP1 serves as a very attractive therapeutic target for alleviating the morbidity and mortality of *P. falciparum* malaria, though directly targeting PfEMP1 as a strategy is greatly limited due to the protein's hypervariable nature. There are approximately 60 PfEMP1-encoding *var* genes per *P. falciparum* genome, and a recent study examining over 8,000 sequences of the DBLα sub-domain from 89 parasite isolates has revealed the staggering diversity of PfEMP1[191]. Interfering with the trafficking of PfEMP1 to the pRBC surface is an attractive approach, as hypervariability becomes relatively inconsequential and previous studies have demonstrated that reduced surface PfEMP1 levels significantly weaken pRBC cytoadherence[165,322], likely lessening the severity of malaria symptoms and promoting parasite clearance by the spleen. Although several proteins essential for the proper pRBC surface display of PfEMP1 are now known, further examination of the trafficking pathway will deepen the current understanding of *P. falciparum* pathogenesis and potentially lead to the discovery of novel therapeutic targets for interfering with PfEMP1 display.

The work presented in this thesis was performed to expand the current knowledge of PfEMP1 export by identifying novel pathway components using a phenotype-to-genotype experimental approach, summarized in Figure 5.1. This began by first challenging the common assumption that, although the particular variant may differ, all parasite lines naturally display the same amount of PfEMP1 on the pRBC surface. Previously reported Western blotting results indicated that 3D7 possessed an inherent defect in trafficking

PfEMP1 to the pRBC surface[326], leading to the general hypothesis that 3D7 harbors one or more genetic determinants of impaired PfEMP1 trafficking. Knowing that a genetic cross had been conducted with 3D7 and the presumably trafficking-competent parasite line HB3[331], there was an opportunity to identify the genetic determinant in 3D7 using QTL analysis as long as surface PfEMP1 level phenotypes could be obtained for both parents and several of their sequenced progeny.

Chapter 2 of this thesis details efforts to establish those phenotypes initially by Western blotting but more successfully by flow cytometry. Western blotting with an antibody against the conserved intracellular ATS domain of PfEMP1 is a well-established, quantifiable technique that overcomes the obstacle of PfEMP1 hypervariability[319,322,326]. Importantly, the success of this method in localizing PfEMP1 to the pRBC surface relies on the trypsin-sensitivity and Triton-insolubility of the protein[316]. Western blots of Triton-soluble and Triton-insoluble extracts from HB3 revealed a highly unusual pattern suggestive of parasites expressing at least 1 surface-exposed but Triton-soluble PfEMP1 variant and at least 1 trypsin-resistant but Triton-insoluble PfEMP1 variant, the presence of which immediately compromised any chance of localizing PfEMP1 to the pRBC surface. Trypsin-resistant PfEMP1 variants, though presumably uncommon, have been reported previously[236,388–390]. However, Triton-soluble, surface-exposed PfEMP1 has never been reported and seems to contradict all published work on PfEMP1 solubility.

The Triton-insoluble nature of PfEMP1 suggests that it is anchored to the RBC cytoskeleton, likely placing parasites expressing non-anchored PfEMP1 variants at a survival disadvantage given the essential role the RBC cytoskeleton and parasite knob architectural proteins play in pRBC cytoadherence[177,255,256,326]. The HB3 line used in this thesis was examined for the presence of pRBC surface knobs, but *in vitro* endothelial cytoadherence experiments were not performed. Furthermore, HB3 was never selected for a cytoadhering phenotype or for the expression of a particular PfEMP1 variant, meaning that

Chapter 2

Determine phenotype

Aims:

-Establish and characterize the natural difference in surface PfEMP1 levels between the *P. falciparum* laboratory lines HB3 and 3D7

-Establish surface PfEMP1 level phenotypes for 16 progeny from an HB3 x 3D7 genetic cross

Approaches:

-Western blotting using differential detergent extracts and an anti-ATS antibody specific to PfEMP1

-Flow cytometry using PfEMP1-unselected pRBCs and pooled hyperimmune plasma

Results:

-Distinct parental phenotypes and unimodal distribution of progeny phenotypes

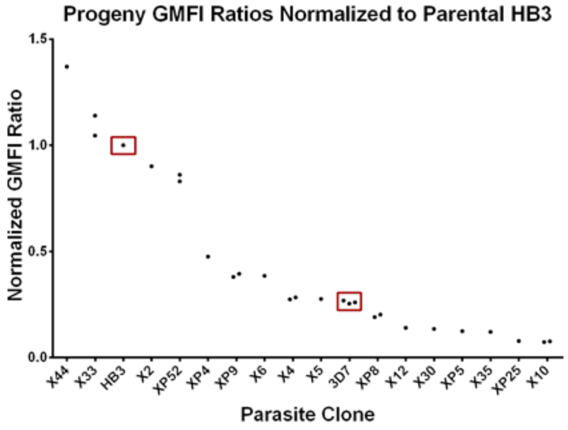

Chapter 3

Identify genotype

Aim:

-Identify any genetic polymorphisms associated with the impaired trafficking of PfEMP1 in 3D7

Approach:

-QTL analysis using genome-wide SNP markers and surface PfEMP1 level phenotypes

Results:

-Near-significant QTL on chromosome 12 containing the single gene *Pf3D7_1245600*

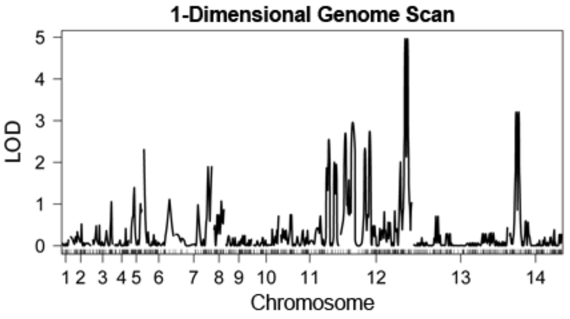

Chromosome	Marker Position (cM)	LOD Score
12	740.4	4.963
14	112.1	3.207

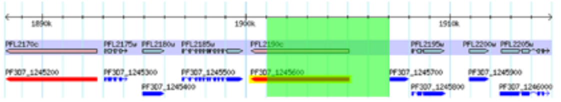

Chapter 4

Establish causality

Aims:

-Establish a causal relationship between the gene *Pf3D7_1245600* and PfEMP1 trafficking

-Examine the involvement of microtubules, and by extension kinesins, in the trafficking of PfEMP1

Approaches:

-Transfection of HB3 and 3D7 to achieve CRISPR-Cas9-driven allele-exchange of *Pf3D7_1245600*

-Flow cytometry analysis of HB3 and 3D7 parasites treated with the microtubule disruptor colchicine

Results:

-Failed to obtain double-transfected, allele-exchanged HB3 and 3D7 parasites

-Colchicine delays parasite growth and reduces surface PfEMP1 levels of HB3, but not 3D7, pRBCs

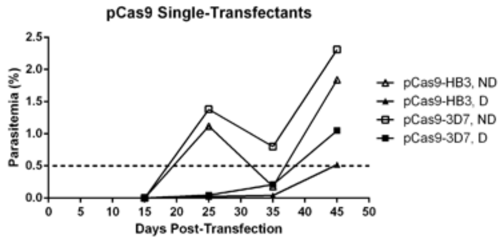

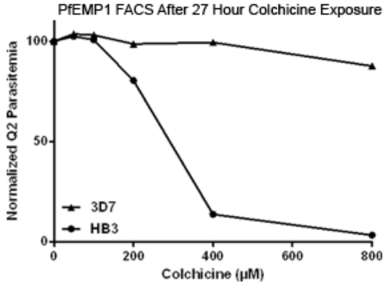

Figure 5.1: Overview of each experimental chapter, with summarized aims, approaches, and results.

the unusual Western blotting result may truly reflect the natural phenotype assumed by a proportion of the parasites during *in vitro* culture. If this is the case, prolonged *in vitro* culturing may have resulted in function-disrupting mutations affecting the internal knob architecture of HB3, echoing the common observation that laboratory-adapted parasites may not be representative of parasites in the field.

To overcome the issues encountered with Western blotting, a flow cytometry assay was developed to directly detect surface-displayed PfEMP1 using pooled, hyperimmune plasma. Though FACS has the advantages of being more reliable, more quantifiable, and higher throughput, it has the notable disadvantage of relying on the extracellular, hypervariable region of PfEMP1 for detection. The use of pooled, hyperimmune plasma to detect PfEMP1, which has been shown to be the primary target of naturally acquired blood-stage antibodies[153,154,198,257], mostly addresses the issue of hypervariability. No matter which PfEMP1 variant the parasite is expressing, it should be detectable. However, it may be possible for some variants to be more immuno-reactive than others, resulting in more plasma antibody binding and a brighter signal. In this case, parasites could display the same amount of PfEMP1, but some would appear much brighter simply because they display highly immuno-reactive PfEMP1 variants. Unfortunately, this potential problem cannot be totally resolved without using a monoclonal antibody directed against pRBCs selected for the expression of a particular PfEMP1 variant. A very preliminary attempt was made using a monoclonal antibody to detect VAR2CSA on unselected HB3 and 3D7 pRBCs, but neither parasite line reacted with the antibody even when a positive control line did.

To mitigate the potential problem of variable PfEMP1 immuno-reactivity, a pool of hyperimmune plasma samples was developed. If a particular PfEMP1 variant was strongly and weakly recognized by different plasma pool components, then 2 distinct plasma-positive populations would be expected. This was seen in HB3, but the different trypsin-sensitivity profiles of the populations suggested that they were 2 distinct PfEMP1 variants. Among the progeny that were only partially sensitive to trypsinization, a single plasma-positive population was always observed. This suggests that, despite displaying trypsin-sensitive and trypsin-resistant PfEMP1 variants, both were recognized equally well by the hyperimmune plasma pool. Ultimately, since 2 plasma-positive populations were only seen in HB3, the phenotypic distribution of the progeny would not be affected if the phenotypes were all normalized to HB3 in the same manner.

Given the PfEMP1-characteristic trypsin-sensitivity and frequent plasma pool component recognition of the brightest HB3 plasma-positive population, only those pRBCs were used to establish the phenotype of HB3. This resulted in HB3 possessing a normalized APC signal intensity approximately 75% brighter than 3D7. Such contrasting parental phenotypes suggested that the genetic determinant responsible could potentially be mapped by QTL analysis. With this goal in mind, surface PfEMP1 level phenotypes were successfully determined by FACS for 16 genetically unique progeny from an HB3 x 3D7 genetic cross. The resulting unimodal distribution of phenotypes demonstrated enough phenotypic variation to be considered for QTL analysis instead of simple linkage analysis. However, the somewhat bimodal nature of the distribution suggested that the phenotype could be driven by a single dominant locus with minor loci contributing to variation around the parental phenotypes.

With parental and progeny surface PfEMP1 levels established, existing full-genome and SNP data were refined into genetic marker maps for association with the phenotypes in QTL analysis as described in chapter 3. The results of the analysis identified a single near-significant QTL on chromosome 12 that, after refinement, was shown to contain a single protein-coding gene, *Pf3D7_1245600*, with at least 1 definitive non-synonymous SNP between HB3 and 3D7. The identification of such a narrow region in the genome was possible due to both the availability of full genome SNP data and naturally occurring genetic recombination events between HB3 and 3D7. Prior to using the SNP-based genetic marker maps described in this thesis, a very preliminary QTL analysis was conducted using maps constructed from 275 microsatellite markers, only 25 of which were on chromosome 12[483]. This analysis identified the same near-significant QTL, but the width of the peak spanned close to 100 kb and contained over 20 candidate genes. The large size of the QTL was the consequence of having microsatellite markers positioned far from the actual sites of recombination; an issue that was resolved with the use of SNP-based maps.

While an extensive set of genome-wide markers can significantly aid in the precise identification of a QTL, the occurrence and location of parental crossover events in the phenotyped progeny are far more important. It has been shown that, although the *P. falciparum* genome has a high recombination rate, the general rule for eukaryotic organisms of one crossover event per chromosome per meiosis is still followed[360]. Additionally, recombination does not generally occur around putative centromeres but occurs frequently at chromosomal ends and genomic "hotspots." If a putative QTL is located within a centromeric block of many genes, then no quantity of markers or phenotyped progeny will be able to refine its specific location to the single gene level since the recombination events nearest to the QTL would likely be many genes away. Conversely, just because a putative QTL is located within a genomic hotspot or near common recombination sites does not mean that it will be easily detected, as refining a QTL to the specific gene level is dependent on the inclusion of enough sufficiently recombined progeny in the analysis. However, QTL in genomic hotspots are likely to be detected with fewer progeny given that the high rates of recombination in those areas of the genome result in a higher probability of randomly selecting sufficiently recombined progeny for phenotyping.

Fortunately, *Pf3D7_1245600* appears to be located near a genomic hotspot in the HB3 x 3D7 genetic cross, which explains why only 16 progeny were needed to obtain a near-significant LOD score and gene-level refinement of the QTL. Though recombination maps are not freely available for the HB3 x 3D7 genetic cross progeny, a recently published analysis of 35 progeny from the HB3 x Dd2 genetic cross identified 2 progeny with crossover events at the nearest marker immediately upstream of *Pf3D7_1245600* and 1 progeny with a crossover event at the nearest marker immediately downstream of the gene[360]. Despite this being the most recombinogenic area on the distal arm of chromosome 12, excluding the subtelomeric region, this observed level of recombination would be considered too low for a crossover hotspot. However, the crossover behavior of HB3 and Dd2 may not be representative of the crossover behavior of HB3 and 3D7. Interestingly, the 7G8 x GB4 nonsubtelomeric hotspot-predictive sequence 5’-TGATGATGA[A/T][A/G][A/C]-3’ is found at base 1900145 on chromosome 12 in 3D7 as 5’-TGATGATGAAAA-3’, just upstream of *Pf3D7_1245600* at base 1900249. This may be indicative of a hotspot near *Pf3D7_1245600*, but HB3 x 3D7 progeny crossover maps are necessary to confirm if that is indeed the case.

It is interesting to speculate on the contribution of *Pf3D7_1245600* to *P. falciparum* virulence simply based on its location at a potential genomic hotspot. A survey of gene ontology terms in the 7G8 x GB4 recombination hotspots found statistically significant associations with genes responsible for antigenic variation, rosetting, cytoadherence, and very similar terms[360]. The only non-virulence term, and coincidentally the least significant, was protein deubiquitination. The survival of *P. falciparum* absolutely relies on the parasite’s ability to evade and adapt to the sophisticated human immune system. It has become increasingly clear that unique gene regulation mechanisms, high levels of polymorphisms, and frequent recombination, particularly among the *var* genes, all facilitate parasite survival. The location of *Pf3D7_1245600* at a potential hotspot suggests that the gene may play a crucial role in key virulence functions of *P. falciparum*, though neither *Pf3D7_1245600* nor any other putative parasite kinesins have been studied in the context of parasite virulence.

The prediction that *Pf3D7_1245600* encodes a putative kinesin is based on high sequence homology with the KISc motor domain of the human kinesin-like protein KIF20B, also known as KRMP1 and MPP1. KIF20B was originally identified as an M-phase phosphoprotein through a screen of proteins specifically phosphorylated at the mammalian cell cycle G_2/M transition[484,485]. It has since been characterized as a plus-end-directed kinesin-related protein necessary for the proper progression of cytokinesis in human cells[486]. The protein possesses an amino-terminal KISc-type motor domain, an unusually long coiled-coil stalk capable of dimerizing, and a carboxy-terminal domain that interacts with the WW domain of the essential peptidyl-prolyl isomerase Pin1[418]. The predicted *P. falciparum* gene *Pf3D7_0823200* likely encodes a WW domain based on high sequence homology, with an E-value of 1.31e-07, but an interaction between *Pf3D7_1245600* and *Pf3D7_0823200* would not necessarily be predicted given that the carboxy-terminus of *Pf3D7_1245600* is not at all homologous with that of KIF20B. If an association similar to KIF20B and Pin1 does occur between *Pf3D7_1245600* and *Pf3D7_0823200*, then the putative kinesin would be expected to play an important role in the regulation of mRNA transcription, splicing, and transport. However, Western blotting data for 3D7 suggests that PfEMP1 is transcribed normally but trafficked improperly, reducing the likelihood that *Pf3D7_1245600* contributes to impaired PfEMP1 trafficking in this manner.

A particularly intriguing potential role of *Pf3D7_1245600* can be inferred from an analysis of KIF20A, a kinesin-like protein very similar to KIF20B. KIF20A, also known as RB6K, and KIF20B both belong to the MKLP-1 protein subfamily and each contain the highly conserved KISc motor domain[418]. KIF20A and KIF20B are 890 and 1820 residues long, respectively, which partly explains why the 1605 residue *Pf3D7_1245600* associated with KIF20B over KIF20A when searching for protein homologs. Like KIF20B, KIF20A serves an essential role in cytokinesis[487], although the protein was first identified by its interaction with GTP-bound forms of Rab6 at the Golgi apparatus[488]. Rab6, which is homologous to PfRab6 encoded by *Pf3D7_1144900* in *P. falciparum*[489], plays a key role in directing intracellular vesicle transport[490]. The association of KIF20A with the protein fit nicely with previous observations of kinesin-mediated Golgi-to-endoplasmic reticulum vesicle transport in human cells[491–493]. Additionally, anti-kinesin antibodies and brefeldin A treatment were able to disrupt vesicle transport equally well, further solidifying the role of KIF20A in protein transport by vesicles.

This role of KIF20A has clear implications for the potential involvement of *Pf3D7_1245600* in *P. falciparum* protein transport. The generally conserved process of vesicle-mediated protein trafficking is present in *P. falciparum*, as demonstrated by the disruption of parasite protein export by brefeldin A treatment and the direct observation of PfEMP1-containing vesicles by electron microscopy[308,310,494,495]. Furthermore, *P. falciparum* possesses the basic components of a vesicle transport system, including a Rab6 homolog, an endoplasmic reticulum, and an endoplasmic reticulum-associated Golgi complex[496,497]. Additionally, when parasites are treated with AlF_4, an activator of GTP-binding proteins such as Rab6, the number of parasite-derived vesicles increases dramatically[494]. With so many of the components in place, it seems possible that *Pf3D7_1245600* could localize to the site of the Golgi-endoplasmic reticulum interaction and fulfill the vesicle transport role performed by KIF20A in human cells. Unfortunately, this potential role remains speculative since the Rab6-interacting carboxy-terminus of KIF20A is not homologous with the predicted carboxy-terminus of *Pf3D7_1245600*.

The identification of *Pf3D7_1245600* by QTL analysis was a very promising result from a functional standpoint. However, this did not guarantee that the gene was responsible for the impaired trafficking of PfEMP1 in 3D7. To better understand the role of *Pf3D7_1245600*, a causal relationship between the gene and PfEMP1 trafficking was sought through the application of CRISPR-Cas9 genome editing to HB3 and 3D7 allele-exchange transfection experiments (chapter 4). This approach would provide the most accurate and true-to-life results regarding the role of *Pf3D7_1245600* in PfEMP1 export while also using a highly accurate and novel genomic manipulation system. The first step in the process required the PCR amplification and sequencing of both parental alleles of *Pf3D7_1245600*, which verified the presence of the previously known SNP as well as identified several unreported indels and non-synonymous SNPs. 2 plasmids, pCas9 and pCGT, were then designed to efficiently exchange all of the sequence differences between HB3 and 3D7. Additionally, the placement of the Cas9 guide RNA and the break-site repair template together on pCGT ensured that parasites stably expressing pCas9 alone would not experience Cas9-medaited DNA cutting.

Unfortunately, parasites transfected with both pCas9 and pCGT failed to appear after 95 days of continuous culture in the presence and absence of drug pressure. Without allele-exchanged transfectants, a definitive causal relationship between *Pf3D7_1245600* and the impaired trafficking of PfEMP1 in 3D7 could not be established. The transfections could have failed for several reasons, the most likely being that transfecting 2 plasmids at once is simply too inefficient with current *P. falciparum* transfection technologies. This is understandable given that, after electroporation, a single RBC must hold both plasmids and still remain intact enough for a parasite to invade and grow. Even if this does occur, there is no guarantee that the parasite will spontaneously take up either of the plasmids. Alternatively, transfected parasites may have acquired both plasmids, but the double-strand DNA break induced by Cas9 could have been improperly repaired. This would likely have resulted in a frameshift mutation, effectively knocking out *Pf3D7_1245600*. If the putative kinesin fulfills roles similar to those of the human homologs KIF20A and KIF20B, then parasite mitosis would have been significantly impacted, likely killing the parasite.

Though the double transfections failed, single transfections with pCas9 alone resulted in HB3 and 3D7 parasites stably expressing the plasmid. These parasites will serve as a unique resource that can be further transfected with pCGT or any other pCas9 partner plasmid. Since the efficiency of single plasmid transfections is much higher than that of double plasmid transfections, allele-exchanging *Pf3D7_1245600* with the introduction of pCGT should not be a problem. If those re-transfections fail, then there would likely be a biological explanation accounting for the result, such as the improper repair of the DNA cut-site.

The overall aim of this thesis was to identify genetic determinants of impaired PfEMP1 trafficking in *P. falciparum*-infected erythrocytes. The completed work went as far as identifying and characterizing a promising candidate gene, but a definitive conclusion regarding the role of *Pf3D7_1245600* in PfEMP1 trafficking cannot be made without clear allele-exchange transfection results to establish causality. While those experiments will certainly be completed in the near future, an immediate effort was made to indirectly assess the potential contribution of the putative kinesin to PfEMP1 trafficking by disrupting the essential framework kinesins act upon– microtubules. The experiments described in chapter 4 provide the first known examination of microtubule involvement in PfEMP1 trafficking specifically, forming a foundation from which to explore a variety of novel research questions.

Microtubules have been examined in *P. falciparum* previously, most notably for their role in merozoite invasion[472,498,499], schizogony[499–501], and gametocyte development[502–504]. A recent study of microtubule expression throughout the asexual blood stage showed that microtubules generally compose <0.08% of the total protein in ring stage parasites, approximately 0.08% of the total protein in trophozoites, and approximately 0.15% of the total protein in schizonts[505]. This pattern is consistent with the well-defined role of microtubules in mitosis, or schizogony in *P. falciparum*. However, kinesins have been detected at each stage of the parasite[499], suggesting that microtubules may play important roles prior to mitosis. One of these roles has been identified as protein synthesis at the post-transcriptional level[479], where it has been proposed that microtubules may provide a scaffold on which ribosomes attach, as seen in other organism[480–482]. Interestingly, the inhibition of protein synthesis with the less-toxic colchicine derivative colcemid is achieved with an IC_{50}

of 260 µM, which is 2.4-fold higher than its IC_{50} for general parasite growth[479]. Since microtubules are known to be essential for merozoite invasion, this higher concentration may simply reflect the inability of colcemid to easily access protein synthesis compartments within the developing parasite compared to free merozoites.

The experiments described in chapter 4 were designed to elucidate the role of microtubules specifically during *P. falciparum* asexual development, between RBC invasion and schizogony. The strong reduction in surface PfEMP1 levels observed in HB3 suggested that microtubules played a crucial role in protein trafficking. However, a closer examination of colchicine-treated parasites revealed an overall reduction in growth, suggesting that the role of microtubules may not be PfEMP1-specific but broadly parasite development-specific. This finding is potentially in agreement with the previous observation that microtubule-depolymerizing agents globally reduce parasite protein synthesis[479], though proteins other than PfEMP1 were not examined as part of this thesis.

An interesting alternative role for microtubules can be inferred from previously reported experiments using Rab6-inhibitory analogs of GTP in *P. falciparum*[320]. In humans, Rab6 and other GTP-hydrolyzing enzymes are responsible for regulating and targeting vesicle transport from the Golgi apparatus to other destinations throughout the cell, as well as to the cell membrane[506]. The introduction of slowly hydrolyzable analogs of GTP to A4 parasites resulted in decreased surface PfEMP1 levels and a general reduction in parasite growth; the same effects observed in HB3 upon colchicine treatment. Furthermore, when treated A4 parasites were re-examined after an additional 10 hours of growth, surface PfEMP1 levels recovered and resembled those of untreated parasites, just like in the re-examined colchicine-treated HB3 parasites. These striking parallels seem to suggest that classical vesicle-mediated transport is essential to PfEMP1 trafficking and *P. falciparum* development. However, this system in *P. falciparum* is missing a key piece considering that Rab6 and microtubules have not been shown to interact directly. As described above, KIF20A has been shown to interact with both Rab6 and microtubules, facilitating the transport of vesicles between the Golgi and endoplasmic reticulum. The high sequence homology of *Pf3D7_1245600* with KIF20B, an extremely close relative of KIF20A, could reasonably place *Pf3D7_1245600* at the point of interaction between PfRab6 and microtubules.

The resistance of 3D7 to colchicine treatment, while intriguing, does not provide clear information on the role of microtubules, and by extension kinesins, in PfEMP1 trafficking. It is possible that microtubules do not play a significant role in protein export in 3D7, but this seems contrary to the general conservation of export processes in eukaryotes and the clear effects seen in HB3 parasites after colchicine treatment. However, if this is indeed the case, then 3D7 may have evolved to rely on a less-efficient, microtubule-independent pathway for PfEMP1 trafficking to compensate for a nonfunctional *Pf3D7_1245600*-encoded kinesin. It is also possible, and more likely, that 3D7 microtubules still function in protein trafficking but are fully resistant to depolymerization by colchicine. Though resistance to colchicine has not been reported in *P. falciparum*, resistance to the microtubule destabilizing agent vinblastine, which actively binds the β-tubulin subunit[507], has been reported[508]. Given that there are at least 4 SNPs in the β-tubulin gene *Pf3D7_1008700* of 3D7 compared to HB3, resistance to colchicine can reasonably explain the results seen in 3D7. If this is the case, then *Pf3D7_1245600* would have a microtubule framework to act upon, assuming the putative kinesin is at all functional in 3D7.

Since it appears that traditional vesicle-mediated protein trafficking does occur in *P. falciparum* to some extent, it is interesting to speculate on the functionality of the putative kinesin encoded by *Pf3D7_1245600* in 3D7. The numerous SNPs and indels detected between HB3 and 3D7 may simply result in a less functional kinesin rather than a totally non-functional one. This would explain why some PfEMP1 still appears on the pRBC surface. However, if *Pf3D7_1245600* is completely non-functional in 3D7, it is possible that another kinesin would compensate for the loss. It has been shown in human cells that the tasks of genetically knocked out kinesins are still accomplished, albeit less efficiently, indicating that systems of redundancy are in place among motor proteins[509–511]. *P. falciparum* encodes 9 putative kinesins, 3 of which are predicted to be kinesin-6 proteins[421]. If the other 2 kinesin-6 proteins are able to compensate for a non-functional *Pf3D7_1245600*, then PfEMP1 trafficking would still be able to occur, though in a less-efficient manner.

The putative roles of *P. falciparum* kinesins are still largely speculative since the protein class remains significantly understudied in the parasite. The first report on *P. falciparum* kinesins broadly addressed their general presence and role in merozoite development[499]. Subsequent studies focused exclusively on the catalytic core of the putative kinesin-13 protein encoded by *Pf3D7_1245100*[512–516]. This subclass of kinesins is unusual in that members possess a KinI-type motor domain that functions in depolymerizing microtubules rather than walking along them[517]. The most recent report on *P. falciparum* kinesins describes a small molecule screen against the putative kinesin-5 protein encoded by *Pf3D7_0317500*[421]. In all of the kinesin-13 and kinesin-5 studies, the experiments were conducted *in vitro* using bacterially-expressed protein, not actual kinesins in blood stage parasites. It seems unusual that an entire protein class known to be essential for the survival of virtually all cell types has been largely ignored in the *P. falciparum* research community. Most of the parasite kinesins remain putative and have only been categorized based on sequence homology with known human kinesins, of which there are 45[421]. *P. falciparum* only encodes 9 kinesins, yet this seems sufficient for the parasite to experience several morphologically distinct forms in multiple cell types within two incredibly different hosts. This extreme diversity, combined with the common lack of carboxy-terminus homology regions, suggests that parasite kinesins may play multiple roles depending on which stage of the parasite they are present in. However, this will remain speculation until more direct research is conducted on *P. falciparum* kinesins.

This thesis describes the application of a well-established phenotype-to-genotype approach to identify genetic determinants responsible for the impaired export of PfEMP1 in *P. falciparum*. The success of this strategy relied on the thorough characterization and direct comparison of the surface PfEMP1 levels of HB3, 3D7, and 16 progeny from an HB3 x 3D7 genetic cross. For only the second time[358], phenotypes developed for this specific cross were used in QTL analysis, leading to the identification of the putative kinesin *Pf3D7_1245600*. Despite being characteristically known for their roles in transporting intracellular cargo, kinesins have not been directly implicated in PfEMP1 trafficking or any specific parasite process until now. Though efforts to establish a causal link between *Pf3D7_1245600* and impaired PfEMP1 trafficking were unsuccessful, experiments examining the relationship between microtubules and surface PfEMP1 levels clearly implicate microtubules, and by extension kinesins, in the PfEMP1 trafficking process.

The association of *Pf3D7_1245600* and microtubules with PfEMP1 trafficking potentially resolves some persistent questions regarding the initial stages of PfEMP1 export. In particular, very little is currently known about how proteins within the parasite itself travel from site to site on their journey to the parasitophorous vacuole. A network of microtubules with cargo-transporting kinesins would elegantly explain the movement of PfEMP1 from the nucleus to the endoplasmic reticulum to the Golgi to anywhere else in the parasite. However, this remains largely speculative due to the significant lack of experimental evidence regarding *P. falciparum* kinesins and microtubules during blood stage development. With such an open line of questioning now available, there are many future experiments worth conducting to better understand PfEMP1 trafficking within the parasite.

First and foremost, a causal relationship between *Pf3D7_1245600* and impaired PfEMP1 export needs to be established by exchanging the alleles of HB3 and 3D7. This can be quickly accomplished by re-transfecting the stable pCas9-only HB3 and 3D7 parasites with pCGT, subcloning the stable transfectants, and measuring the surface PfEMP1 levels of the expanded clones. HB3 and 3D7 clones possessing exchanged surface PfEMP1 level phenotypes can then be sequenced to identify the specific SNP(s) responsible for the impaired function of *Pf3D7_1245600*. Once the role of the putative kinesin in PfEMP1 trafficking has been established, several basic functional experiments can be conducted to determine molecular characteristics of the protein, the most pertinent being cargo recognition and binding. Since *Pf3D7_1245600* possesses syntenic orthologs in every species of *Plasmodium*, it most likely serves in a trafficking role that is not PfEMP1-specific. Identifying what cargo the carboxy-terminus binds would help in localizing the protein to a specific region of the cell, such as the Golgi-endoplasmic reticulum interaction site, and further clarify what export pathway PfEMP1 likely proceeds through.

In addition to direct experiments with *Pf3D7_1245600*, it is certainly worth further exploring the roles of microtubules in PfEMP1 export, particularly given the unexpected phenotype of 3D7 parasites after colchicine treatment. To determine if 3D7 utilizes a microtubule-independent PfEMP1 trafficking pathway, parasites could be treated with microtubule disruptors such as vinblastine, curcumin, and nocodazole, which do not bind at the colchicine interaction site. If surface PfEMP1 levels are affected, then the β-tubulin subunit of 3D7 may harbor a SNP(s) capable of conferring colchicine resistance. If surface PfEMP1 levels remain unaffected, then 3D7 likely utilizes a trafficking pathway that HB3 seemingly does not. In that case, it would be interesting to phenotype the HB3 x 3D7 genetic cross progeny for their “resistance” to colchicine in order to potentially identify components of the alternative PfEMP1 trafficking pathway. To determine if microtubules contribute more to PfEMP1 expression or trafficking, colchicine can be added to and removed from HB3 parasites every hour to identify a specific window of colchicine activity.

An early window of activity would suggest that PfEMP1 expression is microtubule-dependent, while a later window would suggest that trafficking is.

The significant lack of research into *P. falciparum* kinesins and microtubules, particularly in protein export, presents a staggering abundance of possible experiments to pursue. The work described in this thesis has introduced parasite kinesins as likely contributors to PfEMP1 trafficking, but it remains unclear just how many kinesins are involved and at which specific steps they are involved in. The presence of kinesins in all species of *Plasmodium* suggests that they facilitate the general trafficking of parasite proteins, placing kinesins in a position to contribute much more significantly to *P. falciparum* virulence than previously considered. Furthermore, since kinesins likely facilitate the trafficking of the primary virulence factor during the blood stage, they may also traffic other critical proteins during the sexual and mosquito stages. The scope of this thesis remains limited to the specific involvement of *Pf3D7_1245600* in the trafficking of PfEMP1, but the implication of a significantly understudied class of proteins in the virulence of *P. falciparum* calls for a new perspective on these conserved eukaryotic systems in parasite-specific behaviors.

6 Bibliography

1. WHO. *World Malaria Report 2014*. (World Health Organization Press, 2014).

2. Liu, W. *et al.* Origin of the human malaria parasite Plasmodium falciparum in gorillas. *Nature* **467,** 420–425 (2010).

3. Prugnolle, F. *et al.* A fresh look at the origin of Plasmodium falciparum, the most malignant malaria agent. *PLoS Pathog.* **7,** (2011).

4. Liu, W. *et al.* African origin of the malaria parasite Plasmodium vivax. *Nat. Commun.* **5,** 3346 (2014).

5. Sternberg, G. M. The Malarial Germ of laveran. *Science* **7,** 297–299 (1886).

6. Ross, R. Observations on a Condition Necessary to the Transformation of the Malaria Crescent. *Br. Med. J.* **1,** 251–255 (1897).

7. Ross, R. The role of the mosquito in the evolution of the malarial parasite: the recent researches of Surgeon-Major Ronald Ross, I.M.S. 1898. *Yale J. Biol. Med.* **75,** 103–105 (2002).

8. Grassi, B., Bignami, A. & Bastianelli, G. Ulteriore ricerche sul ciclo dei parassiti malarici umani sul corpo del zanzarone. *Atti R. Accad Lincei* **8,** 21–28 (1899).

9. Grassi, B. *Studi di uno Zoologo Sulla Malaria*. (1900).

10. Ascenzi, A. Malaria diseases and parasites. *Parassitologia* **41,** 33–8 (1999).

11. Garnham, P. C. C. *Malaria Parasites and other Haemosporidia*. (Blackwell Scientific Publications, 1966).

12. Singh, B. *et al.* A large focus of naturally acquired Plasmodium knowlesi infections in human beings. *Lancet* **363,** 1017–1024 (2004).

13. Bruce, M. C., Alano, P., Duthie, S. & Carter, R. Commitment of the malaria parasite Plasmodium falciparum to sexual and asexual development. *Parasitology* **100 Pt 2,** 191–200 (1990).

14. Hawking, F., Wilson, M. E. & Gammage, K. Evidence for cyclic development and short-lived maturity in the gametocytes of Plasmodium falciparum. *Trans. R. Soc. Trop. Med. Hyg.* **65,** 549–559 (1971).

15. Sinden, R. E. Malaria, sexual development and transmission: retrospect and prospect. *Parasitology* **136,** 1427–1434 (2009).

16. Sinden, R. E. & Hartley, R. H. Identification of the meiotic division of malarial parasites. *J. Protozool.* **32,** 742–744 (1985).

17. Pimenta, P. F., Touray, M. & Miller, L. The journey of malaria sporozoites in the mosquito salivary gland. *J. Eukaryot. Microbiol.* **41,** 608–624 (1994).

18. Mota, M. M. *et al.* Migration of Plasmodium sporozoites through cells before infection. *Science* **291,** 141–144 (2001).

19. Müller, H. M. *et al.* Thrombospondin related anonymous protein (TRAP) of Plasmodium falciparum binds specifically to sulfated glycoconjugates and to HepG2 hepatoma cells suggesting a role for this molecule in sporozoite invasion of hepatocytes. *EMBO J.* **12,** 2881–2889 (1993).

20. Robson, K. J. H. Thrombospondin-related adhesive protein (TRAP) of Plasmodium falciparum: Expression during sporozoite ontogeny and binding to human hepatocytes. *Parasitol. Today* **11,** 410 (1995).

21. Cogswell, F. B. The hypnozoite and relapse in primate malaria. *Clinical Microbiology Reviews* **5,** 26–35 (1992).

22. Markus, M. B. Dormancy in mammalian malaria. *Trends Parasitol.* **28,** 39–45 (2012).

23. Clark, I. A., Alleva, L. M., Mills, A. C. & Cowden, W. B. Pathogenesis of malaria and clinically similar conditions. *Clinical Microbiology Reviews* **17,** 509–539 (2004).

24. Cowman, A. F. & Crabb, B. S. Invasion of red blood cells by malaria parasites. *Cell* **124,** 755–766 (2006).

25. Crosnier, C. *et al.* Basigin is a receptor essential for erythrocyte invasion by Plasmodium falciparum. *Nature* **480,** 534–537 (2011).

26. Cowman, A. F., Berry, D. & Baum, J. The cellular and molecular basis for malaria parasite invasion of the human red blood cell. *J. Cell Biol.* **198,** 961–71 (2012).

27. Nguitragool, W. *et al.* Malaria parasite clag3 genes determine channel-mediated nutrient uptake by infected red blood cells. *Cell* **145,** 665–677 (2011).

28. Lew, V. L., Tiffert, T. & Ginsburg, H. Excess hemoglobin digestion and the osmotic stability of Plasmodium falciparum - Infected red blood cells. *Blood* **101,** 4189–4194 (2003).

29. Liu, J., Istvan, E. S., Gluzman, I. Y., Gross, J. & Goldberg, D. E. Plasmodium falciparum ensures its amino acid supply with multiple acquisition pathways and redundant proteolytic enzyme systems. *Proc. Natl. Acad. Sci. U. S. A.* **103,** 8840–8845 (2006).

30. Sullivan, D. J., Gluzman, I. Y., Russell, D. G. & Goldberg, D. E. On the molecular mechanism of chloroquine's antimalarial action. *Proc. Natl. Acad. Sci. U. S. A.* **93,** 11865–11870 (1996).

31. Rowe, J. A., Claessens, A., Corrigan, R. A. & Arman, M. Adhesion of Plasmodium falciparum-infected erythrocytes to human cells: molecular mechanisms and therapeutic implications. *Expert Rev. Mol. Med.* **11,** e16 (2009).

32. Marchiafava, E. & Bignami, A. *On Summer-Autumn Malarial Fevers*. (New Sydenham Society, 1894).

33. Glushakova, S. *et al.* Hemoglobinopathic erythrocytes affect the intraerythrocytic multiplication of Plasmodium falciparum in vitro. *J. Infect. Dis.* **210,** 1100–1109 (2014).

34. Portugal, S., Pierce, S. K. & Crompton, P. D. Young lives lost as B cells falter: what we are learning about antibody responses in malaria. *J. Immunol.* **190,** 3039–46 (2013).

35. Smith, T. G., Lourenço, P., Carter, R., Walliker, D. & Ranford-Cartwright, L. C. Commitment to sexual differentiation in the human malaria parasite, Plasmodium falciparum. *Parasitology* **121 (Pt 2,** 127–133 (2000).

36. Baker, D. A. Malaria gametocytogenesis. *Mol. Biochem. Parasitol.* **172,** 57–65 (2010).

37. Williams, J. L. Stimulation of Plasmodium falciparum gametocytogenesis by conditioned medium from parasite cultures. *Am. J. Trop. Med. Hyg.* **60,** 7–13 (1999).

38. Mantel, P. Y. *et al.* Malaria-infected erythrocyte-derived microvesicles mediate cellular communication within the parasite population and with the host immune system. *Cell Host Microbe* **13,** 521–534 (2013).

39. Hay, S. I., Rogers, D. J., Toomer, J. F. & Snow, R. W. Annual Plasmodium falciparum entomological inoculation rates (EIR) across Africa: literature survey, Internet access and review. *Trans. R. Soc. Trop. Med. Hyg.* **94,** 113–127 (2000).

40. Smith, D. L., Dushoff, J., Snow, R. W. & Hay, S. I. The entomological inoculation rate and Plasmodium falciparum infection in African children. *Nature* **438,** 492–495 (2005).

41. Kilama, M. *et al.* Estimating the annual entomological inoculation rate for Plasmodium falciparum transmitted by Anopheles gambiae s.l. using three sampling methods in three sites in Uganda. *Malar. J.* **13,** 111 (2014).

42. Elissa, N. *et al.* Relationship between entomological inoculation rate, Plasmodium falciparum prevalence rate, and incidence of malaria attack in rural Gabon. *Acta Trop.* **85,** 355–361 (2003).

43. Snow, R. W., Guerra, C. A., Noor, A. M., Myint, H. Y. & Hay, S. I. The global distribution of clinical episodes of Plasmodium falciparum malaria. *Nature* **434,** 214–217 (2005).

44. Mwangangi, J. M. *et al.* Shifts in malaria vector species composition and transmission dynamics along the Kenyan coast over the past 20 years. *Malar. J.* **12,** 13 (2013).

45. Smith, D. L., Dushoff, J. & McKenzie, F. E. The risk of a mosquito-borne infectionin a heterogeneous environment. *PLoS Biol.* **2,** (2004).

46. Takken, W. & Knols, B. G. Odor-mediated behavior of Afrotropical malaria mosquitoes. *Annu. Rev. Entomol.* **44,** 131–157 (1999).

47. Noor, A. M. *et al.* The use of mosquito nets and the prevalence of Plasmodium falciparum infection in rural South Central Somalia. *PLoS One* **3,** e2081 (2008).

48. Sullivan, D. Uncertainty in mapping malaria epidemiology: Implications for control. *Epidemiol. Rev.* **32,** 175–187 (2010).

49. Greenwood, B., Marsh, K. & Snow, R. Why do some African children develop severe malaria? *Parasitol. Today* **7,** 277–281 (1991).

50. Gething, P. W. *et al.* A new world malaria map: Plasmodium falciparum endemicity in 2010. *Malar. J.* **10,** 378 (2011).

51. Karl, S. *et al.* A sub-microscopic gametocyte reservoir can sustain malaria transmission. *PLoS One* **6,** (2011).

52. Bousema, T., Okell, L., Felger, I. & Drakeley, C. Asymptomatic malaria infections: detectability, transmissibility and public health relevance. *Nat. Rev. Microbiol.* **12,** 833–840 (2014).

53. Dal-Bianco, M. P. *et al.* High prevalence of asymptomatic Plasmodium falciparum infection in Gabonese adults. *Am. J. Trop. Med. Hyg.* **77,** 939–942 (2007).

54. Guindo, A., Fairhurst, R. M., Doumbo, O. K., Wellems, T. E. & Diallo, D. A. X-linked G6PD deficiency protects hemizygous males but not heterozygous females against severe malaria. *PLoS Med.* **4,** 516–522 (2007).

55. Wilairatana, P., Tangpukdee, N. & Krudsood, S. Definition of hyperparasitemia in severe falciparum malaria should be updated. *Asian Pac. J. Trop. Biomed.* **3,** 586 (2013).

56. WHO. *Guidelines for the treatment of malaria*. (World Health Organization Press, 2010).

57. Karunaweera, N. D., Grau, G. E., Gamage, P., Carter, R. & Mendis, K. N. Dynamics of fever and serum levels of tumor necrosis factor are closely associated during clinical paroxysms in Plasmodium vivax malaria. *Proc. Natl. Acad. Sci. U. S. A.* **89,** 3200–3203 (1992).

58. Karunaweera, N. D., Wijesekera, S. K., Wanasekera, D., Mendis, K. N. & Carter, R. The paroxysm of Plasmodium vivax malaria. *Trends Parasitol.* **19,** 188–193 (2003).

59. Taylor, T. E. *et al.* Differentiating the pathologies of cerebral malaria by postmortem parasite counts. *Nat. Med.* **10,** 143–145 (2004).

60. Perkins, D. J. *et al.* Severe malarial anemia: Innate immunity and pathogenesis. *Int. J. Biol. Sci.* **7,** 1427–1442 (2011).

61. Taylor, W. R. J., Hanson, J., Turner, G. D. H., White, N. J. & Dondorp, A. M. Respiratory manifestations of malaria. *Chest* **142,** 492–505 (2012).

62. Pasvol, G. The treatment of complicated and severe malaria. *British Medical Bulletin* **75-76,** 29–47 (2005).

63. Mishra, S. K., Panigrahi, P., Mishra, R. & Mohanty, S. Prediction of outcome in adults with severe falciparum malaria: a new scoring system. *Malar. J.* **6,** 24 (2007).

64. Van den Steen, P. E. *et al.* Pathogenesis of malaria-associated acute respiratory distress syndrome. *Trends Parasitol.* **29,** 346–358 (2013).

65. Reyburn, H. *et al.* Association of transmission intensity and age with clinical manifestations and case fatality of severe Plasmodium falciparum malaria. *JAMA* **293,** 1461–1470 (2005).

66. Carneiro, I. *et al.* Age-patterns of malaria vary with severity, transmission intensity and seasonality in sub-Saharan Africa: A systematic review and pooled analysis. *PLoS One* **5,** (2010).

67. Dondorp, A. M. *et al.* The relationship between age and the manifestations of and mortality associated with severe malaria. *Clin. Infect. Dis.* **47,** 151–157 (2008).

68. Marks, M. E. *et al.* Severe imported falciparum malaria among adults requiring intensive care: a retrospective study at the hospital for tropical diseases, London. *BMC Infect. Dis.* **13,** 118 (2013).

69. Genton, B. *et al.* Plasmodium vivax and mixed infections are associated with severe malaria in children: A prospective cohort study from Papua New Guinea. *PLoS Med.* **5,** 0881–0889 (2008).

70. Tjitra, E. *et al.* Multidrug-resistant Plasmodium vivax associated with severe and fatal malaria: A prospective study in Papua, Indonesia. *PLoS Med.* **5,** 0890–0899 (2008).

71. Kochar, S. K. *et al.* Acute attack of AIP (acute intermittent porphyria) with severe vivax malaria associated with convulsions: A case report. *J. Vector Borne Dis.* **46,** 307–309 (2009).

72. Andrade, B. B. *et al.* Severe Plasmodium vivax malaria exhibits marked inflammatory imbalance. *Malar. J.* **9,** 13 (2010).

73. Marsh, K. *et al.* Indicators of life-threatening malaria in African children. *N. Engl. J. Med.* **332,** 1399–1404 (1995).

74. Von Seidlein, L. *et al.* Predicting the clinical outcome of severe falciparum malaria in African children: Findings from a large randomized trial. *Clin. Infect. Dis.* **54,** 1080–1090 (2012).

75. Schantz-Dunn, J. & Nour, N. M. Malaria and pregnancy: a global health perspective. *Rev. Obstet. Gynecol.* **2,** 186–192 (2009).

76. McGregor, I. A., Wilson, M. E. & Billewicz, W. Z. Malaria infection of the placenta in The Gambia, West Africa; its incidence and relationship to stillbirth, birthweight and placental weight. *Trans. R. Soc. Trop. Med. Hyg.* **77,** 232–244 (1983).

77. Brabin, B. Fetal anaemia in malarious areas: its causes and significance. *Ann. Trop. Paediatr.* **12,** 303–10 (1992).

78. Beadle, C. *et al.* Diagnosis of malaria by detection of Plasmodium falciparum HRP-2 antigen with a rapid dipstick antigen-capture assay. *Lancet* **343,** 564–568 (1994).

79. Ashley, E. A. *et al.* Evaluation of three parasite lactate dehydrogenase-based rapid diagnostic tests for the diagnosis of falciparum and vivax malaria. *Malar. J.* **8,** 241 (2009).

80. Schlitzer, M. Antimalarial drugs - What is in use and what is in the pipeline. *Arch. Pharm. (Weinheim).* **341,** 149–163 (2008).

81. Olatunde, A. Chloroquine-resistant Plasmodium falciparum and malaria in Africa. *Trans. R. Soc. Trop. Med. Hyg.* **71,** 80–81 (1977).

82. White, N. J. *et al.* Averting a malaria disaster. *Lancet* **353,** 1965–1967 (1999).

83. Lengeler, C. Insecticide-treated bed nets and curtains for preventing malaria. *Cochrane Database Syst. Rev.* CD000363 (2004). doi:10.1002/14651858.CD000363.pub2

84. Pluess, B., Tanser, F. C., Lengeler, C. & Sharp, B. L. Indoor residual spraying for preventing malaria. *Cochrane Database Syst. Rev.* (2010). doi:10.1002/14651858.CD006657

85. Tusting, L. S. *et al.* Mosquito larval source management for controlling malaria. *Cochrane database Syst. Rev.* **8,** CD008923 (2013).

86. Agnandji, S. T. *et al.* A phase 3 trial of RTS,S/AS01 malaria vaccine in African infants. *N. Engl. J. Med.* **367,** 2284–95 (2012).

87. Wilby, K. J., Lau, T. T., Gilchrist, S. E. & Ensom, M. H. Mosquirix (RTS,S): A Novel Vaccine for the Prevention of Plasmodium falciparum Malaria. *Ann. Pharmacother.* **46,** 384–393 (2012).

88. Vanderberg, J. P., Nussenzweig, R. S., Most, H. & Orton, C. G. Protective immunity produced by the injection of x-irradiated sporozoites of plasmodium berghei. *J. Parasitol.* **54,** 1175–80 (1968).

89. Nussenzweig, R. S., Vanderberg, J. P., Most, H. & Orton, C. Specificity of protective immunity produced by x-irradiated Plasmodium berghei sporozoites. *Nature* **222,** 488–489 (1969).

90. Seder, R. A. *et al.* Protection against malaria by intravenous immunization with a nonreplicating sporozoite vaccine. *Science* **341,** 1359–65 (2013).

91. Sherman, I. W. Biochemistry of Plasmodium (malarial parasites). *Microbiol. Rev.* **43,** 453–495 (1979).

92. Thien, H. V., Kager, P. A. & Sauerwein, H. P. Hypoglycemia in falciparum malaria: is fasting an unrecognized and insufficiently emphasized risk factor? *Trends Parasitol.* **22,** 410–415 (2006).

93. Zolg, J. W., Macleod, A. J., Scaife, J. G. & Beaudoin, R. L. The accumulation of lactic acid and its influence on the growth of Plasmodium falciparum in synchronized cultures. *In Vitro* **20,** 205–215 (1984).

94. Sasi, P. *et al.* Metabolic acidosis and other determinants of hemoglobin-oxygen dissociation in severe childhood Plasmodium falciparum malaria. *Am. J. Trop. Med. Hyg.* **77,** 256–260 (2007).

95. Chotivanich, K. *et al.* Parasite multiplication potential and the severity of Falciparum malaria. *J. Infect. Dis.* **181,** 1206–1209 (2000).

96. Deans, A. M. *et al.* Low multiplication rates of African Plasmodium falciparum isolates and lack of association of multiplication rate and red blood cell selectivity with malaria virulence. *Am. J. Trop. Med. Hyg.* **74,** 554–563 (2006).

97. Simpson, J. A., Silamut, K., Chotivanich, K., Pukrittayakatnee, S. & White, N. J. Red cell selectivity in malaria: A study of multiple-infected erythrocytes. *Trans. R. Soc. Trop. Med. Hyg.* **93,** 165–168 (1999).

98. Rowe, J. A., Obiero, J., Marsh, K. & Raza, A. Short report: Positive correlation between rosetting and parasitemia in Plasmodium falciparum clinical isolates. *Am. J. Trop. Med. Hyg.* **66,** 458–460 (2002).

99. Rowe, J. A., Moulds, J. M., Newbold, C. I. & Miller, L. H. P. falciparum rosetting mediated by a parasite-variant erythrocyte membrane protein and complement-receptor 1. *Nature* **388,** 292–295 (1997).

100. Schnitzer, B., Sodeman, T., Mead, M. L. & Contacos, P. G. Pitting function of the spleen in malaria: ultrastructural observations. *Science* **177,** 175–177 (1972).

101. Buffet, P. A. *et al.* The pathogenesis of Plasmodium falciparum malaria in humans: Insights from splenic physiology. *Blood* **117,** 381–392 (2011).

102. David, P. H., Hommel, M., Miller, L. H., Udeinya, I. J. & Oligino, L. D. Parasite sequestration in Plasmodium falciparum malaria: spleen and antibody modulation of cytoadherence of infected erythrocytes. *Proc. Natl. Acad. Sci. U. S. A.* **80,** 5075–5079 (1983).

103. Pongponratn, E., Riganti, M., Punpoowong, B. & Aikawa, M. Microvascular sequestration of parasitized erythrocytes in human falciparum malaria: A pathological study. *Am. J. Trop. Med. Hyg.* **44,** 168–175 (1991).

104. Sherman, I. W., Eda, S. & Winograd, E. Cytoadherence and sequestration in Plasmodium falciparum: Defining the ties that bind. *Microbes Infect.* **5,** 897–909 (2003).

105. Magistrado, P. *et al.* VAR2CSA expression on the surface of placenta-derived Plasmodium falciparum-infected erythrocytes. *J. Infect. Dis.* **198,** 1071–1074 (2008).

106. Turner, L. *et al.* Severe malaria is associated with parasite binding to endothelial protein C receptor. *Nature* **498,** 502–5 (2013).

107. Kaul, D. K., Roth, E. F., Nagel, R. L., Howard, R. J. & Handunnetti, S. M. Rosetting of Plasmodium falciparum-infected red blood cells with uninfected red blood cells enhances microvascular obstruction under flow conditions. *Blood* **78,** 812–819 (1991).

108. Dondorp, A. M., Pongponratn, E. & White, N. J. Reduced microcirculatory flow in severe falciparum malaria: Pathophysiology and electron-microscopic pathology. *Acta Tropica* **89,** 309–317 (2004).

109. Faille, D. *et al.* Platelet-endothelial cell interactions in cerebral malaria: The end of a cordial understanding. *Thromb. Haemost.* **102,** 1093–1102 (2009).

110. Francischetti, I. M. B., Seydel, K. B. & Monteiro, R. Q. Blood coagulation, inflammation, and malaria. *Microcirculation* **15,** 81–107 (2008).

111. Turrini, F. *et al.* Phagocytosis of Plasmodium falciparum-infected human red blood cells by human monocytes: involvement of immune and nonimmune determinants and dependence on parasite developmental stage. *Blood* **80,** 801–808 (1992).

112. Looareesuwan, S. *et al.* Reduced erythrocyte survival following clearance of malarial parasitaemia in Thai patients. *Br. J. Haematol.* **67,** 473–478 (1987).

113. Looareesuwan, S. *et al.* Erythrocyte survival in severe falciparum malaria. *Acta Trop.* **48,** 263–270 (1991).

114. Jakeman, G. N., Saul, A., Hogarth, W. L. & Collins, W. E. Anaemia of acute malaria infections in non-immune patients primarily results from destruction of uninfected erythrocytes. *Parasitology* **119 (Pt 2,** 127–133 (1999).

115. Dörmer, P., Dietrich, M., Kern, P. & Horstmann, R. D. Ineffective erythropoiesis in acute human P. falciparum malaria. *Blut* **46,** 279–88 (1983).

116. Prentice, A. M. & Cox, S. E. Iron and Malaria Interactions: Research Needs From Basic Science to Global Policy. *Advances in Nutrition: An International Review Journal* **3,** 583–591 (2012).

117. Rubin, H. *et al.* Cloning, sequence determination, and regulation of the ribonucleotide reductase subunits from Plasmodium falciparum: a target for antimalarial therapy. *Proc. Natl. Acad. Sci. U. S. A.* **90,** 9280–9284 (1993).

118. Van Dooren, G. G., Stimmler, L. M. & McFadden, G. I. Metabolic maps and functions of the Plasmodium mitochondrion. *FEMS Microbiol. Rev.* **30,** 596–630 (2006).

119. Sato, S., Clough, B., Coates, L. & Wilson, R. J. M. Enzymes for heme biosynthesis are found in both the mitochondrion and plastid of the malaria parasite Plasmodium falciparum. *Protist* **155,** 117–125 (2004).

120. Demeure, C. E. *et al.* Anopheles mosquito bites activate cutaneous mast cells leading to a local inflammatory response and lymph node hyperplasia. *J. Immunol.* **174,** 3932–3940 (2005).

121. Lawaly, R. *et al.* Impact of mosquito bites on asexual parasite density and gametocyte prevalence in asymptomatic chronic plasmodium falciparum infections and correlation with IgE and IgG titers. *Infect. Immun.* **80,** 2240–2246 (2012).

122. Donovan, M. J. *et al.* Uninfected mosquito bites confer protection against infection with malaria parasites. *Infect. Immun.* **75,** 2523–2530 (2007).

123. Stoute, J. A. *et al.* A preliminary evaluation of a recombinant circumsporozoite protein vaccine against Plasmodium falciparum malaria. RTS,S Malaria Vaccine Evaluation Group. *N. Engl. J. Med.* **336,** 86–91 (1997).

124. John, C. C. *et al.* Antibodies to pre-erythrocytic Plasmodium falciparum antigens and risk of clinical malaria in Kenyan children. *J. Infect. Dis.* **197,** 519–526 (2008).

125. Behet, M. C. *et al.* Sporozoite immunization of human volunteers under chemoprophylaxis induces functional antibodies against pre-erythrocytic stages of Plasmodium falciparum. *Malar. J.* **13,** 136 (2014).

126. Finney, O. C. *et al.* Immunization with genetically attenuated P. falciparum parasites induces long-lived antibodies that efficiently block hepatocyte invasion by sporozoites. *Vaccine* **32,** 2135–2138 (2014).

127. Schmieg, J., Gonzalez-Aseguinolaza, G. & Tsuji, M. The role of natural killer T cells and other T cell subsets against infection by the pre-erythrocytic stages of malaria parasites. *Microbes Infect.* **5,** 499–506 (2003).

128. Epstein, J. E. *et al.* Live Attenuated Malaria Vaccine Designed to Protect Through Hepatic CD8+ T Cell Immunity. *Science* **334,** 475–480 (2011).

129. Hermsen, C. C. *et al.* Circulating concentrations of soluble granzyme A and B increase during natural and experimental Plasmodium falciparum infections. *Clin. Exp. Immunol.* **132,** 467–472 (2003).

130. Narum, D. L. *et al.* Antibodies against the Plasmodium falciparum receptor binding domain of EBA-175 block invasion pathways that do not involve sialic acids. *Infect. Immun.* **68,** 1964–1966 (2000).

131. Collins, C. R., Withers-Martinez, C., Hackett, F. & Blackman, M. J. An inhibitory antibody blocks interactions between components of the malarial invasion machinery. *PLoS Pathog.* **5,** (2009).

132. Triglia, T. *et al.* Plasmodium falciparum merozoite invasion is inhibited by antibodies that target the PfRH2a and b binding domains. *PLoS Pathog.* **7,** (2011).

133. Villasis, E. *et al.* Anti-Plasmodium falciparum invasion ligand antibodies in a low malaria transmission region, Loreto, Peru. *Malar. J.* **11,** 361 (2012).

134. Osier, F. H. *et al.* Opsonic phagocytosis of Plasmodium falciparum merozoites: mechanism in human immunity and a correlate of protection against malaria. *BMC Med.* **12,** 108 (2014).

135. Smith, J. D. *et al.* Identification of a Plasmodium falciparum intercellular adhesion molecule-1 binding domain: a parasite adhesion trait implicated in cerebral malaria. *Proc. Natl. Acad. Sci. U. S. A.* **97,** 1766–1771 (2000).

136. Beeson, J. G. *et al.* Antibodies to variant surface antigens of Plasmodium falciparum-infected erythrocytes and adhesion inhibitory antibodies are associated with placental malaria and have overlapping and distinct targets. *J. Infect. Dis.* **189,** 540–551 (2004).

137. Mo, M. *et al.* The C-terminal segment of the cysteine-rich interdomain of Plasmodium falciparum erythrocyte membrane protein 1 determines CD36 binding and elicits antibodies that inhibit adhesion of parasite-infected erythrocytes. *Infect. Immun.* **76,** 1837–1847 (2008).

138. Ghumra, A. *et al.* Immunisation with recombinant PfEMP1 domains elicits functional rosette-inhibiting and phagocytosis-inducing antibodies to Plasmodium falciparum. *PLoS One* **6,** (2011).

139. Celada, A., Cruchaud, A. & Perrin, L. H. Opsonic activity of human immune serum on in vitro phagocytosis of Plasmodium falciparum infected red blood cells by monocytes. *Clin. Exp. Immunol.* **47,** 635–644 (1982).

140. Muniz-Junqueira, M. I. & Tosta, C. E. Stages of in vitro phagocytosis of Plasmodium falciparum-infected erythrocytes by human monocytes. *Rev. Soc. Bras. Med. Trop.* **42,** 103–106 (2009).

141. Parroche, P. *et al.* Malaria hemozoin is immunologically inert but radically enhances innate responses by presenting malaria DNA to Toll-like receptor 9. *Proc. Natl. Acad. Sci. U. S. A.* **104,** 1919–1924 (2007).

142. Andersen, E. *et al.* Assessment of age-dependent immunity to malaria in transmigrants. *Am. J. Trop. Med. Hyg.* **56,** 647–649 (1997).

143. Doolan, D. L., Dobaño, C. & Baird, J. K. Acquired immunity to Malaria. *Clinical Microbiology Reviews* **22,** 13–36 (2009).

144. Griffin, J. T. *et al.* Gradual acquisition of immunity to severe malaria with increasing exposure. *Proc. R. Soc. B* **282,** 20142657 (2015).

145. Marsh, K. & Snow, R. W. Host-parasite interaction and morbidity in malaria endemic areas. *Philos. Trans. R. Soc. Lond. B. Biol. Sci.* **352,** 1385–1394 (1997).

146. Owusu-Agyei, S. *et al.* Incidence of symptomatic and asymptomatic Plasmodium falciparum infection following curative therapy in adult residents of northern Ghana. *Am. J. Trop. Med. Hyg.* **65,** 197–203 (2001).

147. Cohen, S., McGregor, I. A. & Carrington, S. Gamma-globulin and acquired immunity to human malaria. *Nature* **192,** 733–737 (1961).

148. Bouharoun-Tayoun, H., Attanath, P., Sabchareon, A., Chongsuphajaisiddhi, T. & Druilhe, P. Antibodies that protect humans against Plasmodium falciparum blood stages do not on their own inhibit parasite growth and invasion in vitro, but act in cooperation with monocytes. *J. Exp. Med.* **172,** 1633–1641 (1990).

149. Sabchareon, A. *et al.* Parasitologic and clinical human response to immunoglobulin administration in falciparum malaria. *Am. J. Trop. Med. Hyg.* **45,** 297–308 (1991).

150. Stanisie, D. I. *et al.* Immunoglobulin G subclass-specific responses against Plasmodium falciparum merozoite antigens are associated with control of parasitemia and protection from symptomatic illness. *Infect. Immun.* **77,** 1165–1174 (2009).

151. Greenhouse, B. *et al.* Antibodies to Plasmodium falciparum antigens predict a higher risk of malaria but protection from symptoms once parasitemic. *J. Infect. Dis.* **204,** 19–26 (2011).

152. Marsh, K. & Howard, R. J. Antigens induced on erythrocytes by P. falciparum: expression of diverse and conserved determinants. *Science* **231,** 150–153 (1986).

153. Bull, P. C. *et al.* Parasite antigens on the infected red cell surface are targets for naturally acquired immunity to malaria. *Nat. Med.* **4,** 358–360 (1998).

154. Piper, K. P., Roberts, D. J. & Day, K. P. Plasmodium falciparum: analysis of the antibody specificity to the surface of the trophozoite-infected erythrocyte. *Exp. Parasitol.* **91,** 161–169 (1999).

155. Mackintosh, C. L. *et al.* Acquisition of naturally occurring antibody responses to recombinant protein domains of Plasmodium falciparum erythrocyte membrane protein 1. *Malar. J.* **7,** 155 (2008).

156. Beeson, J. G., Chan, J.-A. & Fowkes, F. J. I. PfEMP1 as a target of human immunity and a vaccine candidate against malaria. *Expert Rev. Vaccines* **12,** 105–8 (2013).

157. Fried, M., Nosten, F., Brockman, a, Brabin, B. J. & Duffy, P. E. Maternal antibodies block malaria. *Nature* **395,** 851–852 (1998).

158. Ricke, C. H. *et al.* Plasma antibodies from malaria-exposed pregnant women recognize variant surface antigens on Plasmodium falciparum-infected erythrocytes in a parity-dependent manner and block parasite adhesion to chondroitin sulfate A. *J. Immunol.* **165,** 3309–3316 (2000).

159. Tuikue Ndam, N. G. *et al.* Dynamics of anti-VAR2CSA immunoglobulin G response in a cohort of senegalese pregnant women. *J. Infect. Dis.* **193,** 713–720 (2006).

160. Salanti, A. *et al.* Evidence for the involvement of VAR2CSA in pregnancy-associated malaria. *J. Exp. Med.* **200,** 1197–1203 (2004).

161. Chan, J.-A., Fowkes, F. J. I. & Beeson, J. G. Surface antigens of Plasmodium falciparum-infected erythrocytes as immune targets and malaria vaccine candidates. *Cell. Mol. Life Sci.* 3633–3657 (2014).

162. McCavit, T. L. Sickle cell disease. *Pediatr. Rev.* **33,** 195–204; quiz 205–6 (2012).

163. Taylor, S. M., Parobek, C. M. & Fairhurst, R. M. Haemoglobinopathies and the clinical epidemiology of malaria: A systematic review and meta-analysis. *Lancet Infect. Dis.* **12,** 457–468 (2012).

164. Fairhurst, R. M. *et al.* Abnormal display of PfEMP-1 on erythrocytes carrying haemoglobin C may protect against malaria. *Nature* **435,** 1117–1121 (2005).

165. Cholera, R. *et al.* Impaired cytoadherence of Plasmodium falciparum-infected erythrocytes containing sickle hemoglobin. *Proc. Natl. Acad. Sci. U. S. A.* **105,** 991–996 (2008).

166. Fairhurst, R. M., Bess, C. D. & Krause, M. A. Abnormal PfEMP1/knob display on Plasmodium falciparum-infected erythrocytes containing hemoglobin variants: Fresh insights into malaria pathogenesis and protection. *Microbes Infect.* **14,** 851–862 (2012).

167. Miller, L. H., Mason, S. J., Clyde, D. F. & McGinniss, M. H. The resistance factor to Plasmodium vivax in blacks. The Duffy-blood-group genotype, FyFy. *N. Engl. J. Med.* **295,** 302–304 (1976).

168. Welch, S. G., McGregor, I. A. & Williams, K. The Duffy blood group and malaria prevalence in Gambian West Africans. *Trans. R. Soc. Trop. Med. Hyg.* **71,** 295–296 (1977).

169. Langhi, D. M. & Bordin, J. O. Duffy blood group and malaria. *Hematology* **11,** 389–398 (2006).

170. Courtin, D. *et al.* G6PD A-variant influences the antibody responses to Plasmodium falciparum MSP2. *Infect. Genet. Evol.* **11,** 1287–1292 (2011).

171. The Malaria Genomic Epidemiology Network. Reappraisal of known malaria resistance loci in a large multicenter study. *Nat. Genet.* **46,** 1197–1204 (2014).

172. Louicharoen, C. *et al.* Positively selected G6PD-Mahidol mutation reduces Plasmodium vivax density in Southeast Asians. *Science* **326,** 1546–9 (2009).

173. Chen, Q., Schlichtherle, M. & Wahlgren, M. Molecular aspects of severe malaria. *Clinical Microbiology Reviews* **13,** 439–450 (2000).

174. Kyes, S., Horrocks, P. & Newbold, C. Antigenic variation at the infected red cell surface in malaria. *Annu. Rev. Microbiol.* **55,** 673–707 (2001).

175. Gardner, M. J. *et al.* Genome sequence of the human malaria parasite Plasmodium falciparum. *Nature* **419,** 498–511 (2002).

176. Su, X. Z. *et al.* The large diverse gene family var encodes proteins involved in cytoadherence and antigenic variation of Plasmodium falciparum-infected erythrocytes. *Cell* **82,** 89–100 (1995).

177. Oh, S. S. *et al.* Plasmodium falciparum erythrocyte membrane protein 1 is anchored to the actin-spectrin junction and knob-associated histidine-rich protein in the erythrocyte skeleton. *Mol. Biochem. Parasitol.* **108,** 237–247 (2000).

178. Mayer, C., Slater, L., Erat, M. C., Konrat, R. & Vakonakis, I. Structural analysis of the Plasmodium falciparum erythrocyte membrane protein 1 (PfEMP1) intracellular domain reveals a conserved interaction epitope. *J. Biol. Chem.* **287,** 7182–7189 (2012).

179. Knuepfer, E., Rug, M., Klonis, N., Tilley, L. & Cowman, A. F. Trafficking of the major virulence factor to the surface of transfected P falciparum-infected erythrocytes. *Blood* **105,** 4078–4087 (2005).

180. Smith, J. D., Subramanian, G., Gamain, B., Baruch, D. I. & Miller, L. H. Classification of adhesive domains in the Plasmodium falciparum Erythrocyte Membrane Protein 1 family. *Mol. Biochem. Parasitol.* **110,** 293–310 (2000).

181. Hiller, N. L. *et al.* A host-targeting signal in virulence proteins reveals a secretome in malarial infection. *Science* **306,** 1934–1937 (2004).

182. Marti, M., Good, R. T., Rug, M., Knuepfer, E. & Cowman, A. F. Targeting malaria virulence and remodeling proteins to the host erythrocyte. *Science* **306,** 1930–1933 (2004).

183. Smith, J. D. Molecular & Biochemical Parasitology The role of PfEMP1 adhesion domain classification in Plasmodium falciparum pathogenesis research. *Mol. Biochem. Parasitol.* **195,** 82–87 (2014).

184. Kraemer, S. M. *et al.* Patterns of gene recombination shape var gene repertoires in Plasmodium falciparum: comparisons of geographically diverse isolates. *BMC Genomics* **8,** 45 (2007).

185. Lavstsen, T., Salanti, A., Jensen, A. T. R., Arnot, D. E. & Theander, T. G. Sub-grouping of Plasmodium falciparum 3D7 var genes based on sequence analysis of coding and non-coding regions. *Malar. J.* **2,** 27 (2003).

186. Rask, T. S., Hansen, D. A., Theander, T. G., Gorm Pedersen, A. & Lavstsen, T. Plasmodium falciparum erythrocyte membrane protein 1 diversity in seven genomes--divide and conquer. *PLoS Comput. Biol.* **6,** (2010).

187. Lavstsen, T. *et al.* Plasmodium falciparum erythrocyte membrane protein 1 domain cassettes 8 and 13 are associated with severe malaria in children. *Proc. Natl. Acad. Sci.* **109,** E1791–E1800 (2012).

188. Oleinikov, A. V. *et al.* High throughput functional assays of the variant antigen PfEMP1 reveal a single domain in the 3D7 plasmodium falciparum genome that binds ICAM1 with high affinity and is targeted by naturally acquired neutralizing antibodies. *PLoS Pathog.* **5,** (2009).

189. Fowler, E. V, Peters, J. M., Gatton, M. L., Chen, N. & Cheng, Q. Genetic diversity of the DBLalpha region in Plasmodium falciparum var genes among Asia-Pacific isolates. *Mol. Biochem. Parasitol.* **120,** 117–126 (2002).

190. Trimnell, A. R. *et al.* Global genetic diversity and evolution of var genes associated with placental and severe childhood malaria. *Mol. Biochem. Parasitol.* **148,** 169–180 (2006).

191. Barry, A. E. *et al.* Population genomics of the immune evasion (var) genes of Plasmodium falciparum. *PLoS Pathog.* **3,** 1–9 (2007).

192. Sulistyaningsih, E., Fitri, L. E., Löscher, T. & Berens-Riha, N. Diversity of the var gene family of Indonesian Plasmodium falciparum isolates. *Malar. J.* **12,** 80 (2013).

193. Aguiar, J. C. *et al.* Agglutination of Plasmodium falciparum-infected erythrocytes from east and west African isolates by human sera from distant geographic regions. *Am J Trop Med Hyg* **47,** 621–32 (1992).

194. Bull, P. C. *et al.* Plasmodium falciparum-infected erythrocytes: agglutination by diverse Kenyan plasma is associated with severe disease and young host age. *J. Infect. Dis.* **182,** 252–259 (2000).

195. Nielsen, M. A. *et al.* Plasmodium falciparum variant surface antigen expression varies between isolates causing severe and nonsevere malaria and is modified by acquired immunity. *J. Immunol.* **168,** 3444–3450 (2002).

196. Cham, G. K. K. *et al.* Sequential, ordered acquisition of antibodies to Plasmodium falciparum erythrocyte membrane protein 1 domains. *J. Immunol.* **183,** 3356–3363 (2009).

197. Turner, L. *et al.* Antibodies against PfEMP1, RIFIN, MSP3 and GLURP are acquired during controlled Plasmodium falciparum malaria infections in naïve volunteers. *PLoS One* **6,** 1–8 (2011).

198. Chan, J. A. *et al.* Targets of antibodies against Plasmodium falciparum-infected erythrocytes in malaria immunity. *J. Clin. Invest.* **122,** 3227–3238 (2012).

199. Delves, C. J. *et al.* Identification of Plasmodium falciparum-infected mosquitoes using a probe containing repetitive DNA. *Mol. Biochem. Parasitol.* **32,** 105–112 (1989).

200. De Bruin, D., Lanzer, M. & Ravetch, J. V. The polymorphic subtelomeric regions of Plasmodium falciparum chromosomes contain arrays of repetitive sequence elements. *Proc. Natl. Acad. Sci. U. S. A.* **91,** 619–623 (1994).

201. Rubio, J. P., Thompson, J. K. & Cowman, A. F. The var genes of Plasmodium falciparum are located in the subtelomeric region of most chromosomes. *EMBO J.* **15,** 4069–4077 (1996).

202. Fischer, K. *et al.* Expression of var genes located within polymorphic subtelomeric domains of Plasmodium falciparum chromosomes. *Mol. Cell. Biol.* **17,** 3679–3686 (1997).

203. Freitas-Junior, L. H. *et al.* Frequent ectopic recombination of virulence factor genes in telomeric chromosome clusters of P. falciparum. *Nature* **407,** 1018–1022 (2000).

204. Taylor, H. M., Kyes, S. A. & Newbold, C. I. Var gene diversity in Plasmodium falciparum is generated by frequent recombination events. *Mol. Biochem. Parasitol.* **110,** 391–397 (2000).

205. Claessens, A. *et al.* Generation of Antigenic Diversity in Plasmodium falciparum by Structured Rearrangement of Var Genes During Mitosis. *PLoS Genet.* **10,** e1004812 (2014).

206. Hernandez-Rivas, R. *et al.* Expressed var genes are found in Plasmodium falciparum subtelomeric regions. *Mol. Cell. Biol.* **17,** 604–611 (1997).

207. Chen, Q. *et al.* Developmental selection of var gene expression in Plasmodium falciparum. *Nature* **394,** 392–395 (1998).

208. Scherf, A. *et al.* Antigenic variation in malaria: In situ switching, relaxed and mutually exclusive transcription of var genes during intra-erythrocytic development in Plasmodium falciparum. *EMBO J.* **17,** 5418–5426 (1998).

209. Joergensen, L. *et al.* Surface co-expression of two different PfEMP1 antigens on single plasmodium falciparum-infected erythrocytes facilitates binding to ICAM1 and PECAM1. *PLoS Pathog.* **6,** (2010).

210. Marty, A. J. *et al.* Evidence that Plasmodium falciparum chromosome end clusters are cross-linked by protein and are the sites of both virulence gene silencing and activation. *Mol. Microbiol.* **62,** 72–83 (2006).

211. Duraisingh, M. T. *et al.* Heterochromatin silencing and locus repositioning linked to regulation of virulence genes in Plasmodium falciparum. *Cell* **121,** 13–24 (2005).

212. Freitas-Junior, L. H. *et al.* Telomeric heterochromatin propagation and histone acetylation control mutually exclusive expression of antigenic variation genes in malaria parasites. *Cell* **121,** 25–36 (2005).

213. Tonkin, C. J. *et al.* Sir2 paralogues cooperate to regulate virulence genes and antigenic variation in Plasmodium falciparum. *PLoS Biol.* **7,** 0771–0788 (2009).

214. Jiang, L. *et al.* PfSETvs methylation of histone H3K36 represses virulence genes in Plasmodium falciparum. *Nature* **499,** 223–7 (2013).

215. Ralph, S. a, Scheidig-Benatar, C. & Scherf, A. Antigenic variation in Plasmodium falciparum is associated with movement of var loci between subnuclear locations. *Proc. Natl. Acad. Sci. U. S. A.* **102,** 5414–5419 (2005).

216. Lemieux, J. E. *et al.* Genome-wide profiling of chromosome interactions in Plasmodium falciparum characterizes nuclear architecture and reconfigurations associated with antigenic variation. *Mol. Microbiol.* **90,** 519–537 (2013).

217. Voss, T. S. *et al.* A var gene promoter controls allelic exclusion of virulence genes in Plasmodium falciparum malaria. *Nature* **439,** 1004–1008 (2006).

218. Zhang, Q. *et al.* A Critical role of perinuclear filamentous Actin in spatial repositioning and mutually exclusive expression of virulence genes in malaria parasites. *Cell Host Microbe* **10,** 451–463 (2011).

219. Kyes, S., Pinches, R. & Newbold, C. A simple RNA analysis method shows var and rif multigene family expression patterns in Plasmodium falciparum. *Mol. Biochem. Parasitol.* **105,** 311–315 (2000).

220. Horrocks, P., Pinches, R., Christodoulou, Z., Kyes, S. A. & Newbold, C. I. Variable var transition rates underlie antigenic variation in malaria. *Proc. Natl. Acad. Sci. U. S. A.* **101,** 11129–11134 (2004).

221. Roberts, D. J. *et al.* Rapid switching to multiple antigenic and adhesive phenotypes in malaria. *Nature* **357,** 689–692 (1992).

222. Peters, J. *et al.* High diversity and rapid changeover of expressed var genes during the acute phase of Plasmodium falciparum infections in human volunteers. *Proc. Natl. Acad. Sci. U. S. A.* **99,** 10689–10694 (2002).

223. Peters, J. M., Fowler, E. V, Krause, D. R., Cheng, Q. & Gatton, M. L. Differential changes in Plasmodium falciparum var transcription during adaptation to culture. *J. Infect. Dis.* **195,** 748–755 (2007).

224. Kaestli, M., Cortes, A., Lagog, M., Ott, M. & Beck, H.-P. Longitudinal assessment of Plasmodium falciparum var gene transcription in naturally infected asymptomatic children in Papua New Guinea. *J. Infect. Dis.* **189,** 1942–1951 (2004).

225. Wunderlich, G. *et al.* Rapid turnover of Plasmodium falciparum var gene transcripts and genotypes during natural non-symptomatic infections. *Rev. Inst. Med. Trop. Sao Paulo* **47,** 195–201 (2005).

226. Bachmann, A. *et al.* Highly co-ordinated var gene expression and switching in clinical Plasmodium falciparum isolates from non-immune malaria patients. *Cell. Microbiol.* **13,** 1397–1409 (2011).

227. Recker, M. *et al.* Antigenic variation in Plasmodium falciparum malaria involves a highly structured switching pattern. *PLoS Pathog.* **7,** (2011).

228. Gatton, M. L., Peters, J. M., Fowler, E. V. & Cheng, Q. Switching rates of Plasmodium falciparum var genes: Faster than we thought? *Trends Parasitol.* **19,** 202–208 (2003).

229. Frank, M., Dzikowski, R., Amulic, B. & Deitsch, K. Variable switching rates of malaria virulence genes are associated with chromosomal position. *Mol. Microbiol.* **64,** 1486–1498 (2007).

230. Wang, C. W. *et al.* The Plasmodium falciparum var gene transcription strategy at the onset of blood stage infection in a human volunteer. *Parasitol. Int.* **58,** 478–480 (2009).

231. Udeinya, I. J., Graves, P. M., Carter, R., Aikawa, M. & Miller, L. H. Plasmodium falciparum: effect of time in continuous culture on binding to human endothelial cells and amelanotic melanoma cells. *Exp. Parasitol.* **56,** 207–214 (1983).

232. Noble, R. *et al.* The antigenic switching network of Plasmodium falciparum and its implications for the immuno-epidemiology of malaria. *Elife* **2,** e01074 (2013).

233. Robinson, B. a., Welch, T. L. & Smith, J. D. Widespread functional specialization of Plasmodium falciparum erythrocyte membrane protein 1 family members to bind CD36 analysed across a parasite genome. *Mol. Microbiol.* **47,** 1265–1278 (2003).

234. Howell, D. P. G. *et al.* Mapping a common interaction site used by Plasmodium falciparum Duffy binding-like domains to bind diverse host receptors. *Mol. Microbiol.* **67,** 78–87 (2008).

235. Bengtsson, A. *et al.* A novel domain cassette identifies Plasmodium falciparum PfEMP1 proteins binding ICAM-1 and is a target of cross-reactive, adhesion-inhibitory antibodies. *J. Immunol.* **190,** 240–9 (2013).

236. Baruch, D. I., Gormely, J. A., Ma, C., Howard, R. J. & Pasloske, B. L. Plasmodium falciparum erythrocyte membrane protein 1 is a parasitized erythrocyte receptor for adherence to CD36, thrombospondin, and intercellular adhesion molecule 1. *Proc. Natl. Acad. Sci. U. S. A.* **93,** 3497–3502 (1996).

237. Janes, J. H. *et al.* Investigating the host binding signature on the Plasmodium falciparum PfEMP1 protein family. *PLoS Pathog.* **7,** (2011).

238. Berger, S. S. *et al.* Plasmodium falciparum Expressing Domain Cassette 5 Type PfEMP1 (DC5-PfEMP1) Bind PECAM1. *PLoS One* **8,** 1–14 (2013).

239. Yipp, B. G. *et al.* Differential roles of CD36, ICAM-1, and P-selectin in Plasmodium falciparum cytoadherence in vivo. *Microcirculation* **14,** 593–602 (2007).

240. Udomsangpetch, R. *et al.* Promiscuity of clinical Plasmodium falciparum isolates for multiple adhesion molecules under flow conditions. *J. Immunol.* **158,** 4358–4364 (1997).

241. Li, A. *et al.* Molecular mechanistic insights into the endothelial receptor mediated cytoadherence of Plasmodium falciparum-infected erythrocytes. *PLoS One* **6,** (2011).

242. Avril, M. *et al.* From the Cover: PNAS Plus: A restricted subset of var genes mediates adherence of Plasmodium falciparum-infected erythrocytes to brain endothelial cells. *Proceedings of the National Academy of Sciences* **109,** E1782–E1790 (2012).

243. Davis, S. P. *et al.* Plasmodium falciparum-induced CD36 clustering rapidly strengthens cytoadherence via p130CAS-mediated actin cytoskeletal rearrangement. *The FASEB Journal* **26,** 1119–1130 (2012).

244. Heddini, A. *et al.* Fresh isolates from children with severe Plasmodium falciparum malaria bind to multiple receptors. *Infect. Immun.* **69,** 5849–5856 (2001).

245. Bertin, G. I. *et al.* Expression of the Domain Cassette 8 Plasmodium falciparum Erythrocyte Membrane Protein 1 Is Associated with Cerebral Malaria in Benin. *PLoS One* **8,** 4–11 (2013).

246. Gamain, B., Smith, J. D., Viebig, N. K., Gysin, J. & Scherf, A. Pregnancy-associated malaria: Parasite binding, natural immunity and vaccine development. *Int. J. Parasitol.* **37,** 273–283 (2007).

247. Carlson, J. *et al.* Human cerebral malaria: association with erythrocyte rosetting and lack of anti-rosetting antibodies. *Lancet* **336,** 1457–1460 (1990).

248. Treutiger, C. J. *et al.* Rosette formation in Plasmodium falciparum isolates and anti-rosette activity of sera from Gambians with cerebral or uncomplicated malaria. *Am. J. Trop. Med. Hyg.* **46,** 503–510 (1992).

249. Rowe, J. A., Obeiro, J., Newbold, C. I. & Marsh, K. Plasmodium falciparum rosetting is associated with malaria severity in Kenya. *Infect. Immun.* **63,** 2323–2326 (1995).

250. Udomsangpetch, R., Todd, J., Carlson, J. & Greenwood, B. M. The effects of hemoglobin genotype and ABO blood group on the formation of rosettes by Plasmodium falciparum-infected red blood cells. *Am. J. Trop. Med. Hyg.* **48,** 149–153 (1993).

251. Chen, Q. *et al.* The semiconserved head structure of Plasmodium falciparum erythrocyte membrane protein 1 mediates binding to multiple independent host receptors. *J. Exp. Med.* **192,** 1–10 (2000).

252. Vogt, A. M. *et al.* Heparan sulfate on endothelial cells mediates the binding of Plasmodium falciparum-infected erythrocytes via the DBL1alpha domain of PfEMP1. *Blood* **101,** 2405–2411 (2003).

253. Vogt, A. M., Winter, G., Wahlgren, M. & Spillmann, D. Heparan sulphate identified on human erythrocytes: a Plasmodium falciparum receptor. *Biochem. J.* **381,** 593–597 (2004).

254. Kriek, N. *et al.* Characterization of the pathway for transport of the cytoadhereince-mediating protein, PfEMP1, to the host cell surface in malaria parasite-infected erythrocytes. *Mol. Microbiol.* **50,** 1215–1227 (2003).

255. Crabb, B. S. *et al.* Targeted gene disruption shows that knobs enable malaria-infected red cells to cytoadhere under physiological shear stress. *Cell* **89,** 287–296 (1997).

256. Rug, M., Prescott, S. W., Fernandez, K. M., Cooke, B. M. & Cowman, A. F. The role of KAHRP domains in knob formation and cytoadherence of P falciparum-infected human erythrocytes. *Blood* **108,** 370–378 (2006).

257. Leech, J. H., Barnwell, J. W., Miller, L. H. & Howard, R. J. Identification of a strain-specific malarial antigen exposed on the surface of Plasmodium falciparum-infected erythrocytes. *J. Exp. Med.* **159,** 1567–1575 (1984).

258. Scherf, A., Lopez-Rubio, J. J. & Riviere, L. Antigenic variation in Plasmodium falciparum. *Annu. Rev. Microbiol.* **62,** 445–470 (2008).

259. Zhang, Q. *et al.* From in vivo to in vitro: Dynamic analysis of plasmodium falciparum var gene expression patterns of patient isolates during adaptation to culture. *PLoS One* **6,** e20591 (2011).

260. Deitsch, K. W., Moxon, E. R. & Wellems, T. E. Shared themes of antigenic variation and virulence in bacterial, protozoal, and fungal infections. *Microbiol. Mol. Biol. Rev.* **61,** 281–293 (1997).

261. Kyes, S. A., Kraemer, S. M. & Smith, J. D. Antigenic variation in Plasmodium falciparum: Gene organization and regulation of the var multigene family. *Eukaryot. Cell* **6,** 1511–1520 (2007).

262. Maurer, G. Die malaria perniciosa. *Zentralbl Bakteriol Parasitenkd.* **23,** 695–719 (1902).

263. Langreth, S. G., Jensen, J. B., Reese, R. T. & Trager, W. Fine structure of human malaria in vitro. *J. Protozool.* **25,** 443–452 (1978).

264. Atkinson, C. T. & Aikawa, M. Ultrastructure of malaria-infected erythrocytes. *Blood Cells* **16,** 351–68 (1990).

265. Henrich, P., Kilian, N., Lanzer, M. & Cyrklaff, M. 3-D analysis of the Plasmodium falciparum Maurer's clefts using different electron tomographic approaches. *Biotechnol. J.* **4,** 888–894 (2009).

266. Lanzer, M., Wickert, H., Krohne, G., Vincensini, L. & Braun Breton, C. Maurer's clefts: A novel multi-functional organelle in the cytoplasm of Plasmodium falciparum-infected erythrocytes. *Int. J. Parasitol.* **36,** 23–36 (2006).

267. Hanssen, E. *et al.* Electron tomography of the Maurer's cleft organelles of Plasmodium falciparum-infected erythrocytes reveals novel structural features. *Mol. Microbiol.* **67,** 703–718 (2008).

268. Wickert, H., Göttler, W., Krohne, G. & Lanzer, M. Maurer's cleft organization in the cytoplasm of plasmodium falciparum-infected erythrocytes: new insights from three-dimensional reconstruction of serial ultrathin sections. *Eur. J. Cell Biol.* **83,** 567–582 (2004).

269. Wickert, H. *et al.* Evidence for trafficking of PfEMP1 to the surface of P. falciparum-infected erythrocytes via a complex membrane network. *Eur. J. Cell Biol.* **82,** 271–284 (2003).

270. Hanssen, E. *et al.* Cryo transmission X-ray imaging of the malaria parasite, P. falciparum. *J. Struct. Biol.* **173,** 161–168 (2011).

271. Behari, R. & Haldar, K. Plasmodium falciparum: protein localization along a novel, lipid-rich tubovesicular membrane network in infected erythrocytes. *Exp. Parasitol.* **79,** 250–259 (1994).

272. Elmendorf, H. G. & Haldar, K. Plasmodium falciparum exports the Golgi marker sphingomyelin synthase into a tubovesicular network in the cytoplasm of mature erythrocytes. *J. Cell Biol.* **124,** 449–462 (1994).

273. Spycher, C. *et al.* Genesis of and trafficking to the Maurer's clefts of Plasmodium falciparum-infected erythrocytes. *Mol. Cell. Biol.* **26,** 4074–4085 (2006).

274. Mcmillan, P. J. *et al.* Spatial and temporal mapping of the PfEMP1 export pathway in Plasmodium falciparum. *Cell. Microbiol.* **15,** 1401–1418 (2013).

275. Przyborski, J. M. The Maurer's clefts of Plasmodium falciparum: parasite-induced islands within an intracellular ocean. *Trends Parasitol.* **24,** 285–288 (2008).

276. Pachlatko, E. *et al.* MAHRP2, an exported protein of Plasmodium falciparum, is an essential component of Maurer's cleft tethers. *Mol. Microbiol.* **77,** 1136–1152 (2010).

277. Külzer, S. *et al.* Parasite-encoded Hsp40 proteins define novel mobile structures in the cytosol of the P. falciparum-infected erythrocyte. *Cell. Microbiol.* **12,** 1398–1420 (2010).

278. Külzer, S. *et al.* Plasmodium falciparum-encoded exported hsp70/hsp40 chaperone/co-chaperone complexes within the host erythrocyte. *Cell. Microbiol.* **14,** 1784–1795 (2012).

279. Grüring, C. *et al.* Development and host cell modifications of Plasmodium falciparum blood stages in four dimensions. *Nat. Commun.* **2,** 165 (2011).

280. Blisnick, T. *et al.* Pfsbp1, a Maurer's cleft Plasmodium falciparum protein, is associated with the erythrocyte skeleton. *Mol. Biochem. Parasitol.* **111,** 107–121 (2000).

281. Cooke, B. M. *et al.* A Maurer's cleft-associated protein is essential for expression of the major malaria virulence antigen on the surface of infected red blood cells. *J. Cell Biol.* **172,** 899–908 (2006).

282. Kilian, N. *et al.* Haemoglobin s and c affect the motion of maurer's clefts in plasmodium falciparum-infected erythrocytes. *Cell. Microbiol.* **15,** 1111–1126 (2013).

283. Cyrklaff, M. *et al.* Hemoglobins S and C Interfere with Actin Remodeling in Plasmodium falciparum-Infected Erythrocytes. *Science* **334,** 1283–1286 (2011).

284. Dixon, M. W. A. *et al.* Genetic ablation of a Maurer's cleft protein prevents assembly of the Plasmodium falciparum virulence complex. *Mol. Microbiol.* **81,** 982–993 (2011).

285. Lauer, S. A., Ghori, N. & Haldar, K. Sphingolipid synthesis as a target for chemotherapy against malaria parasites. *Proc. Natl. Acad. Sci. U. S. A.* **92,** 9181–9185 (1995).

286. Lauer, S. A., Rathod, P. K., Ghori, N. & Haldar, K. A membrane network for nutrient import in red cells infected with the malaria parasite. *Science* **276,** 1122–1125 (1997).

287. Lauer, S. *et al.* Vacuolar uptake of host components, and a role for cholesterol and sphingomyelin in malarial infection. *EMBO J.* **19,** 3556–3564 (2000).

288. Tamez, P. A. *et al.* An erythrocyte vesicle protein exported by the malaria parasite promotes tubovesicular lipid import from the host cell surface. *PLoS Pathog.* **4,** (2008).

289. Klemba, M. & Goldberg, D. E. Characterization of plasmepsin V, a membrane-bound aspartic protease homolog in the endoplasmic reticulum of Plasmodium falciparum. *Mol. Biochem. Parasitol.* **143,** 183–191 (2005).

290. Boddey, J. A. *et al.* An aspartyl protease directs malaria effector proteins to the host cell. *Nature* **463,** 627–631 (2010).

291. Russo, I. *et al.* Plasmepsin V licenses Plasmodium proteins for export into the host erythrocyte. *Nature* **463,** 632–636 (2010).

292. Chang, H. H. *et al.* N-terminal processing of proteins exported by malaria parasites. *Mol. Biochem. Parasitol.* **160,** 107–115 (2008).

293. Boddey, J. A., Moritz, R. L., Simpson, R. J. & Cowman, A. F. Role of the Plasmodium export element in trafficking parasite proteins to the infected erythrocyte. *Traffic* **10,** 285–299 (2009).

294. Osborne, A. R. *et al.* The host targeting motif in exported Plasmodium proteins is cleaved in the parasite endoplasmic reticulum. *Mol. Biochem. Parasitol.* **171,** 25–31 (2010).

295. Boddey, J. A. *et al.* Role of Plasmepsin V in Export of Diverse Protein Families from the Plasmodium falciparum Exportome. *Traffic* **14,** 532–550 (2013).

296. Sargeant, T. J. *et al.* Lineage-specific expansion of proteins exported to erythrocytes in malaria parasites. *Genome Biol.* **7,** R12 (2006).

297. Bhattacharjee, S., Stahelin, R. V., Speicher, K. D., Speicher, D. W. & Haldar, K. Endoplasmic reticulum PI(3)P lipid binding targets malaria proteins to the host cell. *Cell* **148,** 201–212 (2012).

298. De Koning-Ward, T. F. *et al.* A newly discovered protein export machine in malaria parasites. *Nature* **459,** 945–949 (2009).

299. Bullen, H. E. *et al.* Biosynthesis, localization, and macromolecular arrangement of the Plasmodium falciparum translocon of exported proteins (PTEX). *J. Biol. Chem.* **287,** 7871–7884 (2012).

300. Beck, J. R., Muralidharan, V., Oksman, A. & Goldberg, D. E. PTEX component HSP101 mediates export of diverse malaria effectors into host erythrocytes. *Nature* **511,** 592–595 (2014).

301. Matthews, K. *et al.* The Plasmodium translocon of exported proteins (PTEX) component thioredoxin-2 is important for maintaining normal blood-stage growth. *Mol. Microbiol.* **89,** 1167–1186 (2013).

302. Matz, J. M., Matuschewski, K. & Kooij, T. W. A. Two putative protein export regulators promote Plasmodium blood stage development in vivo. *Mol. Biochem. Parasitol.* **191,** 44–52 (2013).

303. Riglar, D. T. *et al.* Spatial association with PTEX complexes defines regions for effector export into Plasmodium falciparum-infected erythrocytes. *Nat. Commun.* **4,** 1415 (2013).

304. Maier, A. G., Cooke, B. M., Cowman, A. F. & Tilley, L. Malaria parasite proteins that remodel the host erythrocyte. *Nat. Rev. Microbiol.* **7,** 341–354 (2009).

305. Sleebs, B. E. *et al.* Inhibition of Plasmepsin V Activity Demonstrates Its Essential Role in Protein Export, PfEMP1 Display, and Survival of Malaria Parasites. *PLoS Biol.* **12,** 1–16 (2014).

306. Heiber, A. *et al.* Identification of New PNEPs Indicates a Substantial Non-PEXEL Exportome and Underpins Common Features in Plasmodium falciparum Protein Export. *PLoS Pathog.* **9,** (2013).

307. Hinterberg, K. *et al.* Plasmodium falciparum: the Pf332 antigen is secreted from the parasite by a brefeldin A-dependent pathway and is translocated to the erythrocyte membrane via the Maurer's clefts. *Experimental parasitology* **79,** 279–291 (1994).

308. Benting, J., Mattei, D. & Lingelbach, K. Brefeldin A inhibits transport of the glycophorin-binding protein from Plasmodium falciparum into the host erythrocyte. *Biochem. J.* **300 (Pt 3,** 821–826 (1994).

309. Grüring, C. *et al.* Uncovering common principles in protein export of malaria parasites. *Cell Host Microbe* **12,** 717–729 (2012).

310. Wickham, M. E. *et al.* Trafficking and assembly of the cytoadherence complex in Plasmodium falciparum-infected human erythrocytes. *EMBO J.* **20,** 5636–5649 (2001).

311. Lopez-Estraño, C., Bhattacharjee, S., Harrison, T. & Haldar, K. Cooperative domains define a unique host cell-targeting signal in Plasmodium falciparum-infected erythrocytes. *Proc. Natl. Acad. Sci. U. S. A.* **100,** 12402–12407 (2003).

312. Melcher, M. *et al.* Identification of a role for the PfEMP1 semi-conserved head structure in protein trafficking to the surface of Plasmodium falciparum infected red blood cells. *Cell. Microbiol.* **12,** 1446–1462 (2010).

313. Jiang, R. H. Y., Stahelin, R. V., Bhattacharjee, S. & Haldar, K. Eukaryotic virulence determinants utilize phosphoinositides at the ER and host cell surface. *Trends Microbiol.* **21,** 145–156 (2013).

314. Kale, S. D. *et al.* External Lipid PI3P Mediates Entry of Eukaryotic Pathogen Effectors into Plant and Animal Host Cells. *Cell* **142,** 284–295 (2010).

315. Fernandez, V. *et al.* Mosaic-like transcription of var genes in single Plasmodium falciparum parasites. *Mol. Biochem. Parasitol.* **121,** 195–203 (2002).

316. Papakrivos, J., Newbold, C. I. & Lingelbach, K. A potential novel mechanism for the insertion of a membrane protein revealed by a biochemical analysis of the Plasmodium falciparum cytoadherence molecule PfEMP-1. *Mol. Microbiol.* **55,** 1272–1284 (2005).

317. Spycher, C. *et al.* The Maurer's cleft protein MAHRP1 is essential for trafficking of PfEMP1 to the surface of Plasmodium falciparum-infected erythrocytes. *Mol. Microbiol.* **68,** 1300–1314 (2008).

318. Glenister, F. K. *et al.* Functional alteration of red blood cells by a megadalton protein of Plasmodium falciparum. *Blood* **113,** 919–928 (2009).

319. Maier, A. G. *et al.* Exported Proteins Required for Virulence and Rigidity of Plasmodium falciparum-Infected Human Erythrocytes. *Cell* **134,** 48–61 (2008).

320. Frankland, S. *et al.* Delivery of the malaria virulence protein PfEMP1 to the erythrocyte surface requires cholesterol-rich domains. *Eukaryot. Cell* **5,** 849–860 (2006).

321. Quadt, K. A. *et al.* The Density of Knobs on Plasmodium falciparum-Infected Erythrocytes Depends on Developmental Age and Varies among Isolates. *PLoS One* **7,** 1–8 (2012).

322. Horrocks, P. *et al.* PfEMP1 expression is reduced on the surface of knobless Plasmodium falciparum infected erythrocytes. *J. Cell Sci.* **118,** 2507–2518 (2005).

323. Barnwell, J. W., Howard, R. J. & Miller, L. H. Influence of the spleen on the expression of surface antigens on parasitized erythrocytes. *Ciba Found. Symp.* **94,** 117–36 (1983).

324. Aley, S. B., Sherwood, J. A. & Howard, R. J. Knob-positive and knob-negative Plasmodium falciparum differ in expression of a strain-specific malarial antigen on the surface of infected erythrocytes. *J. Exp. Med.* **160,** 1585–1590 (1984).

325. Israeli, A., Shapiro, M. & Ephros, M. A. Plasmodium falciparum malaria in an asplenic man. *Trans. R. Soc. Trop. Med. Hyg.* **81,** 233–234 (1987).

326. Waterkeyn, J. G. *et al.* Targeted mutagenesis of Plasmodium falciparum erythrocyte membrane protein 3 (PfEMP3) disrupts cytoadherence of malaria-infected red blood cells. *EMBO J.* **19,** 2813–2823 (2000).

327. Hanssen, E. *et al.* Targeted mutagenesis of the ring-exported protein-1 of Plasmodium falciparum disrupts the architecture of Maurer's cleft organelles. *Mol. Microbiol.* **69,** 938–953 (2008).

328. Day, K. P. *et al.* Genes necessary for expression of a virulence determinant and for transmission of Plasmodium falciparum are located on a 0.3-megabase region of chromosome 9. *Proc. Natl. Acad. Sci. U. S. A.* **90,** 8292–8296 (1993).

329. Barnes, D. A., Thompson, J., Triglia, T., Day, K. & Kemp, D. J. Mapping the genetic locus implicated in cytoadherence of Plasmodium falciparum to melanoma cells. *Mol. Biochem. Parasitol.* **66,** 21–29 (1994).

330. Bourke, P. F., Holt, D. C., Sutherland, C. J. & Kemp, D. J. Disruption of a novel open reading frame of Plasmodium falciparum chromosome 9 by subtelomeric and internal deletions can lead to loss or maintenance of cytoadherence. *Mol. Biochem. Parasitol.* **82,** 25–36 (1996).

331. Walliker, D. *et al.* Genetic analysis of the human malaria parasite Plasmodium falciparum. *Science* **236,** 1661–1666 (1987).

332. Trager, W. & Jensen, J. B. Human malaria parasites in continuous culture. *Science* **193,** 673–675 (1976).

333. Scott, K. L., Lecak, J. & Acker, J. P. Biopreservation of red blood cells: Past, present, and future. *Transfusion Medicine Reviews* **19,** 127–142 (2005).

334. Diggs, C., Joseph, K., Flemmings, B., Snodgrass, R. & Hines, F. Protein synthesis in vitro by cryopreserved Plasmodium falciparum. *Am. J. Trop. Med. Hyg.* **24,** 760–763 (1975).

335. Margos, G., Maier, W. A. & Seitz, H. M. Experiments on cryopreservation of Plasmodium falciparum. *Trop. Med. Parasitol.* **43,** 13–6 (1992).

336. Mathai, E. & Singh, B. A comparative study of two methods for the cryopreservation of Plasmodium falciparum. *Trans. R. Soc. Trop. Med. Hyg.* **83,** 469–70 (1989).

337. Hawking, F., Worms, M. J. & Gammage, K. 24- and 48-hour cycles of malaria parasites in the blood; their purpose, production and control. *Trans. R. Soc. Trop. Med. Hyg.* **62,** 731–65 (1968).

338. Hawking, F. The clock of the malaria parasite. *Sci. Am.* **222,** 123–31 (1970).

339. Garcia, C. R., Markus, R. P. & Madeira, L. Tertian and quartan fevers: temporal regulation in malarial infection. *J. Biol. Rhythms* **16,** 436–443 (2001).

340. Haynes, J. D., Diggs, C. L., Hines, F. A. & Desjardins, R. E. Culture of human malaria parasites Plasmodium falciparum. *Nature* **263,** 767–769 (1976).

341. Hoppe, H. C., Verschoor, J. A. & Louw, A. I. Plasmodium falciparum: a comparison of synchronisation methods for in vitro cultures. *Exp. Parasitol.* **72,** 464–467 (1991).

342. Naughton, J. A. & Bell, A. Studies on cell-cycle synchronization in the asexual erythrocytic stages of Plasmodium falciparum. *Parasitology* **134,** 331–337 (2007).

343. Lambros, C. & Vanderberg, J. P. Synchronization of Plasmodium falciparum erythrocytic stages in culture. *J. Parasitol.* **65,** 418–420 (1979).

344. Vernes, A. *et al.* Plasmodium falciparum strain-specific human antibody inhibits merozoite invasion of erythrocytes. *Am. J. Trop. Med. Hyg.* **33,** 197–203 (1984).

345. Wagner, M. A., Andemariam, B. & Desai, S. A. A two-compartment model of osmotic lysis in Plasmodium falciparum-infected erythrocytes. *Biophys. J.* **84,** 116–123 (2003).

346. Lanzer, M., Wertheimer, S. P., de Bruin, D. & Ravetch, J. V. Chromatin structure determines the sites of chromosome breakages in Plasmodium falciparum. *Nucleic Acids Res.* **22,** 3099–3103 (1994).

347. Pologe, L. G. & Ravetch, J. V. Large deletions result from breakage and healing of P. falciparum chromosomes. *Cell* **55,** 869–874 (1988).

348. Biggs, B. A., Kemp, D. J. & Brown, G. V. Subtelomeric chromosome deletions in field isolates of Plasmodium falciparum and their relationship to loss of cytoadherence in vitro. *Proc. Natl. Acad. Sci. U. S. A.* **86,** 2428–2432 (1989).

349. Pasvol, G., Wilson, R. J., Smalley, M. E. & Brown, J. Separation of viable schizont-infected red cells of Plasmodium falciparum from human blood. *Ann. Trop. Med. Parasitol.* **72,** 87–8 (1978).

350. Reese, R. T., Langreth, S. G. & Trager, W. Isolation of stages of the human parasite Plasmodium falciparum from culture and from animal blood. *Bull. World Health Organ.* **57,** 53–61 (1979).

351. Jensen, J. B. Concentration from continuous culture of erythrocytes infected with trophozoites and schizonts of Plasmodium falciparum. *Am. J. Trop. Med. Hyg.* **27,** 1274–1276 (1978).

352. Waterkeyn, J. G., Cowman, A. F. & Cooke, B. M. Plasmodium falciparum: gelatin enrichment selects for parasites with full-length chromosome 2. implications for cytoadhesion assays. *Exp. Parasitol.* **97,** 115–118 (2001).

353. Lelièvre, J., Berry, A. & Benoit-Vical, F. An alternative method for Plasmodium culture synchronization. *Exp. Parasitol.* **109,** 195–197 (2005).

354. Bhasin, V. K. & Trager, W. Gametocyte-forming and non-gametocyte-forming clones of Plasmodium falciparum. *Am. J. Trop. Med. Hyg.* **33,** 534–537 (1984).

355. Delemarre, B. J. & van der Kaay, H. J. Tropical malaria contracted the natural way in the Netherlands. *Ned. Tijdschr. Geneeskd.* **123,** 1981–2 (1979).

356. Ponnudurai, T., Leeuwenberg, A. D. & Meuwissen, J. H. Chloroquine sensitivity of isolates of Plasmodium falciparum adapted to in vitro culture. *Trop. Geogr. Med.* **33,** 50–4 (1981).

357. Berendt, a R., Simmons, D. L., Tansey, J., Newbold, C. I. & Marsh, K. Intercellular adhesion molecule-1 is an endothelial cell adhesion receptor for Plasmodium falciparum. *Nature* **341,** 57–59 (1989).

358. Ranford-Cartwright, L. C. & Mwangi, J. M. Analysis of malaria parasite phenotypes using experimental genetic crosses of Plasmodium falciparum. *International Journal for Parasitology* **42,** 529–534 (2012).

359. The Malaria Genomic Epidemiology Network. A global network for investigating the genomic epidemiology of malaria. *Nature* **456,** 732–737 (2008).

360. Jiang, H. *et al.* High recombination rates and hotspots in a Plasmodium falciparum genetic cross. *Genome Biology* **12,** R33 (2011).

361. Snounou, G. *et al.* Biased distribution of msp1 and msp2 allelic variants in Plasmodium falciparum populations in Thailand. *Trans. R. Soc. Trop. Med. Hyg.* **93,** 369–374 (1999).

362. Gardner, J. P., Pinches, R. A., Roberts, D. J. & Newbold, C. I. Variant antigens and endothelial receptor adhesion in Plasmodium falciparum. *Proc. Natl. Acad. Sci. U. S. A.* **93,** 3503–3508 (1996).

363. Maier, A. G. *et al.* Skeleton-binding protein 1 functions at the parasitophorous vacuole membrane to traffic PfEMP1 to the Plasmodium falciparum-infected erythrocyte surface. *Blood* **109,** 1289–1297 (2007).

364. Leech, J. H., Barnwell, J. W., Aikawa, M., Miller, L. H. & Howard, R. J. Plasmodium falciparum malaria: Association of knobs on the surface of infected erythrocytes with a histidine-rich protein and the erythrocyte skeleton. *J. Cell Biol.* **98,** 1256–1264 (1984).

365. Van Schravendijk, M. R., Pasloske, B. L., Baruch, D. I., Handunnetti, S. M. & Howard, R. J. Immunochemical characterization and differentiation of two ~300-KD erythrocyte membrane-associated proteins of Plasmodium falciparum, PfEMP1 and PfEMP3. *Am. J. Trop. Med. Hyg.* **49,** 552–565 (1993).

366. Laemmli, U. K. Cleavage of structural proteins during the assembly of the head of bacteriophage T4. *Nature* **227,** 680–685 (1970).

367. Fagan, T. Structural, functional and antigenic analysis of PfEMP-1, the major variant surface antigen of P. falciparum infected erythrocytes. (University of Oxford, 1999).

368. Staalsoe, T., Giha, H. A., Dodoo, D., Theander, T. G. & Hviid, L. Detection of antibodies to variant antigens on Plasmodium falciparum-infected erythrocytes by flow cytometry. *Cytometry* **35,** 329–336 (1999).

369. Dodoo, D. *et al.* Antibodies to variant antigens on the surfaces of infected erythrocytes are associated with protection from malaria in Ghanaian children. *Infect. Immun.* **69,** 3713–3718 (2001).

370. Pattanapanyasat, K., Webster, H. K., Udomsangpetch, R., Wanachiwanawin, W. & Yongvanitchit, K. Flow cytometric two-color staining technique for simultaneous determination of human erythrocyte membrane antigen and intracellular malarial DNA. *Cytometry* **13,** 182–187 (1992).

371. Schuck, D. C., Ribeiro, R. Y., Nery, A. A., Ulrich, H. & Garcia, C. R. S. Flow cytometry as a tool for analyzing changes in Plasmodium falciparum cell cycle following treatment with indol compounds. *Cytom. Part A* **79 A,** 959–964 (2011).

372. Wachsmuth, E. D. & Woodhams, R. L. A quantitative approach for immunofluorescence in microscopy: the use of antibody multilayers on nuclei. *Histochemistry* **38,** 339–350 (1974).

373. Zola, H., Neoh, S. H., Mantzioris, B. X., Webster, J. & Loughnan, M. S. Detection by immunofluorescence of surface molecules present in low copy numbers. High sensitivity staining and calibration of flow cytometer. *J. Immunol. Methods* **135,** 247–255 (1990).

374. Beaudry, J. T. *et al.* Ex-Vivo cytoadherence phenotypes of Plasmodium falciparum strains from Malian children with hemoglobins A, S, and C. *PLoS One* **9,** 1–7 (2014).

375. Duffy, M. F. *et al.* Broad analysis reveals a consistent pattern of var gene transcription in Plasmodium falciparum repeatedly selected for a defined adhesion phenotype. *Mol. Microbiol.* **56,** 774–788 (2005).

376. Silvestrini, F., Tibúrcio, M., Bertuccini, L. & Alano, P. Differential adhesive properties of sequestered asexual and sexual stages of Plasmodium falciparum on human endothelial cells are tissue independent. *PLoS One* **7,** 1–8 (2012).

377. Gölnitz, U., Albrecht, L. & Wunderlich, G. Var transcription profiling of Plasmodium falciparum 3D7: assignment of cytoadherent phenotypes to dominant transcripts. *Malar. J.* **7,** 14 (2008).

378. Hughes, K. R., Biagini, G. A. & Craig, A. G. Continued cytoadherence of Plasmodium falciparum infected red blood cells after antimalarial treatment. *Mol. Biochem. Parasitol.* **169,** 71–78 (2010).

379. Bengtsson, D. *et al.* A method for visualizing surface-exposed and internal PfEMP1 adhesion antigens in Plasmodium falciparum infected erythrocytes. *Malar. J.* **7,** 101 (2008).

380. Gruenberg, J., Allred, D. R. & Sherman, I. W. Scanning electron microscope-analysis of the protrusions (knobs) present on the surface of Plasmodium falciparum-infected erythrocytes. *J. Cell Biol.* **97,** 795–802 (1983).

381. Morel, F. M., Baker, R. F. & Wayland, H. Quantitation of human red blood cell fixation by glutaraldehyde. *J. Cell Biol.* **48,** 91–100 (1971).

382. Frankland, S. *et al.* Serum lipoproteins promote efficient presentation of the malaria virulence protein PfEMP1 at the erythrocyte surface. *Eukaryot. Cell* **6,** 1584–1594 (2007).

383. Sheetz, M. P. & Sawyer, D. Triton shells of intact erythrocytes. *J. Supramol. Struct.* **8,** 399–412 (1978).

384. Baruch, D. I. *et al.* Cloning the P. falciparum gene encoding PfEMP1, a malarial variant antigen and adherence receptor on the surface of parasitized human erythrocytes. *Cell* **82,** 77–87 (1995).

385. Sheetz, M. P. Integral membrane protein interaction with Triton cytoskeletons of erythrocytes. *Biochim. Biophys. Acta* **557,** 122–34 (1979).

386. Hsu, L. & Morrison, M. The interaction of human erythrocyte Band 3 with cytoskeletal components. *Arch. Biochem. Biophys.* **227,** 31–38 (1983).

387. Taylor, A. M., Boulter, J., Harding, S. E., Cölfen, H. & Watts, A. Hydrodynamic properties of human erythrocyte band 3 solubilized in reduced Triton X-100. *Biophys. J.* **76,** 2043–2055 (1999).

388. Chaiyaroj, S. C., Coppel, R. L., Magowan, C. & Brown, G. V. A Plasmodium falciparum isolate with a chromosome 9 deletion expresses a trypsin-resistant cytoadherence molecule. *Mol. Biochem. Parasitol.* **67,** 21–30 (1994).

389. Chaiyaroj, S. C., Coppel, R. L., Novakovic, S. & Brown, G. V. Multiple ligands for cytoadherence can be present simultaneously on the surface of Plasmodium falciparum-infected erythrocytes. *Proc. Natl. Acad. Sci. U. S. A.* **91,** 10805–10808 (1994).

390. Nielsen, M. a. *et al.* Plasmodium falciparum: VAR2CSA expressed during pregnancy-associated malaria is partially resistant to proteolytic cleavage by trypsin. *Exp. Parasitol.* **117,** 1–8 (2007).

391. Wellems, T. E. *et al.* Chloroquine resistance not linked to mdr-like genes in a Plasmodium falciparum cross. *Nature* **345,** 253–255 (1990).

392. Hayton, K. *et al.* Erythrocyte Binding Protein PfRH5 Polymorphisms Determine Species-Specific Pathways of Plasmodium falciparum Invasion. *Cell Host Microbe* **4,** 40–51 (2008).

393. Fisher, R. A. The Systematic Location of Genes by Means of Crossover Observations. *Am. Nat.* **56,** 406–411 (1922).

394. Haldane, J. B. S. & Smith, C. A. B. A new estimate of the linkage between the genes for colourblindness and haemophilia in man. *Ann. Eugen.* **14,** 10–31 (1947).

395. Barnard, G. A. Statistical Inference. *J. R. Stat. Soc. Ser. B-Methodological* **11,** 115–149 (1949).

396. Morton, N. E. Sequential tests for the detection of linkage. *Am. J. Hum. Genet.* **7,** 277–318 (1955).

397. Sidhu, A. B. S., Verdier-Pinard, D. & Fidock, D. A. Chloroquine resistance in Plasmodium falciparum malaria parasites conferred by pfcrt mutations. *Science* **298,** 210–213 (2002).

398. Geldermann, H. Investigations on inheritance of quantitative characters in animals by gene markers I. Methods. *Theor. Appl. Genet.* **46,** 319–330 (1975).

399. Lander, E. S. & Botstein, S. Mapping mendelian factors underlying quantitative traits using RFLP linkage maps. *Genetics* **121,** 185 (1989).

400. Broman, K. W. Review of statistical methods for QTL mapping in experimental crosses. *Lab Anim. (NY).* **30,** 44–52 (2001).

401. Soller, M., Brody, T. & Genizi, A. On the power of experimental designs for the detection of linkage between marker loci and quantitative loci in crosses between inbred lines. *Theor. Appl. Genet.* **47,** 35–39 (1976).

402. Sen, Ś. & Churchill, G. A. A statistical framework for quantitative trait mapping. *Genetics* **159,** 371–387 (2001).

403. Reilly Ayala, H. B., Wacker, M. A., Siwo, G. & Ferdig, M. T. Quantitative trait loci mapping reveals candidate pathways regulating cell cycle duration in Plasmodium falciparum. *BMC Genomics* **11,** 577 (2010).

404. R Core Team. R: A Language and Environment for Statistical Computing. (2014). at <http://www.r-project.org>

405. Broman, K. W., Wu, H., Sen, Ś. & Churchill, G. A. R/qtl: QTL mapping in experimental crosses. *Bioinformatics* **19,** 889–890 (2003).

406. Aurrecoechea, C. *et al.* PlasmoDB: A functional genomic database for malaria parasites. *Nucleic Acids Res.* **37,** 539–543 (2009).

407. Rutherford, K. *et al.* Artemis: sequence visualization and annotation. *Bioinformatics* **16,** 944–945 (2000).

408. Berriman, M. & Rutherford, K. Viewing and annotating sequence data with Artemis. *Brief. Bioinform.* **4,** 124–132 (2003).

409. Mitchell, A. *et al.* The InterPro protein families database : the classification resource after 15 years. *Nucleic Acids Res.* **43,** D213–221 (2015).

410. Apweiler, R. *et al.* A large-scale protein-function database. *Nature chemical biology* **6,** 785 (2010).

411. Apweiler, R. *et al.* Ongoing and future developments at the Universal Protein Resource. *Nucleic Acids Res.* **39,** 214–219 (2011).

412. Marchler-Bauer, A. & Bryant, S. H. CD-Search: Protein domain annotations on the fly. *Nucleic Acids Res.* **32,** 327–331 (2004).

413. Marchler-Bauer, A. *et al.* CDD: Specific functional annotation with the Conserved Domain Database. *Nucleic Acids Res.* **37,** 205–210 (2009).

414. Marchler-Bauer, A. *et al.* CDD: A Conserved Domain Database for the functional annotation of proteins. *Nucleic Acids Res.* **39,** 225–229 (2011).

415. Schultz, J., Copley, R. R., Doerks, T., Ponting, C. P. & Bork, P. SMART: a web-based tool for the study of genetically mobile domains. *Nucleic Acids Res.* **28,** 231–234 (2000).

416. Letunic, I., Doerks, T. & Bork, P. SMART : recent updates , new developments and status in 2015. *Nucleic Acids Res.* **43,** D257–260 (2015).

417. Finn, R. D. *et al.* Pfam: The protein families database. *Nucleic Acids Res.* **42,** 222–230 (2014).

418. Kamimoto, T., Zama, T., Aoki, R., Muro, Y. & Hagiwara, M. Identification of a Novel Kinesin-related Protein, KRMP1, as a Target for Mitotic Peptidyl-prolyl Isomerase Pin1. *J. Biol. Chem.* **276,** 37520–37528 (2001).

419. Janisch, K. M. *et al.* The vertebrate-specific Kinesin-6, Kif20b, is required for normal cytokinesis of polarized cortical stem cells and cerebral cortex size. *Development* **23,** 1–11 (2013).

420. Sapir, T. *et al.* Shootin1 acts in concert with KIF20B to promote polarization of migrating neurons. *J. Neurosci.* **33,** 11932–48 (2013).

421. Liu, L., Richard, J., Kim, S. & Wojcik, E. J. Small molecule screen for candidate antimalarials targeting Plasmodium Kinesin-5. *J. Biol. Chem.* **289,** 16601–16614 (2014).

422. Rovira-Graells, N. *et al.* Transcriptional variation in the malaria parasite Plasmodium falciparum. *Genome Res.* **22,** 925–938 (2012).

423. Sá, J. M. *et al.* Geographic patterns of Plasmodium falciparum drug resistance distinguished by differential responses to amodiaquine and chloroquine. *Proc. Natl. Acad. Sci. U. S. A.* **106,** 18883–18889 (2009).

424. Lewis, I. A. *et al.* Metabolic QTL Analysis Links Chloroquine Resistance in Plasmodium falciparum to Impaired Hemoglobin Catabolism. *PLoS Genet.* **10,** e1004085 (2014).

425. Mu, J. *et al.* Recombination hotspots and population structure in Plasmodium falciparum. *PLoS Biol.* **3,** (2005).

426. Verhey, K. J. & Hammond, J. W. Traffic control: regulation of kinesin motors. *Nat. Rev. Mol. Cell Biol.* **10,** 765–777 (2009).

427. Mullis, K. *et al.* Specific enzymatic amplification of DNA in vitro: The polymerase chain reaction. *Cold Spring Harb. Symp. Quant. Biol.* **51,** 263–273 (1986).

428. Saiki, R. K. *et al.* Primer-directed enzymatic amplification of DNA with a thermostable DNA polymerase. *Science* **239,** 487–491 (1988).

429. Benson, D. A. *et al.* GenBank. *Nucleic Acids Res.* **41,** 36–42 (2013).

430. Boratyn, G. M. *et al.* BLAST: a more efficient report with usability improvements. *Nucleic Acids Res.* **41,** 29–33 (2013).

431. Marsischky, G. & LaBaer, J. Many paths to many clones: A comparative look at high-throughput cloning methods. *Genome Research* **14,** 2020–2028 (2004).

432. Berrow, N. S., Alderton, D. & Owens, R. J. The precise engineering of expression vectors using high-throughput In-Fusion PCR cloning. *Methods Mol. Biol.* **498,** 75–90 (2009).

433. Hemsley, A., Arnheim, N., Toney, M. D., Cortopassi, G. & Galas, D. J. A simple method for site-directed mutagenesis using the polymerase chain reaction. *Nucleic Acids Research* **17,** 8915 (1989).

434. Sanger, F., Nicklen, S. & Coulson, A. R. DNA sequencing with chain-terminating inhibitors. *Proc. Natl. Acad. Sci. U. S. A.* **74,** 5463–5467 (1977).

435. Heiner, C. R., Hunkapiller, K. L., Chen, S. M., Glass, J. I. & Chen, E. Y. Sequencing multimegabase-template DNA with BigDye terminator chemistry. *Genome Res.* **8,** 557–561 (1998).

436. Thompson, J. D., Higgins, D. G. & Gibson, T. J. CLUSTAL W: improving the sensitivity of progressive multiple sequence alignment through sequence weighting, position-specific gap penalties and weight matrix choice. *Nucleic Acids Res.* **22,** 4673–4680 (1994).

437. Straimer, J. *et al.* K13-propeller mutations confer artemisinin resistance in Plasmodium falciparum clinical isolates. *Science (80-.).* 1–7 (2014). doi:10.1126/science.1260867

438. Comeaux, C. A., Coleman, B. I., Bei, A. K., Whitehurst, N. & Duraisingh, M. T. Functional analysis of epigenetic regulation of tandem RhopH1/clag genes reveals a role in Plasmodium falciparum growth. *Mol. Microbiol.* **80,** 378–390 (2011).

439. Bhaya, D., Davison, M. & Barrangou, R. CRISPR-Cas Systems in Bacteria and Archaea: Versatile Small RNAs for Adaptive Defense and Regulation. *Annual Review of Genetics* **45,** 273–297 (2011).

440. Jinek, M. *et al.* A Programmable Dual-RNA-Guided DNA Endonuclease in Adaptive Bacterial Immunity. *Science* **337,** 816–821 (2012).

441. Ghorbal, M. *et al.* Genome editing in the human malaria parasite Plasmodium falciparum using the CRISPR-Cas9 system. *Nat. Biotechnol.* **32,** 819–821 (2014).

442. Wagner, J. C., Platt, R. J., Goldfless, S. J., Zhang, F. & Niles, J. C. Efficient CRISPR-Cas9–mediated genome editing in Plasmodium falciparum. *Nat. Methods* **11,** 1–6 (2014).

443. Li, K., Wang, G., Andersen, T., Zhou, P. & Pu, W. T. Optimization of genome engineering approaches with the CRISPR/Cas9 system. *PLoS One* **9,** e105779 (2014).

444. Fidock, D. A. *et al.* Mutations in the P. falciparum digestive vacuole transmembrane protein PfCRT and evidence for their role in chloroquine resistance. *Mol. Cell* **6,** 861–871 (2000).

445. Raabe, A. *et al.* Genetic and transcriptional analysis of phosphoinositide-specific phospholipase C in Plasmodium. *Exp. Parasitol.* **129,** 75–80 (2011).

446. Hliscs, M., Nahar, C., Frischknecht, F. & Matuschewski, K. Expression Profiling of Plasmodium berghei HSP70 Genes for Generation of Bright Red Fluorescent Parasites. *PLoS One* **8,** e72771 (2013).

447. Fidock, D. A. & Wellems, T. E. Transformation with human dihydrofolate reductase renders malaria parasites insensitive to WR99210 but does not affect the intrinsic activity of proguanil. *Proc. Natl. Acad. Sci. U. S. A.* **94,** 10931–10936 (1997).

448. Mamoun, C. B., Gluzman, I. Y., Goyard, S., Beverley, S. M. & Goldberg, D. E. A set of independent selectable markers for transfection of the human malaria parasite Plasmodium falciparum. *Proc. Natl. Acad. Sci. U. S. A.* **96,** 8716–8720 (1999).

449. Barany, F. The TaqI ‘star’ reaction: strand preferences reveal hydrogen-bond donor and acceptor sites in canonical sequence recognition. *Gene* **65,** 149–165 (1988).

450. Wu, Y., Sifri, C. D., Lei, H. H., Su, X. Z. & Wellems, T. E. Transfection of Plasmodium falciparum within human red blood cells. *Proc. Natl. Acad. Sci. U. S. A.* **92,** 973–977 (1995).

451. Wu, Y., Kirkman, L. A. & Wellems, T. E. Transformation of Plasmodium falciparum malaria parasites by homologous integration of plasmids that confer resistance to pyrimethamine. *Proc. Natl. Acad. Sci. U. S. A.* **93,** 1130–1134 (1996).

452. Crabb, B. S., Triglia, T., Waterkeyn, J. G. & Cowman, A. F. Stable transgene expression in Plasmodium falciparum. *Mol. Biochem. Parasitol.* **90,** 131–144 (1997).

453. Wilson, D. W., Crabb, B. S. & Beeson, J. G. Development of fluorescent Plasmodium falciparum for in vitro growth inhibition assays. *Malar. J.* **9,** 152 (2010).

454. Lopaticki, S. *et al.* Reticulocyte and erythrocyte binding-like proteins function cooperatively in invasion of human erythrocytes by malaria parasites. *Infect. Immun.* **79,** 1107–1117 (2011).

455. Deitsch, K., Driskill, C. & Wellems, T. Transformation of malaria parasites by the spontaneous uptake and expression of DNA from human erythrocytes. *Nucleic Acids Res.* **29,** 850–853 (2001).

456. O'Donnell, R. A. *et al.* A genetic screen for improved plasmid segregation reveals a role for Rep20 in the interaction of Plasmodium falciparum chromosomes. *EMBO J.* **21,** 1231–1239 (2002).

457. Hasenkamp, S., Russell, K. T. & Horrocks, P. Comparison of the absolute and relative efficiencies of electroporation-based transfection protocols for Plasmodium falciparum. *Malar. J.* **11,** 210 (2012).

458. Janse, C. J., Ramesar, J. & Waters, A. P. High-efficiency transfection and drug selection of genetically transformed blood stages of the rodent malaria parasite Plasmodium berghei. *Nat. Protoc.* **1,** 346–356 (2006).

459. Caro, F., Miller, M. G. & DeRisi, J. L. Plate-based transfection and culturing technique for genetic manipulation of Plasmodium falciparum. *Malaria Journal* **11,** 22 (2012).

460. Kasozi, D., Mohring, F., Rahlfs, S., Meyer, A. J. & Becker, K. Real-Time Imaging of the Intracellular Glutathione Redox Potential in the Malaria Parasite Plasmodium falciparum. *PLoS Pathog.* **9,** 1–18 (2013).

461. Smilkstein, M., Sriwilaijaroen, N., Kelly, J. X., Wilairat, P. & Riscoe, M. Simple and Inexpensive Fluorescence-Based Technique for High-Throughput Antimalarial Drug Screening. *Antimicrob. Agents Chemother.* **48,** 1803–1806 (2004).

462. Johnson, J. D. *et al.* Assessment and continued validation of the malaria SYBR Green I-based fluorescence assay for use in malaria drug screening. *Antimicrob. Agents Chemother.* **51,** 1926–1933 (2007).

463. Skinner-Adams, T. S., Lawrie, P. M., Hawthorne, P. L., Gardiner, D. L. & Trenholme, K. R. Comparison of Plasmodium falciparum transfection methods. *Malar. J.* **2,** 19 (2003).

464. Crabb, B. S. *et al.* Transfection of the human malaria parasite Plasmodium falciparum. *Methods Mol. Biol.* **270,** 263–276 (2004).

465. Amaratunga, C., Neal, A. T. & Fairhurst, R. M. Flow cytometry-based analysis of artemisinin-resistant Plasmodium falciparum in the ring-stage survival assay. *Antimicrob. Agents Chemother.* **58,** 4938–4940 (2014).

466. Witkowski, B. *et al.* Novel phenotypic assays for the detection of artemisinin-resistant Plasmodium falciparum malaria in Cambodia: In-vitro and ex-vivo drug-response studies. *Lancet Infect. Dis.* **13,** 1043–1049 (2013).

467. Bloom, G. S. & Endow, S. A. Motor proteins 1: kinesins. *Protein Profile* **2,** 1105–71 (1995).

468. Vale, R. D. & Fletterick, R. J. The design plan of kinesin motors. *Annu. Rev. Cell Dev. Biol.* **13,** 745–777 (1997).

469. Hirokawa, N. Kinesin and dynein superfamily proteins and the mechanism of organelle transport. *Science (80-.).* **279,** 519–526 (1998).

470. Hastie, S. B. Interactions of colchicine with tubulin. *Pharmacol. Ther.* **51,** 377–401 (1991).

471. Uppuluri, S., Knipling, L., Sackett, D. L. & Wolff, J. Localization of the colchicine-binding site of tubulin. *Proc. Natl. Acad. Sci. U. S. A.* **90,** 11598–11602 (1993).

472. Bejon, P. A. *et al.* A role for microtubules in Plasmodium falciparum merozoite invasion. *Parasitology* **114 (Pt 1,** 1–6 (1997).

473. De Koning-Ward, T. F. *et al.* The selectable marker human dihydrofolate reductase enables sequential genetic manipulation of the Plasmodium berghei genome. *Mol. Biochem. Parasitol.* **106,** 199–212 (2000).

474. Roncalés, M., Vidal-Mas, J., Leroy, D. & Herreros, E. Comparison and optimization of different methods for the in vitro production of plasmodium falciparum gametocytes. *J. Parasitol. Res.* **2012,** 1–7 (2012).

475. Burns, R. G. Analysis of the colchicine-binding site of B-tubulin. *FEBS Lett.* **297,** 205–208 (1992).

476. Bell, A. Microtubule inhibitors as potential antimalarial agents. *Parasitology Today* **14,** 234–240 (1998).

477. Hardman, J. G., Limbird, L. E. & Gilman, A. G. *Goodman and Gilman's The Pharmacological Basis of Therapeutics*. 707 (McGraw-Hill, 2006).

478. Dieckmann-Schuppert, A. & Franklin, R. M. Mode of action of tubulozoles against Plasmodium falciparum in vitro. *Antimicrob. Agents Chemother.* **34,** 1529–1534 (1990).

479. Bell, A., Wernli, B. & Franklin, R. M. Effects of microtubule inhibitors on protein synthesis in Plasmodium falciparum. *Parasitol. Res.* **79,** 146–152 (1993).

480. Suprenant, K. A. Microtubules, ribosomes, and RNA: evidence for cytoplasmic localization and translational regulation. *Cell Motil. Cytoskeleton* **25,** 1–9 (1993).

481. Wilhelm, J. E. & Vale, R. D. RNA on the move: The mRNA localization pathway. *Journal of Cell Biology* **123,** 269–274 (1993).

482. Hamill, D., Davis, J., Drawbridge, J. & Suprenant, K. A. Polyribosome targeting to microtubules: Enrichment of specific mRNAs in a reconstituted microtubule preparation from sea urchin embryos. *J. Cell Biol.* **127,** 973–984 (1994).

483. Su, X. *et al.* A genetic map and recombination parameters of the human malaria parasite Plasmodium falciparum. *Science* **286,** 1351–1353 (1999).

484. Westendorf, J. M., Rao, P. N. & Gerace, L. Cloning of cDNAs for M-phase phosphoproteins recognized by the MPM2 monoclonal antibody and determination of the phosphorylated epitope. *Proc. Natl. Acad. Sci. U. S. A.* **91,** 714–718 (1994).

485. Matsumoto-Taniura, N., Pirollet, F., Monroe, R., Gerace, L. & Westendorf, J. M. Identification of novel M phase phosphoproteins by expression cloning. *Mol. Biol. Cell* **7,** 1455–1469 (1996).

486. Abaza, A. *et al.* M phase phosphoprotein 1 is a human plus-end-directed kinesin-related protein required for cytokinesis. *J. Biol. Chem.* **278,** 27844–27852 (2003).

487. Hill, E., Clarke, M. & Barr, F. a. The Rab6-binding kinesin, Rab6-KIFL, is required for cytokinesis. *EMBO J.* **19,** 5711–5719 (2000).

488. Echard, A. *et al.* Interaction of a Golgi-associated kinesin-like protein with Rab6. *Science* **279,** 580–585 (1998).

489. De Castro, F. A. *et al.* Identification of a family of Rab G-proteins in Plasmodium falciparum and a detailed characterisation of pfrab6. *Mol. Biochem. Parasitol.* **80,** 77–88 (1996).

490. Novick, P. & Zerial, M. The diversity of Rab proteins in vesicle transport. *Current Opinion in Cell Biology* **9,** 496–504 (1997).

491. Feiguin, F., Ferreira, A., Kosik, K. S. & Caceres, A. Kinesin-mediated organelle translocation revealed by specific cellular manipulations. *J. Cell Biol.* **127,** 1021–1039 (1994).

492. Lippincott-Schwartz, J., Cole, N. B., Marotta, A., Conrad, P. A. & Bloom, G. S. Kinesin is the motor for microtubule-mediated Golgi-to-ER membrane traffic. *J. Cell Biol.* **128,** 293–306 (1995).

493. Brown, A. K., Hunt, S. D. & Stephens, D. J. Opposing microtubule motors control motility, morphology and cargo segregation during ER-to-Golgi transport. *Biol. Open* 1–7 (2014). doi:10.1242/bio.20147633

494. Trelka, D. P., Schneider, T. G., Reeder, J. C. & Taraschi, T. F. Evidence for vesicle-mediated trafficking of parasite proteins to the host cell cytosol and erythrocyte surface membrane in Plasmodium falciparum infected erythrocytes. *Mol. Biochem. Parasitol.* **106,** 131–145 (2000).

495. Taraschi, T. F., Trelka, D., Martinez, S., Schneider, T. & O’Donnell, M. E. Vesicle-mediated trafficking of parasite proteins to the host cell cytosol and erythrocyte surface membrane in Plasmodium falciparum infected erythrocytes. *International Journal for Parasitology* **31,** 1381–1391 (2001).

496. Adisa, A. *et al.* Re-assessing the locations of components of the classical vesicle-mediated trafficking machinery in transfected Plasmodium falciparum. *Int. J. Parasitol.* **37,** 1127–1141 (2007).

497. Struck, N. S. *et al.* Spatial dissection of the cis- and trans-Golgi compartments in the malaria parasite Plasmodium falciparum. *Mol. Microbiol.* **67,** 1320–1330 (2008).

498. Fowler, R. E., Fookes, R. E., Lavin, F., Bannister, L. H. & Mitchell, G. H. Microtubules in Plasmodium falciparum merozoites and their importance for invasion of erythrocytes. *Parasitology* **117 (Pt 5,** 425–433 (1998).

499. Fowler, R. E. *et al.* Microtubule associated motor proteins of Plasmodium falciparum merozoites. *Mol. Biochem. Parasitol.* **117,** 187–200 (2001).

500. Read, M., Sherwin, T., Holloway, S. P., Gull, K. & Hyde, J. E. Microtubular organization visualized by immunofluorescence microscopy during erythrocytic schizogony in Plasmodium falciparum and investigation of post-translational modifications of parasite tubulin. *Parasitology* **106 (Pt 3,** 223–232 (1993).

501. Bannister, L. H. *et al.* Plasmodium falciparum apical membrane antigen 1 (PfAMA-1) is translocated within micronemes along subpellicular microtubules during merozoite development. *J. Cell Sci.* **116,** 3825–3834 (2003).

502. Sinden, R. E. Gametocytogenesis of Plasmodium falciparum in vitro: ultrastructural observations on the lethal action of chloroquine. *Ann. Trop. Med. Parasitol.* **76,** 15–23 (1982).

503. Dearnley, M. K. *et al.* Origin, composition, organization and function of the inner membrane complex of Plasmodium falciparum gametocytes. *J. Cell Sci.* **125,** 2053–2063 (2012).

504. Hliscs, M. *et al.* Organization and function of an actin cytoskeleton in Plasmodium falciparum gametocytes. *Cell. Microbiol.* (2014). doi:10.1111/cmi.12359

505. Fennell, B. J., Al-shatr, Z. A. & Bell, A. Isotype expression, post-translational modification and stage-dependent production of tubulins in erythrocytic Plasmodium falciparum. *Int. J. Parasitol.* **38,** 527–539 (2008).

506. Grigoriev, I. *et al.* Rab6 Regulates Transport and Targeting of Exocytotic Carriers. *Dev. Cell* **13,** 305–314 (2007).

507. Rai, S. S. & Wolff, J. Localization of the vinblastine-binding site on beta-tubulin. *J. Biol. Chem.* **271,** 14707–14711 (1996).

508. Usanga, E. A., O'Brien, E. & Luzzato, L. Mitotic inhibitors arrest the growth of Plasmodium falciparum. *FEBS Lett.* **209,** 23–27 (1986).

509. Goldstein, L. S. The kinesin superfamily: tails of functional redundancy. *Trends Cell Biol.* **1,** 93–98 (1991).

510. Uchida, A., Alami, N. H. & Brown, A. Tight functional coupling of kinesin-1A and dynein motors in the bidirectional transport of neurofilaments. *Mol. Biol. Cell* **20,** 4997–5006 (2009).

511. Hirokawa, N., Noda, Y., Tanaka, Y. & Niwa, S. Kinesin superfamily motor proteins and intracellular transport. *Nat. Rev. Mol. Cell Biol.* **10,** 682–696 (2009).

512. Moores, C. A. *et al.* A mechanism for microtubule depolymerization by KinI kinesins. *Mol. Cell* **9,** 903–909 (2002).

513. Moores, C. A., Hekmat-Nejad, M., Sakowicz, R. & Milligan, R. A. Regulation of KinI kinesin ATPase activity by binding to the microtubule lattice. *J. Cell Biol.* **163,** 963–971 (2003).

514. Shipley, K. *et al.* Structure of a kinesin microtubule depolymerization machine. *EMBO J.* **23,** 1422–1432 (2004).

515. Moores, C. A. & Milligan, R. A. Visualisation of a Kinesin-13 Motor on Microtubule End Mimics. *J. Mol. Biol.* **377,** 647–654 (2008).

516. Mulder, A. M. *et al.* A new model for binding of kinesin 13 to curved microtubule protofilaments. *J. Cell Biol.* **185,** 51–57 (2009).

517. Desai, A., Verma, S., Mitchison, T. J. & Walczak, C. E. Kin I kinesins are microtubule-destabilizing enzymes. *Cell* **96,** 69–78 (1999).